

2013

PHOTON FACTORY ACTIVITY REPORT

PART A : HIGHLIGHT AND FACILITY REPORT #31

Editorial Board

J. ADACHI
H. BAN
K. HIRANO*
A. HIRATA
G. ISHIKAWA
M. KAWASAKI
T. KIKEGAWA
M. KIMURA
Y. MISUMI
T. MIYAJIMA
H. NAKAO
K. ONO
H. SAKAI
H. SUGIYAMA
H. TOYAMA
N. USAMI
T. YAMASAKI

* editor in chief

KEK Progress Report 2014-5

© High Energy Accelerator Research Organization (KEK), 2014

KEK Reports are available from:

Library and Archives
High Energy Accelerator Research Organization (KEK)
1-1 Oho, Tsukuba, Ibaraki, 305-0801
JAPAN

E-mail: irdlib@mail.kek.jp

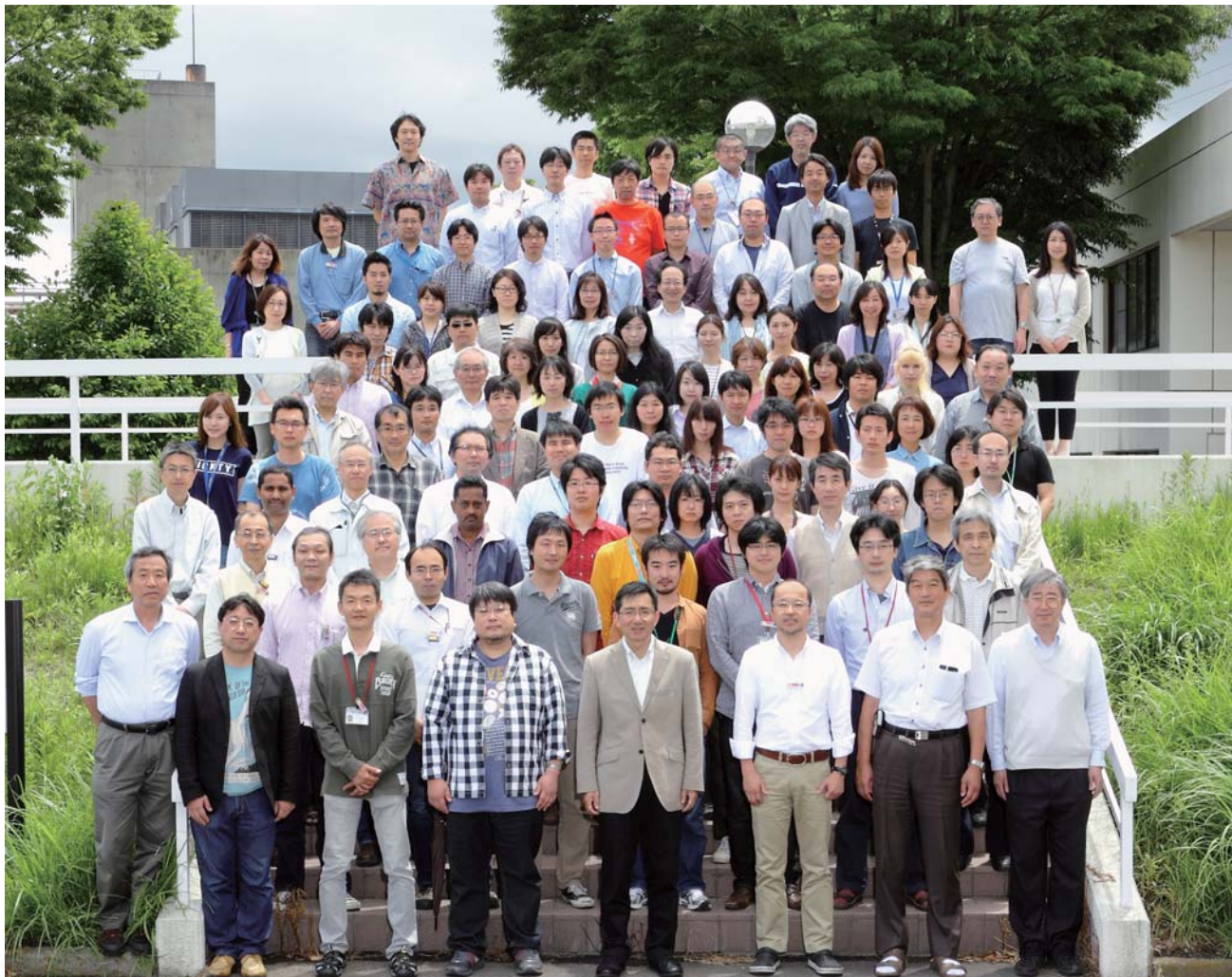
URL: <http://www.kek.jp/>

#31

PHOTON FACTORY ACTIVITY REPORT

2013

April 2013 to March 2014





1 K. Yamada	22 R. Kato	43 H. Sagayama	64 A. Hashimoto	85 Y. Yamashita
2 T. Senda	23 Ta. Honda	44 N. Nagata	65 K. Kitazawa	86 N. Adachi
3 M. Kimura	24 H. Makio	45 A. Harada	66 M. Kitamura	87 T. Nagae
4 R. Kumai	25 Y. Yamaguchi	46 N. Suzuki	67 A. Kikuchi	88 J. Adachi
5 Y. Murakami	26 Y. Sato	47 M. Senda	68 K. Yoshida	89 K. Wada
6 S. Adachi	27 A. Tomita	48 G. Ishikawa	69 X. Jin	90 Y. Uchida
7 H. Kawata	28 K. Horiba	49 T. Hyodo	70 R. Fukaya	91 N. Usami
8 Y. Kobayashi	29 S. Nagahashi	50 T. Uchiyama	71 T. Zeniya	92 R. Takai
9 N. Nakamura	30 H. Miyauchi	51 S. Yamamoto	72 K. Ichianagi	93 M. Yamamoto
10 H. Kumigashira	31 To. Honda	52 Y. Tanimoto	73 M. Ito	94 Y. Kitajima
11 M. Minohara	32 S. Velaga	53 R. Sukegawa	74 K. Sasajima	95 H. Sagehashi
12 Y. Takeichi	33 M. Kawasaki	54 Y. Misumi	75 K. Hirooka	96 K. Amemiya
13 S. Nozawa	34 Y. Lo	55 R. Sagayama	76 K. Mase	97 H. Abe
14 T. Miyajima	35 H. Nakao	56 N. Sato	77 T. Yamasaki	98 M. Shimada
15 T. Nogami	36 K. Hirano	57 A. Unjoh	78 A. Toyoshima	99 A. Ueda
16 S. Kishimoto	37 F. Yumoto	58 H. Toyama	79 M. Tanaka	100 K. Harada
17 K. Haga	38 K. Inoue	59 K. Takanashi	80 A. Hirata	101 H. Suga
18 S. Bhunia	39 T. Aoki	60 O. Konstantinova	81 A. Koyama	102 T. Kikuchi
19 T. Ohba	40 T. Oota	61 K. Hyodo	82 M. Sakamaki	103 K. Nigorikawa
20 H. Nitani	41 Y. Yamada	62 K. Yatabe	83 H. Tanaka	104 N. Igarashi
21 M. Kobayashi	42 T. Sasaki	63 Y. Takahashi	84 T. Sudayama	

Editorial

This is the 31st edition of the Photon Factory (PF) Activity Report, and covers scientific activities for the Japanese fiscal year 2013 (April 2013 to March 2014). The report is divided into two parts. PART A summarizes scientific highlights achieved by users, newly developed experimental facilities including beamlines and experimental apparatuses, topical in-house research activities, research and development of storage rings and an energy recovery linac based future light source, reports of public events, and an outline of the organization of the PF. PART B presents a number of users' short reports and a list of research proposals.

For the past several editions we have promoted the electronic distribution of the PF Activity Report. Accordingly, the List of Awards, Theses and Publications in the Appendices of PART A and the entire contents of PART B are published on the PF's website at <http://pfwww.kek.jp/publications/acrpubl.html>.

In this volume we made several changes to the process of editing users' reports. One major change is that we decided to accept reports throughout the year and upload them one by one on the website after a quick check by our staff. We hope that this new editing policy will promote faster distribution of research results to the broad scientific community.

Finally, we would like to express our sincere gratitude to all of those who have contributed to this volume.

Keiichi Hirano, Editor-in-Chief

CONTENTS

Introduction	1
Memorials 2013	3
Highlights	
1. Materials Science	12
2. Chemical Science	30
3. Earth Science	38
4. Life Science	42
5. Imaging and Optics	58
6. Instrumentation and Methodology	60
7. Accelerators	62
Experimental Facilities	
1. Newly Developed Experimental Facilities	67
2. Structural Biology Research Center	75
3. Condensed Matter Research Center	78
4. Slow Positron Facility	81
5. IMSS Instrument R&D Team	83
6. Summary of Experimental Stations	84
Accelerators	
1. Outline of the Accelerators	97
2. PF Ring	100
3. PF-AR	103
Future Light Source	
1. ERL Project Overview	109
2. cERL	110
Users Program & Outreach Activities	
1. Experimental Proposals	119
2. Workshops and Seminars	122
3. Graduate School Education	123
4. International Collaboration	124
Appendices	
1. Site and Organization	126

Awards, Theses and Publication List are available on the PF's website(<http://pfwww.kek.jp/acr2013pdf/>).

Introduction

On behalf of the staff of the Photon Factory (PF) we are pleased to present Photon Factory Activity Report 2013. This report covers the research activities carried out in the fiscal year 2013 (April 2013 - March 2014). The inter-university research program has been going well and the number of proposals is steadily increasing. This year there were about 900 active approved proposals, 3,400 registered users, and more than 600 publications. The PF leadership has been partially changed. Prof. Kenji Ito retired from the Head of Synchrotron Radiation Science Division 1 and Prof. Reiji Kumai was nominated in his place (from April 2013). Prof. Masao Kimura joined us as the head responsible for industrial application of synchrotron radiation (from October 2013).

Operation and upgrades of the PF and the PF-AR

The PF was constructed as a second-generation synchrotron radiation source and the first photon came out in 1982. During the intervening 32 years the PF underwent two large upgrades of the ring. In the 1997 upgrade the emittance was reduced from 130 to 36 nmrad. During the shutdown in 2005 the number of straight sections was increased from 10 to 14, among which 4 short straight sections were created and 10 straight sections were lengthened. In the long straight sections we have reconstructed Vacuum Ultraviolet (VUV)/Soft X-ray (SX) beamlines (BL-2, -13, -16, -28) with undulators in recent years. BL-16A was already operated as a variable polarization soft X-ray spectroscopy station, which provides circular and elliptical polarizations mainly to investigate magnetic materials, especially thin films. BL-28A is dedicated to high-resolution Angle-Resolved Photoemission Spectroscopy (ARPES) in order to study strongly correlated electron systems. An undulator covering the energy range of 30–300 eV will be installed during January to March 2015. BL-13B has been mainly used for the study of surface chemistry using ARPES, X-ray photoelectron spectroscopy (XPS), and X-ray absorption spectroscopy (XAS). A compact scanning transmission X-ray microscope (STXM) was installed at BL-13A and opened to users in October 2013. An undulator covering the energy range of 50–2000 eV will be installed during January to March 2015. BL-2 is under construction. The beamline has two types of undulators in tandem alignment for the VUV region (30–300 eV) and for the SX region (250–2000 eV). These undulators enable us to use wide energy-range light with high brilliance and high energy resolution. Moreover, BL-2B has an additional double-crystal monochromator with the energy range of 2000–4000 eV by using the wiggler mode of the SX undulator. This beamline was built in collaboration with a private company, Hitachi, Ltd.



Youichi Murakami

Meanwhile, we have upgraded the X-ray beamlines (BL-1, -3, -17) by installing short gap undulators in the short straight sections to gain long-term competitiveness in the field of X-ray science. The last short straight section in which a short gap undulator was installed is in BL-15 which produces high-brilliance X-rays ranging from 2.1 keV to 15 keV. This beamline is dedicated to both Small Angle X-ray Scattering (SAXS) experiments using collimated softer and hard X-rays and X-ray Absorption Fine Structure (XAFS)/X-ray Fluorescence (XRF)/X-ray Diffraction (XRD) studies using semi-micro focus beams. This beamline will be opened to general users in October 2014.

BL-18A and BL-19A/B were operated by the Institute for Solid State Physics (ISSP) of the University of Tokyo for more than 20 years. BL-18A was an ARPES beamline for surfaces and interfaces, while BL-19A was dedicated to experiments using spin-resolved PES. These beamlines were shut down at the end of fiscal 2013 for reasons of the ISSP. We are now discussing the future of these beamlines; BL-19B will be used as a test beamline by PF staff for the time being at least. Meanwhile, the new operation of BL-4A was started by a user group. Though experiments using the multi-layer monochromator have ended, micro-beam experiments using a double crystal monochromator are continuing in this beamline. BL-6C, which is also operated by a user group, was upgraded in the available energy region up to 18 keV by reforming the focusing mirror. This improvement enables experiments such as fluorescence X-ray holography of various samples.

Future plan of the PF

KEK published a draft of the KEK roadmap at the end of August 2012 and solicited the opinions of user communities. KEK then modified the roadmap based on the opinions for the roadmap from the Photon Factory User Association (PF-UA) and the Japanese Society for Synchrotron Radiation Research (JSSRR). The KEK roadmap was reviewed by the international review committee

in April and finally published in May 2013. Based on the discussion in the international review committee, KEK made the following additional statement in October 2013: "After publication of KEK Roadmap 2013, the Japanese Society for Synchrotron Radiation Research submitted its proposal for a 3-GeV class high-brilliance light source to be incorporated in the Master Plan of Large Research Projects which is to be prepared by the Science Council of Japan. With inputs from the synchrotron radiation user community concerning this proposal, KEK is adding the following statement to the part of photon science in KEK Roadmap 2013. While KEK is engaged in a long-term effort to construct a 3-GeV ERL (Energy Recovery Linac) facility, KEK will play a leading role in the realization of a low-emittance storage ring as a high-brilliance light source in the mid-term. KEK is now beginning specific studies on this possibility in view of the value of this nationwide effort. Such a light source facility with high brilliance, currently not present in Japan, is strongly desired by user communities in a wide range of academic and industrial fields, and is considered to be an indispensable research platform in the near future."

We will intensively discuss this storage ring through collaboration across Japan and the ERL Project in the meetings of the Committee for Future Plans of the PF, which is established under the Advisory Committee for IMSS in 2014. The Committee for Future Plans of the PF will announce the mid-term summary and report the results to the steering committee at the end of financial year 2014.

Collaboration among universities and institutes

KEK is promoting inter-university collaboration to activate joint research projects. In particular, the IMSS is pursuing joint research projects using synchrotron radiation, neutrons, muons, and positrons in collaboration with universities such as Hokkaido University, Tohoku University, University of Tsukuba, and the University of Tokyo. In addition to these inter-university collaborations we strongly support nanotechnology research and education in the Tsukuba area, namely the Tsukuba Innovation Arena for Nanotechnology (TIA-nano). TIA-nano is striving to build a global nanotechnology research and education center with the support of the government and is expected to serve as an engine of innovation. TIA-nano had been led by the National Institute of Advanced Industrial Science and Technology (AIST), the National Institute for Materials Science (NIMS), and the University of Tsukuba as the core institutes, together with industry. KEK joined TIA-nano as a core institute in April 2012. The PF will be used as one of the Nanotech Open User Facilities to promote advanced nanotechnology research in the research collaboration domains of TIA-nano in the future.

International collaboration

The Australian beamline BL-20B was closed in March 2013 after completing its mission. The first synchrotron

light in BL-20B was produced in October 1992. For about 20 years (more than 3,000 days of experiments), more than 2,500 Australian researchers used this beamline and some 900 proposals were made. The beamline was actively used and about 1,000 papers were published during this period. This great success led to the construction of the Australian Synchrotron in Australia. We greatly appreciate all those involved with this beamline for their remarkable accomplishments.

The first users' meeting of the Indian beamline BL-18B was held on October 7-8, 2013 at the Saha Institute of Nuclear Physics in Kolkata, India. The Indian beamline BL-18B was established in 2009 after the Department of Science and Technology of India (DST) and KEK signed a Letter of Intent in July 2007, and both Indian and Japanese prime ministers welcomed it in a joint statement in 2007. The aim of this project is to provide a substantial amount of quality beamtime for the use of Indian scientists. BL-18B is conceived as a multipurpose beamline, allowing experiments on powder diffraction under extreme conditions, reflectivity and diffuse scattering from solid and liquid surfaces and interfaces and so on. This beamline is opened to general users in April 2014. We expect that further progress of this project will enhance the collaboration between India and Japan.

Photon beam platform

At present, a top-priority issue in Japan is how to focus on research and development and achieve further innovation. In order to promote networking among cutting-edge fundamental research bases and encourage the use of synchrotron radiation and laser by industry, the Ministry of Education, Culture, Sports, Science and Technology (MEXT) established a new operation for the collaboration of synchrotron radiation and laser facilities: the Photon Beam Platform. This platform consists of seven implementing facilities (Osaka University Institute of Laser Engineering, Kyushu Synchrotron Light Research Center, University of Hyogo New Subaru, Ritsumeikan University SR Center, Aichi Synchrotron Radiation Center, Tokyo University of Science Infrared Free Electron Laser Research Center and KEK/ISSS/PF) and one collaborative facility (SPring-8). The PF serves as an administrative facility in this platform. We expect users of this platform to open new research fields of industrial use through this unique collaboration of synchrotron radiation and laser facilities. This platform for innovation in many industrial fields will continue to play an important role in the decade ahead.



Youichi Murakami

Memorials 2013

April 2013 Spring Break of the Photon Factory



At the Photon Factory, continual efforts have been made to replace older beamlines and instruments with newer ones that suit the latest technology and users' needs. During the spring shut-down period, the construction of new beamlines was busily conducted.

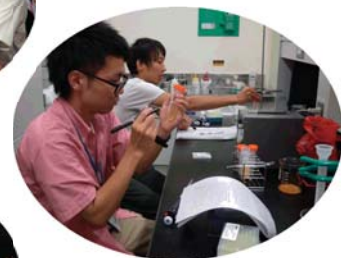
May 29, 2013 Successful Acceleration of Electron Beam at the Injection Line of the Compact ERL

At the proof-of-principle machine of the Energy Recovery Linac (Compact ERL), the electron beam emitted from the photo-cathode DC electron gun was successfully accelerated up to the energy of 5 MeV by the superconducting accelerator.



August 16-24, 2013 Summer Challenge

The 7th summer school on "particle and nuclear physics" and "material and biological science" was held at KEK. About 90 undergraduate students from 57 universities attended this school, which included basic lectures, facility tours of the Tsukuba and Tokai campuses and practical experiments.



August 28-31, 2013
LPBMS2013 at the Tsukuba International Congress Center

LPBMS2013 ("Light and Particle Beams in Materials Science") was held to discuss the latest scientific results of materials science obtained by quantum beams such as synchrotron light, neutrons, muons and slow positrons.

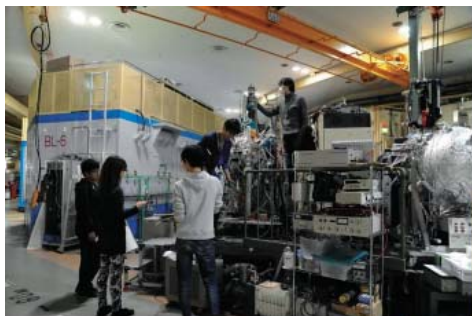


September 8, 2013
Open House

Open House of the KEK Tsukuba campus was held and attracted about 4,300 visitors. All visitors enjoyed the pioneering world of modern materials, biology and accelerator science.



November 9-10, 2013
Summer Challenge in Autumn



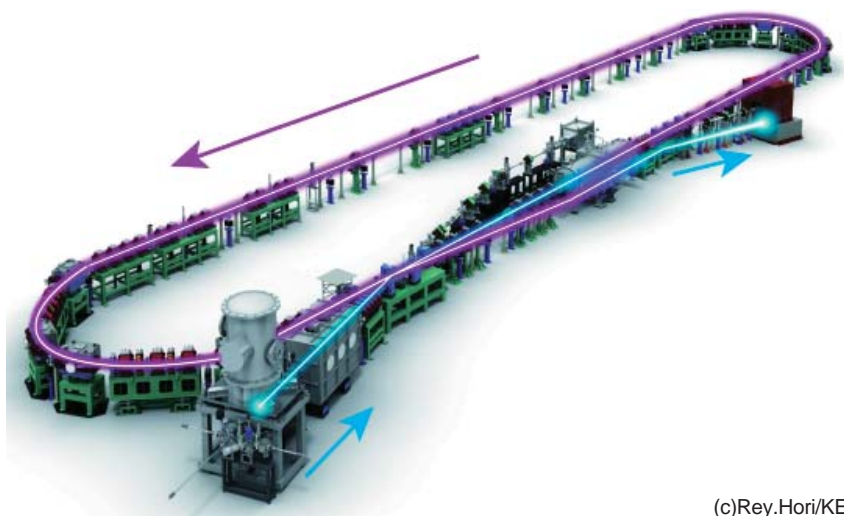
The students who participated in the summer challenge in August performed actual experiments using synchrotron X-rays in the PF and PF-AR.



March 12, 2014

Energy Recovery Operation Successfully Achieved at the Compact ERL

Energy recovery operation was successfully achieved at the Compact ERL which was built for proof-of-principle studies of the Energy Recovery Linac (ERL).



(c)Rey.Hori/KEK


March 18-19, 2014

The IMSS Science Festa 2013

The IMSS Science Festa 2013 was held with about 450 participants. The main purpose of this Festa is to promote complementary use of four quantum beams (synchrotron light, neutrons, muons and slow positrons) offered by IMSS.



International Collaboration

 *June 13-22, 2013*
SESAME School in Turkey

The 5th SESAME school was held in Turkey with 35 participants. SESAME (Synchrotron-light for Experimental Science and Applications in the Middle East) is a synchrotron light facility under construction in Amman, the capital of Jordan, and is scheduled to start operation in 2014. Five scientists from KEK gave lectures on photo-electron spectroscopy, XAFS, protein crystallography, X-ray powder diffraction and X-ray fluorescence spectroscopy.



September 9-13, 2013
ERL2013

The 53rd ICFA Advanced Beam Dynamics Workshop on Energy Recovery Linacs "ERL-2013" was held at Budker Institute of Nuclear Physics (Novosibirsk, Russia). Scientists engaged in ERL projects from around the world gathered together and discussed various issues on accelerator technology.





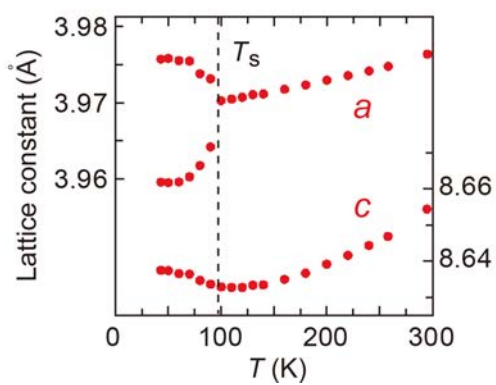
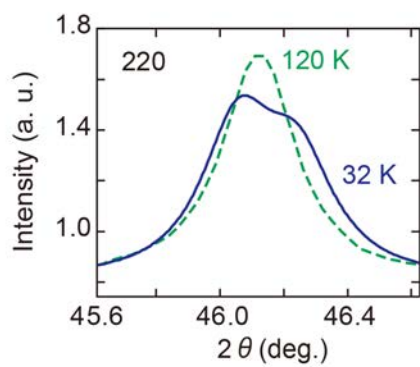
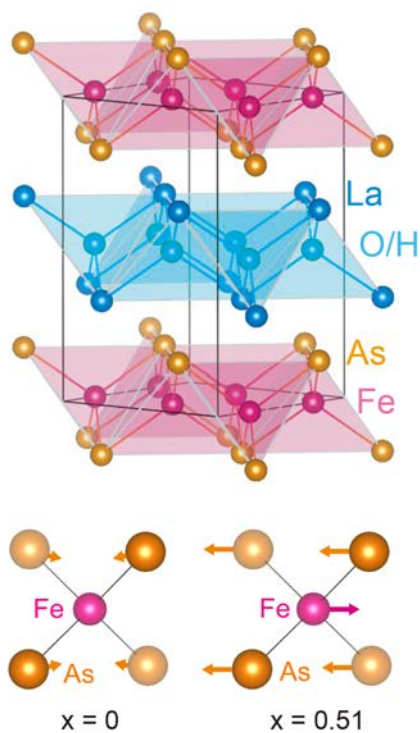
January 25, 2014

Japanese Prime Minister Mentions PF Indian Beamline

The Japanese Prime Minister Shinzo Abe attended the Japan-India Science and Technology Seminar held in Delhi and gave a talk in the closing session in front of about 90 people. In his greeting, he mentioned the Indian beamline constructed at the Photon Factory saying "This beamline is used for various experiments. I look forward to the results brought by future cooperation".



Highlights



HIGHLIGHTS

1. Materials Science	12
1-1 Strain Induced Spontaneous Magnetization in Perovskite Cobalt Oxide	
1-2 Charge-Cluster Glass in an Organic Conductor with Triangular Lattice	
1-3 Concealed Magnetic Parent Phase in Iron Oxypnictide Superconductor	
1-4 Solvent-Dependent Molecular Structure of Ionic Species Directly Measured by Ultrafast X-Ray Solution Scattering	
1-5 Role of the Free Surface for Orientations in Liquid Crystalline Polymer Films	
1-6 Structure of Silicene on a Ag(111) Surface Studied by TRHEPD	
1-7 Novel Electronic States of Topological Crystalline Insulators Revealed by ARPES	
1-8 Magnetic Structure of the Single-Layer Graphene/Nickel Interface	
1-9 Strain Mediated Control of Magnetic Anisotropy in Alternately Layered FeNi Thin Films	
2. Chemical Science	30
2-1 The Specific Deoxidation Behavior of Iron Titanate Catalyst Characterized by the XAFS Technique for the Selective Catalytic Removal of NO _x by NH ₃	
2-2 Atomicity-Precise Non-Magic Number Pt Clusters	
2-3 High Catalytic Performance of USY-Supported Manganese Oxides for VOC Control	
2-4 Monitoring of Electron Flow in Layered Double Hydroxides to Photoreduce Carbon Dioxide into Fuels	
3. Earth Science	38
3-1 Stability of Forsterite in the Presence of H ₂ Fluid under High Pressure and Temperature	
3-2 Synchrotron Radiation Study of the Reaction-Deformation Coupling Processes in Earth's Mantle Minerals at High Pressures	

4. Life Science	42
4-1 Crystal Structures of Innate Immune RNA Receptor TLR8	
4-2 Structural and Functional Mechanism of a New Protein Complex Promoting the Stabilization of Genome during Homologous Recombination	
4-3 Crystallographic Study of Bacterial Selenocysteine Formation	
4-4 Mechanism of Template-Independent RNA Polymerization by tRNA Nucleotidyltransferase	
4-5 Molecular Basis of Binding between Novel Human Coronavirus MERS-CoV and its Receptor CD26	
4-6 Sequence-Specific DNA Glycosylase Found in a Restriction-Modification System	
4-7 Structural Analysis of Intrinsically Partially Folded EspB from Enterohaemorrhagic <i>E. coli</i> O157:H7 by Combination of CD and SAXS in Conjunction with Protein Dissection Technique	
4-8 X-Ray-Induced Nitric Oxide-Mediated Bystander Cell Death Suppresses Spontaneous Mutagenesis in V79 Cells	
5. Imaging and Optics	58
5-1 Z_{eff} Imaging Using X-Ray Interferometer	
6. Instrumentation and Methodology	60
6-1 Development of a Compact Scanning Transmission X-Ray Microscope (STXM)	
7. Accelerators	62
7-1 Minimization of the Emittance Growth in a Superconducting Radio Frequency Cavity at cERL Injector	

Strain Induced Spontaneous Magnetization in Perovskite Cobalt Oxide

Electronic phases with the nanometer-scale self-organization of electrons are ubiquitously observed in correlated electron systems. In d -electron transition metal oxides, versatile quantum states have been realized by tuning the effective one-electron band-filling or band-width. Here we show that control of the spin-state degree of freedom (low/intermediate/high spin states) gives rise to a new complex spin-orbital superstructure with spontaneous magnetization in a thin film of perovskite LaCoO_3 . A tiny crystal-lattice strain can promote the spin-state transition of Co ions and the ordering of Co-3d orbitals modulates the spin exchange interactions to produce the unique ferrimagnetic structure.

Entanglement among the charge, spin and orbital degrees of freedom in d -electron transition-metal compounds is a key ingredient to control emergent quantum states such as unconventional superconductivity and magnetically induced ferroelectrics (multiferroelectricity). The control of magnetic/electronic states has been ubiquitously achieved by tuning material parameters such as the effective d -electron band-width or band-filling. In addition to these well-known approaches, in a certain class of the transition-metal compounds, there is a unique material tuning parameter, the spin-state variability (such as low, intermediate, and high spin states) of constituent magnetic ions, which is strongly tied with the orbital degree of freedom for correlated electrons.

The perovskite LaCoO_3 is known as a prototype of the spin-state crossover material and has attracted much attention in recent decades. In this system, the nominally trivalent Co-ion (Co^{3+}) may take three different spin states as shown in Fig. 1: the low-spin (LS) state with filled 3d t_{2g} manifold ($S=0$), intermediate-spin (IS) state with active e_g and t_{2g} orbital degrees of freedom ($S=1$), and high-spin (HS) state with active t_{2g} orbital

degree of freedom ($S=2$). Although the ground state is a nonmagnetic phase with LS-state in the bulk form as shown in Fig. 2(a), it has been reported that spontaneous magnetization is observed in the epitaxial thin film of LaCoO_3 while keeping its insulating nature [1, 2]. Several models have been proposed to explain the strain induced magnetization: the chemically inhomogeneous state including ferromagnetic metallic patches originating from unintentionally doped carriers or the ferromagnetism mediated by the orbital ordering. However, to the best of our knowledge, there is no experimental report exploring the microscopic spin-orbital structure for this enigmatic magnetic phase. Here we investigated the spin-orbital state for the epitaxial thin film of LaCoO_3 by magnetization measurements and resonant X-ray diffraction [3].

A single crystalline film (60 nm thick) of LaCoO_3 was fabricated on $(\text{LaAlO}_3)_{0.3}(\text{SrAl}_{0.5}\text{Ta}_{0.5}\text{O}_3)_{0.7}$ (LSAT) substrate with (110) orientation by pulsed laser deposition. Synchrotron-radiation X-ray diffraction was performed to detect the fundamental and superlattice reflections at BL-3A and BL-4C, Photon Factory of KEK, Japan.












	Low-spin (LS)	Intermediate-spin (IS)	High-spin (HS)
	e_g  t_{2g} 	 	 
Spin	$S=0$	$S=1$	$S=2$
Orbital	N/A	e_g orbital  x^2-y^2  $3z^2-r^2$	t_{2g} orbital  xy  yz  zx

Figure 1: The spin state variability of Co^{3+} -ion. The schematic of t_{2g} orbitals for the IS-state is omitted for clarity.

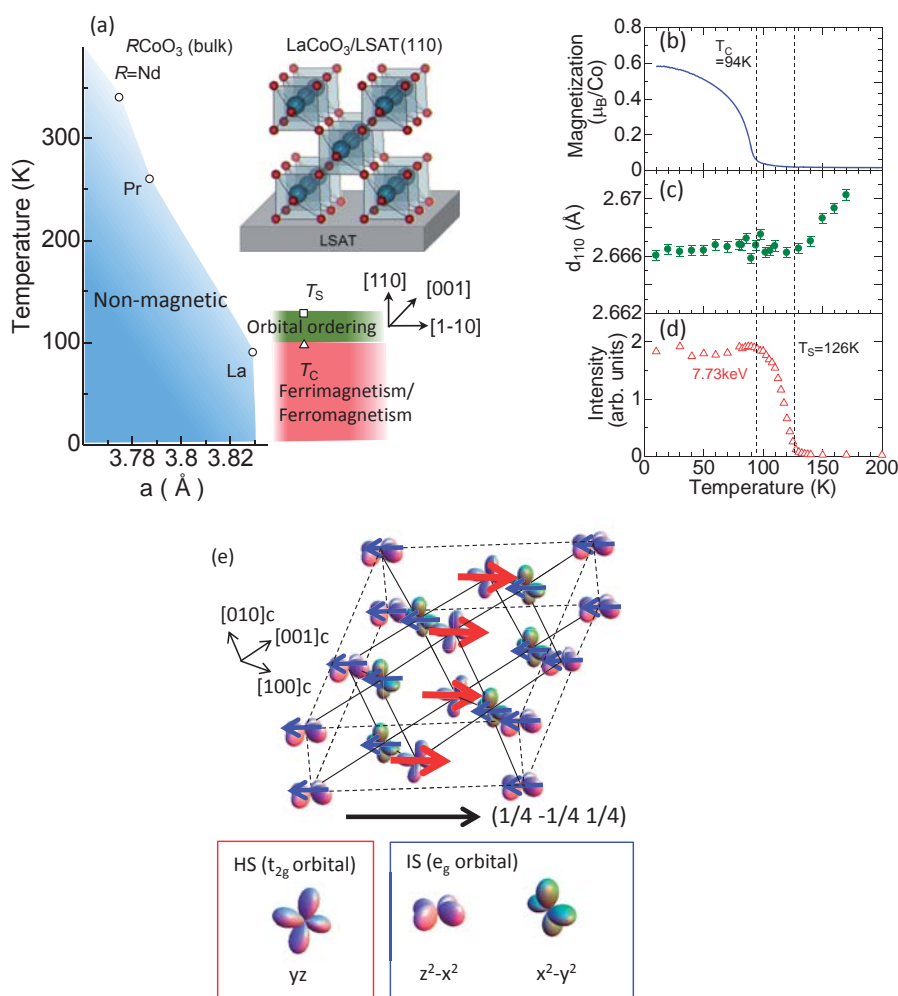


Figure 2: (a) Electronic phase diagram of $LaCoO_3$. Temperature dependence of (b) magnetization, (c) out-of-plane lattice constant and (d) intensity of superlattice reflection at $(1/4 -1/4 1/4)$. (e) Schematic view of possible spin/orbital ordered structure. Red (blue) arrows denote the spins of HS-state (IS-state).

Figure 2(b) shows the temperature dependence of magnetization. Magnetization increases at $T_c=94$ K and the spontaneous magnetization is about $0.6\mu_B/Co$ at 10 K. Figure 2(c) shows the temperature dependence of the out-of-plane lattice constant (d_{110}). As the temperature is lowered, d_{110} steeply decreases down to 126 K and shows minimal temperature dependence below 126 K. Moreover, we identified a superlattice reflection characterized by the propagation vector $q = (1/4, -1/4, 1/4)$ below 126 K. The intensity gradually increases below 126 K and nearly saturates below T_c [Fig. 2(d)].

These results point to the existence of a structural phase transition at 126 K (T_s), which quadruples the unit cell of pseudo-cubic setting along the $[100]$, $[010]$ and $[001]$ axes. On the basis of the resonant X-ray scattering at Co K -edge, we attributed this structural phase transition to the ordering of Co-3d orbital in the IS- or HS-state. Figure 2(e) shows one plausible model of spin-orbital ordering; the spin and orbital alignment is viewed as the stacking of two-dimensional sheets of IS- and HS-state sites in order of IS-IS-HS-IS with

$dz^2-x^2 - dx^2-y^2 - dyz - dx^2-y^2 \dots$ orbital configuration along the $[1 -1 1]$ direction. This model is also consistent with the observed net magnetization and result of resonant soft X-ray diffraction [4].

REFERENCES

- [1] D. Fuchs, C. Pinta, T. Schwarz, P. Schweiss, P. Nagel, S. Schuppler, R. Schneider, M. Merz, G. Roth and H.v. Löhneysen, *Phys. Rev. B* **75**, 144402 (2007).
- [2] J.W. Freeland, J.X. Ma and J. Shi, *Appl. Phys. Lett.* **93**, 212501 (2008).
- [3] J. Fujioka, Y. Yamasaki, H. Nakao, R. Kumai, Y. Murakami, M. Nakamura, M. Kawasaki and Y. Tokura, *Phys. Rev. Lett.* **111**, 027206 (2013).
- [4] Y. Yamasaki et al., unpublished.

BEAMLINES

BL-3A and BL-4C

J. Fujioka¹, Y. Yamasaki^{1, 2}, H. Nakao², R. Kumai², Y. Murakami², M. Nakamura³, M. Kawasaki^{1, 3} and Y. Tokura^{1, 3} (¹The Univ. of Tokyo, ²KEK-PF, ³RIKEN)

Charge-Cluster Glass in an Organic Conductor with Triangular Lattice

Spin interactions can lead to unconventional states, such as quantum spin liquids and spin glasses, in which long-range ordering is prohibited by geometric frustration. Here, we report observations of unconventional electronic states resulting from charge frustration. Using a combination of frequency-resolved transport measurements and X-ray diffraction, we have demonstrated that a charge cluster glass is formed in a high-quality organic system with a triangular lattice. Surprisingly, these observations correspond to recent ideas regarding the structural glass formation of supercooled liquids, potentially opening up a new area of interdisciplinary physics.

Interacting many-body systems comprised of molecules, electrons, or spins can spontaneously exhibit long-range order when thermal agitations are suppressed. This tendency may be avoided in several ways and, as a result, the systems freeze in inhomogeneous or glassy states [1]. Though not well-established, correlated electrons confined in a triangular lattice may be good candidates for charge-glass formers. A new paradigm might be a Wigner-type charge ordering (CO), in which an equal number of charge-rich and charge-poor sites tile the entire lattice to avoid neighboring rich-rich (or poor-poor) pairs as much as possible. However, in a triangular lattice, this constraint is insufficiently stringent to determine a specific CO from the various charge configurations, thereby potentially undermining the tendency toward long-range ordering, analogous to a situation in geometrically frustrated spin systems [Fig. 1(a)] [2]. As a result, glassy electronic states may be realized; however, such a charge-glass-forming nature has not been identified thus far. Research groups at the University of Tokyo, RIKEN CEMS and KEK revealed that the charge-glass state is formed in an organic conductor with a triangular lattice [3].

The material investigated is the organic conductor θ -(ET)₂RbZn(SCN)₄ (denoted θ -RbZn), where ET denotes bis(ethylenedithio)tetrathiafulvalene [4]. The crystal structure has an alternate stacking of conducting ET layers and insulating anion layers, and the ET

molecules form a two-dimensional triangular lattice [Fig. 1(b)]. The ET conduction band is hole-1/4-filled and exhibits CO instability [5], and the charge frustration caused by the underlying triangular lattice may prevent long-range ordering. In reality, a structural transition occurs at ~ 200 K and relaxes the charge frustration; as a result, horizontal CO that is compatible with the structural modulation is formed with a charge disproportionation ratio of $\sim 0.15:0.85$ accompanied by a steep increase in resistivity [Fig. 1(c)] [6, 7]. The structural transition can be avoided by rapid cooling at >5 K/min [8], and the “charge-liquid” phase above 200 K can be thus maintained below 200 K [Fig. 1(c)]. Therefore, to observe the possible charge-glass state, the electronic properties below 200 K in a rapidly cooled condition should be examined. To demonstrate the charge-glass, several key concepts need to be tested, for example, the temperature evolution of the slow charge dynamics, the absence of long-range ordering, and the electronic-glass transition. The slow dynamics in the charge-liquid phase were detected using resistance fluctuation spectroscopy [3]. The typical dynamics are found to be 10 – 10^4 Hz (strongly temperature dependent) and it slows down at low temperatures. These slow dynamics appear to be understood by considering that the charge-liquid state above 200 K is transforming into a classically disordered state, that is, a charge glass.

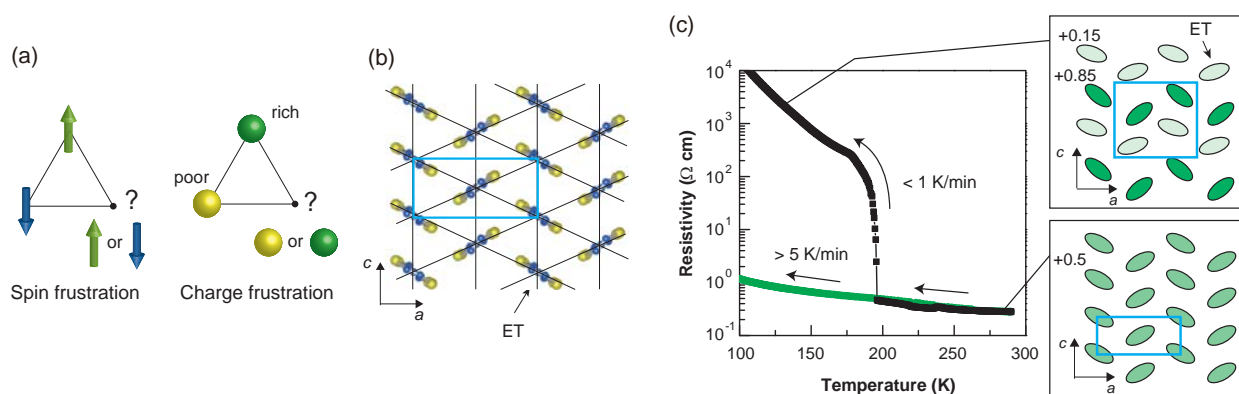


Figure 1: Charge frustration and crystal structure of θ -(ET)₂RbZn(SCN)₄. (a) An illustration of the analogy between spin frustration and charge frustration. (b) The structure of the ET layer. (c) The temperature dependence of the resistivity during cooling for different temperature-sweeping rates. The insets indicate the crystal structures of the high-temperature phase (lower inset) and the low-temperature phase (upper inset). In the upper inset, the charge-ordering pattern is also shown.

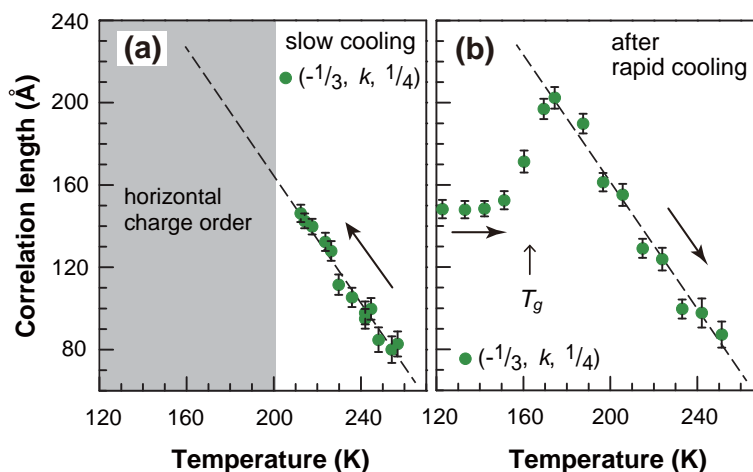


Figure 2: Spatial correlation of the charge clusters investigated using X-ray diffuse scattering. (a) Temperature dependence of the charge-cluster correlation length ξ during slow cooling. (b) Temperature dependence of ξ during heating after rapid cooling to 120 K. The value of ξ is estimated along the $-2a^*c^*$ direction on the $(1/3 k 1/4)$ diffuse rod. The broken lines in (a, b) are drawn as guides for the eye.

To obtain further insight into the observed glassy dynamics, it is necessary to determine whether some type of metastable “crystalline” islands evolve with the slow dynamics [9-12]. To this end, X-ray diffuse scattering measurements were conducted. It was revealed that diffuse spots characterized by $q_d \sim (\pm 1/3 k \pm 1/4)$ exist around the Bragg spots, where k denotes negligible coherence between the ET layers. In Fig. 2(a), the evolution of the correlation length ξ as a function of temperature can be clearly seen. ξ is not short-ranged but is ~ 140 Å at 210 K, which corresponds to ~ 25 triangular spacings. This behavior is essentially distinct from conventional critical phenomena, where ξ diverges for a continuous transition; here, ξ goes to a medium-range length in a non-divergent (i.e., non-critical) manner. The growth of the slow dynamics and of ξ seems well correlated, indicating that the charge clusters cause the slow dynamics.

The charge-glass transition is clearly observed in the correlation length ξ -temperature profile when measured during a warming process after rapid cooling (~ 90 K/min) [Fig. 2(b)]. From 120 to 150 K, ξ is temperature insensitive with an appreciably shorter length than expected. Such a “frozen” metastable state with no long-range order is characteristic of glassy states, demonstrating that a charge-glass is formed in the quenched state. Upon further warming, ξ increases abruptly to the expected value at $T_g \sim 160$ – 165 K and becomes temperature-dependent above this temperature. This behavior demonstrates that the charge-liquid nature is recovered above T_g , and T_g can therefore be regarded as the charge-glass transition temperature.

Generally, correlated electrons are neither well itinerant nor well localized at high temperatures, so they are considered a “bad metal” [13]. The present results suggest that the bad metallic regime in charge-frustrated systems can be better described as a glass-forming charge-liquid, although the actual charge-glass transition may be avoided by a preceding frustration-relaxing structural transition.

REFERENCES

- [1] E. Dagotto, *Science* **309**, 257 (2005).
- [2] L. Balents, *Nature* **464**, 199 (2010).
- [3] F. Kagawa, T. Sato, K. Miyagawa, K. Kanoda, Y. Tokura, K. Kobayashi, R. Kumai and Y. Murakami, *Nat. Phys.* **9**, 419 (2013).
- [4] H. Mori, S. Tanaka and T. Mori, *Phys. Rev. B* **57**, 12023 (1998).
- [5] H. Seo, *J. Phys. Soc. Jpn.* **69**, 805 (2000).
- [6] K. Miyagawa, A. Kawamoto and K. Kanoda, *Phys. Rev. B* **62**, R7679 (2000).
- [7] M. Watanabe, Y. Noda, Y. Nogami and H. Mori, *J. Phys. Soc. Jpn.* **73**, 116 (2004).
- [8] F. Nad, P. Monceau and H.M. Yamamoto, *Phys. Rev. B* **76**, 205101 (2007).
- [9] J.P. Doye, D.J. Wales, F.H.M. Zetterling and M. Dzugutov, *J. Chem. Phys.* **118**, 2792 (2003).
- [10] A.W.-Cooper, P. Harrowell and H. Fynewever, *Phys. Rev. Lett.* **93**, 135701 (2004).
- [11] H. Shintani and H. Tanaka, *Nat. Phys.* **2**, 200 (2006).
- [12] H. Tanaka, T. Kawasaki, H. Shintani and K. Watanabe, *Nat. Mat.* **9**, 324 (2010).
- [13] M. Imada, A. Fujimori and Y. Tokura, *Rev. Mod. Phys.* **70**, 1039 (1998).

BEAMLINe

BL-8A

F. Kagawa¹ and T. Sato² (¹RIKEN, ²The Univ. of Tokyo)

Concealed Magnetic Parent Phase in Iron Oxypnictide Superconductor

High-temperature superconductivity appears by carrier doping to an undoped parent compound; therefore, the physical properties of the parent are strongly related to the superconducting state. We report the discovery of a unique structural transition as well as an antiferromagnetic phase in $\text{LaFeAsO}_{1-x}\text{H}_x$ ($x \sim 0.5$) even though the electrical and magnetic interactions are generally expected to be weak in the overdoped region. The unprecedented two-dome superconducting phases can be interpreted as a consequence of the carrier doping starting from the original ($x \sim 0$) and advanced ($x \sim 0.5$) parent phases towards the intermediate region.

A new class of high-temperature (high- T_c) superconductors, iron-based materials, following the cuprates has been widely studied since their discovery in 2008 [1, 2]. In the first obtained iron-based superconductor, tetragonal ZrCuSiAs-type LaFeAsO [Fig. 1(a)], the superconductivity appears by carrier doping to the undoped parent of the magnetic- and structural-ordered state [3, 4]. An advanced doping method using a hydrogen anion instead of fluorine in LaFeAsO surpassed the doping limit of fluorine, and revealed a second superconducting phase (SC2) ($T_{c,\text{max}} = 36$ K at $x \sim 0.35$), in addition to the first dome (SC1) ($T_{c,\text{max}} = 26$ K at $x \sim 0.1$) [5]. In order to determine whether a certain hidden phase exists beyond the SC2 region, we performed a multi-probe study using X-ray, neutron, and muon beams in the range $0.40 \leq x \leq 0.51$.

X-ray powder diffraction measurements were performed on the beamlines of 8A/8B at KEK-PF. Neutron powder diffractions were measured on Super HRPD and NOVA at J-PARC. The muon spin relaxations were conducted at J-PARC MUSe and PSI.

Figure 1(c) shows the X-ray profile of the $(2, 2, 0)_T$ reflection in the non-superconducting specimen with $x = 0.51$. On cooling, the peak of $(2, 2, 0)_T$ broadened, while no broadening of the $(0, 0, 6)_T$ and $(2, 0, 0)_T$ peaks was observed [6]. These experimental findings indicate that the tetragonal to orthorhombic structural transition emerges clearly for $x = 0.51$. Figure 1(d) shows the temperature dependence of the lattice parameters for $x = 0.51$. The a -axis length splits in two below the structural transition of $T_s \sim 95$ K, and the c -axis shows an upturn at T_s . Precise X-ray powder-diffraction structural analysis with the RIETAN-FP program [7] using a high-resolution synchrotron radiation source indicates that the $x = 0.51$ compound crystallizes in an orthorhombic non-centrosymmetric $Aem2$ structure below T_s in contrast to the centrosymmetric $Cmme$ structure for $x = 0$. Across the structural transition, only the As atoms move slightly in $x = 0$, while the Fe and As atoms move in antiphase in $x = 0.51$ as shown in the inset of Fig. 1(b).

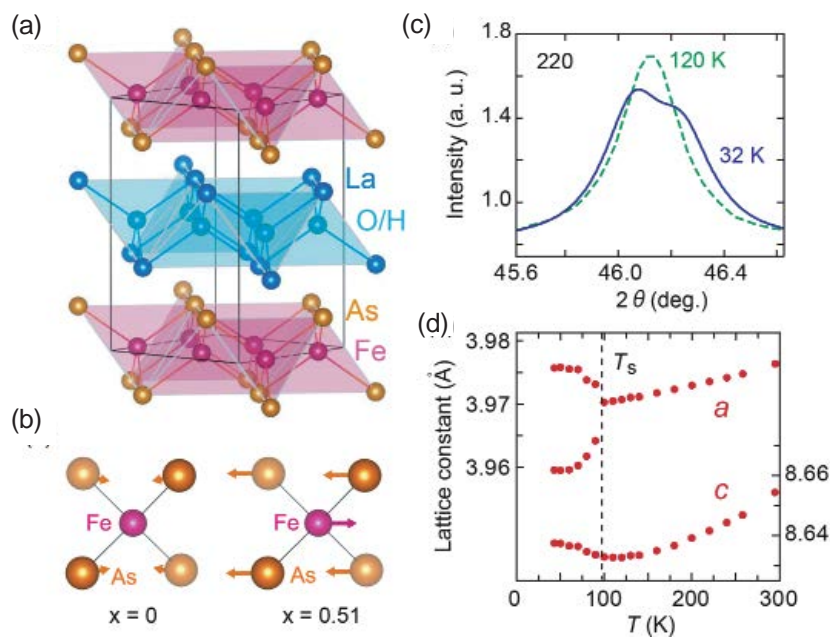


Figure 1: (a) Crystal structure of LaFeAsO . (b) Arrows on the FeAs_4 tetrahedra across the structural transitions represent the displacements of the Fe and As atoms by 0.07 \AA (0 \AA) and 0.06 \AA (0.01 \AA) in $x = 0.51$ ($x = 0$), respectively. (c) X-ray profile of $(2, 2, 0)_T$ reflection in $\text{LaFeAsO}_{0.49}\text{H}_{0.51}$. (d) Temperature dependence of the lattice constant of $\text{LaFeAsO}_{0.49}\text{H}_{0.51}$.

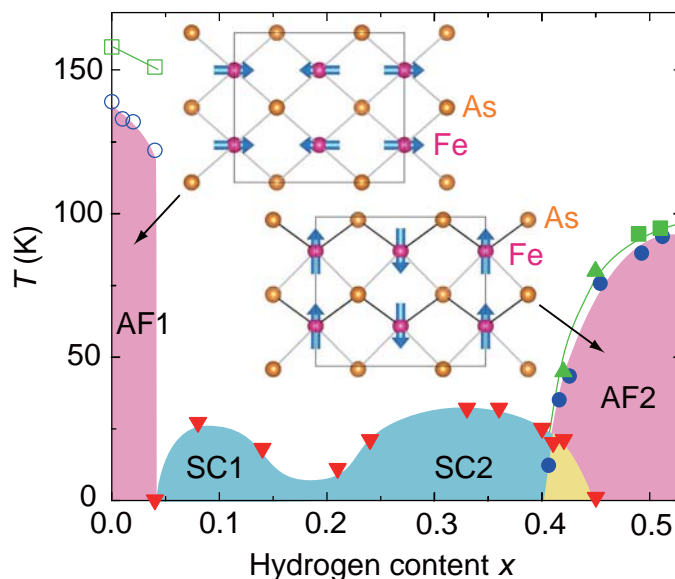


Figure 2: Magnetic, structural and superconducting phase diagram of $\text{LaFeAsO}_{1-x}\text{H}_x$. First and second superconducting phases (SC1 and SC2) are thought to be generated by starting from the original and advanced antiferromagnetic phases (AF1 and AF2), respectively. The crystal structures and magnetic Fe spin arrangements of AF1 and AF2 in the Fe-As planes are illustrated [9]. The structural, magnetic, and superconducting transitions are indicated by the green, blue, and red marks, respectively.

In the neutron powder diffraction measurement for $x = 0.51$, we observed magnetic peaks below $T_N = 89$ K with the propagation vector of $\mathbf{q} = (1/2, 1/2, 0)$. The result of magnetic structure analysis using the FullProf program [8] reveals an exceptional stripe-type arrangement among the iron-pnictides as shown in the inset of Fig. 2. The estimated magnetic moment $1.2 \mu_B$ per iron atom is significantly larger than the value of $0.63 \mu_B$ for $x = 0$ [6]. In the muon spin relaxation measurements, we observed that the value of T_N and the magnetic volume fraction decrease in unison with decreasing hydrogen content from $x = 0.51$. Moreover, the coexistence state of the antiferromagnetic static order and the superconducting state was found in the range $0.40 \leq x \leq 0.45$ despite the absence of the coexistence state in the undoped region [6].

Figure 2 illustrates the phase diagram of $\text{LaFeAsO}_{1-x}\text{H}_x$ [6]. We consider that a new antiferromagnetic phase with the structural transition next to the superconducting phase can be regarded as the *doped parent phase* by analogy of the undoped antiferromagnetic parent phase with the structural transition. This is unexpected because magnetic and electronic interactions are usually perceived as being weak in the highly carrier-doped region. In the iron-pnictides, the parent compound not only refers to the undoped compound but also more generally indicates a certain critical point of the magnetic and electronic correlations. Moreover, we can definitely state

that the two SC domes are generated by carrier-doping to the left- and right-hand parent compounds towards the intermediate region of the phase diagram.

REFERENCES

- [1] Y. Kamihara, H. Hiramoto, M. Hirano, R. Kawamura, H. Yanagi, T. Kamiya and H. Hosono, *J. Am. Chem. Soc.* **128**, 10012 (2006).
- [2] Y. Kamihara, T. Watanabe, M. Hirano and H. Hosono, *J. Am. Chem. Soc.* **130**, 3296 (2008).
- [3] J. Paglione and R.L. Greene, *Nature Phys.* **6**, 645 (2010).
- [4] D.J. Singh and M.-H. Du, *Phys. Rev. Lett.* **100**, 237003 (2008).
- [5] S. Iimura, S. Matsuishi, H. Sato, T. Hanna, Y. Muraba, S.W. Kim, J.E. Kim, M. Takata and H. Hosono, *Nature Commun.* **3**, 943 (2012).
- [6] M. Hiraishi, S. Iimura, K.M. Kojima, J. Yamaura, H. Hiraka, K. Ikeda, P. Miao, Y. Ishikawa, S. Torii, M. Miyazaki, I. Yamauchi, A. Koda, K. Ishii, M. Yoshida, J. Mizuki, R. Kadono, R. Kumai, T. Kamiyama, T. Otomo, Y. Murakami, S. Matsuishi and H. Hosono, *Nature Phys.* **10**, 300 (2014).
- [7] F. Izumi and K. Momma, *Solid State Phenom.* **130**, 15 (2007).
- [8] J. Rodriguez-Carvajal, *Physica B* **192**, 55 (1993).
- [9] K. Momma and F. Izumi, *J. Appl. Crystallogr.*, **44**, 1272 (2011).

BEAMLINES

BL-8A and BL-8B

J. Yamaura¹, M. Hiraishi², K. M. Kojima², H. Hiraka², R. Kadono², T. Kamiyama², T. Otomo², R. Kumai^{2,3} and Y. Murakami^{2,3} (¹MCES Tokyo Insti. of Tech., ²KEK-IMSS, ³KEK-PF)

Solvent-Dependent Molecular Structure of Ionic Species Directly Measured by Ultrafast X-Ray Solution Scattering

Triiodide ion has a molecular structure that sensitively changes depending on the type of solvent and its symmetry can be broken by strong solute-solvent interaction. Here, by applying pump-probe X-ray solution scattering, we characterize the exact molecular structure of the I_3^- ion in water, methanol and acetonitrile with sub-angstrom accuracy. The data reveal that the I_3^- ion has an asymmetric and bent structure in water. In contrast, the ion keeps its symmetry in acetonitrile, while the symmetry breaking occurs to a lesser extent in methanol than in water.

The triiodide ion (I_3^-) in solution offers a good example of the role played by solvent in determining the structure of ionic species. In the gas phase and aprotic solvents, the structure is linear and symmetric with equal I-I bond lengths. In contrast, in protic solvents such as water and methanol, an antisymmetric stretching mode was observed in the resonance Raman spectrum and a rotationally excited I_2^- fragment was detected in the transient anisotropy measurement of the photoexcited I_3^- ion, suggesting the existence of an asymmetric and bent structure of the I_3^- ion, respectively. However, despite these evidences, the exact structure of the I_3^- ion has never been directly characterized experimentally.

To characterize the exact structure of the I_3^- ion, we applied time-resolved X-ray solution scattering [1] to the I_3^- ion in three different solvents: water, acetonitrile, and methanol [2]. The key ideas of the experiment and data

analysis are schematically summarized in Fig. 1. By taking the difference between scattering patterns measured before and 100 ps after laser excitation, only the laser-induced changes of solution sample are extracted with all other background contributions being eliminated. To extract the structure of the I_3^- ion from the difference in scattering intensity, the maximum likelihood estimation with chi-square estimator was employed with five variable parameters. The parameters are three bond distances for the I_3^- ion, the bond distance for the I_2^- fragment, and temperature change. The theoretical scattering patterns were calculated by considering solute contribution, solvent hydrodynamics, and the contribution from solute-solvent interaction (cage). As a result, the lengths of the three bonds in the I_3^- ion are identified with sub-angstrom accuracy.

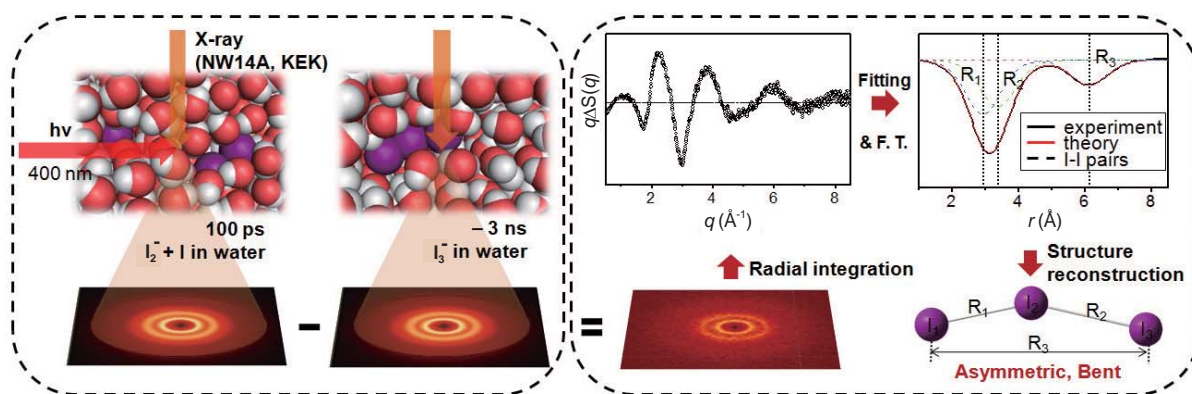


Figure 1: Schematic of our experimental method (left) and the data analysis (right).

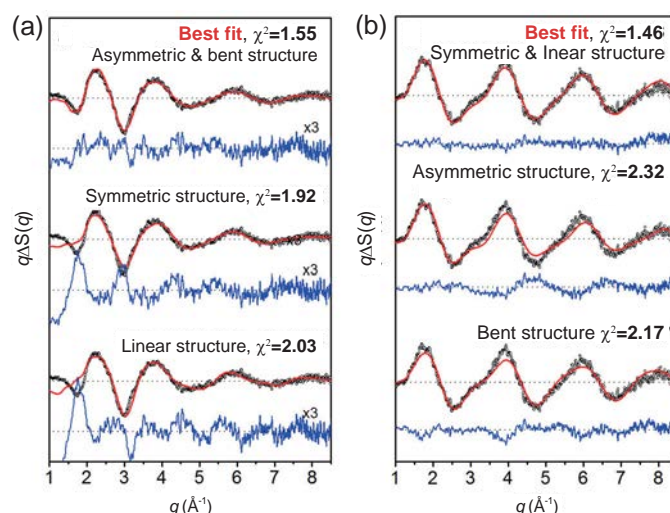


Figure 2: Difference scattering curves from the I_3^- photolysis in water (a) and acetonitrile (b) solution. Experimental (black) and theoretical (red) curves using various candidate structures of I_3^- ion are compared. Residuals (blue) obtained by subtracting the theoretical curve from the experimental one are displayed at the bottom.

To reveal the symmetry breaking of the I_3^- ion induced by hydrogen-bonding interaction with the solvent, the structure of the I_3^- ion was characterized in the three different solvents. The solvents of water, acetonitrile, and methanol have two, zero, and one functional group available for hydrogen bonding, respectively. Figure 2 shows experimental and theoretical difference scattering curves at 100 ps for the I_3^- ion in water and acetonitrile solutions. In water solution, the asymmetric and bent structure of the I_3^- ion gave the best fit when every parameter was adjusted freely. If a symmetric structure or a linear structure is assumed as a constraint, the fit between theory and experiment deteriorates. In contrast, in acetonitrile, the symmetric and linear structure gave the best fit within the error range when every parameter was adjusted freely. If an asymmetric structure or a bent structure is assumed as a constraint, the agreement deteriorates. The optimized structure in methanol lies between those in water and acetonitrile solutions, as expected from the number of functional groups available for hydrogen bonding.

Our experimental results well account for the results of previous experimental and theoretical studies [3, 4]. For example, the I–I–I angle of the bent I_3^- ion in water was estimated to be 153° from transient anisotropy measurement. This estimated value closely matches the value extracted from our data. Also, a theoretical study using MD simulation suggested an asymmetric structure of I_3^- in water with one bond longer by 0.49 \AA than the

other. This prediction is very similar to the result of our measurement (0.45 \AA).

In summary, by applying time-resolved X-ray solution scattering, we characterized the structure of the I_3^- ion in three different solvents, elucidating subtle structural changes of the ion depending on the hydrogen-bonding ability of the solvent. In water solution, the I_3^- ion was found to take an asymmetric and bent structure, lowering the structural symmetry. This phenomenon is also weakly present in methanol but not in acetonitrile.

REFERENCES

- [1] H. Ihee, M. Lorenc, T.K. Kim, Q.Y. Kong, M. Cammarata, J.H. Lee, S. Bratos and M. Wulff, *Science* **309**, 1223 (2005).
- [2] K.H. Kim, J.H. Lee, J. Kim, S. Nozawa, T. Sato, A. Tomita, K. Ichiyangi, H. Ki, J. Kim, S. Adachi and H. Ihee, *Phys. Rev. Lett.* **110**, 165505 (2013).
- [3] T. Kuhne and P. Vohringer, *J. Phys. Chem. A* **102**, 4177 (1998).
- [4] F.S. Zhang and R.M. Lynden-Bell, *Phys. Rev. Lett.* **90**, 185505 (2003).

BEAMLIN

AR-NW14A

K.H. Kim^{1,2}, J.H. Lee^{1,2}, J. Kim³, S. Nozawa⁴, T. Sato⁴, A. Tomita⁴, K. Ichiyangi⁴, H. Ki^{1,2}, J. Kim⁵, S. Adachi⁴ and H. Ihee^{1,2} (¹Inst. for Basic Science, ²KAIST, ³The Catholic Univ. of Korea, ⁴KEK-PF, ⁵Inha Univ.)

Role of the Free Surface for Orientations in Liquid Crystalline Polymer Films

There is a strong tendency for side chain liquid crystalline (LC) polymers to exhibit homeotropic orientation in thin films. We have shown the control of homeotropic-to-planar LC alignment in a side chain LC polymer, P5Az10MA, thin film by “free surface” modification. Adding a small amount of surface-active block copolymer composed of poly(butyl methacrylate) and P5Az10MA blocks, PBMA-*b*-P5Az10MA, to a LC homopolymer thin film induced orientational alternations of the LC phase from homeotropic to planar alignment effected by surface segregation and coverage of PBMA at the *free surface*. The present result demonstrates that the free surface and surface segregation are important for controlling the inner structure of the polymer LC film.

The molecular orientation of liquid crystals (LCs) depends strongly on the surface characters [1]. LC alignment techniques include surface molecular orientations and topographical grooves and undulations of the substrate. Controlling the LC alignment layers is an important technique in applications for LC optical devices. LC surface alignment by mechanically rubbing the polymer surface on a substrate is the most widespread and popular industrial process for LC devices [2]. Recently, LC alignment was carried out on photoreactive polymer films by anisotropic irradiation [3]. Currently, the photoalignment method has begun to be used in the industrial production of liquid crystal televisions. Most LC devices are made of fluid low molecular LCs; the LC active layer in these devices is sandwiched between the alignment layers on substrates. On the other hand, polymer LCs can form robust thin films on substrates by themselves, and so there are expectations that polymer LCs could form free-standing films with a free surface for applications. At a free surface (an air surface), calamitic LC molecules strongly prefer the homeotropic (vertical) molecular alignment; this has been shown experimentally [4] and has also been verified by theoretical simulations

[5]. Actually, homeotropic alignment dominated by the free surface is generally preferable in side chain LC polymer films. Furthermore, the low birefringence character of the homeotropic alignment narrows down the application of LC polymers to display devices.

Recently, we reported the LC orientational alternation of a polymer LC induced by free surface modification in polymer thin films through polymer surface segregation [6]. Surface segregation is one of the interfacial phenomena in polymer thin films, involving enrichment of a specific polymer component at the surface by self-assembly in polymer blend films [7]. Polymer components with low free energy, relatively low surface tension [8] and high mobility [9] are easily concentrated at the surface. To modify the free surface of the LC polymer film, we apply the surface segregation of a small amount of a free-surface-active polymer. Coverage of the film surface with the free-surface-active polymer leads to homeotropic-to-parallel orientational alternations of LC mesogens, which further enable efficient in-plane photoalignment of LC and microphase separation (MPS) domains of a relevant LC polymer and block copolymer by linearly polarized light (LPL).

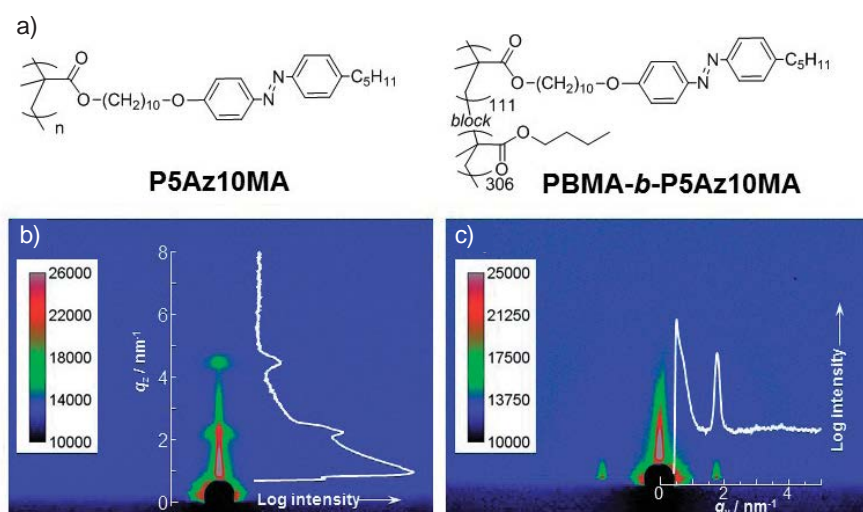


Figure 1: Chemical structures for P5Az10MA and PBMA-*b*-P5Az10MA (a). 2D GI-SAXS images of a pure P5Az10MA thin film (b) and PBMA-*b*-P5Az10MA (10%)/P5Az10MA blend thin film (c) after annealing at 130°C. In the SAXS patterns, 1D intensity profiles are indicated as curves in white.

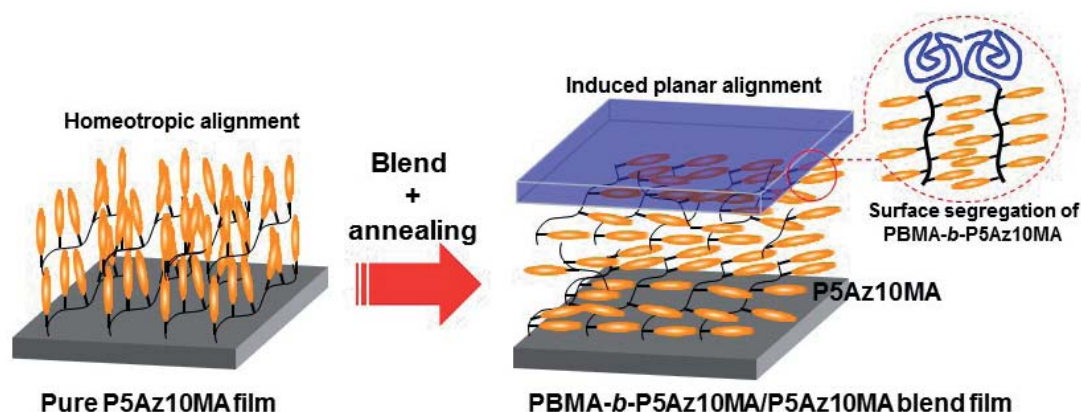


Figure 2: Schematic illustrations of the orientational alternation and alignment process for the P5Az10MA homopolymer.

The smectic liquid crystalline azobenzene polymer P5Az10MA [Fig. 1(a)] exhibits homeotropic alignment in a thin film. In grazing incidence small angle X-ray scattering (GI-SAXS) measurements, scattering corresponding to the smectic lamella structure was observed in the out-of-plane direction [Fig. 1(b)]. On the other hand, adding 10 weight% (%) of PBMA-*b*-P5Az10MA [Fig. 1(a)] induced the opposite LC orientation in the film. In the PBMA-*b*-P5Az10MA (10%)/P5Az10MA film, scattering spots due to the smectic layer were observed in the in-plane position by GI-SAXS 2D imaging [Fig. 1(c)], suggesting that the smectic LC layer aligned normal to the substrate with planar aligned azobenzene side chains. Contact angle measurements demonstrate that the PBMA component is segregated and enriched at the film surface in the PBMA-*b*-P5Az10MA (10%)/P5Az10MA film. The surface segregated top layer of the PBMA block provides a microphase separated interface parallel to the surface plane. As a result, a random planar aligned smectic LC layer is induced with perpendicularly oriented rigid rod LC polymer backbone from the surface segregated layer. The present approach through the surface-active layer can be also applied to in-plane alignment for the microphase separated cylinder structure for a P5Az10MA block copolymer. The homeotropic alignment has a disadvantage for efficient photoalignment by LPL irradiation because the transition moment for azobenzene side chains is normal to the actinic LPL electric field. In the normal aligned smectic layer, LPL irradiation can lead to efficient angular selective photoisomerization of the azobenzene LC.

The orientation and photoalignment behaviors proposed in the present processes are illustrated in Fig. 2. In the pure P5Az10MA film, the normal anchoring from the free surface of azobenzene side chain mesogens induces the homeotropic LC orientation. Adding the surface-active PBMA-*b*-P5Az10MA and subsequent annealing leads to the formation of a skin layer on the surface and provides planar orientation of mesogens. Owing to the preformed parallel orientation, LPL irradiation

efficiently leads to homogeneous in-plane alignment orthogonal to the electric field of the LPL. The proposed alignment process via surface segregation is very simple and therefore provides new possibilities for orientation control of various types of LC materials. Selective surface segregation of a surface-active polymer component offers promising applications for imposing surface functions such as adhesive and frictional properties and for improving biocompatibility. In addition to such functions accessing the exterior phase, the present work indicates that the free surface and surface segregation are also important for controlling the inner structure of the polymer LC film.

REFERENCES

- [1] B. Jerome, *Rep. Prog. Phys.* **54**, 391 (1991).
- [2] a) P. Chatelain, *Bull. Soc. Fr. Mineral.*, **66**, 105 (1943). b) J. Cognard, *Mol. Cryst. Liq. Cryst. Suppl. Ser.*, **1**(supp1), 1 (1982).
- [3] K. Ichimura, *Chem. Rev.*, **100**, 1847 (2000).
- [4] a) B. Ocko, A. Braslau, P. Pershan, J. Alsnielsen and M. Deutsch, *Phys. Rev. Lett.*, **57**, 94(1986). b) P. S. Pershan, *Faraday Discuss. Chem. Soc.*, **89**, 231 (1990).
- [5] a) N. Scaramuzza, C. Berlic, E. Barna, G. Strangi, V. Barna and A. Ionescu, *J. Phys. Chem. B*, **108**, 3207(2004). b) S.-M. Chen, T.-C. Hsieh and R.-P. Pan, *Phys. Rev. A*, **43**, 2848 (1991). c) A.A. Canabarro, I.N. de Oliveira and M.L. Lyra, *Phys. Rev. E*, **77**, 011704 (2008).
- [6] K. Fukuhara, Y. Fujii, Y. Nagashima, M. Hara, S. Nagano and T. Seki, *Angew. Chem. Int. Ed.*, **52**, 5988 (2013).
- [7] a) Q. Bhatia, D. Pan and J. Koberstein, *Macromolecules*, **21**, 2166 (1988). b) K. Tanaka, A. Takahara and T. Kajiyama, *Macromolecules*, **31**, 863 (1998). c) E. Huang, T. Russell, C. Harrison, P. Chaikin, R. Register, C. Hawker and J. Mays, *Macromolecules*, **31**, 7641 (1998).
- [8] M. Khayet, M. Alvarez, K. Khulbe and T. Matsuura, *Surf. Sci.*, **601**, 885 (2007).
- [9] S. Wu, *J. Phys. Chem.*, **74**, 632 (1970).

BEAMLINe

BL-6A

S. Nagano¹, Y. Nagashima², K. Fukuhara², M. Hara² and T. Seki² (¹Nagoya Univ.-VBL, ²Nagoya Univ.)

Structure of Silicene on a Ag(111) Surface Studied by TRHEPD

The structure of silicene, which consists of a single layer of silicon deposited on a single-crystal silver Ag(111) surface, was experimentally determined for the first time using total-reflection high-energy positron diffraction (TRHEPD) [1]. It was confirmed that silicene has a buckling structure unlike graphene, which consists of a flat single layer of carbon atoms.

The Slow Positron Facility (SPF) of the Institute of Materials Structure Science (IMSS), KEK increased the intensity of the slow positron beam ten-fold in 2010 [2] to create one of the world's highest-intensity slow positron beams. The beam is about 1000 times stronger than a beam obtained by using a commercially-available positron source of radioisotope ^{22}Na . TRHEPD, formerly called reflection high-energy positron diffraction (RHEPD), can accurately determine atomic positions on the topmost surface and immediate subsurface of a crystal. TRHEPD was first developed and applied to surface science by the Japan Atomic Energy Agency (JAEA) [3]. In order to improve this method further, KEK and JAEA installed a TRHEPD station at SPF, KEK in 2011 [2]. Later, the brightness of the beam was enhanced by using a method characteristic to a positron beam, the remission of thermalized positrons.

Since the discovery of a method to isolate a single sheet of carbon (C) atoms in a hexagonal honeycomb lattice structure, graphene, in 2004, the fundamental properties of graphene have been extensively studied as well as its potential application to high carrier-mobility electronic devices. Stimulated by this, extensive efforts to create a similar structure of silicon (Si) atoms have been made, along with theoretical investigations. Theories predict that, unlike carbon which has a layer structure as in graphite as well as diamond structures, silicene would have a buckling structure as shown in Fig. 1 since Si has a diamond structure alone.

In 2012 a number of different procedures were successfully developed for the synthesis of silicene, including one on an Ag(111) surface.

While the theoretically predicted two-dimensional (4x4) symmetry of silicene grown in this way was verified by scanning tunneling microscopy (STM) observations, a buckled structure due to the strong sp^3 bonding character also predicted by the theories was not confirmed. It is also predicted that the Dirac cone of the energy dispersion in silicene depends on the magnitude of the buckling as well as on interactions with the Ag(111) substrate. Thus, the amount of the buckling (spacing between the top and bottom Si layers in silicene, Δ) and the spacing between the bottom Si layer and the top Ag layer, d , are important factors in understanding its electronic properties.

A collaboration of researchers from JAEA, KEK, University of Tokyo and Nagoya University used KEK's high-intensity, high-brightness positron beam with an energy of 10 keV (wavelength of 0.12 Å) to measure the TRHEPD pattern of silicene while varying the glancing angle ($\theta = 0^\circ - 6^\circ$) of the incident positron beam. Then rocking curves, i.e., plots of the glancing angle dependence of the diffraction spot intensity, for the specular diffraction spot were extracted. By analyzing the rocking curves the detailed structure of the silicene was successfully determined.

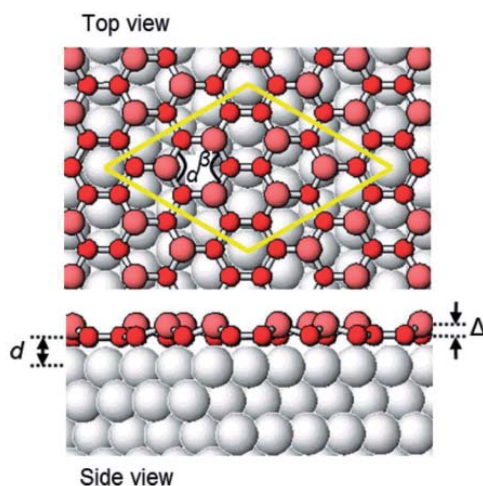


Figure 1: Top and side views of proposed silicene on Ag(111) surface. Large and small red spheres are the top and bottom Si atoms, respectively. The gray spheres are the underlying Ag atoms of the substrate. The spacing between the top and bottom Si layers is denoted by Δ . The distance between the bottom layer of silicene and the underlying first Ag layer is denoted by d . The bond angles are labeled as α and β .

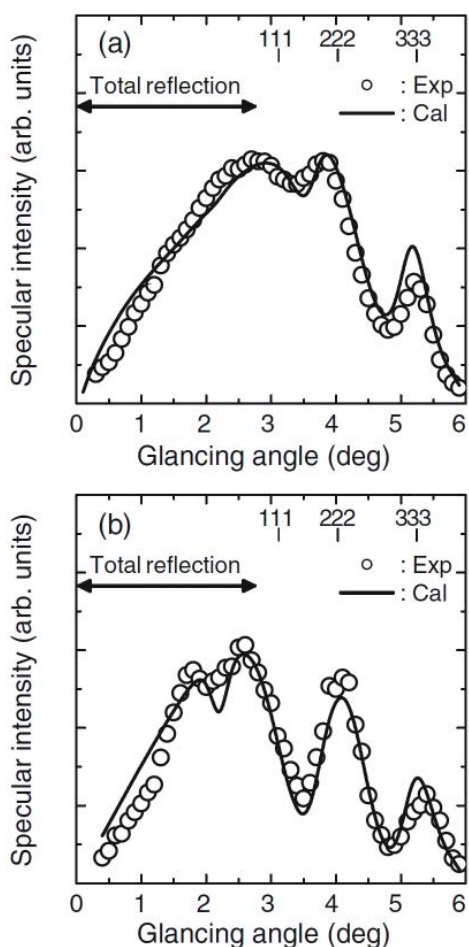


Figure 2: TRHEPD rocking curves for (a) Ag(111)-1 \times 1 surface before the Si deposition and (b) silicene on an Ag(111) surface in the one-beam condition at room temperature. Circles are the experimental data. Solid curves indicate the results calculated with the optimum values for the adjustable parameters.

A single-crystal Ag(111) film comprising 20 atomic layers was grown on an Si (111) surface, subsequent to which Si was vapor-deposited onto the surface of the Ag film to form silicene. The expected symmetry of (4 \times 4) was confirmed using reflection high-energy electron diffraction (RHEED). It is worth noting that the symmetry of the surface atomic configuration can be easily identified by using various surface-sensitive methods such as RHEED, but it is not easy to determine the accurate position of each surface atom by analyzing the data in detail.

The rocking curve measurements were conducted both under the one-beam condition which is sensitive to atomic coordinates perpendicular to the surface and the many-beam condition which is also sensitive to the atomic arrangement parallel to the surface.

By analyzing the rocking curve shown in Fig. 2 (b), measured in the one-beam condition (beam incident

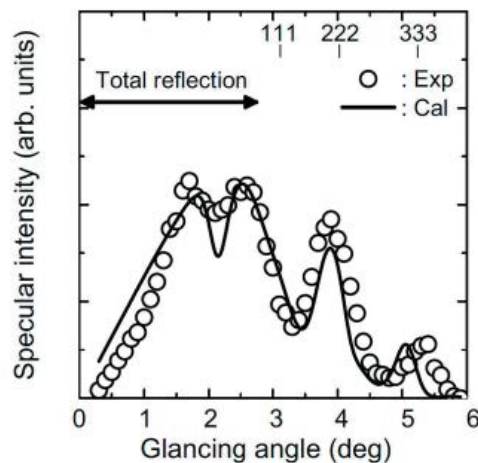


Fig. 3. TRHEPD rocking curve for silicene on an Ag(111) surface in the many-beam condition at room temperature. Circles indicate the experimental data. The solid line indicates the calculated curve using the optimum parameters.

from 13° off the [11 $\bar{2}$] direction), the buckling structure was confirmed where the buckling distance Δ was 0.83 Å and the Si-Ag layer distance d was 2.14 Å.

Next, the rocking curve shown in Fig. 3, measured under the many-beam condition (beam incident from the [11 $\bar{2}$] direction), was analyzed. The two Si-Si bond angles (see Fig. 1) were determined to be $\alpha = 112^\circ$ and $\beta = 119^\circ$, confirming the buckling structure which leads to (4 \times 4) symmetry. These results agree well with the theoretical predictions ($\Delta = 0.78$ Å, $d = 2.17$ Å, $\alpha = 110^\circ$, and $\beta = 118^\circ$) [4].

These experimental results highlight the fact that TRHEPD with the high-brightness, high-intensity variable-energy positron beam at KEK is very useful for determining the atomic arrangement of a surface. This method is expected to become a standard method for surface structure determination, as X-ray and neutron diffraction is the standard method for structural determination of bulk structures.

REFERENCES

- [1] Y. Fukaya, I. Mochizuki, M. Maekawa, K. Wada, T. Hyodo, I. Matsuda and A. Kawasuso, *Phys. Rev. B* **88**, 205413 (2013).
- [2] K. Wada, T. Hyodo, A. Yagishita, M. Ikeda, S. Ohsawa, T. Shidara, K. Michishio, T. Tachibana, Y. Nagashima, Y. Fukaya, M. Maekawa and A. Kawasuso, *Eur. Phys. J. D* **66**, 37 (2012).
- [3] A. Kawasuso and S. Okada, *Phys. Rev. Lett.* **81**, 2695 (1998).
- [4] P. Vogt, P. De Padova, C. Quaresima, J. Avila, E. Frantzeskakis, M.C. Asensio, A. Resta, B. Ealet and G.L. Lay, *Phys. Rev. Lett.* **108**, 155501 (2012).

BEAMLINER

SPF-A3

T. Hyodo¹ and Y. Fukaya² (¹KEK-PF, ²JAEA-ASRC)

Novel Electronic States of Topological Crystalline Insulators Revealed by ARPES

Topological insulators are a novel quantum state of matter where unusual gapless metallic states protected by time-reversal symmetry appear within the bulk band gap. A recent theory predicted another type of topological material called topological crystalline insulator (TCI), where the surface states are protected by mirror symmetry of the crystal. We have performed angle-resolved photoemission spectroscopy of narrow-gap IV-VI semiconductor $\text{Pb}_{1-x}\text{Sn}_x\text{Te}$ as a function of Pb content x and found clear evidence for the topological phase transition from TCI to trivial insulator. The present result establishes the essential role of the crystal mirror symmetry in realization of the TCI phase.

The discovery of topological insulators (TIs) triggered the search for new types of topological materials protected by various symmetries, and a recent theory predicted the existence of *topological crystalline insulators* (TCIs) in which metallic surface states are protected by mirror symmetry of the crystal structure [1, 2]. Such a TCI phase has been experimentally verified by angle-resolved photoemission spectroscopy (ARPES) experiments for narrow-gap IV-VI semiconductor SnTe [3, 4] and related compounds [5]. In those materials, the topological surface states on the (001) surface consist of Dirac cones located at momenta slightly away from the time-reversal-invariant momentum (TRIM) $\bar{\Gamma}$ point in the (110) mirror plane of the crystal [Fig. 1(a)], producing a characteristic double Dirac-cone band dispersion. This is distinct from the three-dimensional TIs whose surface states are characterized by an odd number of Dirac cones. In contrast to the double Dirac-cone signature observed in the TCI phase, the ARPES measurements for isostructural PbTe [3] revealed the absence of any surface states, which strongly suggests a trivial-to-non-trivial topological quantum phase transition in the solid-solution system $\text{Pb}_{1-x}\text{Sn}_x\text{Te}$. However, it is still unclear how the surface and bulk electronic states evolve as a function of Sn composition x , which would be useful for attaining a practical understanding of TCIs.

To elucidate the electronic states of $\text{Pb}_{1-x}\text{Sn}_x\text{Te}$, we have performed high-resolution ARPES experiments at BL-28A and Tohoku University [6, 7].

Figure 1(b) shows the Fermi-surface mapping around the $\bar{\Gamma}$ point of the surface Brillouin zone (BZ) for $\text{Pb}_{1-x}\text{Sn}_x\text{Te}$ with four representative Sn compositions x including both end members SnTe ($x = 1.0$) and PbTe ($x = 0.0$). At $x = 1.0$, we immediately notice a dumbbell-shaped intensity pattern elongated along the $\bar{\Gamma}\bar{X}$ direction (k_x direction) with its intensity maxima located away from the $\bar{\Gamma}$ point. This feature arises from the double Dirac-cone surface state [3] whose Dirac points are located at each intensity maxima, as one can see from the near- E_F band dispersion along the $\bar{\Gamma}\bar{X}$ cut in Fig. 1(c) showing the band maxima on both sides of the $\bar{\Gamma}$ point. The M-shaped dispersion and the dumbbell-shaped Fermi surface are also observed for $x = 0.5$, which sig-

nifies that the system still belongs to the TCI phase, although the intensity distribution around E_F appears to be weaker and broader than that for $x = 1.0$. At $x = 0.3$, the observed ARPES intensity looks different, and neither the dumbbell-shaped Fermi surface nor the M-shaped dispersion are clearly resolved. Nevertheless, we are still able to trace the surface-band dispersion by taking second derivatives of the intensity and, as shown in Fig. 1(d), the M-shaped dispersion is still discernible. In contrast, the spectral feature for $x = 0.0$ looks substantially different. The near- E_F intensity is strongly suppressed and no Dirac-cone surface band is observed, reflecting the topologically trivial (ordinary) nature of PbTe [3]. A more systematic ARPES experiment for various x and photon energies further revealed that the topological phase transition takes place at $x \sim 0.25$ [6].

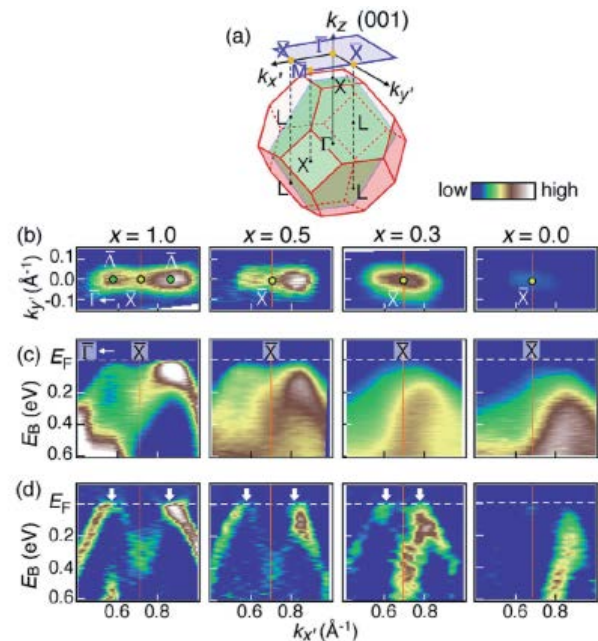


Figure 1: (a) Bulk Brillouin zone (BZ) and corresponding surface BZ of $\text{Pb}_{1-x}\text{Sn}_x\text{Te}$. The (110) mirror plane is indicated by the green shaded area. (b) ARPES intensity at E_F around the \bar{X} point for various x values plotted as a function of in-plane wave vector at $T = 30 \text{ K}$ [6]. (c) Corresponding near- E_F ARPES intensity along the $\bar{\Gamma}\bar{X}$ cut plotted as a function of k_x and binding energy E_B . (d) Band dispersions derived from the second derivatives of the momentum distribution curves (MDCs) along the $\bar{\Gamma}\bar{X}$ cut. The \mathbf{k} location of the Dirac point is indicated by white arrows in (d).

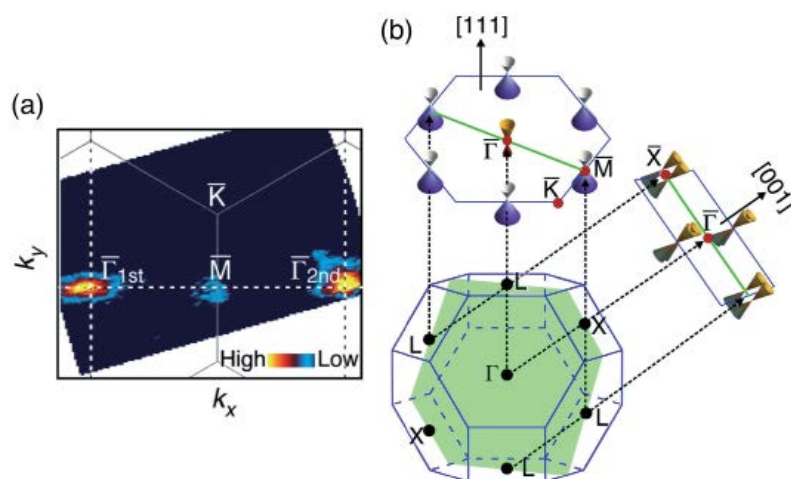


Figure 2: (a) ARPES intensity mapping at E_F of SnTe on the (111) surface plotted as a function of in-plane wave vector [7]. (b) Schematic picture of the Dirac-cone surface state on two different surface planes of (001) and (111). The green shaded area and green line represent the (110) mirror plane and the mirror-symmetric line on the surface BZ, respectively.

The most important feature is the evolution of the surface state in the TCI phase. In particular, as seen in Fig. 1(d), the \mathbf{k} position of the Dirac point in the BZ systematically *moves* toward the \bar{X} point with decreasing x (see white arrows). Such a degree of freedom is obviously a unique feature of the mirror-symmetry protected TCIs, in contrast to the TIs where the Dirac point is bound to the TRIM. Intuitively, the double Dirac-cone structure in TCIs is a result of the hybridization of two Dirac cones, because, on the (001) surface, two L points (which are each responsible for a surface Dirac cone due to the band inversion at L) are projected onto the same \bar{X} point; therefore, the separation of the two Dirac cones can be taken as a measure of this hybridization. Our finding is of crucial importance for establishing a better understanding of the physical mechanism to create the peculiar double Dirac-cone structure in TCIs. Also, the mobile Dirac cone is particularly useful in applications requiring Fermi-surface matching with other materials, like spin injection.

To see whether or not the Dirac-cone band dispersion is a unique feature of the (001) surface, we also performed an ARPES measurement on the (111) surface. As shown in Fig. 2(a), one can immediately recognize the bright intensity centered at the first and second $\bar{\Gamma}$ points as well as the relatively weak intensity at the \bar{M} point of the hexagonal surface BZ. This intensity pattern originates from the Dirac-cone surface states centered at the $\bar{\Gamma}$ and \bar{M} points, respectively [7]. Figure 2(b) compares the observed Dirac-cone surface states between the (001) and (111) surfaces. The surface states for the (001) surface consist of a double-Dirac-cone structure. On the other hand, for the (111) surface, always a single L point is projected onto either the $\bar{\Gamma}$ or \bar{M} point to

produce a single Dirac cone centered at those TRIMs, and no band hybridization takes place. As a result, the Dirac point coincides with the $\bar{\Gamma}$ and \bar{M} points. The present ARPES result thus allows for the first time a direct comparison of topological surface states on different crystal faces of a topological material, and establishes the essential role of the crystal mirror symmetry in realization of the TCI phase.

REFERENCES

- [1] L. Fu, *Phys. Rev. Lett.* **106**, 106802 (2011).
- [2] T.H. Hsieh, H. Lin, J. Liu, W. Duan, A. Bansil and L. Fu, *Nature Commun.* **3**, 982 (2012).
- [3] Y. Tanaka, Z. Ren, T. Sato, K. Nakayama, S. Souma, T. Takahashi, K. Segawa and Y. Ando, *Nature Phys.* **8**, 800 (2012).
- [4] S.-Y. Xu, C. Liu, N. Alidoust, M. Neupane, D. Qian, I. Belopolski, J.D. Denlinger, Y.J. Wang, H. Lin, L.A. Wray, G. Landolt, B. Slomski, J.H. Dil, A. Marcinkova, E. Morosan, Q. Gibson, R. Sankar, F.C. Chou, R.J. Cava and A. Bansil, *Nature Commun.* **3**, 1192 (2012).
- [5] P. Dziawa, B.J. Kowalski, K. Dybko, R. Buczko, A. Szczerbakow, M. Szot, E. Łusakowska, T. Balasubramanian, B.M. Wojek, M.H. Berntsen, O. Tjernberg and T. Story, *Nature Mater.* **11**, 1023 (2012).
- [6] Y. Tanaka, T. Sato, K. Nakayama, S. Souma, T. Takahashi, Z. Ren, M. Novak, K. Segawa and Y. Ando, *Phys. Rev. B* **87**, 155105 (2013).
- [7] Y. Tanaka, T. Shoman, K. Nakayama, S. Souma, T. Sato, T. Takahashi, M. Novak, K. Segawa and Y. Ando, *Phys. Rev. B* **88**, 235126 (2013).

BEAMLINE

BL-28A

T. Sato¹, Y. Tanaka¹, T. Shoman¹, K. Nakayama¹, S. Souma¹, T. Takahashi¹, M. Novak², K. Segawa² and Y. Ando² (¹Tohoku Univ., ²Osaka Univ.)

Magnetic Structure of the Single-Layer Graphene/Nickel Interface

We investigated the magnetic structure of the single-layer graphene/Ni(111) interface with depth-resolved X-ray magnetic circular dichroism spectroscopy. Ni *L*-edge analysis clarified that the easy magnetization direction changes from in-plane to out-of-plane in the Ni atomic layers near the interface, possibly associated with π -*d* hybridization. C *K*-edge analysis demonstrated that intensification of the spin-orbit interactions and spin polarization are induced in the π band region by the Ni atoms located near the interface. These results indicate the importance of understanding the interfacial magnetic structures for the development of graphene-based spin devices.

Spintronics is a new field of electronics that may lead to novel devices taking advantage of both the charge and spin of electrons. Graphene-based spintronics is a particularly active area of research because of the great potential of graphene for spin transport as represented by the long spin-diffusion length and extremely high carrier mobility. Efficient injection of spin-polarized currents into graphene is one of the most significant issues in developing graphene-based spintronics. Despite the theoretical prediction of the spin filtering effect of graphene/ferromagnetic metal (FM) interfaces [1], a satisfactory high efficiency of spin injection has not been reported yet [2]. Elucidation of the magnetic structures of graphene/FM interfaces may clarify the underlying reasons for the difficulty of efficient spin injection in graphene-based devices. In the present study, the electronic and magnetic structures of graphene/FM interfaces are being investigated for the bilayer structure of single-layer graphene (SLG) and Ni(111) thin film by applying X-ray magnetic circular dichroism (XMCD) with atomic-layer level depth-resolution [3].

Figures 1(a) and (b) show the Ni *L*-edge XMCD spectra measured at two different incident angles of the circularly-polarized X-ray beam. The X-ray incident angles of 30° and 60° are sensitive to the magnetic

moments aligned in the in-plane and out-of-plane directions, respectively. The XMCD spectra were obtained by collecting the Auger electrons at different values of detection angle θ using a 2D electron detector. Since the effective escape depth of the emitted electrons changes depending on the detection angle due to the scattering attenuation in the sample, the relative fraction of the signals from the Ni atomic layer near the interface increases with decreasing detection angle θ . In Fig. 1(a), the XMCD intensity at $\theta = 30^\circ$ (red line) is larger than that at $\theta = 3^\circ$ (blue line), and this relationship is inverted in Fig. 1(b). This contrasting behavior indicates that the state of the magnetic moment in the Ni(111) thin film changes depending on the distance from the interface. To gain insight into the magnetic structure of the interface, the total magnetic moment (M_{tot}) and its angle γ from the in-plane direction were estimated for the Ni atoms near and far from the interface ($Ni_{interface}$ and Ni_{bulk}) by applying the magnetic sum rules [4, 5]. The obtained values were $M_{tot} = 0.55\mu_B$ and $\gamma = 87^\circ$ for $Ni_{interface}$, and $M_{tot} = 0.66\mu_B$ and $\gamma = 3^\circ$ for Ni_{bulk} . M_{tot} of Ni_{bulk} agrees well with that of the Ni(111) thin film [6]. This indicates that the Ni magnetic moment shows perpendicular magnetic anisotropy (PMA) at the interface, different from the in-plane orientation in the Ni(111) thin film.

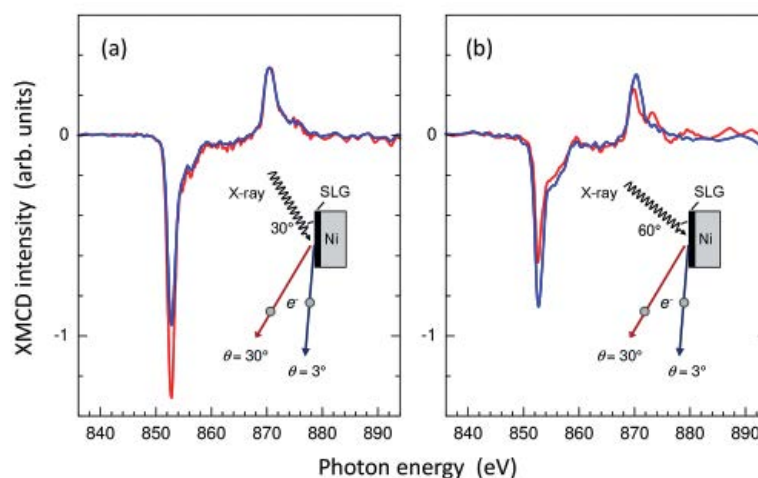


Figure 1: Depth-resolved Ni *L*-edge XMCD spectra at the X-ray incidence angles of 30° (left panel) and 60° (right panel). The blue and red lines in the spectra represent the data at the detection angle θ of 3° and 30°, respectively.

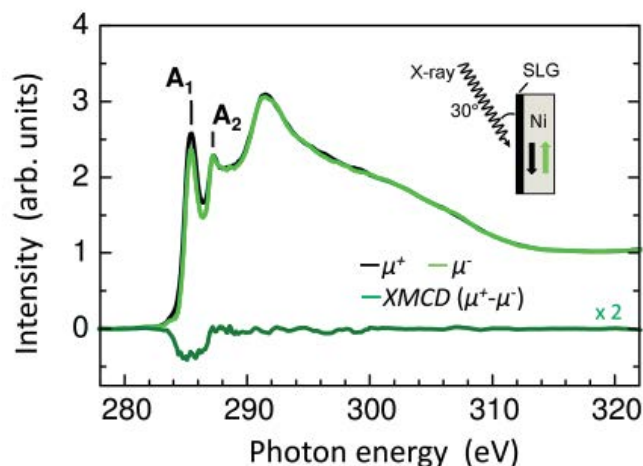


Figure 2: C *K*-edge XMCD spectra at the X-ray incidence angle of 30°. The black and light green spectra are the X-ray absorption spectra measured with the parallel (μ^+) and antiparallel (μ^-) Ni remanent magnetization to the propagation direction of the circularly-polarized X-ray beam.

Figure 2 shows the C *K*-edge XMCD spectrum measured at the X-ray incidence angle of 30° in remanence. Prominent XMCD signals can be seen at around the A_1 and A_2 peaks, which are assigned to the excitations from the 1s states to the hybridized states between the π^* (p_z) states around the *K*- and *M*-points of graphene and the Ni 3*d* states, respectively. Due to the absence of spin-orbit interactions (SOI) in the 1s initial states, the C *K*-edge XMCD is expected to reflect only the orbital magnetic moment of the 2*p* states. The intrinsic SOI strength of graphene is too small to generate sufficiently large orbital magnetic moment to be detectable as XMCD signals. It is therefore concluded that the spin polarization and also the enhancement of SOI are induced in SLG through π -*d* hybridization. This conclusion is in good agreement with theoretical studies [7].

In summary, the interface magnetic structure in SLG/Ni(111) thin film was investigated by depth-resolved XMCD spectroscopy. The results showed that on the Ni side of the interface the preferable spin orientation direction changes from in-plane to out-of-plane toward the interface, and on the SLG side not only the spin polarization but also the SOI enhancement are induced in the π^* states. The interfacial PMA could disturb the operation of graphene-based spin devices

with conventional FM electrodes with in-plane magnetization. The present study highlights the importance of the design of interface magnetic structures at the atomic layer level for graphene-based spin devices.

REFERENCES

- [1] V.M. Karpan, G. Giovannetti, P.A. Khomyakov, M. Talanana, A.A. Starikov, M. Zwierzycki, J. van den Brink, G. Brocks and P.J. Kelly, *Phys. Rev. Lett.* **99**, 176602 (2007).
- [2] M. Ohishi, M. Shiraishi, R. Nouchi, T. Nozaki, T. Shinjo and Y. Suzuki, *Jpn. J. Appl. Phys.* **46**, L605 (2007).
- [3] K. Amemiya, *Phys. Chem. Phys. Chem.* **14**, 10477 (2012).
- [4] B.T. Thole, P. Carra, F. Sette and G. van der Laan, *Phys. Rev. Lett.* **68**, 1943 (1992).
- [5] P. Carra, B.T. Thole, M. Altarelli and X. Wang, *Phys. Rev. Lett.* **70**, 694 (1993).
- [6] G.Y. Guo, W.M. Temmerman and H. Ebert, *Physica B* **172**, 61 (1991).
- [7] Z.Y. Li, Z.Q. Yang, S. Qiao, J. Hu and R.Q. Wu, *J. Phys.: Condens. Matter* **23**, 225502 (2011).

BEAMLINE

BL-7A

Y. Matsumoto^{1,2}, S. Entani¹, A. Koide³, P.V. Avramov¹, H. Naramoto¹, K. Amemiya⁴, T. Fujikawa³ and S. Sakai¹ (1)JAEA, (2)CROSS, (3)Chiba Univ. (4)KEK-PF)

Strain Mediated Control of Magnetic Anisotropy in Alternately Layered FeNi Thin Films

The $L1_0$ -type FeNi multilayer has attracted attention as a candidate material for rare metal-free perpendicularly magnetized films for high-density recording media. To understand the fundamental magnetic properties, *in situ* observation of the growth process is important. In this study, we investigated the effect of the lattice strain on magnetic anisotropy of alternately layered FeNi ultrathin films by X-ray magnetic circular dichroism (XMCD) analysis, and showed that perpendicular magnetic anisotropy of Fe is enhanced when compressive strain in the in-plane direction is applied to the FeNi films.

The $L1_0$ ordered alloy, which consists of alternate stacking of two different atomic planes along the fcc [001] direction, is expected to exhibit uniaxial magnetic anisotropy in the c axis, [001]. Various efforts have been made to realize perpendicular magnetic anisotropy (PMA) in $L1_0$ -type FeNi [1-3], however, it has not yet been achieved in the multilayered system. On the other hand, it is known that magnetic anisotropy is closely correlated with the surface/interface structure, strain, and so forth. Our previous *in situ* XMCD study revealed element-specific magnetic anisotropy energies (MAE) in FeNi thin films on a Cu(001) substrate [4], and indicated that PMA is enhanced in the case of Fe-terminated FeNi films, while that of Ni-terminated films is reduced.

In this article, we demonstrate from the XMCD study combined with reflection high-energy electron diffraction (RHEED) analysis that PMA is enhanced when compressive strain in the in-plane direction is applied to the Fe layer [5], and confirm that the magnetic anisotropy of FeNi is controlled by the lattice strain by changing the thickness of the Cu spacer layer on a NiCu/Cu(001) substrate [6].

All the experiments were performed *in situ* in an ultra-high vacuum chamber at the beamlines BL-7A and 16A of the Photon Factory. Figure 1 shows the ratio of orbital to spin magnetic moments, and MAE of the Fe

and Ni layers in FeNi films grown on Ni/Cu(001) substrate, as functions of the in-plane lattice constant. Here, we call the nearest in-plane interatomic distance as the in-plane lattice constant, a_{in} . The results showed that the perpendicular component of the orbital magnetic moment increases and the in-plane component decreases as a_{in} gets smaller, suggesting that PMA is enhanced when compressive strain in the in-plane direction is applied. To confirm the enhancement of PMA in FeNi film itself, we used a non-magnetic Cu(t_{Cu} ML)/Ni₄₈Cu₅₂/Cu(001) substrate, where t_{Cu} indicates the thickness of the Cu spacer layer. The in-plane lattice constant was continuously modulated by changing t_{Cu} . 1 ML Fe and Ni layers were alternately grown starting with an Fe layer on the substrate, so that the effect of strain on the magnetic property of the FeNi layer could be investigated at the same time by using wedged-shaped substrates with various lattice constants. XMCD spectra were taken in total electron yield mode at room temperature. A pulsed magnetic field of 2 kOe was applied before each measurement. We first estimate a_{in} of Cu(t_{Cu} ML)/NiCu(124 ML)/Cu(001) as a function of t_{Cu} . a_{in} changes from 0.2536 to 0.2546 nm when t_{Cu} increases from 0 to 88 ML, while that of bare Cu(001) is reported to be 0.2550 nm.

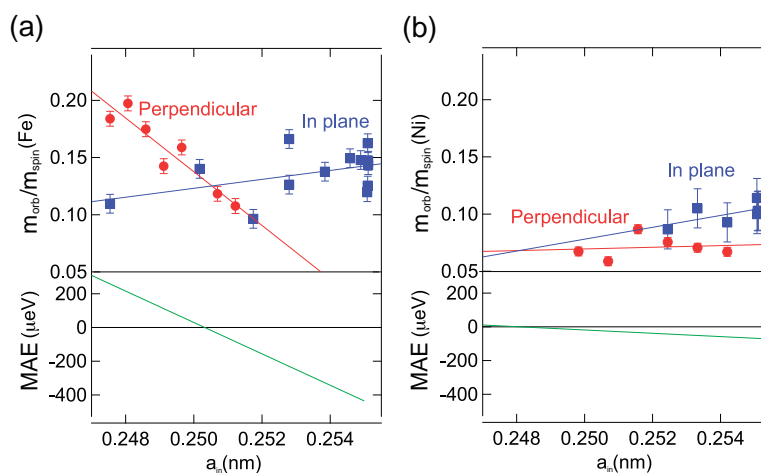


Figure 1: Ratios of orbital to spin magnetic moments in the perpendicular and in-plane directions, and MAE of sandwiched (a) Fe and (b) Ni layers as functions of in-plane lattice constant, a_{in} .

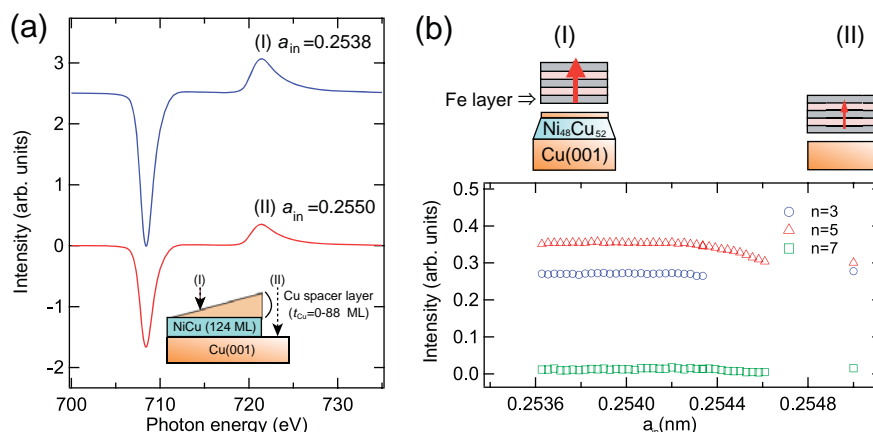


Figure 2: (a) Fe L-edge XMCD spectra for 5 ML FeNi films grown on regions (I) and (II). XMCD were measured at the normal incidence configuration. A cross-sectional view of the substrate is also shown. (b) XMCD intensity at Fe L_3 peak top for n ML FeNi films as a function of a_{in} . XMCD was measured at the normal incidence configuration.

Figure 2(a) shows Fe L-edge XMCD spectra for 5 ML FeNi films grown on regions (I) and (II). a_{in} estimated from RHEED analysis is also shown in the figure. In the present case, the FeNi films show perpendicular magnetization when they are grown on (I) and (II). The XMCD signal is larger for (I), which suggests that PMA is enhanced when the lattice constant of the substrate is smaller. To investigate the relation between the structure and magnetic anisotropy systematically, we plot the XMCD intensity at the Fe L_3 peak top for n ML FeNi films as a function of a_{in} in Fig. 2(b). The 5 ML FeNi film shows perpendicular magnetization in a wide region of a_{in} including (I) and (II), but larger XMCD intensity is observed at smaller a_{in} . This indicates that the compressive strain in the in-plane direction enhances PMA in FeNi films. This is contrary to the earlier result on Ni films, in which Ni thin films showed enhancement of PMA when tensile strain was applied in the in-plane direction [7]. It is reported from first-principles calculations for $L1_0$ -type FeNi that only the Fe components of the orbital density of states exist at the Fermi level [8], and the Fe $d_{x^2-y^2}$ and $d_{yz,zx}$ orbitals delocalize near the Fermi level by the compressive strain [9]. Indeed, we observed diffused magnetic moment in the XMCD spectra of Fe, which would be evidence of the delocalization [6]. We conjecture that such delocalization increases

the perpendicular orbital magnetic moment, and leads to an enhancement of PMA, which cannot be realized in Ni thin films.

REFERENCES

- [1] T. Shima, M. Okamura, S. Mitani and K. Takanashi, *J. Magn. Magn. Mater.* **310**, 2213 (2007).
- [2] M. Mizuguchi, S. Sekiya and K. Takanashi, *J. Appl. Phys.* **107**, 09A716 (2010).
- [3] T. Kojima, M. Mizuguchi and K. Takanashi, *J. Phys.: Conf. Ser.* **266**, 012119 (2011).
- [4] M. Sakamaki and K. Amemiya, *Appl. Phys. Express* **4**, 073002 (2011).
- [5] M. Sakamaki and K. Amemiya, *Phys. Rev. B* **87**, 014428 (2013).
- [6] M. Sakamaki and K. Amemiya, *J. Phys.: Condens. Matter* **26**, 166002 (2014).
- [7] G. Lauhoff, C.A.F. Vaz, J.A.C. Bland, J. Lee and T. Suzuki, *Phys. Rev. B* **61**, 6805 (2000).
- [8] P. Ravindran, A. Kjekshus, H. Fjellvaag, P. James, L. Nordström, B. Johansson and O. Eriksson, *Phys. Rev. B* **63**, 144409 (2001).
- [9] Y. Miura, S. Ozaki, Y. Kuwahara, M. Tsujikawa, K. Abe and M. Shirai, *J. Phys.: Condens. Matter* **25**, 106005 (2013).

BEAMLINES

BL-7A and BL-16A

M. Sakamaki and K. Amemiya (KEK-PF)

The Specific Deoxidation Behavior of Iron Titanate Catalyst Characterized by the XAFS Technique for the Selective Catalytic Removal of NO_x by NH₃

Iron titanate (FeTiO_x) catalyst has been proven to be a potential candidate for the selective catalytic reduction of NO_x with NH₃ (NH₃-SCR). Due to the formation of a unique microstructure as an edge shared Fe-(O)₂-Ti species, the NH₃-SCR activity, N₂ selectivity and SO₂ durability of FeTiO_x catalyst have been greatly improved. Using the XAFS technique in combination with H₂-TPR experiments, we discovered that the highly dispersed Fe species in FeTiO_x catalyst showed a specific deoxidation behavior due to the presence of an electronic inductive effect between Fe and Ti species. The reducibility of Fe³⁺ species in FeTiO_x catalyst was greatly enhanced accordingly, leading to the higher oxidation ability of Fe species in FeTiO_x, which is beneficial to the NO_x reduction process.

Compared to pristine Fe₂O₃ and TiO₂, the particle size of FeTiO_x catalyst was greatly lowered, and no discernable lattice fringes could be observed from the TEM images (Fig. 1). High NH₃-SCR activity and N₂ selectivity with a broadened operating temperature window together with enhanced SO₂ durability could be achieved on FeTiO_x catalyst. From our previous study

using the XAFS technique [1], we concluded that the main active phase in FeTiO_x catalyst was in the form of iron titanate crystallite, with an edge shared Fe-(O)₂-Ti microstructure. An electronic inductive effect between Fe³⁺ species and Ti⁴⁺ species was present in this structure, leading to the enhanced oxidation ability of Fe³⁺ species.

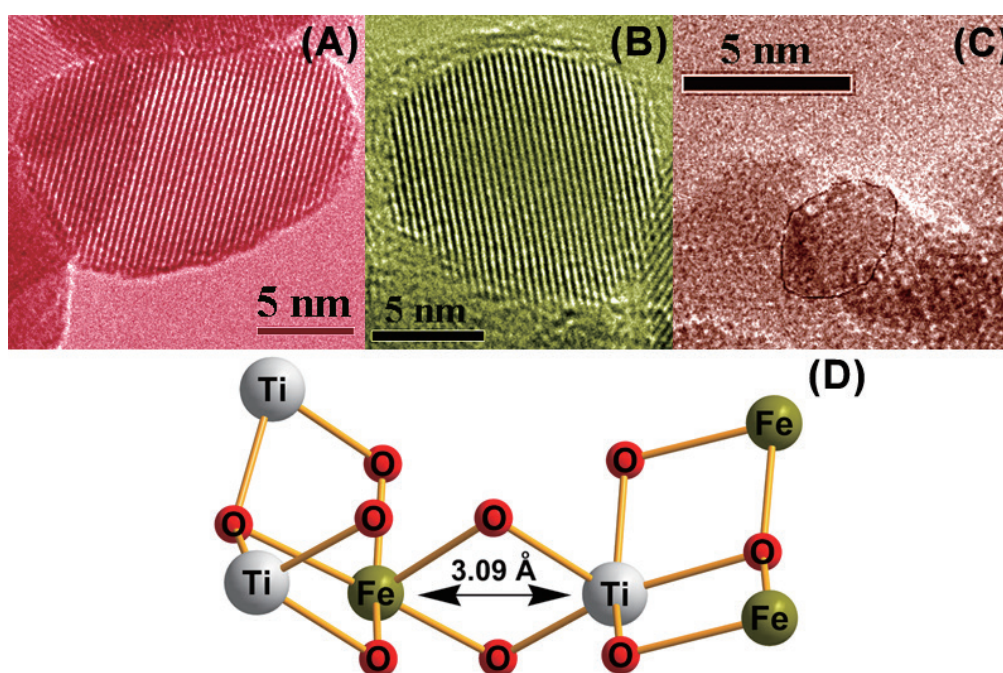


Figure 1: HRTEM images of (A) hematite Fe₂O₃, (B) anatase TiO₂ and (C) FeTiO_x catalyst [2], and (D) proposed structural model of FeTiO_x catalyst derived from EXAFS curve-fitting results [1].

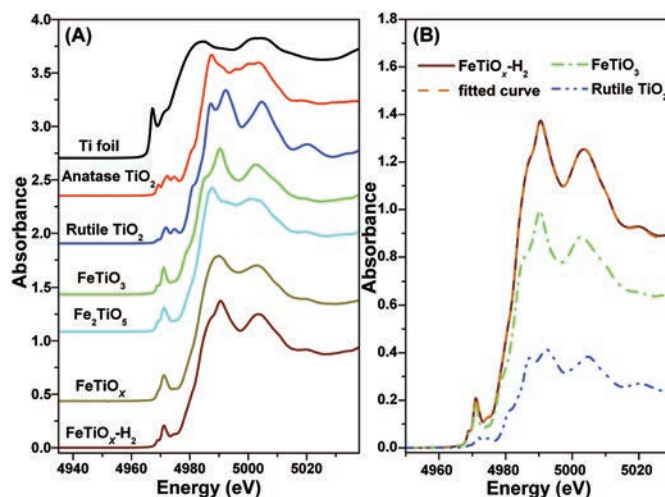


Figure 2: (A) Normalized XANES spectra of Ti-K edges in Ti-containing samples; (B) XANES linear fitting results of Ti-K edges in FeTiO_x catalyst after H₂ reduction using FeTiO₃ and Fe as references [3].

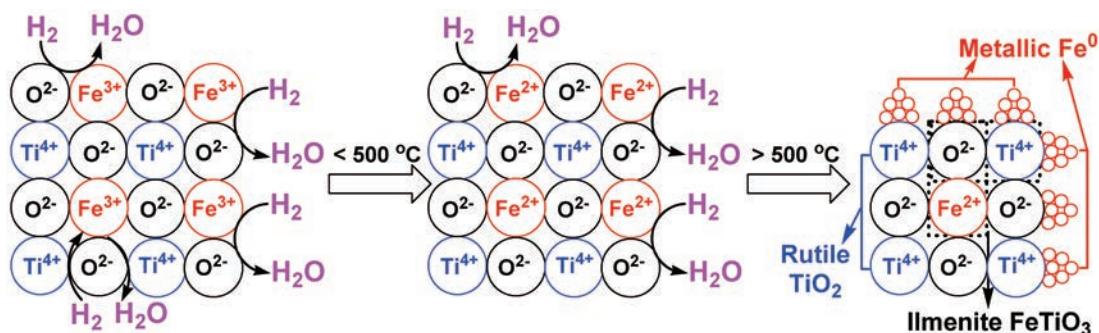


Figure 3: Proposed H₂ reduction process of the FeTiO_x catalyst [3].

In the present study, based on XANES linear fitting (Fig. 2) and EXAFS curve-fitting results in combination with the H₂-TPR process, we discovered that the Fe³⁺ species in the FeTiO_x catalyst could be totally reduced to Fe²⁺ species below 500°C in the form of ilmenite FeTiO₃, while the Fe³⁺ species in pristine Fe₂O₃ could only be reduced to Fe₃O₄ (Fig. 3). The typical NH₃-SCR reaction mainly occurs below 500°C for practical use, and the enhanced redox ability of Fe³⁺ species in FeTiO_x catalyst is very beneficial to enhance its catalytic performance. The as-formed Fe²⁺ species in the H₂-reduced FeTiO_x catalyst combined with Ti⁴⁺ species to exist as ilmenite FeTiO₃, but not as FeO as in the Fe₂O₃ case, indicating that the Fe species and Ti species were present in a high dispersion state at the atomic scale in the original FeTiO_x catalyst. It is interesting that above 500°C, the surface layers of the as-formed FeTiO₃ could be further reduced, resulting in the formation of partial metallic Fe⁰ clusters or particles and residual rutile TiO₂. However, the reduction of Fe²⁺ species in

the bulk FeTiO₃ phase could not be achieved even at temperatures as high as 900°C (Fig. 3). This is a unique deoxidation behavior for the novel FeTiO_x catalyst that has not been reported before. These interesting results will be useful for investigating the local structure and redox ability of active sites in some mixed oxide catalysts simultaneously for certain catalytic reactions, thus clarifying the structure-activity relationships for catalysis.

REFERENCES

- [1] F. Liu, K. Asakura, P. Xie, J. Wang and H. He, *Catal. Today* **201**, 131 (2013).
- [2] F. Liu and H. He, *J. Phys. Chem. C* **114**, 16929 (2010).
- [3] F. Liu, H. He and L. Xie, *ChemCatChem* **5**, 3760 (2013).

BEAMLIN

BL-7C

F. Liu, H. He and L. Xie (CAS-RCEES)

Atomicity-Precise Non-Magic Number Pt Clusters

Metal subnanoparticles composed of several tens of atoms are still unexplored materials despite their potential application for catalysis. The relationship between the atomic coordination structure and the catalytic activity at a one-atom resolution is very important in order to understand these materials. Recently, we have developed a dendrimer-based novel synthetic approach allowing precise control of the atomicity of these subnanoparticles. Because these ultrasmall particles are no longer periodic crystals but discrete molecular-like clusters, the available structural characterization method is limited. We describe how the structure and catalytic activity of these metal clusters are completely different from those of larger nanoparticles, and are quite sensitive to the atomicity.

Miniaturization of a nanoparticle catalyst is a reasonable way to improve its specific mass-catalytic activity by increasing the surface-to-volume ratio. However, it has long been considered that the limit of the size reduction is about 3 nm in the case of platinum particles although further improvement of the platinum-based fuel cell catalyst is strongly demanded. The reason for this limitation is usually explained by the stronger binding energy between the smaller platinum nanoparticle surface and oxygen molecules (atoms) that leads to a loss of surface-catalytic activity. Conventional nanoparticle synthesis can only control the average size (diameter) but not the exact number of the atomicity. Therefore, previous results for the effect of size on the activity just presented the average values of particles over a considerable atomicity distribution. Is every platinum subnanoparticle really inactive? To reveal this important relationship, we carried out the precise synthesis of Pt₁₂, Pt₂₈ and Pt₆₀ clusters, which can be synthesized with a phenylazomethine dendrimer as the template. The atomicities of these clusters deviate from the magic numbers, producing particularly stable clusters. To compare the magic number and non-magic number species, we also prepared Pt₁₃ using a specially designed phenyl-

azomethine dendrimer template (Fig. 1). A comparison of the catalytic activities and structural information between Pt₁₂ and Pt₁₃ can clarify the unknown properties of the non-magic number species.

Contrary to expectation, the smaller subnanoparticles (Pt₁₂, Pt₂₈ and Pt₆₀) are still active catalysts for the oxygen reduction reaction (ORR). In particular, the specific mass-activity of Pt₁₂ was ca. 13 times that of the commercially available Pt/C catalyst (3–5 nm diameter) [1]. A recent experiment demonstrated the surprising result that the catalytic activity of Pt₁₂ is ca. 2.5 times higher than that of Pt₁₃ despite the almost equivalent surface-to-volume ratio [2]. This result suggests that these clusters have a different atomic coordination or electronic structure. However, the standard experimental technique for nanoparticle characterization, such as TEM or XRD, was not suitable for determining this structural difference because the present clusters no longer have a periodic crystal structure and the atomicity difference is only 1. Instead, we measured the Pt-L₃ and -L₂ edge XAFS to reveal the local coordination structure together with the electronic structure such as the d-electron vacancy on the platinum atoms.

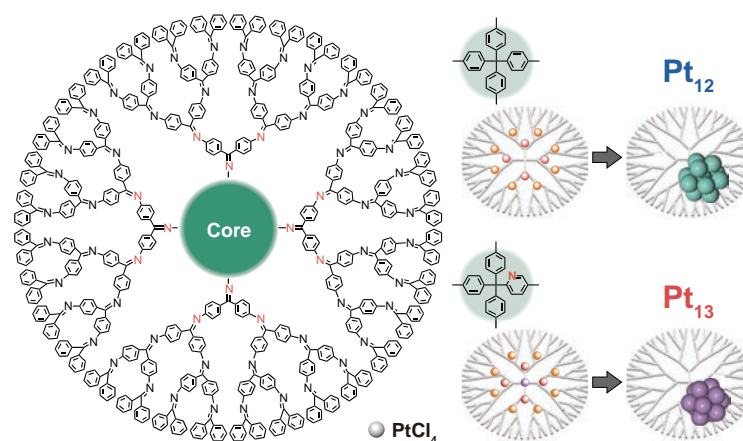


Figure 1: Dendrimer-based template synthesis of platinum subnanoparticles with precise atomicity control.

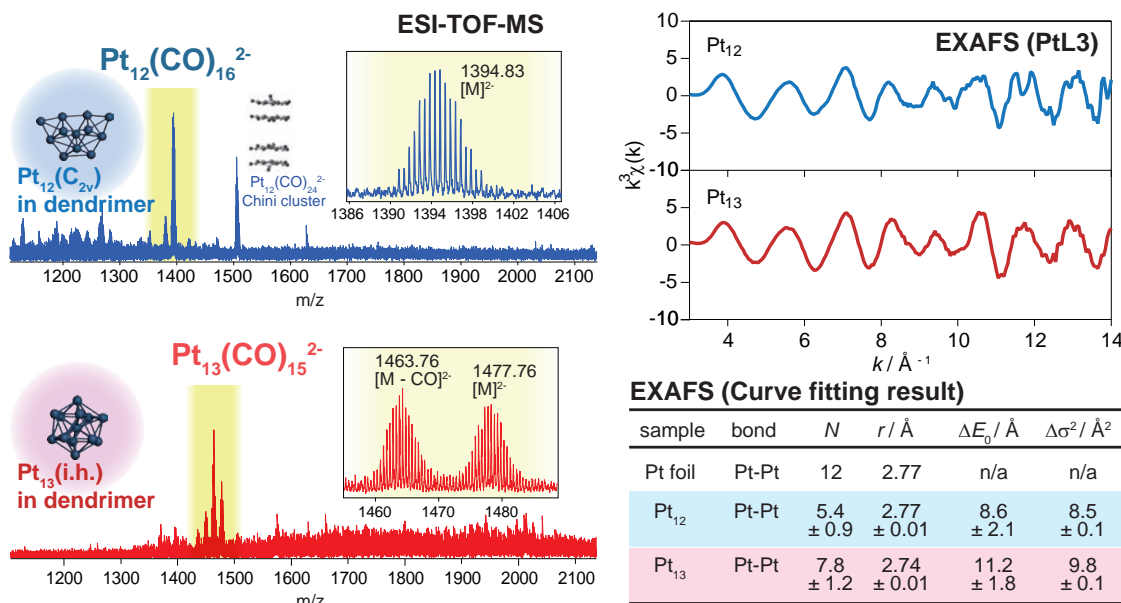


Figure 2: ESI-TOF-MS and Pt-*L*₃ EXAFS of Pt₁₂ and Pt₁₃ clusters.

The ESI-TOF-MS (electron-spray-ionization time-of-flight mass spectra) of Pt₁₂ and Pt₁₃ showed cluster ion peaks of each cluster consistent with the atomicity (Fig. 2). HAADF-STEM (high-angle annular-dark-field scanning transmission electron microscope) images demonstrated that they are ultra-small subnanoparticles (diameter: 0.9 nm). No diffractions by XRD suggested that they are not crystalline compounds. In spite of the significant difference in the ORR catalytic activity, no difference was observed in the XPS and XANES spectra (Pt-*L*₂ and -*L*₃). Beside the similarity of the two clusters, EXAFS showed a difference in the Pt-Pt coordination number (CN). Both clusters provided very small CN, which is consistent with the assumption of subnanoparticles. However, the CN of Pt₁₃ was clearly higher than that of Pt₁₂ (Fig. 2). This result suggests that these two clusters (Pt₁₂ and Pt₁₃) are basically different in their atomic coordination structure whereas their oxidation states are almost identical. The lower CN value of Pt₁₂ indicates a deformed and unsaturated structure. This finding is in line with the ESI-TOF-MS result that the observed Pt₁₂(CO)₁₆²⁻ cluster ion accompanies more carbonyl ligands relative to the Pt₁₃(CO)₁₅²⁻.

Cluster modeling calculations by the density functional theory (DFT) method also suggested a structural transition from Pt₁₃ to Pt₁₂. Several plausible structures were provided for Pt₁₃ and Pt₁₂. In combination with the XAFS and ESI-TOF-MS results, an icosahedral struc-

ture of Pt₁₃ and less symmetric C_{2v} structure of Pt₁₂ were supported. Based on the assumption of these structures, the difference in catalytic activity can be explained based on the oxygen binding energy on the cluster surfaces. Similar to the previously reported smaller platinum nanoparticles, the oxygen binding energy to Pt₁₃ is too strong for efficient ORR. On the contrary, the oxygen binding on Pt₁₂ is weaker and most suitable for ORR. The present observation suggests that the *fcc* structure of the Pt nanoparticle changes to an icosahedral-based structure around 1 nm, and finally becomes a less symmetric structure with a lower CN value below Pt₁₂. The catalytic activity no longer simply correlates to the size of the particles as expected based on common knowledge.

REFERENCES

- [1] K. Yamamoto, T. Imaoka, W.-J. Chun, O. Enoki, H. Katoh and M. Takenaga, *Nature Chem.* **1**, 397 (2009).
- [2] T. Imaoka, H. Kitazawa, W.-J. Chun, S. Omura, K. Albrecht and K. Yamamoto, *J. Am. Chem. Soc.* **135**, 13089 (2013).

BEAMLINE

BL-12C

T. Imaoka¹, H. Kitazawa¹, W.-J. Chun² and K. Yamamoto¹ (¹Tokyo Inst. of Tech., ²International Christian Univ.)

High Catalytic Performance of USY-Supported Manganese Oxides for VOC Control

Catalytic oxidation processes using ozone (catalytic ozonation processes) are effective for controlling volatile organic compounds in indoor air. We investigated the relationship between the local structure of active sites, manganese oxides and their catalytic activity for benzene oxidation. On the basis of EXAFS and XANES studies on the manganese oxide structures, we developed a promising catalyst, which consisted of ultrastable Y (USY) zeolite and manganese oxides. The manganese oxides were highly dispersed on USY and the manganese oxide active sites exhibited high performance for catalytic ozonation of benzene in the temperature range of 300–343 K in the presence of water vapor.

Purification of indoor air polluted with volatile organic compounds (VOCs) is an important area of research on catalysis. Catalytic oxidation with ozone (catalytic ozonation) is effective for complete oxidation of VOCs under mild conditions, particularly compared with other processes such as absorption, adsorption, and catalytic combustion. Catalytic ozonation processes have an advantage over catalytic combustion processes in that metal oxides of the first transition series (Fe, Co, Mn, and Cu) [1-5] can be used for catalytic active sites, eliminating the need for more expensive metals (e.g., Pt and Pd).

We focused on the supported manganese oxide catalysts and investigated the relationship between the structure of manganese oxides and their catalytic activity for benzene oxidation [6-11]. The structure and oxidation state of manganese oxides were investigated using EXAFS and XANES studies. The spectra were taken at the Photon Factory of the High Energy Accelerator Research Organization (KEK-PF) on beamline BL-7C, which has a storage ring operating energy of 2.5 GeV. Catalyst samples were pressed into thin, self-supporting discs. These discs were heated in an O₂ flow for 2 h at 723 K, and then tightly sealed in polyethylene with inert gas. XAFS spectra were recorded at 296 K.

EXAFS studies revealed that the dispersion of manganese oxides can be easily controlled by selectively using the manganese precursors: highly dispersed manganese oxides were formed on the SiO₂ support when manganese acetate was used in the impregnation method. On the other hand, aggregated manganese oxides Mn₂O₃ and Mn₃O₄ were formed when manganese nitrate was used and the calcination temperature was changed. Both the highly dispersed manganese oxides

and aggregated manganese oxides exhibited benzene oxidation activity, and the product distribution (mole fraction of CO₂, CO, and formic acid) and the ratio of the amount of ozone to benzene, which characterized the efficiency of ozone utilization, were hardly affected by the dispersion of manganese oxides.

We have also investigated the effect of the catalyst support on the supported manganese oxides and have reported that the rate of benzene oxidation linearly increased with the increase in catalyst surface area. The ratio of decomposition of ozone to benzene was the lowest for SiO₂-supported manganese oxides. Therefore, SiO₂-supported manganese oxides with large surface area are promising in terms of catalytic activity and efficiency of ozone utilization.

In the case of SiO₂-supported manganese oxides, however, the amount of formic acid formed in the effluent gas stream increased when the benzene oxidation was carried out at low benzene conversion levels. Therefore, we subsequently focused on zeolite as the supporting material because of its large surface area and high capacity for formic acid adsorption. We tested various kinds of zeolite for manganese oxides and found that when zeolite Y was used as the catalyst support, the evolution of formic acid was significantly suppressed: the byproduct formic acid formed in benzene oxidation was trapped in the zeolite support and readily oxidized to CO₂. Furthermore, manganese oxide catalysts supported on ultrastable zeolite Y (Mn/USY) (Zeolyst CBV390H, SiO₂/Al₂O₃ = 180, surface area 875 m²/g) prepared by an impregnation method (Fig. 1) exhibited steady-state activity for benzene oxidation with ozone at room temperature (300 K) in the presence of water vapor.

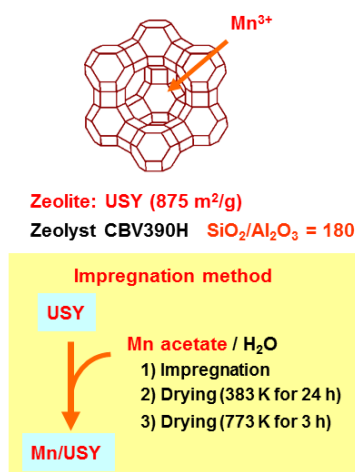


Figure 1: Preparation process for USY-supported manganese oxide catalysts.

EXAFS studies clarified the local structure of manganese active sites on the USY support. As shown in Fig. 2, the Mn-O peak was observed at ~ 1.5 Å for the Mn/USY catalysts, although the Mn-Mn peaks were much lower in intensity. The quantitative analysis performed on the EXAFS spectra demonstrated that the coordination number (CN) of Mn-O was in the range of 5.1–5.2 and that of Mn-Mn was much lower (0.38–0.49). The results indicated that aggregated manganese oxides were absent and manganese oxides were highly dispersed on USY. In addition, the Mn-O and Mn-Mn coordination numbers and their bond distances were essentially unchanged when manganese oxide loading increased from 5 to 15 wt%, showing that the local structure of manganese oxides on USY was essentially independent of Mn loading.

In summary, we developed promising catalysts for reducing VOC using ozone based on XAFS studies for structural analysis of supported manganese oxides. Our next target is to design high-performance catalysts by tuning the active sites and supporting materials.

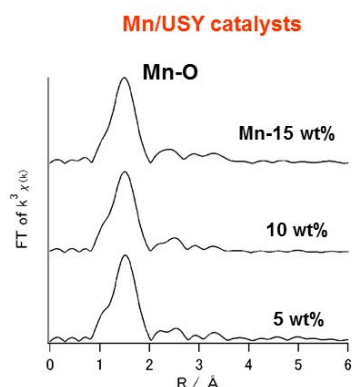


Figure 2: Mn-K edge EXAFS spectra of USY-supported manganese oxide catalysts.

REFERENCES

- [1] A. Gervasini, G.C. Vezzoli and V. Ragaini, *Catalysis Today* **29**, 449 (1996).
- [2] D. Mehandjiev, A. Naydenov and G. Ivanov, *Appl. Catal. A: General* **206**, 13 (2001).
- [3] S. Dimitrova, G. Ivanov and D. Mehandjiev, *Appl. Catal. A: General* **266**, 81 (2004).
- [4] A. Naydenov and D. Mehandjiev, *Appl. Catal. A: General* **97**, 17 (1993).
- [5] C. Reed, Y.-K. Lee and S.T. Oyama, *J. Phys. Chem. B* **110**, 4207 (2006).
- [6] H. Einaga and S. Futamura, *J. Catal.* **227**, 304 (2004).
- [7] H. Einaga and S. Futamura, *J. Catal.* **243**, 446 (2006).
- [8] H. Einaga and A. Ogata, *J. Hazard. Mater.* **164**, 1236 (2009).
- [9] H. Einaga and S. Futamura, *Catal. Commun.* **8**, 557 (2007).
- [10] H. Einaga, Y. Teraoka and A. Ogata, *Catal. Today* **164**, 571 (2011).
- [11] H. Einaga, Y. Teraoka and A. Ogata, *J. Catal.* **305**, 227 (2013).

BEAMLINE

BL-7C

H. Einaga (Kyushu Univ.)

Monitoring of Electron Flow in Layered Double Hydroxides to Photoreduce Carbon Dioxide into Fuels

Photocatalytic conversion of CO_2 into fuel would simultaneously solve the problems of global warming and shortage of sustainable energy. Layered double hydroxides (LDHs), especially comprising Cu^{II} sites, are advantageous to photoreduce CO_2 selectively into methanol using H_2 . By monitoring the pre-edge peak due to 1s-3d transition for Cu sites in LDHs, electron diffusion rates to inlayer Cu sites ($580 \mu\text{mol h}^{-1} \text{g}_{\text{cat}}^{-1}$) and to interlayer Cu sites ($36 \mu\text{mol h}^{-1} \text{g}_{\text{cat}}^{-1}$) were evaluated and was sufficiently fast compared to photocatalysis of CO_2 . The preferable interaction of CO_2 with Cu sites in LDHs was also demonstrated and suggested to control the photoreactivity with CO_2 based on multiple scattering peak intensity for Zn, Cu, and Ga in X-ray absorption near-edge structures.

Carbon dioxide is one of the major greenhouse gases and methods to reduce its concentration in the atmosphere and its emission to the environment require urgent attention [1]. It would be advantageous to capture CO_2 from the atmosphere or factories/power stations and convert it to fuel using natural light, as this approach would simultaneously solve the problems of global warming and shortage of sustainable energy. Recently, many researchers have investigated this topic.

A study of selective CO_2 photoconversion to methanol (68 mol%) was reported using H_2 and layered double hydroxide (LDH) of $[\text{Zn}_{1.5}\text{Cu}_{1.5}\text{Ga}^{\text{III}}(\text{OH})_8]^+\text{CO}_3^{2-}\cdot m\text{H}_2\text{O}$ (**1**) [2]. LDH is one of the families of clays, but is unusual in that the cationic layers intercalate anionic species, e.g. carbonates, whereas in the majority of clays the layers are anionic and intercalate cationic species. The inclusion of Cu ions in the LDH cationic layers improves the selectivity for methanol formation compared to CO formation. Methanol is more favorable as it can be directly used in the existing infrastructure as fuel whereas CO

needs to be converted to hydrocarbons or alcohols for use as an energy. The substitution of interlayer carbonate anions of LDH for $[\text{Cu}(\text{OH})_4]^{2-}$ anions further boosted the methanol selectivity to 88 mol% [3].

In principle, photocatalysis takes place starting from the charge separation in semiconductor/chemical bonds due to light irradiation. For compound **1**, ultraviolet (UV) light of energy greater than 3.5 eV excites electrons (e^- s) at the valence band (major O 2p character) to the conduction band (metal d, s, p character) in the LDH. If the e^- s on metal and holes on oxygen diffuse to the surface of photocatalysts, reduction and oxidation reactions take place independently, e.g. CO_2 reduction and H_2 oxidation [2, 3] or H_2O oxidation [4]. Thus, to understand the photoreduction mechanism of CO_2 into fuels (methanol, CO), it is necessary to monitor the e^- flow in LDH upon light irradiation and the interaction of CO_2 with LDH surface. In this study, these steps were monitored using X-ray absorption near-edge structure (XANES) spectroscopy [5].

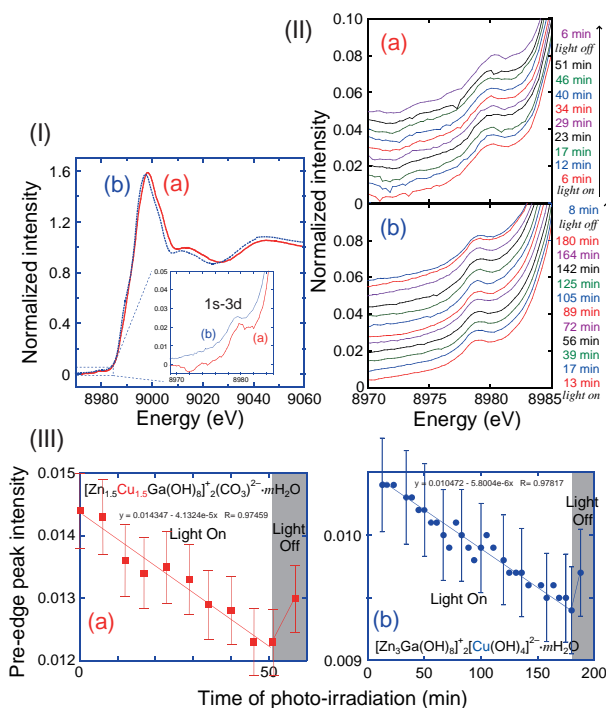


Figure 1: (I) Normalized Cu K-edge XANES spectra of compound **1** preheated at 423 K (a) and fresh compound **2** (b) and (II) under $\text{CO}_2 + \text{H}_2$ and UV-visible light irradiation and subsequent change after the light was turned off, and (III) time course of the 1s-3d peak intensity for the two LDH photocatalysts under $\text{CO}_2 + \text{H}_2$ and UV-visible light irradiation and subsequent change after the light was turned off.

The e^- excitation and flow in compound **1** and $[\text{Zn}_3\text{Ga}(\text{OH})_8]_2^+[\text{Cu}(\text{OH})_4]_2^{2-} \cdot m\text{H}_2\text{O}$ (**2**) under $\text{CO}_2 + \text{H}_2$ and UV-visible light irradiation was monitored by Cu K-edge XANES spectroscopy (Fig. 1). A pre-edge peak at 8979 eV because of a 1s-3d transition was used to evaluate the population of Cu^{II} sites in the LDH compounds [6]. When the Cu^{II} sites trap diffused e^- 's, they are reduced to Cu^{I} . The pre-edge peak does not appear for the Cu^{I} sites with d^{10} configuration.

The pre-edge peak intensity for incipient compound **1** monotonously decreased by 15% within 50 min of irradiation [Fig. 1(II)-(a) & (III)-(a)]. As 0.55 mmol of Cu sites were included in 170 mg of LDH disk, the e^- trap rate was $580 \mu\text{mol h}^{-1} \text{g}_{\text{cat}}^{-1}$. The e^- 's flow was within the cationic layer [Fig. 2(A)].

The 1s-3d pre-edge peak intensity of incipient compound **2** also monotonously decreased by 11% within 180 min of irradiation [Fig. 1(II)-(b) & (III)-(b)]. Based on Cu K-edge extended X-ray absorption fine structure analysis, the $[\text{Cu}(\text{OH})_4]_2^{2-}$ anions dehydrated with hydroxy groups of the cationic layer to form $(\mu\text{-O})_3\text{Cu}(\text{OH})(\text{H}_2\text{O})_2$ [Fig. 2(B)] [5]. " $\mu\text{-O}$ " means an O atom bound to the cationic layer. The reduction rate of 0.17 mmol of out-of-layer Cu^{II} sites in 170 mg of LDH disk was $36 \mu\text{mol h}^{-1} \text{g}_{\text{cat}}^{-1}$. The rate was essentially slower diffusion in the perpendicular direction to inter-layer Cu sites later than the faster e^- diffusion in the cationic layer ($580 \mu\text{mol h}^{-1} \text{g}_{\text{cat}}^{-1}$).

Monitored e^- trap ($36\text{--}580 \mu\text{mol h}^{-1} \text{g}_{\text{cat}}^{-1}$) was fast enough compared to photocatalytic CO_2 conversion into methanol & CO using compounds **1** and **2** ($2.1\text{--}2.2 \mu\text{mol } e^- \text{s}^{-1} \text{used h}^{-1} \text{g}_{\text{cat}}^{-1}$) irradiated under light. The interaction of CO_2 with Cu sites of LDHs was also

monitored using Cu K-edge XANES spectroscopy [2]. For compound **1**, a post-edge peak intensity at 9016 eV decreased to 76% by heating in vacuum at 383 K. Upon introduction of CO_2 , the peak intensity increased back to 87% of the fresh sample at 290 K and 91% of the fresh one at 423 K. As a hydroxy group shares three metal atoms in LDHs (Fig. 2), the post-edge peak intensity at 9689 and 10398 eV above Zn and Ga K-edge, respectively, also exhibited a similar semi-reversible trend. The reversible in-situ peak intensity changes were not observed for the post-edge peaks at 9688 and 10397 eV for Cu-free $[\text{Zn}_3\text{Ga}(\text{OH})_8]_2^+ \cdot m\text{CO}_3^{2-} \cdot m\text{H}_2\text{O}$. Thus, Cu sites adsorbed CO_2 and transferred the trapped e^- 's to CO_2 during the photoconversion to fuel.

REFERENCES

- [1] Y. Izumi, *Coord. Chem. Rev.* **257**, 171 (2013).
- [2] N. Ahmed, Y. Shibata, T. Taniguchi and Y. Izumi, *J. Catal.* **279**, 123 (2011).
- [3] N. Ahmed, M. Morikawa and Y. Izumi, *Catal. Today* **185**, 263 (2012).
- [4] M. Morikawa, Y. Ogura, N. Ahmed, S. Kawamura, G. Mikami, S. Okamoto and Y. Izumi, *Catal. Sci. Technol.* **4**, 1644 (2014).
- [5] M. Morikawa, N. Ahmed, Y. Yoshida and Y. Izumi, *Appl. Catal. B* **144**, 561 (2014).
- [6] Y. Izumi and H. Nagamori, *Bull. Chem. Soc. Jpn.* **73**, 1581 (2000).

BEAMLINES

BL-7C, BL-9C and BL-01B1 (SPring-8, Priority Program for Disaster-Affected Quantum Beam Facilities)

Y. Izumi, S. Kawamura, M. Morikawa and A. Naveed (Chiba Univ.)

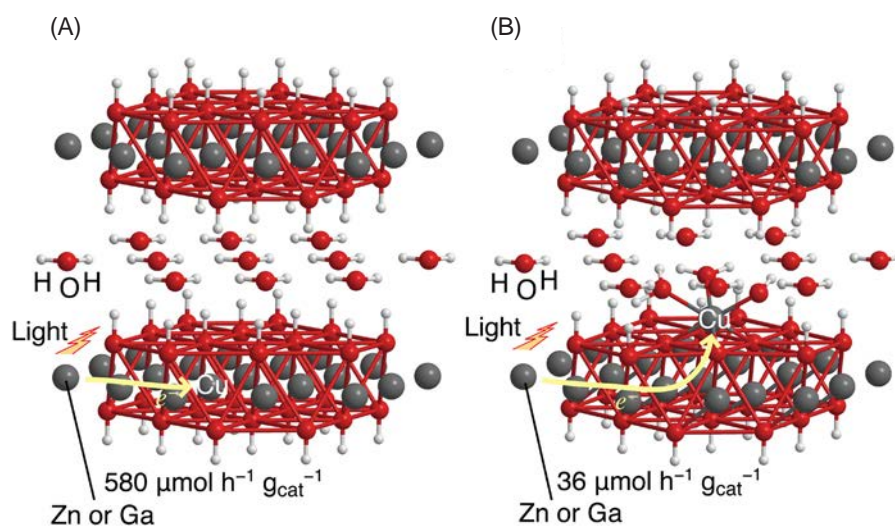


Figure 2: Structure of compound **1** (A) and structure of compound **2** (B). Interlayer carbonates are not drawn in (A) for clarity.

Stability of Forsterite in the Presence of H₂ Fluid under High Pressure and Temperature

The influence of H₂ fluid on the phase stability of forsterite (Mg₂SiO₄) was investigated under high pressure and high temperature using diamond anvil cells. In-situ X-ray diffraction measurements at BL-18C and Raman spectroscopy indicated decomposition of forsterite to periclase (MgO) and stishovite/quartz (SiO₂) in the presence of H₂ fluid, even though the pressure and temperature conditions were consistent with the stability region of forsterite under the dry condition. The microtexture of the recovered samples suggested that periclase crystallized directly from forsterite under high temperature. On the other hand, SiO₂ composition is considered to dissolve into H₂ under high temperature and then crystallize with decreasing temperature.

Fluids such as H₂O drastically change the stability phase of coexisting mantle minerals [1], and thus play an important role in the chemical evolution and dynamics of the Earth's mantle. The composition of the fluid phase is significantly influenced by the surrounding oxidation states. In the reduced mantle, fluids contain a certain amount of H₂ in addition to H₂O [2]. However, the effects of the H₂ fluid on the stability and chemical properties of the coexisting minerals have not been understood. In this study, we performed experiments at high pressure and temperature to clarify the influence of H₂ fluid on the stability of olivine, which is the most abundant mineral in the upper mantle.

The high-pressure and -temperature experiments on the H₂-Mg₂SiO₄ system were conducted using diamond anvil cells (DAC) in the range between 2.5 GPa, 1400 K and 15.0 GPa, 1500 K. Powdered forsterite (iron-free composition of olivine) was first loaded into the sample chamber with a ruby ball for pressure measurements [3]. Then, hydrogen gas (99.99999% purity) was loaded into the sample chamber using high-pressure gas-loading apparatus. At first, the sample was compressed to the target pressure at room temperature, and then heated using a CO₂ laser for around 20 min. The temperature was measured by the spectroradiometric method. The samples were quenched to room temperature by turning off the laser beam. XRD measurements were performed under high pressure and room temperature with a monochromatic X-ray beam ($\lambda = 0.6166 \text{ \AA}$) at BL-18C. The X-ray beam was collimated to 25–100 μm in diameter to obtain the XRD pattern of the sample in DAC.

The XRD patterns were detected using imaging plates (IP). Raman spectra were also measured under high pressure. The microtexture of the quenched samples under the ambient condition was investigated using a scanning electron microscope (SEM) and a transmission electron microscope (TEM).

The XRD measurements were performed after heating under high pressure to confirm the stability of forsterite in the presence of H₂ fluid. The distinct diffractions of periclase (MgO) and stishovite (SiO₂) were observed at the laser heating spot in addition to that of residual forsterite after heating at 10.0 GPa, 1600 K (Fig. 1). The formation of periclase and quartz (polymorph of stishovite) was also observed after heating at 2.5 GPa, 1400 K. The results clearly show decomposition of the forsterite, although the present pressure and temperature range is the stability field of forsterite under the dry condition. From the Raman spectra, H-H stretching mode was observed at around 4200 cm⁻¹ both before and after heating, implying that the decomposition of forsterite was induced by H₂ fluid.

To investigate the decomposition mechanism of forsterite in the presence of H₂ fluid, the microtexture of the recovered samples was investigated after being heated from 15.0 GPa, 1500 K using TEM. The reacted area consisted of aggregates of fine periclase grains, while larger crystals of residual forsterite were observed surrounding the reacted area. Periclase aggregates maintained the shape of the original forsterite like a pseudomorph. Periclase was considered to be crystallized under high temperature from forsterite directly. On

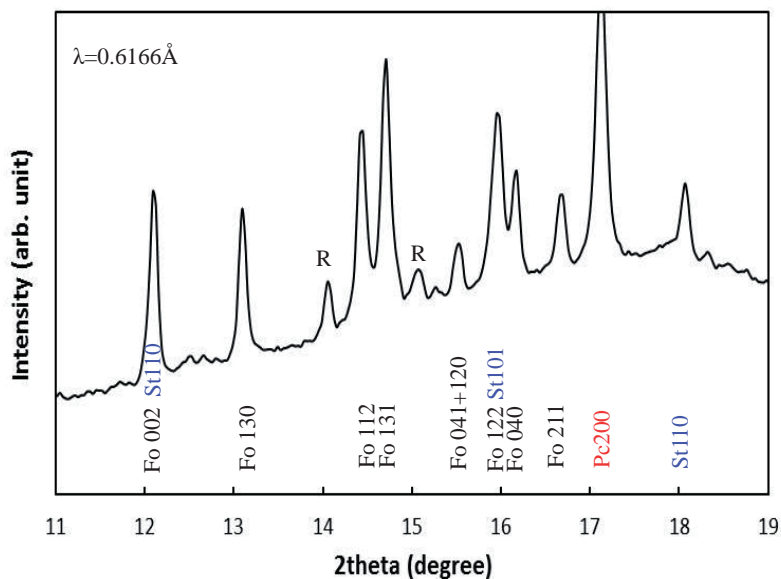


Figure 1: A representative XRD pattern of $\text{Mg}_2\text{SiO}_4\text{-H}_2$ system after heating at around 10 GPa, 1600 K. Fo; forsterite, Pc; periclasite St; stishovite R; Ruby.

the other hand, euhedral crystals of stishovite were observed at the boundary between the reacted periclasite and the residual forsterite. In addition, quench crystals of quartz were observed after heating at 2.5 GPa, 1400K. These results implied that the SiO_2 composition dissolved into H_2 fluid under high temperature and then quartz/stishovite was re-crystallized as the temperature decreased. See [4] for the details of the SEM and TEM observations. The present experimental results indicate that forsterite is incongruently dissolved in the presence of H_2 fluid to form periclasite. Such dissolution of SiO_2 composition was not observed in the H_2O -forsterite system [1]. The present study suggests that the stability of olivine in the mantle is strongly influenced by the composition of the surrounding fluid.

REFERENCES

- [1] T. Inoue, *Phys. Earth Planet. Inter.*, **85**, 237 (1994).
- [2] D. Frost and C. McCammon, *Annu. Rev. Earth Planet. Sci.*, **36**, 389 (2008).
- [3] H.K. Mao, P.M. Bell, J.W. Shaner and D.J. Steinberg, *J. Appl. Phys.*, **49**, 3276 (1978).
- [4] A. Shinozaki, H. Hirai, H. Ohfuji, T. Okada, S. Machida and T. Yagi, *Ame. Mineral.*, **98**, 1604 (2013).

BEAMLIN

BL-18C

A. Shinozaki^{1,2}, H. Hirai², H. Ohfuji², T. Okada¹, S. Machida^{2,3} and T. Yagi¹ (¹Univ. Tokyo, ²Ehime Univ., ³CROSS)

Synchrotron Radiation Study of the Reaction-Deformation Coupling Processes in Earth's Mantle Minerals at High Pressures

The reaction-deformation coupling in silicate minerals is a critical issue to understand the dynamics of subducting oceanic plates in deep Earth. We conducted high-pressure eutectoid transformation experiments with constant strain-rate deformation. High-energy monochromatic X-rays were used to measure reaction kinetics and creep behavior simultaneously at high pressures. These quantitative measurements combined with microstructural observations of recovered samples suggest sequential variation of creep mechanisms from dislocation creep of the eutectoid colonies to grain-size sensitive creep in the deformation-induced degenerated colonies. These reaction-deformation coupling processes are very important to understand the large deformation and the cessation of deep earthquakes in the lower mantle.

Oceanic plates are subducting into deep Earth as cold currents of mantle convection. When the subducted plates (slabs) pass through the mantle transition zone (between the two major seismic discontinuities at 410 and 660 km depths), most of the constituent minerals undergo high-pressure transformations, resulting in significant changes of rock density, microstructures, and viscosity. This has been thought to be responsible for deep slab deformation and deep earthquakes. Seismological and mineral physics studies have revealed that non-equilibrium phase transformations control density and viscosity structures of subducting oceanic slabs [1]. Especially, the processes of reaction-enhanced ductility and reaction-induced faulting are crucial for understanding deep slab deformation and deep earthquakes. In order to reveal such reaction-deformation coupling processes, we have started to conduct simultaneous and quantitative measurements of creep behavior and reaction kinetics at high pressures by combining high-pressure deformation apparatus with synchrotron monochromatic X-ray measurements. Here we report experimental results on creep behavior during eutectoid transformation [2].

When a slab enters the lower mantle across the 660 km discontinuity, post-spinel eutectoid transformation occurs, which is thought to be very important for understanding the slab deformation and the cessation of deep earthquakes [3]. There have been two controversial ideas on the effects of this transformation on the strength of the lower-mantle slab. One is that the slab material in the lower mantle becomes weak due to the grain-size reduction of the eutectoid transformation [3, 4]. Another is that it is not weak because the eutectoid colony is a single crystalline composite material [5]. To solve the problem, we conducted *in-situ* X-ray observations on the creep behavior during the eutectoid transformation using a deformation-DIA (D-DIA) ap-

paratus [6] at the beamline of AR-NE7A of the Photon Factory. The decomposition reaction of $\text{NaAlSi}_3\text{O}_8$ albite into $\text{NaAlSi}_2\text{O}_6$ jadeite and SiO_2 quartz was used as an analogue reaction of the post-spinel transformation. Sintered starting material of albite was deformed at 400–800°C and 1.5–4.0 GPa with constant strain rates of $0.3\text{--}6.1 \times 10^{-5} \text{ s}^{-1}$, and the decomposition reaction started during the deformation (Fig. 1). The overpressures needed for the initiation of the transformation increased with decreasing temperature. The transformation-time data was estimated from time-resolved two-dimensional X-ray diffraction measurements ($2\theta < 10^\circ$) by imaging plate every 3–5 min. The distortion of the Debye ring was used to estimate differential stress of the sample based on the lattice strain equation [7]. The sample strain was measured by using X-ray radiography imaging. In this way, we could quantitatively obtain both transformation-time and stress-strain curves during the deformation with reaction as shown in Fig. 2.

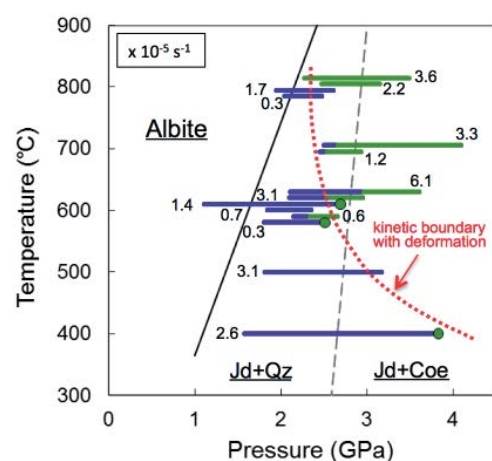


Figure 1: P-T conditions of the transformation-deformation experiment with constant strain-rate mode. The numbers indicate the strain rate ($\times 10^{-5} \text{ s}^{-1}$). Green and blue bars indicate the deformation with and without transformation, respectively.

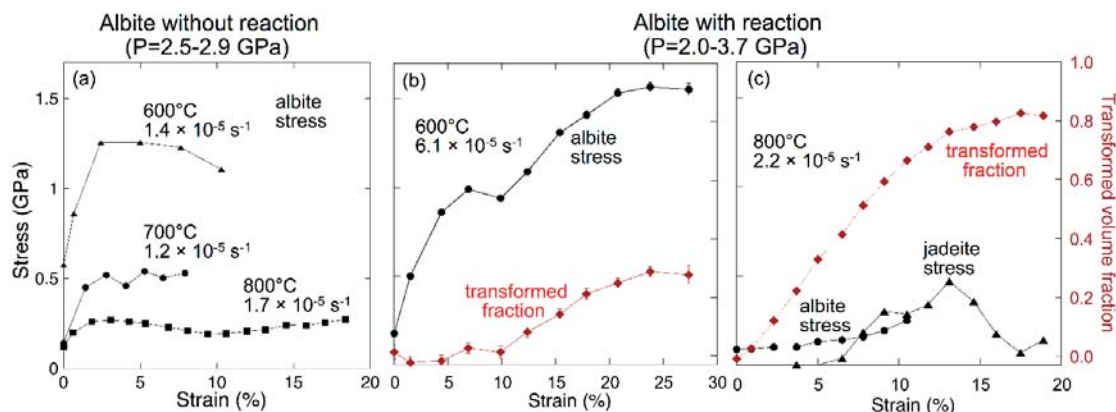


Figure 2: Stress-strain (black) and transformation-time (red) curves obtained during constant strain-rate deformation at high pressure.

In the case of the deformation without reaction, the flow stress of albite was almost constant, showing a steady state at the strain of more than 3% [Fig. 2(a)]. The stress exponent in the flow law was estimated to be 2.4, suggesting dislocation creep of parental albite. On the other hand, hardening occurred when the reaction proceeded [Fig. 2(b, c)]. Scanning electron microscopy (SEM) of recovered samples indicates that eutectoid colonies of fine-textured jadeite and silica nucleated on the albite grain boundaries. Electron back-scattered diffraction (EBSD) analysis suggests that jadeite in a colony is not fine grained but an interconnected single crystal. We also found the deformation-induced lattice preferred orientation of the eutectoid colonies, suggesting that they deform by dislocation creep.

Further transformation after the hardening causes weakening of the sample as shown by the stress drop in jadeite [Fig. 2(c)]. SEM and EBSD analysis of the weakened samples suggests that degeneration of the eutectoid colony occurs by the deformation. This possibly changes the deformation mechanism from dislocation creep to grain-size sensitive creep, resulting in the weakening. Thus, the degeneration process of the interconnected eutectoid colonies is likely to be a key issue for large deformation of the lower-mantle slab.

In a future study, we intend to develop the experimental method demonstrated here to detect shear instability by multiple acoustic emission measurements, which would be a powerful tool for the study of deep earthquakes occurring in subducting slabs.

REFERENCES

- [1] T. Kubo, S. Kaneshima, Y. Torii and S. Yoshioka, *Earth Planet. Sci. Lett.* **287**, 12 (2009).
- [2] N. Doi, T. Kato, T. Kubo, M. Noda, R. Shiraishi, A. Suzuki, E. Ohtani and T. Kikegawa, *Earth Planet. Sci. Lett.* **388**, 92 (2014).
- [3] E. Ito and H. Sato, *Nature* **351**, 140 (1991).
- [4] T. Kubo, E. Ohtani, T. Kato, S. Urakawa, A. Suzuki, Y. Kanbe, K. Funakoshi, W. Utsumi and K. Fujino, *Geophys. Res. Lett.* **27**, 807 (2000).
- [5] S. Zhao, Z. Jin, J. Zhang, H. Xu, G. Xia and H.W. Green II, *Geophys. Res. Lett.* **39**, L10311 (2012).
- [6] R. Shiraishi, E. Ohtani, T. Kubo, N. Doi, A. Suzuki, A. Shimojuku, T. Kato and T. Kikegawa, *High Press. Res.* **31**, 399 (2011).
- [7] A.K. Singh, C. Balasingh, H. Mao, R.J. Hemley and J. Shu, *J. Appl. Phys.* **83**, 7567 (1998).

BEAMLIN

AR-NE7A

T. Kubo, N. Doi and T. Kato (Kyushu Univ.)

Crystal Structures of Innate Immune RNA Receptor TLR8

Toll-like receptor 8 (TLR8) recognizes single-stranded RNA and activates innate immunity. TLR8 is also activated by synthetic imidazoquinoline compounds, which have the potential to be used for antiviral drugs. We report the first crystal structures of the unliganded and ligand-induced activated TLR8 dimers. These structures are m-shaped dimers in which two C-termini converge in the middle. Ligands were recognized at two equivalent sites located within the dimerization interface. The C-termini of the two TLR8 protomers were brought into closer proximity in the liganded form, suggesting that ligand binding enables the subsequent dimerization of the intercellular TIR domains and downstream signaling.

Innate immunity is the first line of defense against microbial invasions into the human body. Microbial components such as lipopeptide, peptidoglycan, and nucleic acids stimulate the innate immunity through a repertoire of pathogen sensor proteins. Toll-like receptors (TLRs) are one of the most important families among the pathogen sensors that recognize a wide variety of pathogens. The TLR molecule consists of an extracellular leucine-rich repeat (LRR) domain, transmembrane domain, and intracellular TIR domain. The LRR and TIR domains are responsible for ligand recognition and signaling, respectively. The typical TLR is believed to exist as a monomer and form an activated dimer upon ligand binding. TLR8 consists of 26 LRR units, and senses guanosine/uridine rich single-stranded RNA whose sequence was derived from virus RNA [1, 2]. Moreover, TLR8 is activated by imidazoquinoline synthetic ligands, some of which are used for medical treatment [3, 4]. Interestingly, TLR8 and TLR9 form preformed dimers, suggesting that their activation mechanisms are different from those of other TLRs [5, 6]. However, the structural basis of the ligand recognition and signaling by these TLRs has not been elucidated.

We determined the crystal structures of unliganded and liganded TLR8 ectodomain [7]. Although recom-

binant TLR8 was already cleaved at the long inserted loop (Z-loop) between LRR14 and LRR15, the resultant N- and C-terminal fragments were associated with each other in the purification steps. Both unliganded and liganded TLR8 were eluted as dimers in gel-filtration chromatography, suggesting that TLR8 ectodomain creates preformed dimers. Crystallization was conducted to determine the structures of an unliganded form of TLR8 and liganded forms of TLR8 with imidazoquinoline synthetic ligands, namely, CL097, CL075, and R848. The crystal structure of the unliganded form was determined at 2.3 Å resolution, and the liganded forms at 2.0–2.7 Å resolutions (TLR8/CL097, TLR8/CL075, TLR8/R848 form 1-3).

One protomer from TLR8 dimers composed a ring-shaped structure in which N- and C-terminal fragments interacted directly (Fig. 1) though Z-loop was cleaved. The consensus β strands of LRR14 and LRR15 interacted to form a β -sheet structure as well as other LRRs, which was positioned within the concave face of TLR8 monomer.

Consistent with the result of gel filtration chromatography, TLR8 formed m-shaped dimers in which two C-termini converged in the middle in both the unliganded and liganded forms (Fig. 1).

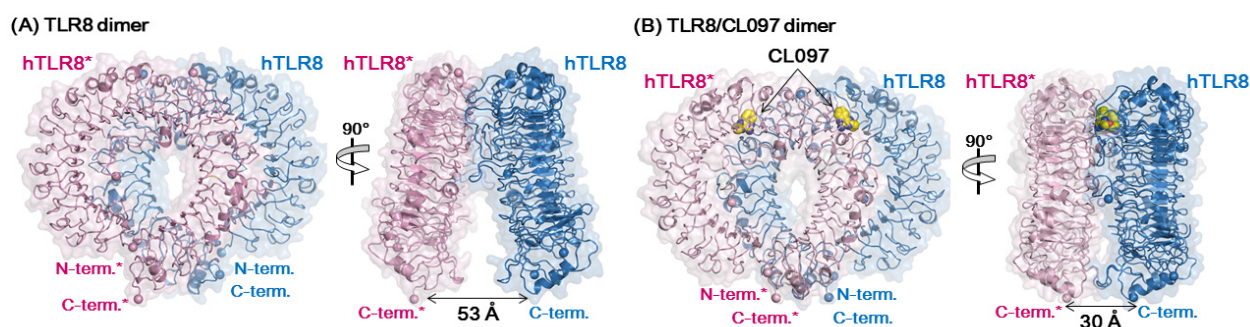


Figure 1: Dimeric structures of TLR8 unliganded form (A) and liganded form (B) (TLR8/CL097 complex) are shown. Two TLR8 protomers are drawn with different colors

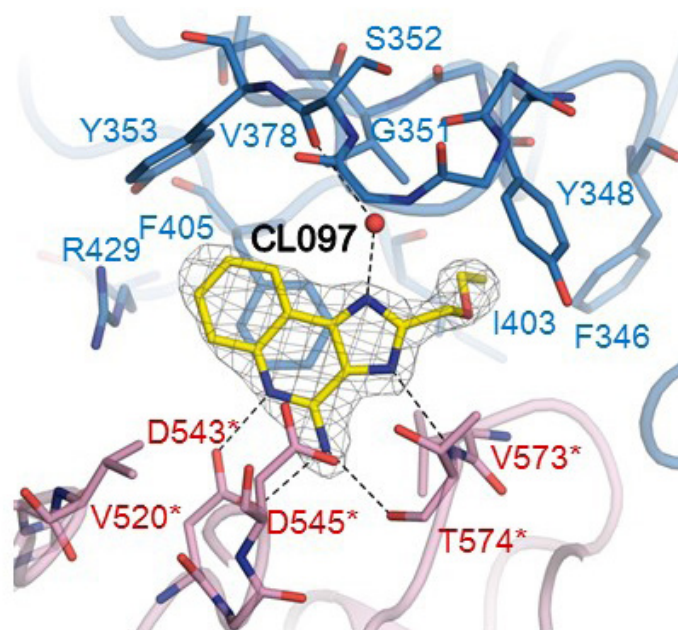


Figure 2: Ligand binding site of TLR8/CL097 complex. The electron density around CL097 was contoured at the 3.0-sigma level in the $F_o - F_c$ map. The water molecule is shown by a red sphere and hydrogen bonds by dashed lines.

The second TLR8 and its residues in the dimeric TLR8 are indicated with asterisks. The C-termini of the two TLR8 protomers were separated by 53 Å in the unliganded form, whereas the C-termini were brought into close proximity (~30 Å) in the liganded forms.

Ligands were located in the two equivalent sites on the dimerization interface, which consisted mainly of LRR14-15 and LRR17*-18*. The electron densities corresponding to the ligands were clearly observed (Fig. 2). Several characteristic interactions between ligand and TLR8 were observed. The benzene ring of chemical ligands formed a stacking interaction with F405. The amidine group formed hydrogen bonds with D543* and T574*. The hydrophobic group of ligands protruded into a hydrophobic pocket formed by F346, Y348, V573* and so on. The functional importance of these residues interacting with ligands at the cellular level was confirmed by NF- κ B reporter assay of their alanine mutants.

Upon ligand binding, the dimerization interface was rearranged to increase the protein-protein and ligand-mediated interactions from 1,290 Å² to 2,150 Å². The C-termini of the two TLR8 protomers were brought into closer proximity in the liganded form than in the unliganded form by hinge motions and ring rotations of the two protomers, thus enabling the subsequent dimerization

of the intercellular TIR domains and downstream signaling. These results will contribute to drug design targeting TLR8.

REFERENCES

- [1] F. Heil, H. Hemmi, H. Hochrein, F. Ampenberger, C. Kirschning, S. Akira, G. Lipford, H. Wagner and S. Bauer, *Science* **303**, 1526 (2004).
- [2] S.S. Diebold, T. Kaisho, H. Hemmi, S. Akira and C.R. e Sousa. *Science* **303**, 1529 (2004).
- [3] H. Hemmi, T. Kaisho, O. Takeuchi, S. Sato, H. Sanjo, K. Hoshino, T. Horiuchi, H. Tomizawa, K. Takeda and S. Akira, *Nat. Immunol.* **3**, 196 (2002).
- [4] M. Jurk, F. Heil, J. Vollmer, C. Schetter, A.M. Krieg, H. Wagner, G. Lipford and S. Bauer, *Nat. Immunol.* **3**, 499 (2002).
- [5] J. Zhu, R. Brownlie, Q. Liu, L.A. Babiuk, A. Potter and G.K. Mutwiri, *Mol. Immunol.* **46**, 978 (2009).
- [6] E. Latz, A. Verma, A. Visintin, M. Gong, C.M. Sirois, D.C.G. Klein, B.G. Monks, C.J. McKnight, M.S. Lamphier, W.P. Duprex, T. Espevik and D.T. Golenbock, *Nat. Immunol.* **8**, 772 (2007).
- [7] H. Tanji, U. Ohto, T. Shibata, K. Miyake and T. Shimizu, *Science* **339**, 1426 (2013).

BEAMLINES

AR-NE3A and AR-NW12A

H. Tanji, U. Ohto and T. Shimizu (The Univ. of Tokyo)

Structural and Functional Mechanism of a New Protein Complex Promoting the Stabilization of Genome during Homologous Recombination

Precise maintenance of DNA/genome is an essential requirement for all living systems. During homologous recombination, Rad51 assembles into a nucleoprotein filament on single-stranded DNA to catalyze homologous pairing and DNA-strand exchange with a homologous template in budding yeast. We identified a new Rad51 mediator complex, PCSS, comprising budding yeast Psy3, Csm2, Shu1 and Shu2 proteins, which binds to recombination sites and is required for Rad51 assembly and function during meiosis. The crystal structure of the Psy3-Csm2 complex suggests that this complex constitutes a core sub-complex with DNA-binding activity and stabilizes Rad51 filament formation.

Precise maintenance of DNA/genome, which is a genetic blueprint for life, is an essential requirement for all living systems. If the information is not maintained precisely, it will cause serious diseases such as cancer, or death. DNA can easily be damaged by various factors such as UV irradiation, reactive oxygen species (ROS) produced by internal metabolisms, ionizing radiation and so on. All living things have various mechanisms for repairing DNA to maintain the genetic information in order to survive. Homologous recombination plays a key role not only in maintaining genome stability, but also in generating genetic diversity. Recognition and exchange between two homologous DNAs are key steps for homologous recombination. These processes are catalyzed by RecA/Rad51 family proteins. Rad51 is

a yeast homologue of a eukaryotic RecA protein. Rad51 assembles into a nucleoprotein filament on single-stranded DNA (ssDNA) to form a right-handed helical filament and catalyzes homologous repair and DNA strand exchange with a homologous template.

This Rad51 nucleoprotein filament is protein machinery essential for homology search and DNA exchange. The assembly and disassembly of Rad51 filaments is highly regulated by various positive and negative factors with dynamic processes. *In vivo*, Rad51 filament assembly necessitates the displacement of replication protein-A (RPA) from ssDNA. Brca2 (Breast cancer responsible gene 2), a product of tumor suppressor gene, is known to stabilize the Rad51 filament by binding to one end of the filament, and it promotes formation of the filament.

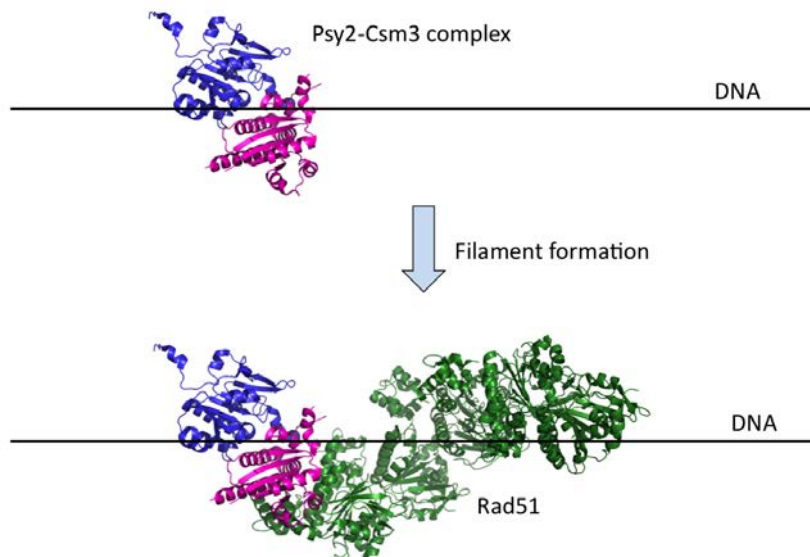


Figure 1: A model of Psy3-Csm2 to promote Rad51 filament formation.

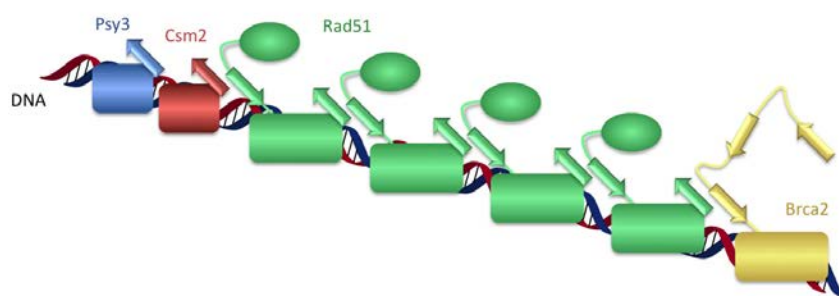


Figure 2: A schematic model of stabilization of Rad51 filament by Psy3-Csm2 complex and Brca2. The inferred site of interaction between Csm2 (red) and Rad51 (green) is completely opposite to the Rad51 interface with Brca2 (yellow).

We have identified a new protein complex that mediates Rad51 filament formation. The PCSS complex, comprising Psy3, Csm2, Shu1 and Shu2 proteins, binds to recombination sites and is required for Rad51 assembly and function during meiosis as well as mitosis in budding yeast, *Saccharomyces cerevisiae*. Within the hetero-tetramer, Psy3-Csm2 constitutes a core sub-complex with DNA-binding activity. We also revealed the high-resolution atomic structure of the Psy3-Csm2 complex using diffraction data collected at the Photon Factory at 1.75 Å resolution. The crystal structure of the Psy3-Csm2 complex showed that it resembles the dimeric structure of Rad51. This structure suggests that this complex constitutes a core sub-complex with DNA-binding activity and stabilizes Rad51 filament formation (Fig. 1). We confirmed that the Psy3-Csm2 complex acts as a core for filament formation by Rad51 by molecular biological approaches [1].

This filament model suggests that Psy3-Csm2, and by inference the PCSS complex, may interact with only one end of the Rad51 filament. It is interesting to note that the inferred site of interaction between Csm2 and Rad51 is completely opposite to the Rad51 interface with Brca2. Like the Psy3-Csm2 dimer, Brca2 is known

to stabilize the Rad51 filament, possibly by binding to one end (Fig. 2).

The PCSS complex is a novel mediator of Rad51 nucleoprotein filament assembly by binding the 5'-end of the filament. The mechanism of PCSS action as a Rad51 mediator is distinct from that of other characterized mediators, such as Rad52, Rad55-Rad57 and Brca2.

The results suggest a paradigm for the mechanism of other Rad51 paralogues.

REFERENCE

- [1] H. Sasanuma, M.S. Tawaramoto, J.P. Lao, H. Hosaka, E. Sanda, M. Suzuki, E. Yamashita, N. Hunter, M. Shinohara, A. Nakagawa and A. Shinohara, *Nature Commun.* **4**, 1676 (2013).

BEAMLIN

BL-17A

H. Sasanuma¹, M.S. Tawaramoto¹, J.P. Lao², H. Hosaka¹, E. Sanda¹, M. Suzuki¹, E. Yamashita¹, N. Hunter², M. Shinohara¹, A. Nakagawa¹ and A. Shinohara¹ (¹Osaka Univ., ²Univ. of California, Davis)

Crystallographic Study of Bacterial Selenocysteine Formation

Selenium is an essential human micronutrient. It is contained in the 21st amino acid selenocysteine (Sec), which is used in the catalytic centers of some redox enzymes. Sec is synthesized from another amino acid, serine (Ser), on its adapter molecule, tRNA^{Sec}. In bacteria, the Sec synthase SelA directly converts Ser to Sec. We determined the crystal structures of SelA with and without tRNA^{Sec}. SelA consists of 10 identical subunits that form a star-shaped pentamer of dimers. SelA binds 10 tRNA^{Sec}s and forms an 800-kDa protein-RNA complex. Based on the crystal structures, the reaction and substrate recognition mechanisms of SelA are discussed.

The element selenium is an essential micronutrient for human and animal health. In living organisms, it exists in the form of the special amino acid selenocysteine (Sec). Selenium has similar chemical properties to those of sulfur. In Sec, selenium replaces the sulfur atom of cysteine (Cys), which is one of the canonical amino acids. Sec-containing proteins, selenoproteins, function mainly as redox enzymes, such as antioxidant proteins, where Sec is utilized in their catalytic centers. Since the selenol group of Sec is easily deprotonated as compared to the thiol group of Cys (pKa 5.2 vs 8.3), Sec has stronger redox activity. Sec is distributed in all three domains of life: bacteria, archaea, and eukaryotes, and there are 25 human selenoproteins [1].

Proteins are macromolecules composed of long chains of amino acid residues. There are 20 types of canonical amino acids, and their sequences are encoded in messenger RNAs (mRNAs), which are transcripts of genes. In addition to the canonical amino acids, Sec is used for a limited number of proteins, and is called the 21st amino acid.

In the translation system, each amino acid is ligated to its cognate adaptor molecule, transfer RNA

(tRNA), and is brought to the protein synthesis factory, the ribosome. Aminoacyl-tRNA synthetases (aaRSs) are responsible for the ligation of their corresponding amino acids; e.g., serine (Ser) is ligated to serine tRNA (tRNA^{Ser}) by seryl-tRNA synthetase (SerRS) (Fig. 1). However, Sec lacks its own aminoacyl-tRNA synthetase, and is synthesized in a tRNA-dependent manner (Fig. 1). In the first step, SerRS ligates serine to Sec tRNA (tRNA^{Sec}), to form seryl-tRNA^{Sec} (Ser-tRNA^{Sec}) [2]. In bacteria, the ligated Ser is directly converted to Sec by the Sec synthase SelA [3], while a two-step conversion is performed in eukaryotes and archaea (Fig. 1) [4, 5]. The eukaryotic and archaeal substrate recognition and reaction mechanisms have been well characterized by crystallographic studies [6, 7]. However, the crystal structure of bacterial SelA has not been determined due to its huge molecular mass, which exceeds 500 kDa.

We crystallized the full-length and N-terminally truncated SelA proteins from the bacterium *Aquifex aeolicus*, and determined their crystal structures at 3.2 and 3.9 Å resolutions, respectively [8]. Several mutational and chemical treatments were performed to improve the crystal quality and X-ray diffraction resolution [9].

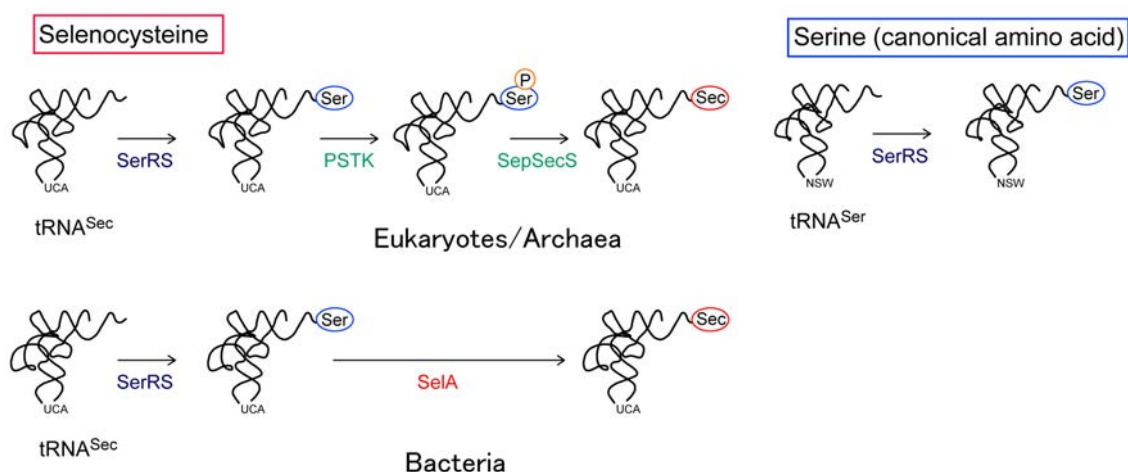


Figure 1: Sec synthesis system. Schematic depiction of tRNA^{Sec}-dependent Ser-to-Sec conversion.

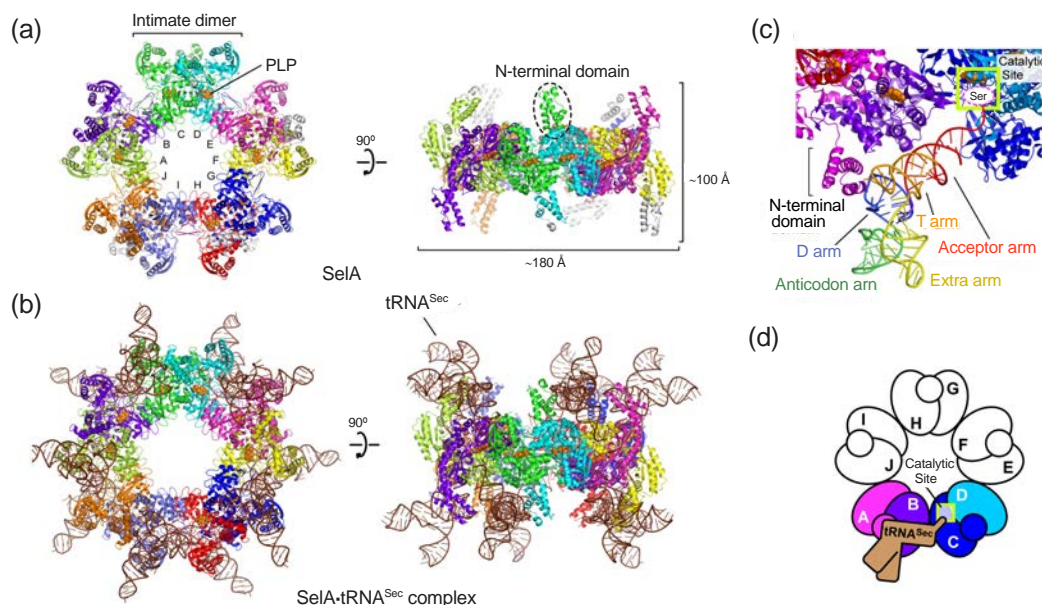


Figure 2: Crystal structures of SelA. (a, b) Overall structures of SelA (without tRNA^{Sec}) and the SelA•tRNA^{Sec} complex. (c, d) Close-up view and scheme of the interaction between the SelA subunits and tRNA^{Sec}.

SelA is a homodecameric protein composed of 10 subunits, and forms a pentamer of intimate dimers. The overall structure is a star-shaped ring [Fig. 2(a)]. The 10 subunits are identical to each other; therefore, the decamer has regular pentagonal symmetry. Each subunit consists of the N-terminal, core, and C-terminal domains, and the N-terminal domains protrude from the central pentagon [Fig. 2(a)]. There are 10 catalytic sites, where the cofactor pyridoxal phosphates (PLP) are bound. PLP is an active form of vitamin B₆, and is utilized in many enzymes involved in amino-acid metabolism.

The complex of SelA and tRNA^{Sec} was also crystallized [8]. Although the diffraction resolution is 7.5 Å, the positions of the bound tRNAs were identified [Fig. 2(b)]. SelA binds 10 tRNAs, and the total molecular mass is about 800 kDa. Each tRNA^{Sec} interacts with four SelA subunits: subunits A–D [Fig. 2(c), (d)]. The N-terminal domain of subunit A interacts with the D arm region of tRNA^{Sec}, subunit B interacts with the acceptor stem, and subunit C interacts with the tip of the acceptor arm. The 3'-terminus of tRNA^{Sec} reaches the catalytic site located on the subunit C-D interface, although tRNA^{Sec} without ligated Ser was used for crystallization.

The Ser-to-Sec conversion requires strict tRNA^{Sec} specificity toward tRNA^{Ser}. If SelA reacted with the Ser-ligated tRNA^{Ser}, then Sec would be misincorporated into proteins by the Ser codons. The N-terminal domain of SelA interacts with the D arm of tRNA^{Sec} [Fig. 2(c)]. The tRNA^{Sec} D arm has long stem and short loop regions, and forms a unique 3D structure [10, 11]. The specificity is achieved by the distinctive interaction between SelA and the D arm.

In the conversion reaction, subunit A recognizes Ser-tRNA^{Sec}, subunits A and B bind Ser-tRNA^{Sec}, sub-

unit C interacts with the tip of the acceptor arm, and subunits C and D convert the ligated Ser to Sec [Fig. 2(d)]. Each subunit can perform the four roles. The star-shaped arrangement of the 10 subunits is critical for catalysis and substrate discrimination [8, 12].

REFERENCES

- [1] G.V. Kryukov, S. Castellano, S.V. Novoselov, A.V. Lobanov, O. Zehtab, R. Guigó and V.N. Gladyshev, *Science* **300**, 1439 (2003).
- [2] A. Böck, K. Forchhammer, J. Heider, W. Leinfelder, G. Sawers, B. Veprek and F. Zinoni, *Mol. Microbiol.* **5**, 515 (1991).
- [3] B.A. Carlson, X.M. Xu, G.V. Kryukov, M. Rao, M.J. Berry, V.N. Gladyshev and D.L. Hatfield, *Proc. Natl. Acad. Sci. USA* **101**, 12848 (2004).
- [4] K. Forchhammer and A. Böck, *J. Biol. Chem.* **266**, 6324 (1991).
- [5] J. Yuan, S. Palioura, J.C. Salazar, D. Su, P. O'Donoghue, M.J. Hohn, A.M. Cardoso, W.B. Whitman and D. Söll, *Proc. Natl. Acad. Sci. USA* **103**, 18923 (2006).
- [6] S. Chiba, Y. Itoh, S. Sekine and S. Yokoyama, *Mol. Cell* **39**, 410 (2010).
- [7] S. Palioura, R.L. Sherrer, T.A. Steitz, D. Söll and M. Simonovic, *Science* **325**, 321 (2009).
- [8] Y. Itoh, M.J. Bröcker, S. Sekine, G. Hammond, S. Suetsugu, D. Söll and S. Yokoyama, *Science* **340**, 75 (2013).
- [9] Y. Itoh, S. Sekine and S. Yokoyama, *Acta Cryst. F* **68**, 678 (2012).
- [10] Y. Itoh, S. Chiba, S. Sekine and S. Yokoyama, *Nucleic Acids Res.* **37**, 6259 (2009).
- [11] Y. Itoh, S. Sekine, S. Suetsugu and S. Yokoyama, *Nucleic Acids Res.* **41**, 6729 (2013).
- [12] Y. Itoh, M.J. Bröcker, S. Sekine, D. Söll and S. Yokoyama, *J. Mol. Biol.* **426**, 1723 (2014).

BEAMLINES

BL-5A, BL-17A and AR-NW12

Y. Itoh^{1,2} and S. Yokoyama^{1,2} (¹The Univ. of Tokyo, ²RIKEN)

Mechanism of Template-Independent RNA Polymerization by tRNA Nucleotidyltransferase

CCA addition onto the 3'-termini of tRNAs, by CCA-adding enzyme, is required for protein synthesis. CCA-adding enzyme adds the CCA without a nucleic acid template, using CTP and ATP as substrates in a single active pocket. However, the mechanism of CCA addition by eubacterial/eukaryotic enzymes has remained elusive. This report presents several crystal structures of *Aquifex aeolicus* CC-adding enzyme complexed with various tRNA primers. The sequence structures, representing the CC addition by the CC-adding enzyme, have clarified the molecular basis for CC addition onto tRNA using a single active pocket, as well as the mechanism for termination of nucleotide addition.

Every tRNA has the CCA sequence at its 3'-terminus (CCA-3' at positions 74 – 76). The invariant CCA-3' is required for amino acid attachment onto the 3'-end of the tRNA by aminoacyl-tRNA synthases, and for peptide-bond formation on ribosome. The invariant 3'-CCA of tRNA is synthesized and repaired by CCA-adding enzymes, using CTP and ATP as substrates, but without a nucleic acid template [1]. The CCA-adding enzymes are classified into two classes: class-I (archaeal CCA-adding enzymes) and class-II (eubacterial/eukaryotic CCA-adding enzymes). There are no significant amino acid similarities between the two classes.

Previous biochemical studies suggested that, during CCA synthesis, the tRNA neither translocates nor rotates relative to the enzyme, but the CCA addition proceeds in a single active pocket [2-4]. Results obtained by detailed crystallographic analyses of the CCA addition by the class-I archaeal CCA-adding enzyme explained the previous biochemical results [5-7]. On the other hand, since no complex structure of a class-II eubacterial/eukaryotic CCA-adding enzyme with tRNA

has been available, the detailed mechanisms of CCA synthesis by eubacterial/eukaryotic enzymes have remained unclear [8-10]. In most organisms, 3'-CCA is synthesized by a single enzyme that adds CCA at one time. However, in some eubacteria, such as *Aquifex aeolicus*, the 3'-CCA is synthesized by two distinct, but closely related, class-II CC-adding and A-adding enzymes in a collaborative manner [11]. The mechanism by which the CC-adding enzyme synthesizes only the C74C75 sequence, without using a nucleic acid template, and the means by which the enzyme terminates RNA polymerization without adding a 3'-terminal A76, were obscure. Moreover, the molecular basis of the different specificities of nucleotides and tRNAs between the A-adding and CC-adding enzymes was unknown.

We determined the crystal structures of *A. aeolicus* CC-adding enzyme (AaS) and its complexes with tRNA primers, representing snapshots of each step of RNA polymerization [12]. Diffraction data were collected at beamlines BL-17A and BL-1A.

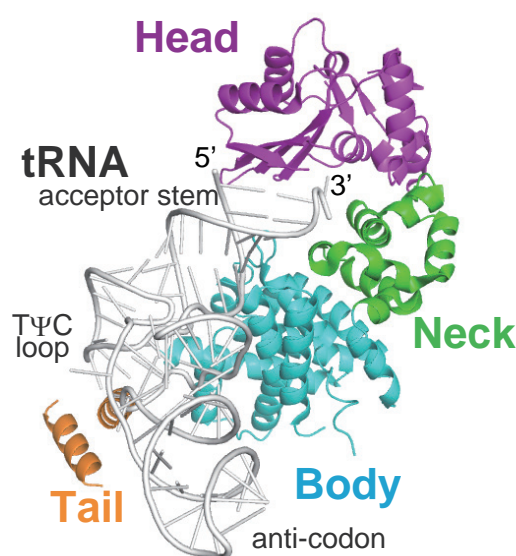


Figure 1: Complex structure of *A. aeolicus* CC-adding enzyme and tRNA lacking CCA.

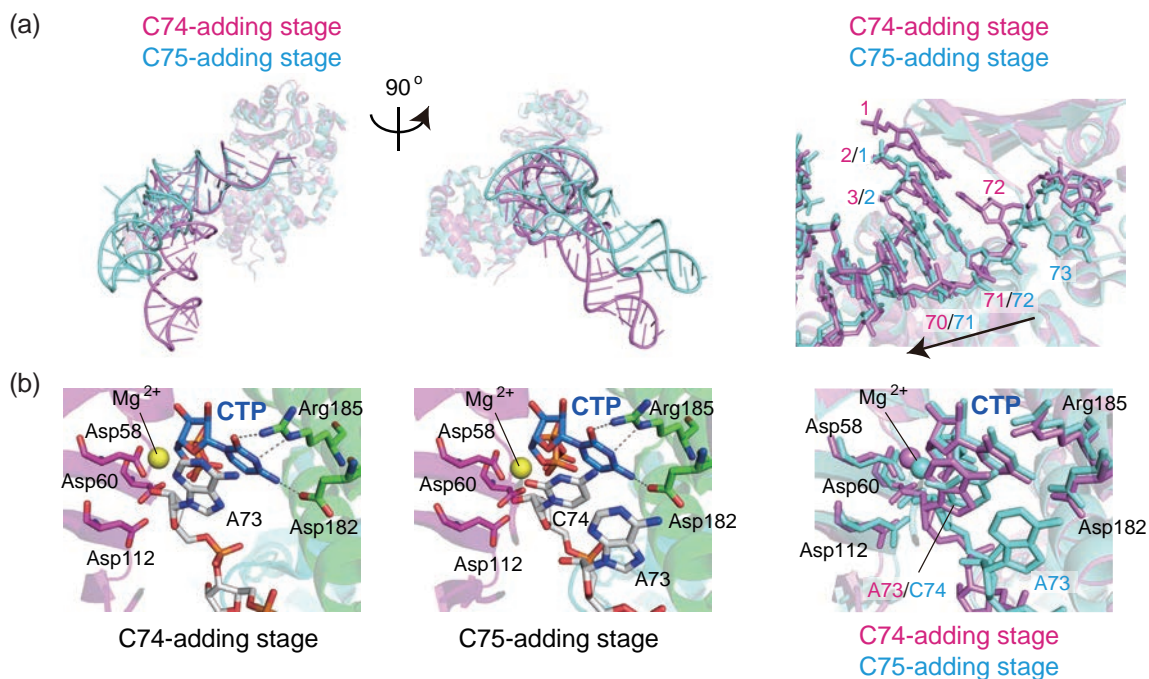


Figure 2: Translocation and rotation of tRNA during C74C75-adding reaction. (a) The superimposition of the two reaction stage structures, the C74-adding stage (magenta) and the C75-adding stage (cyan). (b) The structure of the catalytic pocket at the C74-adding stage (left) and C75-adding stage (middle). The superimposition of the two structures (right).

AaS adopts a seahorse-shaped structure, and consists of four domains: the head, neck, body and tail domains. It recognizes the top-half region of the tRNA, and does not interact with the anticodon region. The T Ψ C loop and D-loop of the tRNA interact with the tail domain of AaS (Fig. 1). We determined structures of AaS representing C74-adding and C75-adding reactions. The comparison of structures representing C74-adding and C75-adding reactions revealed the translocation and rotation of the tRNA, relative to the enzyme, during the CC addition. After C74 addition and pyrophosphate release, the tRNA translocates backward by one nucleoside and rotates relative to the enzyme [Fig. 2(a)]. The C75 addition occurs using the same active pocket as for C74 addition. At both the C74-adding and C75-adding stages, CTP is selected by Watson-Crick-like hydrogen bonds between the cytosine of CTP and the conserved amino acid residues Asp and Arg in the active pocket, in the same manner [Fig. 2(b)]. These results also suggested that after C74C75 addition and pyrophosphate release, the tRNA translocates backward further and drops off the enzyme, and thus the CC-adding enzyme terminates RNA polymerization.

The present study has clarified the molecular mechanism of CC addition by tRNA nucleotidyltransferase, and has solved the long-standing classical problems of eubacterial/eukaryotic CCA-adding enzymes [13]. In addition, the present study is the first to visualize the translocation and rotation of the primer tRNA during the template-independent CC addition, as a movie. Previous biochemical studies using class-II CCA-adding

enzymes showed that C74 addition, like C75 and A76 addition, does not involve tRNA translocation and rotation. The mechanisms of CC addition by the CC-adding and CCA-adding enzymes might be different. Further analyses of the complex structure of the class-II eubacterial/eukaryotic CCA-adding enzyme, representing CCA addition, would solve this issue.

REFERENCES

- [1] A.M. Weiner, *Curr. Biol.* **14**, 883 (2004).
- [2] D. Yue, A.M. Weiner and N. Maizels, *J. Biol. Chem.* **273**, 29693 (1998).
- [3] P.Y. Shi, N. Maizels and A.M. Weiner, *EMBO J.* **17**, 3169 (1998).
- [4] H.D. Cho, Y. Chen, G. Varani and A.M. Weiner, *J. Biol. Chem.* **281**, 9801 (2006).
- [5] Y. Xiong and T.A. Steitz, *Nature* **430**, 640 (2004).
- [6] K. Tomita, R. Ishitani, S. Fukai and O. Nureki, *Nature* **443**, 956 (2006).
- [7] B. Pan, Y. Xiong and T.A. Steitz, *Science* **330**, 937 (2010).
- [8] F. Li, Y. Xiong, J. Wang, H.D. Cho, K. Tomita, A.M. Weiner and T.A. Steitz, *Cell* **111**, 815 (2002).
- [9] K. Tomita, S. Fukai, R. Ishitani, T. Ueda, N. Takeuchi, D.G. Vassylyev and O. Nureki, *Nature* **430**, 700 (2004).
- [10] Y. Toh, D. Takeshita, T. Numata, S. Fukai, O. Nureki and K. Tomita, *EMBO J.* **28**, 3353 (2009).
- [11] K. Tomita and A.M. Weiner, *Science* **294**, 1334 (2001).
- [12] S. Yamashita, D. Takeshita and K. Tomita, *Structure* **22**, 315 (2014).
- [13] K. Tomita and S. Yamashita, *Front. Genet.* **5**, 36 (2014).

BEAMLINES

BL-17A and BL-1A

S. Yamashita and K. Tomita (AIST)

Molecular Basis of Binding between Novel Human Coronavirus MERS-CoV and its Receptor CD26

The newly-emerged Middle East respiratory syndrome coronavirus (MERS-CoV) can specifically engage CD26 via the surface spike protein. We identified the spike region (denoted as receptor binding domain (RBD)) that is responsible for receptor-binding, and solved the RBD structures in both the free and receptor-bound forms. MERS-CoV RBD is composed of a core subdomain and an external receptor binding motif that recognizes blades IV and V of CD26 β -propeller. The viral ligand locates at the membrane-distal tip of the receptor dimer, forming a “U”-shaped structure. Elucidation of the receptor-recognition mechanism for MERS-CoV would facilitate rational design of anti-viral drugs and prophylactic vaccines.

In 2012, a new coronavirus, named the Middle East respiratory syndrome coronavirus (MERS-CoV) [1], first emerged in Saudi Arabia [2], and then rapidly spread to multiple countries in the Middle East and Europe [3, 4]. The virus is highly pathogenic [2, 5]. Patients suffer severe pulmonary diseases, including fever, cough, and an acute respiratory distress syndrome. In some cases, the disease course is accompanied by renal failure, leading to exceptionally high mortality [2, 5]. As of April 10, 2014, the World Health Organization has compiled a total of 211 laboratory-confirmed infection cases globally, including 88 deaths [4]. In addition, there has been accumulating evidence showing the limited local transmission of the virus among close contacts [6]. Consequently, there is concern about a second potential coronavirus pandemic ten years after the SARS outbreak [7]. To combat this virus, there is an urgent need to identify how the virus infects humans.

MERS-CoV belongs to the *betacoronavirus* genus in the *Coronaviridae* family [8]. As with other coronaviruses [9], MERS-CoV utilizes the surface spike protein for receptor recognition [10]. The specific binding of the viral spike to the cellular receptor mediates the attachment of viruses to host cells, which is a crucial step initiating infection.

Recently, CD26 (also known as dipeptidyl peptidase 4, DDP4) was identified as the functional receptor for MERS-CoV [10]. The molecular mechanism of CD26

recognition by the novel coronavirus, however, remains elusive. This is a key question regarding the viral pathogenesis and would be useful for the development of anti-viral drugs targeting the viral entry process.

To delineate the receptor-recognition basis of MERS-CoV, we need first to identify the spike region that is responsible for receptor-engagement. By testing the interaction between CD26 and differently-truncated spike proteins through flow-cytometric assays, this receptor binding domain (RBD) was attributed to the MERS-CoV spike residues 367-606. A specific and potent binding of RBD to CD26 was further demonstrated by the surface plasmon resonance Biacore data, which revealed a dissociation constant (K_d) of about 16.7 nM [Fig. 1(a)].

We then successfully crystallized the free RBD protein and its complex with CD26, and managed to solve both structures at 2.5 Å and 2.7 Å, respectively. The viral RBD is composed of a core subdomain and an external receptor binding motif [Fig. 1(b)]. The former is homologous to that of the SARS-CoV spike protein [11], while the latter is a novel strand-dominated unit which recognizes blades IV and V of CD26 β -propeller. The receptor itself is a type II transmembrane protein, presented on the cell surface as homodimers [12, 13]. MERS-CoV RBD locates at the membrane-distal tip of the receptor dimer, forming an overall “U”-shaped structure [Fig. 1(c)].

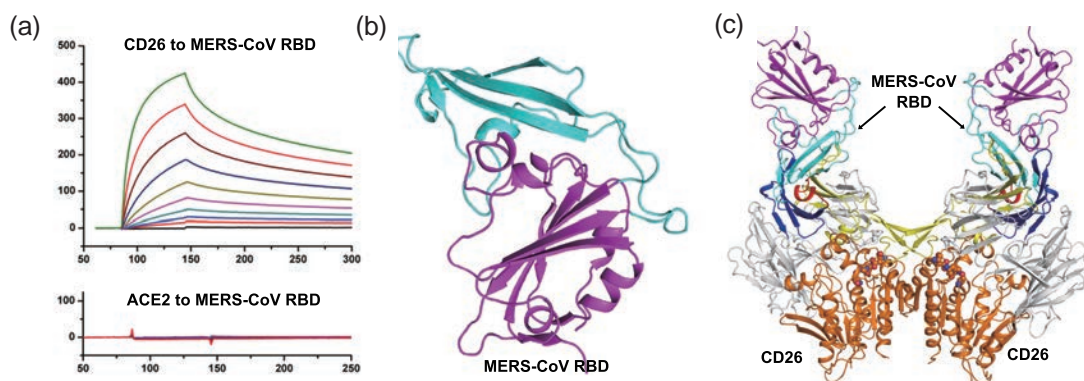


Figure 1: The high-affinity binding and complex structure between MERS-CoV RBD and CD26. (a) A surface plasmon resonance assay showing that MERS-CoV RBD can bind to CD26 but not to the SARS-CoV receptor human ACE2. (b) A schematic representation of the MERS-CoV RBD structure. The core subdomain and the external receptor binding motif are colored magenta and cyan, respectively. (c) The complex structure between MERS-CoV RBD and CD26. The CD26 dimer and its tip-located RBD molecules are shown and labeled.

Detailed analysis revealed that the RBD/CD26 interaction is mainly mediated by salt-bridges and hydrogen-bond contacts among hydrophilic residues at the binding interface. Interestingly, this featured pattern of RBD/CD26 engagement is very similar to those mediating the binding between adenosine deaminase (ADA) and CD26 [14], indicating competition between MERS-CoV and ADA for CD26 receptor. The ADA/CD26 interaction has been shown to play an important role in T cell activation [15], therefore our work indicates potential manipulation of the host immune system by MERS-CoV through competition for the ADA-recognition site. By comparing with other reported coronaviral spike-domain structures and aligning the spike sequences of representative betacoronaviruses, we assumed that members of the *betacoronavirus* genus might have evolved to reserve a similar core-domain fold in the spike protein to present external amino acids with divergent structures for viral pathogenesis, such as receptor recognition.

The emergence of MERS-CoV infections is a worldwide public health concern. The viral entry process represents one of the best drug targets. The identification of key residues, via high-resolution structures, mediating the attachment of MERS-CoV to CD26, could set the direction for future anti-viral research. Our work also indicates a potential application of the properly-folded MERS-CoV RBD proteins in prophylactic vaccination, which is worthy of future study.

REFERENCES

- [1] R.J. de Groot, S.C. Baker, R.S. Baric, C.S. Brown, C. Drosten, L. Enjuanes, R.A.M. Fouchier, M. Galiano, A.E. Gorbalenya, Z.A. Memish, S. Perlman, L.L.M. Poon, E.J. Shijder, G.M. Stephens, P.C.Y. Woo, A.M. Zaki, M. Zambon and J. Ziebuhr, *J. Virol.* **87**, 7790 (2013).

- [2] A.M. Zaki, S. van Boheemen, T.M. Bestebroer, A.D.M.E. Osterhaus and R.A.M. Fouchier, *N. Engl. J. Med.* **367**, 1814 (2012).
- [3] J.A.A.-Tawfiq, *J. Infect. Public Health* **6**, 319 (2013).
- [4] World Health Organization, *Middle East respiratory syndrome coronavirus (MERS-CoV) - update*. http://www.who.int/csr/don/2014_04_10_mers/en/.
- [5] A. Bermingham, M.A. Chand, C.S. Brown, E. Aarons, C. Tong, C. Langrish, K. Hoschler, K. Brown, M. Galiano, R. Myers, R.G. Pebody, H.K. Green, N.L. Boddington, R. Gopal, N. Price, W. Newsholme, C. Drosten, R.A. Fouchier, M. Zambon, *Eurosurveillance* **17**, 20290 (2012).
- [6] R. Breban, J. Riou and A. Fontanet, *Lancet* **382**, 694 (2013).
- [7] World Health Organization, *Cumulative Number of Reported Probable Cases of Severe Acute Respiratory Syndrome (SARS)*. <http://www.who.int/csr/sars/country/en/>.
- [8] G. Lu and D. Liu, *Protein Cell* **3**, 803 (2012).
- [9] M.M. Lai, S. Perlman and L.J. Anderson, *Coronaviridae, in Fields Virology* (ed. D.M. Knipe) 1305 (2007).
- [10] V.S. Raj, H. Mou, S.L. Smits, D.H.W. Dekkers, M.A. Muller, R. Dijkman, D. Muth, J.A.A. Demmers, A. Zaki, R.A.M. Fouchier, V. Thiel, C. Drosten, P.J.M. Rottier, A.D.M.E. Osterhaus, B.J. Bosch and B.L. Haagmans, *Nature* **495**, 251 (2013).
- [11] F. Li, W. Li, M. Farzan and S.C. Harrison, *Science* **309**, 1864 (2005).
- [12] M. Engel, T. Hoffmann, L. Wagner, M. Wermann, U. Heiser, R. Kiefersauer, R. Huber, W. Bode, H.-U. Demuth and H. Brandstetter, *Proc. Natl. Acad. Sci. USA.* **100**, 5063 (2003).
- [13] H.B. Rasmussen, S. Branner, F.C. Wiberg and N. Wagtmann, *Nat. Struct. Biol.* **10**, 19 (2003).
- [14] W.A. Weihofen, J. Liu, W. Reutter, W. Saenger and H. Fan, *J. Biol. Chem.* **279**, 43330 (2004).
- [15] M.D. Gorrell, V. Gysbers and G.W. McCaughan, *Scand. J. Immunol.* **54**, 249 (2001)

BEAMLIN

BL-1A

G. Lu¹, Y. Hu², Q. Wang¹, J. Qi¹, F. Gao^{1, 3}, Y. Li¹, Y. Zhang¹, W. Zhang¹, Y. Yuan⁴, J. Bao³, B. Zhang², Y. Shi¹, J. Yan¹, G.F. Gao^{1, 4, 5} (¹Chinese Academy of Sciences, ²Anhui Univ., ³Sichuan Univ., ⁴Univ. of Sci. and Tech. of China, ⁵China CDC)

Sequence-Specific DNA Glycosylase Found in a Restriction-Modification System

A restriction-modification system consists of genes that encode a restriction enzyme and a cognate methyltransferase. Thus far, it was believed that restriction enzymes are sequence-specific DNA endonucleases. Here we report for the first time that one of the restriction enzymes, R.Pabl, is not an endonuclease but a sequence-specific adenine DNA glycosylase based on the crystal structure and enzymatic activity. R.Pabl captures a 5'-GTAC-3' sequence and removes adenine bases to generate opposing AP sites. The AP sites are cleaved by heat-promoted β elimination, and/or by endogenous AP endonucleases of host cells to introduce a double-strand break.

Restriction enzymes recognize specific DNA sequences and introduce strand breaks unless the sequences are methylated by the cognate methyltransferases. In prokaryotic cells, restriction-modification systems limit transfers of exogenous DNA and protect themselves from infections of phages. Thus far, it was believed that restriction enzymes are sequence-specific endonucleases that leave the 3'-OH end and 5'-phosphate end. Most of the type II restriction enzymes, which are frequently used in the field of biotechnology, have a PD-(D/E)XK motif in their active sites and use Mg^{2+} ions for their enzymatic activities. Other type II restriction enzymes belong to the phospholipase D (PLD) superfamily, the HNH superfamily, and the GIY-YIG superfamily. In addition to these restriction enzyme superfamilies, we found a half-pipe superfamily as represented by R.Pabl from a hyperthermophilic archaea *Pyrococcus abyssi*.

R.Pabl is a type II restriction enzyme that recognizes a 5'-GTAC-3' sequence and cleaves double-stranded DNAs at high temperature without the addition of a divalent cation similar to the PLD superfamily, although R.Pabl shows no sequence similarity to the PLD superfamily. Our previous report showed that R.Pabl forms a homodimeric structure and has a novel DNA-binding fold called a "half pipe," which consists of a highly conserved anti-parallel β -sheet [1]. Among the thousands of confirmed and hypothetical restriction enzymes identified, only a few proteins are predicted to have the half-

pipe fold. To reveal the sequence recognition and DNA cleavage mechanisms of R.Pabl, we determined the crystal structure of the R.Pabl-DNA complex by X-ray crystallography using synchrotron radiation at the Photon Factory AR-NE3A beamline [2].

The structure of the R.Pabl-DNA complex is shown in Fig. 1. R.Pabl bends the double-stranded DNA approximately 90° at the 5'-GTAC-3' sequence and the highly expanded minor groove side of the bent DNA faces the half-pipe region. The 5'-GTAC-3' duplex is unwound by the binding of R.Pabl and the bases are captured between the core region and the $\beta 8$ - $\beta 9$ loop of R.Pabl. The most striking feature of the R.Pabl-DNA complex determined in this study is that the *N*-glycosidic bond between the adenine base and deoxyribose of Ade11 is cleaved (Fig. 1, right panel). This suggests that R.Pabl has catalyzed the cleavage of the *N*-glycosidic bond of Ade11 similar to DNA glycosylases, although R.Pabl shows no sequence similarity to DNA glycosylases. The DNA glycosylase activity of R.Pabl was confirmed by denaturing polyacrylamide gel electrophoresis (denaturing PAGE), high performance liquid chromatography (HPLC) and matrix-assisted laser desorption-ionization time-of-flight mass (MALDI-TOF MS) spectrometry. Mutation analyses of R.Pabl showed that the DNA glycosylase activity of R.Pabl is catalyzed by two highly conserved residues, Tyr68 and Asp214.

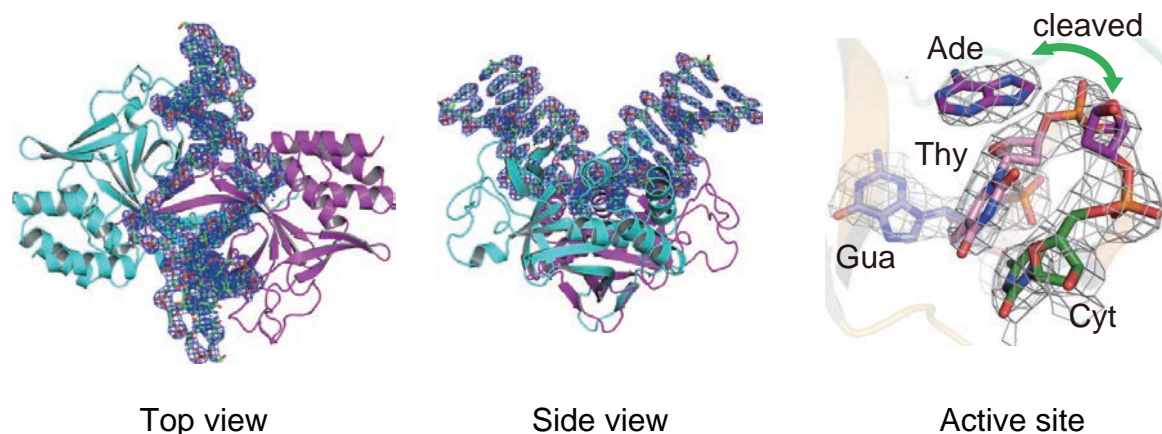


Figure 1: Structure of the R.Pabl-DNA complex.

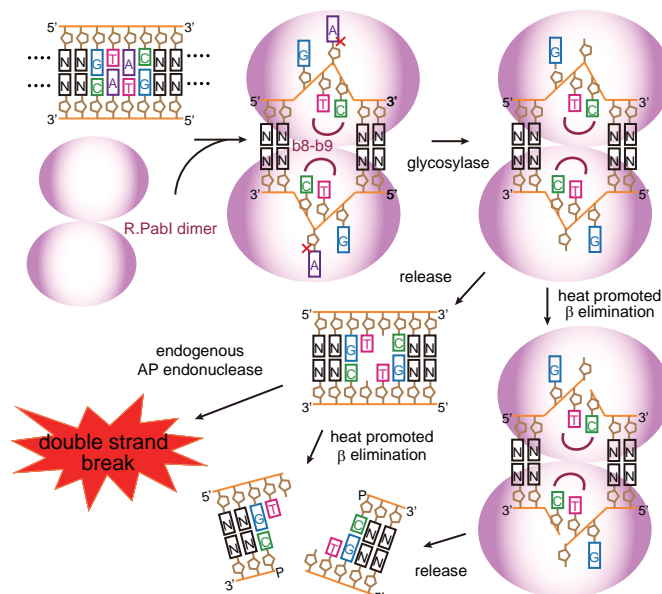


Figure 2: DNA cleavage mechanism by R.PabI.

Although the structural and biochemical analyses of R.PabI indicate that R.PabI is an adenine DNA glycosylase, R.PabI cleaves the DNA duplex at the specific site in a manner similar to restriction endonucleases. The opposing AP sites generated by R.PabI may be cleaved by two different mechanisms to introduce a double-strand break (Fig. 2). First, the R.PabI product is cleaved by heat-promoted β elimination. Because R.PabI is an enzyme from hyperthermophilic archaea, R.PabI shows DNA-cleavage activity at high temperature (60–90°C). Under these conditions, the opposing AP sites generated by R.PabI will be cleaved by heat-promoted β elimination. Second, the R.PabI product is cleaved by AP endonucleases of host cells. This cooperating mechanism would be important for R.PabI homologues from mesophiles to cleave exogenous DNA.

Because the DNA fragments cleaved by the effect of R.PabI lose adenine bases at the cleavage site, it would be hard to repair the R.PabI products by DNA ligase, unlike in the case of DNA fragments produced by typical

restriction endonucleases. This feature may make the restriction-modification system using DNA glycosylase activity more powerful in attacking DNA than the typical restriction-modification system. Because R.PabI does not share any structural similarity with known DNA glycosylases, the half-pipe superfamily represented by R.PabI is a new superfamily of DNA glycosylases.

REFERENCES

- [1] K. Miyazono, M. Watanabe, J. Kosinski, K. Ishikawa, M. Kamo, T. Sawasaki, K. Nagata, J.M. Bujnicki, Y. Endo, M. Tanokura and I. Kobayashi, *Nucleic Acids Res.* **35**, 1908 (2007).
- [2] K. Miyazono, Y. Furuta, M. W.-Matsui, T. Miyakawa, T. Ito, I. Kobayashi and M. Tanokura, *Nat. Commun.* **5**, 3178 (2014).

BEAMLIN

AR-NE3A

K. Miyazono and M. Tanokura (The Univ. of Tokyo)

Structural Analysis of Intrinsically Partially Folded EspB from Enterohaemorrhagic *E. coli* O157:H7 by Combination of CD and SAXS in Conjunction with Protein Dissection Technique

EspB is one of the major intrinsically disordered pathogens from enterohaemorrhagic *Escherichia coli*, which promotes actin reorganization by activating α -catenin from the host cell. EspB assumes a partially folded structure under native conditions. We analyzed the structural properties of EspB by a combination of various spectroscopic techniques including circular dichroism and small-angle X-ray scattering in conjunction with protein dissection. The results suggested that EspB assumes partially folded α -helical segments around G41–Q70 whereas other regions, particularly around the C-terminal half, are almost entirely extended. Furthermore, titration studies by fluorescence anisotropy indicated that the α -helical segments directly interact with α -catenin.

Infection by enterohaemorrhagic *Escherichia coli* (EHEC), O157:H7, can cause various severe symptoms including abdominal cramps, diarrhea and hemolytic uremic syndrome (HUS) [1]. Particularly for young children, HUS can develop into acute renal failure and in the worst case, lead to death.

EHEC produces various virulence factors including Shiga-like toxins as well as proteins that induce morphological rearrangement of host cells [1]. It is therefore important to clarify the structural property of these virulence factors in order to understand the detailed mechanism of EHEC infection.

EspB is one of the virulence factors of EHEC which promote the rearrangement of actin cytoskeleton. EspB is directly injected into host cytosol through the type III secretion system (T3SS) of EHEC and binds to the C-terminal vinculin homology domain of α -catenin in host cytosol. It has been indicated that the binding of EspB to α -catenin induces some conformational rearrangement of α -catenin and enhances the ability of α -catenin to promote actin bundling [2]. Previous studies on the structural property of EspB by various spectroscopic techniques such as circular dichroism (CD), intrinsic tyrosine fluorescence and multi-angle light scattering indicated that this protein assumes a partially folded conformation with an amount of α -helical structures but with well-ordered specific tertiary contacts when in the isolated state [3]. Thus, EspB is one of the intrinsically disordered proteins with some partially folded structure.

This conformational uniqueness is considered to be required for efficient secretion through the narrow tube of T3SS. Further analysis clarified that many T3SS-dependent pathogenic proteins tend to be classified into “intrinsically disordered protein” (IDP) which cannot form a specific well-defined structure by itself unlike the general globular proteins.

Recent developments in modern high-resolution techniques of structural biology enable us to routinely solve the structures of globular or membrane proteins. However, protein crystallization is basically improbable for such a flexible molecule. Line broadening phenomena in solution NMR are observed for EspB probably due to the slow conformational exchange within the ensemble of partially folded structures [3].

To overcome these problems, we employed a combinatorial approach using various low-resolution techniques such as small-angle X-ray scattering (SAXS) and CD spectroscopy in conjunction with a protein dissection strategy [4]. SAXS analysis revealed that this protein possesses highly expanded conformation with a radius of gyration (R_g) of 67.8 Å. Surprisingly, this value is similar to that of an ideal random coil (62.0 Å) or completely unfolded protein [Fig. 1(a)]. However, CD indicates the presence of α -helical structures [Fig. 1(b)]. These results suggested that the protein possesses highly unstructured regions together with partially folded α -helical segments.

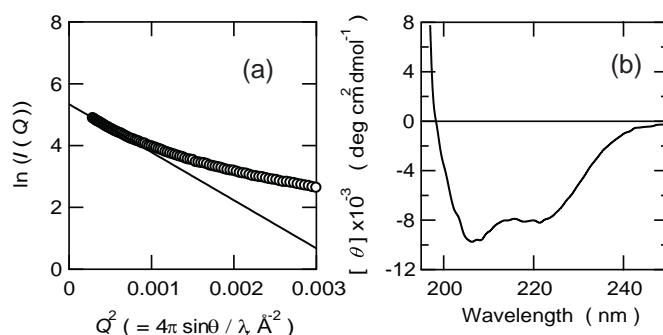


Figure 1: Conformational properties of EspB analyzed by SAXS (a) and CD (b). (a) Guinier plot. The slope of this plot corresponds to $R_g^2/3$. (b) Far-UV CD spectrum of EspB. The minimum at 222 nm indicates the presence of α -helical structures.

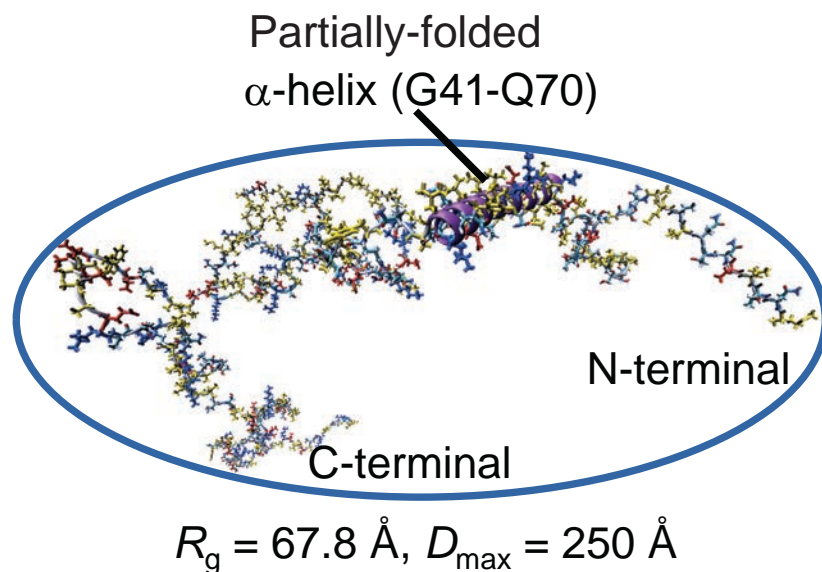


Figure 2: Structural model of EspB estimated from the results of SAXS and CD in combination with the protein dissection. R_g was obtained from the Guinier plot in Fig. 1. D_{\max} corresponds to the maximum distance estimated by the analysis of probability function calculated from the scattering intensity. For more details of the analysis, see reference [4].

In order to identify the α -helical regions within the whole EspB, we employed the protein dissection technique. We analyzed far-UV CD spectra of various peptide fragments corresponding to several parts of EspB and found that the fragments which correspond to G31 to Q70 can be a core region of the α -helical segments. Based on these observations, we constructed structural models of EspB as illustrated in Fig. 2. Moreover, the α -helical fragments having the sequence of G31–Q70 of EspB had high affinity to the C-terminal vinculin homology domain of α -catenin. These results indicate that α -catenin binds to EspB through the preexisting less stable particular conformation in a manner of conformational selection [5].

To date, the structural properties of only a limited number of IDPs have been clarified but none of them assumes a partially folded structure. Our combinatorial approach using protein dissection with CD and SAXS successfully illustrated the structural property of one of such difficult targets. This approach was feasible because of the nature of IDP in which fewer nonlocal contacts between residues apart from each other in amino acid sequences are present. Although the resolution of

our structural model is still low, further developments of this technique, e.g. in combination with molecular dynamics simulation, will be a powerful strategy to clarify the structural detail of IDPs with partially folded conformations.

REFERENCES

- [1] Y. Nguyen and V. Sperandio, *Front. Cell Infect. Microbiol.* **2**, 90 (2012).
- [2] M. Hamaguchi, D. Hamada, K.N. Suzuki, I. Sakata and I. Yanagihara, *FEBS J.* **275**, 6260 (2008).
- [3] D. Hamada, M. Hamaguchi, K.N. Suzuki, I. Sakata and I. Yanagihara, *FEBS J.* **277**, 2409 (2010).
- [4] M. Hamaguchi, H. Kamikubo, K.N. Suzuki, Y. Hagihara, I. Yanagihara, I. Sakata, M. Kataoka and D. Hamada, *PLoS One* **8** e71618 (2013).

BEAMLIN

BL-10C

M. Hamaguchi^{1, 2}, **H. Kamikubo**³, **K.N. Suzuki**², **Y. Hagihara**⁴, **I. Yanagihara**², **S. Sakata**², **M. Kataoka**³ and **D. Hamada**^{5, 6} (¹Kinki Univ., ²Osaka Medical Center for Maternal and Child Health, ³NAIST, ⁴AIST, ⁵Kobe Univ. and ⁶Mie Univ.)

X-Ray-Induced Nitric Oxide-Mediated Bystander Cell Death Suppresses Spontaneous Mutagenesis in V79 Cells

Bystander responses have generated considerable interest in the field of radiobiology because of their non-linear relationship with low-dose radiation. Here, we demonstrated that bystander cell death was biphasically enhanced in a dose-dependent manner by using the synchrotron X-ray microbeam irradiation system. Interestingly, we found that the mutation frequency at the hypoxanthine-guanosine phosphoribosyl transferase (*HPRT*) locus in the bystander cells has a similar biphasic dose response. Both the phenomena were suppressed when the cells were incubated with carboxy-PTIO, a specific scavenger of nitric oxide (NO). These observations suggested that the increase in NO-mediated bystander cell death can be attributed to mutagenesis-suppressing mechanisms.

Radiation-induced bystander response is generally defined as an intercellular response induced in unirradiated cells that receive bystander signals from the directly irradiated cells within the irradiated cell population. The discovery of bystander responses is significant in radiobiology because this response may have important implications for estimating the risk to human health of exposure to low-dose radiation. The microbeam cell irradiation system, which enables observation of cellular responses of individual irradiated and unirradiated cells, is a powerful tool for elucidating the mechanisms underlying biological responses to low-dose radiation. We used the synchrotron X-ray microbeam irradiation system [Fig. 1(A)] developed at the Photon Factory, High Energy Accelerator Research Organization, KEK [1-4] and demonstrated that nitric oxide (NO)-mediated bystander cell death was biphasically enhanced in a dose-dependent manner [Fig. 1(B)] [5, 6]. We then measured the mutation frequency in the bystander cells neighboring the nuclei-irradiated cells.

The experimental procedure is summarized in Fig. 2(A). V79 cells were seeded (1×10^5 cells/dish) into custom-designed dishes for microbeam irradiation and incubated overnight. Five targeted nuclei were irradiated with $10 \times 10\text{-}\mu\text{m}$ square 5.35 keV X-ray beams (9.3×10^3 photons/s/100 μm^2) by using the synchrotron X-ray microbeam irradiation system installed at the BL-27B station located at the Photon Factory [1-4]. After

incubation for 3 h, the surviving fraction of the bystander cells was measured by a clonogenic assay. We also measured the mutation frequency at the hypoxanthine-guanosine phosphoribosyl transferase (*HPRT*) locus in the bystander cells. After irradiation, the cells were incubated for 3 h. The cells were harvested, transferred to a culture flask containing fresh medium, and maintained for 8 days with sub-cultivation every 2 days to allow phenotypic expression. Then, the cells were harvested and seeded (1×10^6 cells/dish) into culture dishes with a fresh medium containing 10 $\mu\text{g/ml}$ of 6-thioguanine. After incubation for 6 days, the number of colonies of the *HPRT* mutants was scored.

When the nuclei were irradiated with approximately 1 Gy, the surviving fraction decreased to 0.87, but at higher doses, the surviving fraction was found to be stable at approximately 0.94 [Fig. 2(B)] [7]; this observation is in concordance with our previous observations [Fig. 1(B)] [5, 6, 8]. The background mutation frequency in the control (unirradiated) cells was 2.6×10^{-5} [Fig. 2(C)] [7]. The mutation frequency in the bystander cells decreased significantly ($p < 0.01$) to 5.3×10^{-6} when the five targeted nuclei were irradiated with approximately 1 Gy, but, at higher doses, the mutation frequency returned to the background level [Fig. 2(C)] [7]. The biphasic dose responses, bystander cell death, and *HPRT* mutation frequency were significantly correlated ($p < 0.05$) [7]. This correlation indicated that the bystander cell death and mutagenesis in the bystander cells were responses

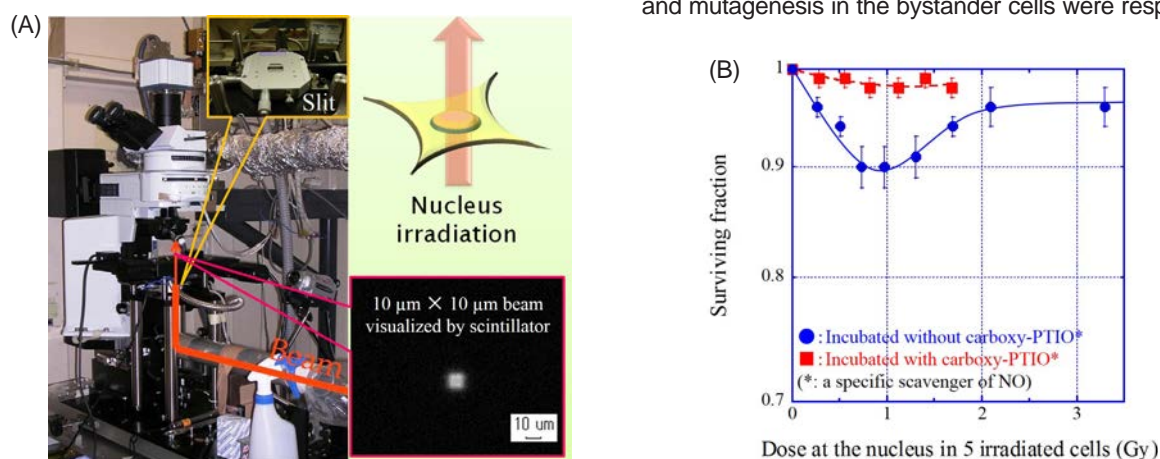


Figure 1: Synchrotron X-ray microbeam irradiation system and the schema of nucleus irradiation with X-ray microbeam (A). The surviving fraction of bystander V79 cells surrounding the nuclei-irradiated V79 cells (B) [5, 6].

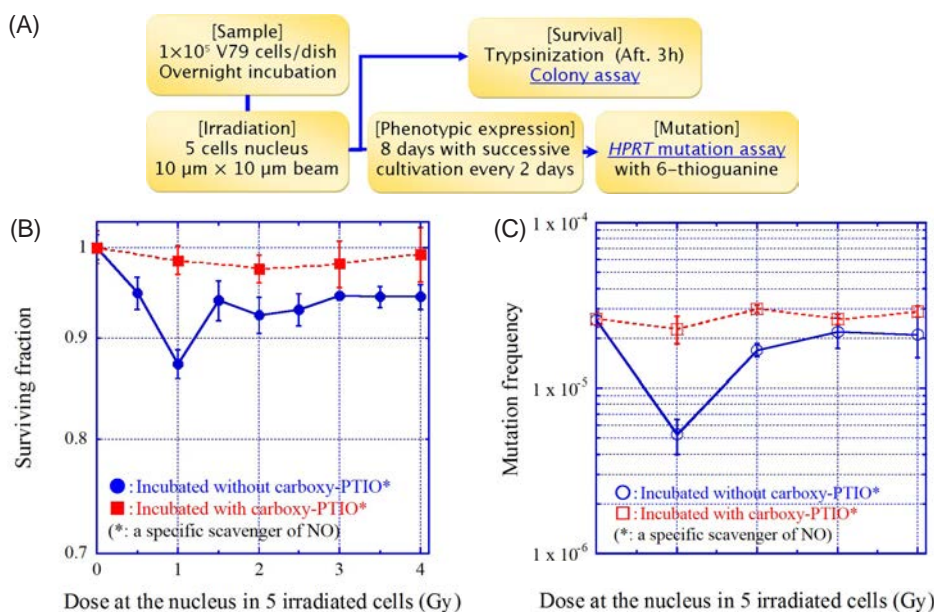


Figure 2: Measurement of the bystander cell survival and the *HPRT* mutation frequency (A), the surviving fraction of bystander V79 cells (B), and the *HPRT* mutation frequencies in the bystander V79 cells (C) [7].

to the same or related stimuli. Recently, we showed that NO is the principal mediator of bystander cell death [6]. Accordingly, we investigated the role of NO in bystander cell death and mutations. The dose-dependent biphasic increase in the bystander cell death was not observed when the cells were incubated with carboxy-PTIO, a specific scavenger of NO [Fig. 2(B)] [7]. Furthermore, the dose-dependent biphasic decrease in the mutation frequency was not observed when the cells were incubated with carboxy-PTIO [Fig. 2(C)] [7]. Recently, Egashira *et al.* reported that exposure to NO causes mitochondrial degeneration and subsequent cell killing in cells with low antioxidative activity [9]. Genetically unstable cells that have defects in antioxidative activities may be selectively killed by the bystander responses because NO is a major mediator of bystander cell death [6]. Thus, the secretion of factors that contributed to the perpetuation of unstable phenotype may have been suppressed, and the antioxidant activity in the surviving cell population may have increased, as a result of which mutagenesis may have been suppressed in the bystander cells. Our group reported that the biphasic NO-mediated bystander cell death was induced by X-ray microbeam irradiation also in normal human fibroblast WI-38 cells [8]. In an ongoing gene expression profiling study with the RT² ProfilerTM PCR Array System (Qiagen), we have found that the expression of *TP73*, which is known to be upregulated by NO [10], was highly upregulated in the bystander WI-38 cells.

Our results indicate that radiation-induced bystander responses can enhance selective cell killing of genetically unstable cells in the bystander cell population and that this selective cell death may act as a protective mechanism that competes with increases in non-lethal

and potentially carcinogenic damages such as mutations.

This work was supported in part by a Grant-in-Aid for Young Scientists (B) (23710076) from Japan Society for the Promotion of Science (JSPS).

REFERENCES

- [1] K. Kobayashi, N. Usami, K. Hieda, K. Takakura, H. Maezawa and T. Hayashi, *Nucl. Instrum. and Methods Phys. Res. A* **467**, 1329 (2001).
- [2] K. Kobayashi, N. Usami, H. Maezawa, T. Hayashi, K. Hieda and K. Takakura, *Int. Congr. Ser.* **1258**, 207 (2003).
- [3] K. Kobayashi, N. Usami, H. Maezawa, T. Hayashi, K. Hieda and K. Takakura, *J. Biomed. Nanotechnol.* **2**, 116 (2006).
- [4] Y. Kobayashi, T. Funayama, N. Hamada, T. Sakashita, T. Konishi, H. Imaseki, K. Yasuda, M. Hatashita, K. Takagi, S. Hatori, K. Suzuki, M. Yamauchi, S. Yamashita, M. Tomita, M. Maeda, K. Kobayashi, N. Usami and L. Wu, *J. Radiat. Res.* **50** Suppl A, A29 (2009).
- [5] M. Maeda, M. Tomita and K. Kobayashi, *J. Radiat. Res.* **50** Suppl A, A119 (2009).
- [6] M. Maeda, M. Tomita, N. Usami and K. Kobayashi, *Radiat. Res.* **174**, 37 (2010).
- [7] M. Maeda, K. Kobayashi, H. Matsumoto, N. Usami and M. Tomita, *J. Radiat. Res.* **54**, 1043 (2013).
- [8] M. Tomita, M. Maeda, H. Maezawa, N. Usami and K. Kobayashi, *Radiat. Res.* **173**, 380 (2010).
- [9] A. Egashira, K. Yamauchi, K. Yoshiyama, H. Kawate, M. Katsuki, M. Sekiguchi, K. Sugimachi, H. Maki and T. Tsuzuki, *DNA Repair* **1**, 881 (2002).
- [10] A. Tebbi, O. Guittet, M.-H. Cottet, M.-F. Vesin and M. Lepoivre, *J. Biol. Chem.* **286**, 7873 (2011).

BEAMLIN

BL-27B

M. Maeda^{1,2}, K. Kobayashi³, H. Matsumoto⁴, N. Usami³ and M. Tomita² (¹WERC, ²CRIEPI, ³KEK-PF, ⁴Univ. of Fukui)

Z_{eff} Imaging Using X-Ray Interferometer

Z_{eff} imaging is a new technique that provides a way to visualize the spatial distribution of the atomic number (Z) in samples (effective atomic number (Z_{eff}) for a plural-element sample). Because Z corresponds to the ratio of the real to imaginary part of the complex refractive index, an elemental map can be calculated from an absorption and phase-contrast image. Feasibility observations of several metal foils were performed using an imaging system fitted with a two-crystal X-ray interferometer. The obtained Z_{eff} image shows that aluminum, iron, nickel, and copper foils were clearly distinguished, and that the Z_{eff} values for nickel and copper coincided with the ideal Z number within 5%.

X-ray imaging is a powerful method for nondestructive observation of samples and is widely used in many fields from medical diagnosis to security checks at airports. Obtained images show the electron density distributions in a sample, and the outer shapes and inner structures are visualized clearly. However, no elemental information of the sample, for example, whether the sample consists of copper or iron, is obtained. An X-ray is an electromagnetic wave with a very short wavelength. The phase is shifted and the amplitude (intensity) is reduced by passing the X-ray through the sample. The phase-shift dp is given by the product of the thickness of the sample (t) and the real part of the complex refractive index (n) of the sample. In the same way, the ratio of the decrease of the intensity dl is given by the product of t and the linear absorption coefficient corresponding to the imaginary part of n . Therefore, the ratio (r) of dp and dl is independent of t , and only depends on the ratio of the real and imaginary parts of n . Since n has a characteristic value for each element, ratio r also has a characteristic value. In summary, ratio r uniquely corresponds to the element, namely the Z -number of the sample, and therefore, elemental information can be obtained from r [1, 2].

An X-ray interferometer is a powerful tool to detect X-ray phase shift, and has been used for phase-contrast X-ray imaging with more than 1000 times higher sensitivity than that of conventional absorption X-ray imaging

[3]. Because of this advantage, it provides a way to visualize small density differences in samples composed of light elements, for example, biological soft tissues and organic materials without using any supplemental methods. We have been developing an imaging system fitted with a two-crystal X-ray interferometer to conduct fine three-dimensional (3D) observations [4]. We used this system to conduct visualizations of cancerous tissues in normal tissues without contrast agents, β -amyloid plaques in brains taken from Alzheimer's disease mice [5], and air hydrates in an ice core drilled 1900 m deep in the Antarctic [6]. By exploiting the high sensitivity of phase-shift detection, highly accurate observations of the Z_{eff} image using the X-ray interferometer were performed [7].

Figure 1 schematically shows the two-crystal X-ray interferometer used in our study. The optical configuration is the same as that of a Mach-Zehnder interferometer of visible light. The incident X-ray is divided at the first wafer (S), reflected by the second (M1) and third (M2) wafers, and recombined to generate two interference beams at the fourth wafer (A). The phase-shift caused by the sample put in the interference path (P1) can be detected by the changes in the interference beam intensity. Absorption images can be obtained by blocking off the beam path (P2) by placing a plate made of a heavy metal such as Pb.

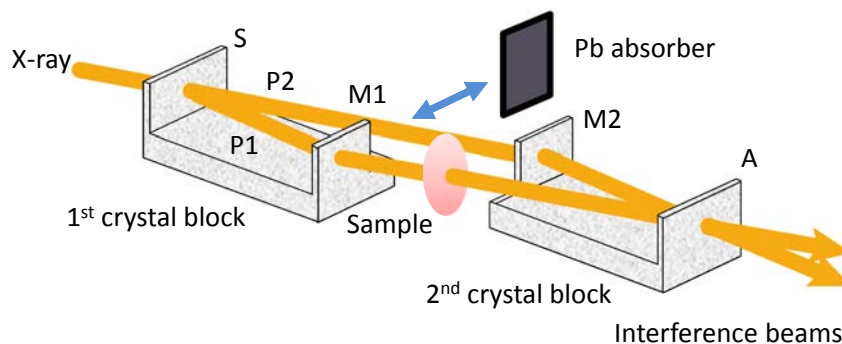


Figure 1: Schematic view of two-crystal X-ray interferometer.

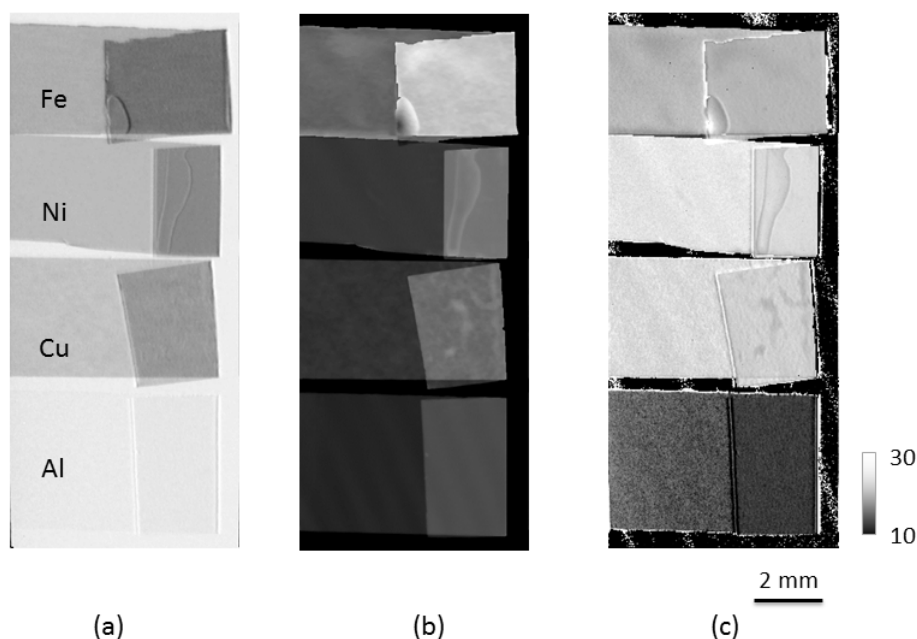


Figure 2: Obtained images of metal foils: (a) absorption image, (b) phase-contrast image, and (c) Z_{eff} image [8].

Figure 2 shows the obtained phase map (spatial distribution of phase-shift of sample), absorption map, and calculated Z_{eff} image. The metal foils were aligned vertically in the following order: iron (10 μm), nickel (5 μm), copper (5 μm), and aluminum (12 μm). Each foil is depicted clearly in ordinary images ((a) and (b)), but it is impossible to distinguish differences in the elements and their thicknesses. In contrast, the Z_{eff} image shows the Z_{eff} value of the samples and indicates that the elements are different. The average Z_{eff} values were 16.4, 25.4, 27.9, and 28.8 for aluminum, iron, nickel, and copper foil, respectively. The differences from the ideal values (13, 26, 28, 29) become smaller as the atomic numbers become larger, and the minimum value is less than 5%, which provides a way to identify the element. In addition, since the thickness information of the sample was canceled by the division of dp and dl , the Z_{eff} in each foil has the same value in the unfolded and folded areas (right side of the foils). This result shows that this imaging technique provides a way to obtain not only the electron density map but also elemental information without using any other imaging techniques. By combining this technique with computed tomography techniques, 3D elemental observations are expected in the future.

REFERENCES

- [1] Z. Qi, J. Zambelli, N. Bevins and G.-H. Chen, *Phys. Med. Biol.* **55**, 2669 (2010).
- [2] T. Mukaide, M. Watanabe, K. Takada, A. Iida, K. Fukuda and T. Noma, *Appl. Phys. Lett.* **98**, 111902 (2011).
- [3] A. Momose, T. Takeda, Y. Itai and K. Hirano, *Nature Med.* **2**, 473 (1996).
- [4] A. Yoneyama, T. Takeda, Y. Tsuchiya, J. Wu, T.T. Lwin, A. Koizumi, K. Hyodo and Y. Itai, *Nucl. Instrum. Methods Phys. Res. A* **523**, 217 (2004).
- [5] K. Noda-Saita, A. Yoneyama, Y. Shitaka, Y. Hirai, K. Terai, J. Wu, T. Takeda, K. Hyodo, N. Osakabe, T. Yamaguchi and M. Okada, *Neuroscience* **138**, 1205 (2006).
- [6] S. Takeya, K. Honda, A. Yoneyama, Y. Hirai, J. Okuyama, T. Hondoh, K. Hyodo and T. Takeda, *Rev. Sci. Instrum.* **77**, 053705 (2006).
- [7] A. Yoneyama, K. Hyodo and T. Takeda, *Appl. Phys. Lett.* **103**, 204108 (2013).
- [8] A. Yoneyama, S. Takeya, K. Hyodo and T. Takeda, *PHOTON FACTORY NEWS* Vol. **32**, 19 (2014).

BEAMLINER

BL-14C

A. Yoneyama¹, R. Baba¹, S. Takeya², K. Hyodo³ and T. Takeda⁴ (¹Hitachi Ltd., ²AIST, ³KEK-PF, ⁴Kitasato Univ.)

Development of a Compact Scanning Transmission X-Ray Microscope (STXM)

A new compact X-ray microscope has been developed at the soft X-ray undulator beamlines of the Photon Factory. Piezo-driven linear stages used as coarse stages realized a microscope with a very compact shape, thermally and vibrationally stable, and suitable for use at the “free-port” endstations of multipurpose beamlines. Fully digitized control electronics for pulse counting, scanner drive, and position sensing have been developed to realize efficient data acquisition. Imaging and microspectroscopic results obtained with the microscope are presented.

Scanning transmission X-ray microscopy (STXM) provides images and absorption spectra of a specific region of interest by scanning the sample position against focused X-rays [1]. STXM provides useful information about elemental composition, chemical states, magnetic properties by using circularly polarized X-rays [2], and molecular orientation by using linear dichroism [3] with a spatial resolution of 20–100 nm. In Japan, however, soft X-ray STXM has not been available until very recently [4].

Figure 1 shows the optics of our new STXM at the Photon Factory [5]. Soft X-rays from an undulator in the Photon Factory ring are monochromatized and focused by a toroidal mirror. The four-way aperture slit is placed at the focal point of the mirror to provide a virtual source point for illuminating the Fresnel zone plate (FZP). The FZP is a diffractive lens which has the focal distance of, in the present case, 0.7–5 mm depending on the photon energy. The first-order diffraction through the order sorting aperture (OSA) is focused onto the sample, and the intensity of the transmitted X-rays is then measured.

The scheme of the coarse stages in our STXM is in principle the same as that of the conventional STXM [1]. We utilized piezo-driven linear stages instead of stepping motors, resulting in: (1) a very compact shape

of the main chamber with interior dimensions of 220 × 310 × 200 mm, (2) precise positioning of ~50 nm by using optical encoders implemented in the stages, and (3) high thermal stability since the piezo-driven stages produce less heat than do stepping motors. As shown in Fig. 1, the components from the aperture slit to the detector are placed on a single optical table, which is vibrationally isolated from the floor with protruding rubber pads. Thanks to this design, the compact STXM can be easily connected to and removed from the beamline, and so is suitable for use at the “free-port” endstations of multipurpose beamlines in the Photon Factory.

The transmitted X-rays can be detected in several ways: using an Si photodiode, Si avalanche photodiode, or the scintillator–optical fiber–photomultiplier (PMT) assembly. The precise sample position is scanned by piezoelectric scanners and the position is monitored with laser interferometric sensors. The X-ray detection, scanner drive, and position sensing functions are implemented in a field-programmable-gate-array (FPGA) circuit to realize fast and efficient data acquisition. The FPGA and user-interface programs were developed on a National Instruments LabVIEW platform, and the output data is fully compatible with the analysis software aXis2000 [6].

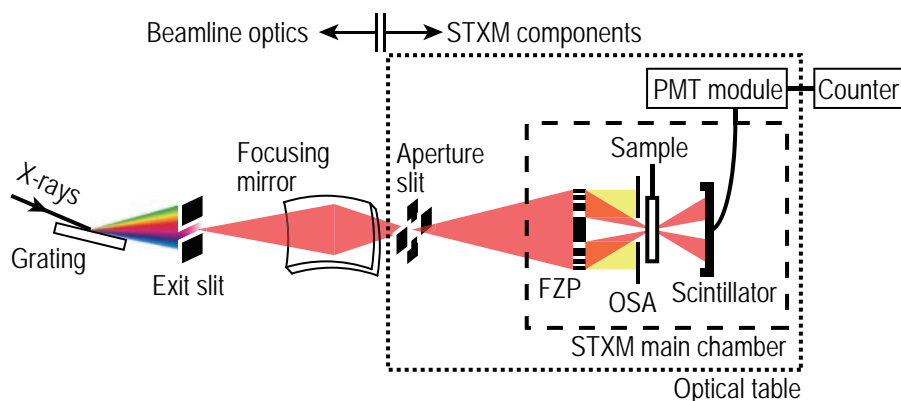


Figure 1: The optics of the compact STXM.

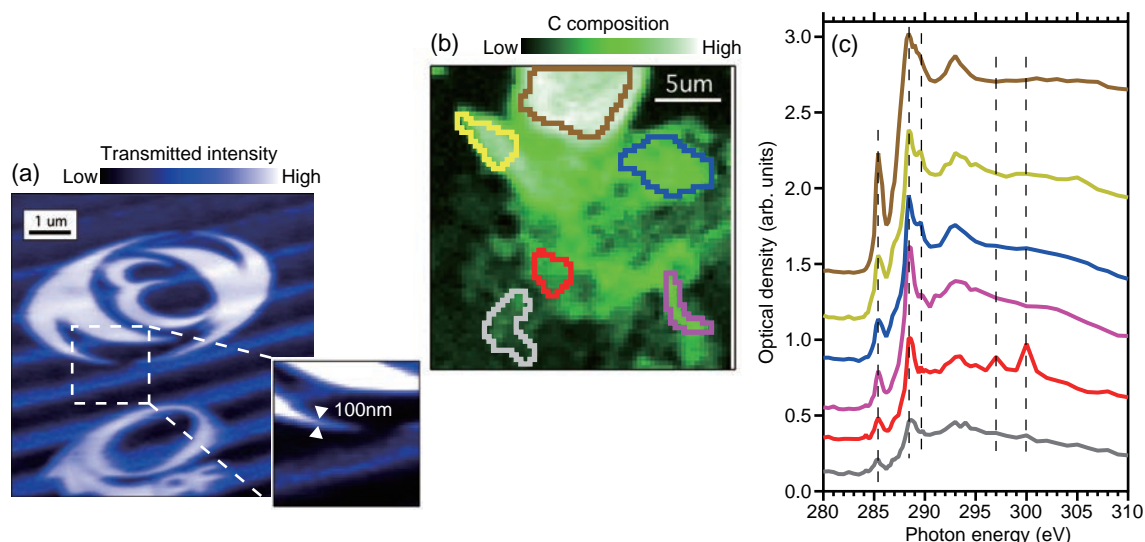


Figure 2: (a) X-ray transmission image of KEK and PF logomarks, which were patterned on ~300 nm-thick tungsten deposited onto an Si_3N_4 membrane. (b) C elemental composition map of particulate matter from the Pripyat River. (c) X-ray absorption spectra of the specific regions of interest. The colors of the spectra correspond to the regions indicated in (b).

Figure 2 shows the results obtained with the compact STXM. Figure 2(a) is the transmission X-ray image of logomark patterns measured using $h\nu = 350$ eV [7]. The patterns were fabricated using a focused ion beam on ~300 nm-thick tungsten film deposited onto an Si_3N_4 membrane. The spatial resolution of our STXM is significantly better than 100 nm. Quantitative evaluation is currently in progress.

Figures 2(b) and (c) show the result of image stack measurement. The sample was particulate matter from the Pripyat River in Chernobyl City [8]. The photon energy was varied from 280 to 310 eV with the energy resolution of $E/\Delta E \sim 5000$. Sixty-four images of 70×70 points were obtained at each point of photon energy. The total acquisition time was about two hours. Figure 2(b) shows the elemental composition map of C obtained by taking the difference of the images taken at the pre- and post-edge of the C K absorption edge. Figure 2(c) shows the absorption spectra obtained by collecting the data points in the region of interest indicated in Fig. 2(b). As shown here, STXM enables spatially resolved chemical speciation based on functional group or valency. Note that great care was taken to reduce carbon contamination in the beamline optics used here (BL-13A) [9], enabling quantitative characterization using C K edge absorption spectra.

A wide range of photon energy from 200 to 1500 eV is available with the compact STXM. It is now being utilized for the characterization of photovoltaic polymer blends [10], aerosols, clay minerals [8], and permanent magnets. Microspectroscopy using the compact STXM will be useful for a wide range of research in physics,

chemistry, environmental science, and material engineering.

REFERENCES

- [1] A.L.D. Kilcoyne, T. Tyliczszak, W.F. Steele, S. Fakra, P. Hitchcock, K. Franck, E. Anderson, B. Harteneck, E.G. Rightor, G.E. Mitchell, A.P. Hitchcock, L. Yang, T. Warwick and H. Ade, *J. Synchrotron Rad.* **10**, 125 (2003).
- [2] K. Ono, T. Araki, M. Yano, N. Miyamoto, T. Shoji, A. Kato, A. Manabe, H. Nozaki, Y. Kaneko and J. Raabe, *IEEE Trans. Magn.* **47**, 2672 (2011).
- [3] B. Watts, T. Schuettfort and C.R. McNeill, *Adv. Funct. Mater.* **21**, 1122 (2011).
- [4] T. Ohigashi, H. Arai, T. Araki, N. Kondo, E. Shigemasa, A. Ito, N. Kosugi and M. Katoh, *J. Phys.: Conf. Ser.* **463**, 012006 (2013).
- [5] Y. Takeichi, N. Inami, H. Suga, K. Ono and Y. Takahashi, *Chem. Lett.* **43**, 373 (2014).
- [6] A.P. Hitchcock, available at <http://unicorn.mcmaster.ca/aXis2000.html>
- [7] Y. Takeichi, N. Inami, H. Suga, T. Ueno, S. Kishimoto, Y. Takahashi and K. Ono, *J. Phys.: Conf. Ser.* **502**, 012009 (2014).
- [8] H. Suga, Q. Fan, Y. Takeichi, K. Tanaka, H. Kondo, V.V. Kanivets, A. Sakaguchi, N. Inami, K. Mase, K. Ono and Y. Takahashi, *Chem. Lett.* **43**, 1128 (2014).
- [9] A. Toyoshima, T. Kikuchi, H. Tanaka, J. Adachi, K. Mase and K. Amemiya, *J. Synchrotron Rad.* **19**, 722 (2012).
- [10] Y. Moritomo, T. Sakurai, T. Yasuda, Y. Takeichi, K. Yonezawa, H. Kamioka, H. Suga, Y. Takahashi, Y. Yoshida, N. Inami, K. Mase and K. Ono, *Appl. Phys. Express* **7**, 052302 (2014).

BEAMLINES

BL-13A and BL-16A

Y. Takeichi¹, N. Inami¹, H. Suga², Y. Takahashi^{2,3} and K. Ono¹ (¹KEK-PF, ²Hiroshima Univ. ³The Univ. of Tokyo)

Minimization of the Emittance Growth in a Superconducting Radio Frequency Cavity at cERL Injector

For the development of future light sources based on linear accelerators such as X-FEL and ERL, beam dynamics for the acceleration and transportation without degradation of ultra-low-emittance beams such as 0.1 mm-mrad for 7.7 pC/bunch in the cERL injector are an important research topic to provide high-brightness and high-quality synchrotron radiation. In particular, a radial electric field of the superconducting radio frequency cavity, which is proportional to the beam offset, can cause transverse emittance growth. We succeeded in compensating the transverse emittance growth in the SRF cavity by a new method of estimating the electrical center of a cavity and adjusting the beam trajectory inside the cavity.

In KEK, the compact energy recovery linac (cERL) was constructed and has been commissioned to demonstrate the production, acceleration, and recirculation of ultra-low-emittance and high-current beams before constructing a 3-GeV ERL that will be used as a super-brilliant and ultra-short pulse synchrotron light source as well as a driver for an X-ray free electron laser oscillator (XFEL-O) [1, 2].

The ERL injector, which is shown in the Fig. 1, requires a high-brightness electron gun, and high-power SRF cavities to generate and accelerate high-current and low-emittance electron beams. Using a GaAs photocathode DC gun, the generation of a low-emittance beam of 0.1 mm-mrad with a bunch charge of a few tens of fC was demonstrated [3]. After generating the high-quality beam, the next step is to accelerate it without deterioration in beam quality. SRF injector cavities, which are used to increase the energy of the beam up to 5.6 MeV, are one source of the emittance growth, since the particles in the head and tail parts of the bunch receive the transverse kick force in a direction opposite to the radial electric field of the cavity, when the bunch is laid on the on-crest acceleration phase. In order to avoid the degradation by injector cavities, it is essential to estimate the electrical center of the cavity and to adjust the beam trajectory inside the cavity, because the strength of the radial electric field depends on the orbit offset inside the cavity [4].

In general, the electrical center in an actual cavity is estimated by measuring the pick-up HOM signal digitized by a fast oscilloscope, and using TE111 this is the 6th HOM mode of the cavity signal [5, 6]. This method, however, requires the fabrication of an additional monitoring system with electronics. Therefore, we proposed a simple new experimental methodology to estimate the electrical center of a cavity by using an orbit corrector magnet to adjust the trajectory inside the cavity and a screen monitor installed in the downstream of the cavity. When the beam does not pass through the electrical center of the cavity, the beam is kicked by the radial electric field, and the position of the kicked beam after the cavity (X_c and Y_c), which is measured on the screen monitor, depends on the phase of the RF field (φ), because it changes the strength of the radial electric field. On the other hand, when the beam passes through the center of the cavity, the beam position is not changed even though the phase of the RF field varies, because the radial electric field is zero at the electromagnetic center of the cavity. This means that the value of $dX_c/d\varphi$ for the horizontal direction and $dY_c/d\varphi$ for the vertical direction is zero. Thus, in our new method, the beam trajectory passing through the electrical center of the cavity is extrapolated by measuring the values of $dX_c/d\varphi$ and $dY_c/d\varphi$.



Figure 1: Photograph of a DC gun and cryomodule for injector cavities in a compact ERL injector.

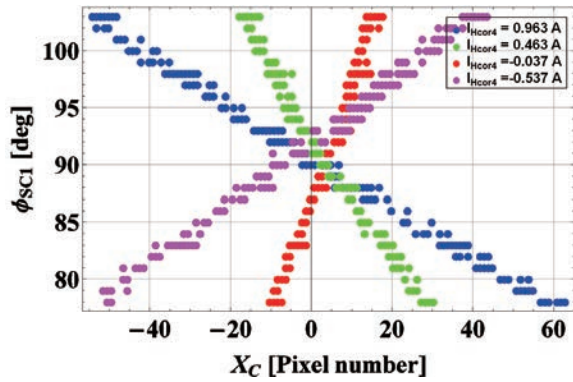


Figure 2: Measurement of $dX_C/d\phi$ for the horizontal direction with various strengths of corrector magnet (I_{Hcor4}) to estimate the electromagnetic center of an injector cavity.

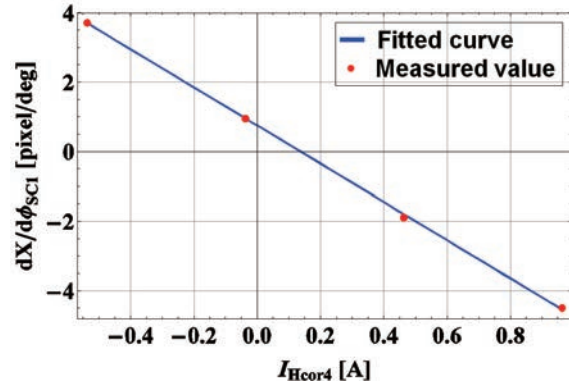


Figure 3: By measuring $dX_C/d\phi$ with various strengths of the corrector magnet, the strength of the corrector magnet for passing the beam through the electromagnetic center of the cavity was estimated to be 0.136 A.

Table 1: Measured normalized transverse emittance with various beam offsets.

Δx (mm)	Δy (mm)	ϵ_{nx} (mm-mrad)	ϵ_{ny} (mm-mrad)
-12.4	0	1.070 ± 0.0533	0.970 ± 0.0337
0	0	0.212 ± 0.0064	0.259 ± 0.0229
0	-4.55	0.243 ± 0.0057	0.497 ± 0.0373
0	-9.10	0.240 ± 0.0151	0.665 ± 0.105

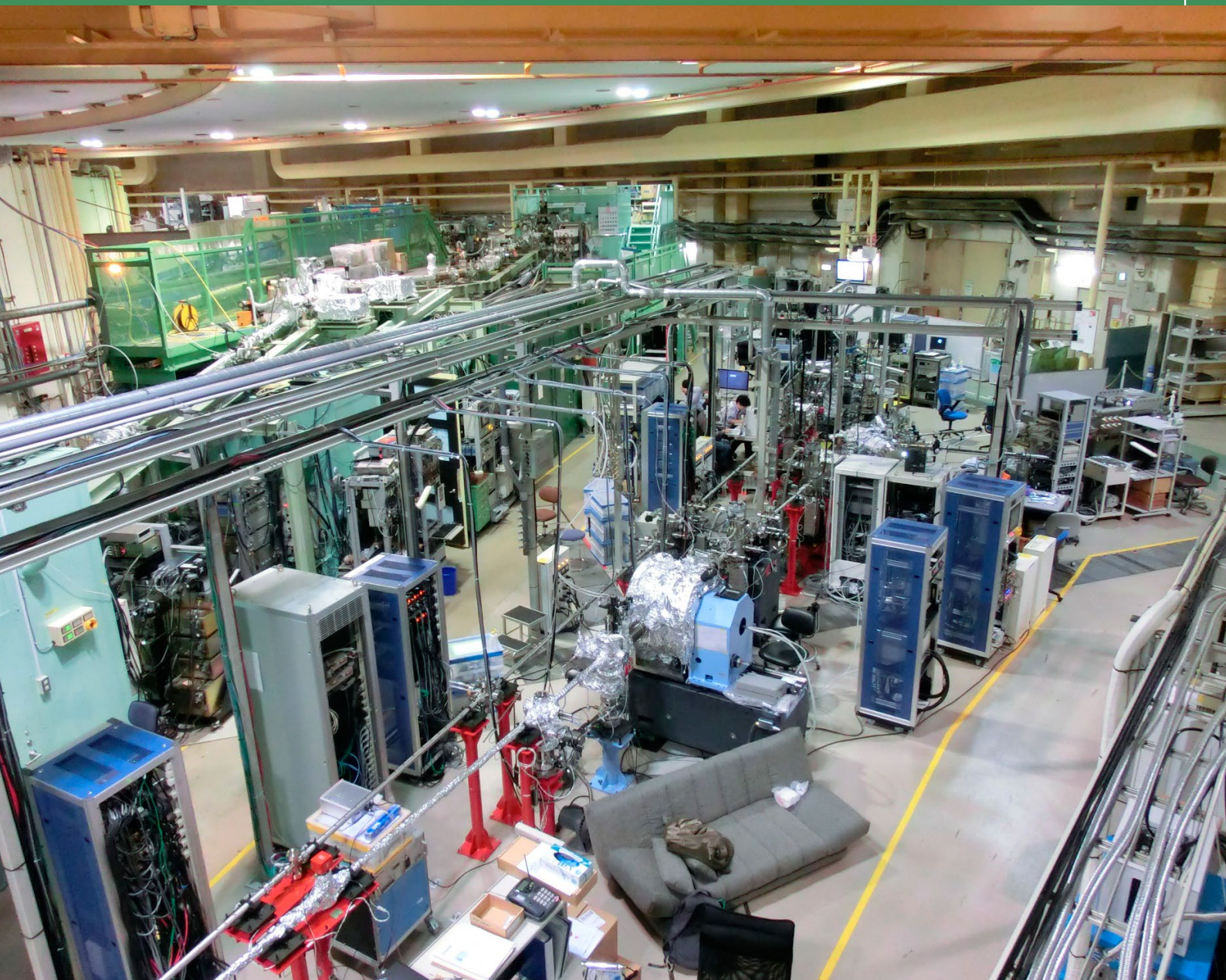
In order to verify the method, $dX_C/d\phi$ and $dY_C/d\phi$ were measured as a function of the orbit corrector magnet, which was used to adjust the trajectory inside the cavity. As shown in Fig. 2, the values of $dX_C/d\phi$ were measured with different strengths of the corrector magnet, and the strength of the horizontal corrector magnet (I_{Hcor4}) for passing the beam through the electrical center of the cavity was estimated to be 0.136 A by fitting the measured $dX_C/d\phi$ values as shown in Fig. 3. Based on this result, the normalized transverse emittance was measured as a function of the beam offset inside the cavity, because the transverse emittance is minimized when the beam passes through the center of the cavity. As shown in Table 1, the electrical center gives the minimum emittance growth due to the cavity. Using our method, we succeeded in minimizing the transverse emittance growth due to the radial electric field of the cavity.

REFERENCES

- [1] "Energy Recovery Linac Conceptual Design Report", KEK Report 2012-4, KEK, October, 2012; <http://ccdb5fs.kek.jp/tiff/2012/1224/1224004.pdf>
- [2] S. Sakanaka, et al., *Proceedings of ERL-2013 Workshop*, Novosibirsk, Russia, WG102 (2013).
- [3] N. Nishimori, R. Nagai, S. Matsuba, R. Hajima, M. Yamamoto, T. Miyajima, Y. Honda, H. Iijima, M. Kuriki and M. Kuwahara, *Appl. Phys. Lett.* **102**, 234103 (2013).
- [4] J.-G. Hwang, E.-S. Kim, T. Miyajima, Y. Honda, K. Harada, M. Shimada, R. Takai, T. Kume, S. Nagahashi, T. Obina, N. Nakamura, S. Sakanaka, R. Hajima, R. Nagai, N. Nishimori, M. Yamamoto, T. Uchiyama, E. Kako, S. Michizono and T. Miura, *Nucl. Instrum. Methods Phys. Res. Sect.* **753**, 97 (2014).
- [5] P. Zhang, N. Baboi, R.M. Jones and N. Eddy, *J. of Instrumentation* **7**, P11016 (2012).
- [6] H. Hayano, *Proceedings of IPAC 2010*, Tokyo, Japan, THXRA02 (2010).

Ji-Gwang Hwang¹, Eun-San Kim¹ and T. Miyajima²
 (¹Kyungpook National Univ. ²KEK-PF)

Experimental Facilities



Experimental Facilities

1. Newly Developed Experimental Facilities	67
1-1 Overview	
1-2 BL-15A, Dedicated to Semi-Microbeam XAFS/XRF/XRD and High-Brilliance SAXS/GI-SAXS Studies	
1-3 Construction of New Wide-Energy Range VUV & SX Beamline BL-2 "MUSASHI"	
1-4 Construction of BL-13B, Optics for Photoelectron Spectroscopy	
1-5 Upgrade of PF SAXS Beamlines: Replacement of the Experimental Stage and the Detector at BL-6A, and Refurbishment of BL-10C	
1-6 Replacement of Main Optional Components of the Wide-Range Soft X-Ray Spectroscopy Station BL-11A	
1-7 Reconstruction of BL-20B for X-Ray Topography and Related X-Ray Diffraction Experiments	
1-8 Upgrading of the BL-6C	
2. Structural Biology Research Center	75
2-1 Overview	
2-2 Leading the National Project for Structural Life Science - PDIS Starting from FY2012	
2-3 Research Progresses under Several External Grants	
3. Condensed Matter Research Center	78
3-1 Overview	
3-2 CMRC Projects	
4. Slow Positron Facility	81
4-1 Overview	
4-2 Projects	
5. IMSS Instrument R&D Team	83
5-1 X-Ray Imaging Using Synchrotron Radiation for Studies on Hierarchic Structure and Dynamics in Materials	
5-2 Ultra-Fast Signal Processing System for a Si-APD Array X-Ray Detector	
5-3 Auger-Electron Detector System for Depth-Resolved X-Ray Magnetic Circular Dichroism (XMCD)	
6. Summary of Experimental Stations	84

1

Newly Developed Experimental Facilities

1-1 Overview

The Photon Factory (PF) is a pioneering light source providing bright X-rays and outstanding user support. The PF produces extremely bright X-rays as a resource for researchers to study materials at the atomic and molecular level. Research at the PF also benefits many sectors of innovation in Japan and leads to major advances in energy production, environmental remediation, nanotechnology, new materials and medicine. The PF provides unique educational experience and serves as a vital training ground for future generations of scientists and engineers.

The PF has been carrying out a beamline refurbishment program since 2006, in which the main strategy is to concentrate investments on insertion-device (ID) beamlines as reported in previous activity reports [1-3]. With the upgrade of the 2.5-GeV PF ring for extending straight sections, the long and medium straight sections have been lengthened so that state-of-the-art insertion devices can be installed to cover the vacuum ultraviolet and soft X-ray regions. Four new straight sections have been newly produced for allowing the installation of short-period and small-gap undulators (SGU) to supply well-focused hard X-rays (HX). We have already constructed three HX beamlines at the short straight sections: BL-3 for materials science, and BL-1 and 17 for macromolecular crystallography. As the last straight section, we are commissioning a new beamline for both small-angle X-ray scattering (SAXS/GI-SAXS) and X-ray spectroscopy (XAFS/XRF/XRD) at BL-15. The details are described below.

BL-2 was the first undulator-based vacuum ultraviolet/soft X-ray (VSX) beamline constructed in the early 1980s, and has been operating for over 25 years. The BL-2 undulator is 3.6-m long, while the length of the straight section is 9 m after the PF upgrade in 2005. A new tandem undulator with 16-cm period was installed in 2014 in collaboration with Hitachi, Ltd. The new beamline optics consist of a grazing-incidence grating monochromator and a double-crystal monochromator, and will supply VUV and soft X-rays in 30–4000 eV. BL-13, 16, and 28 were originally constructed for sharing the photon beam between VSX and HX users by operating the insertion device in the undulator and multipole wiggler mode. Among the three beamlines, BL-28 was renewed first in 2006 as a high-performance spectroscopic beamline dedicated to photoelectron spectroscopy in the VSX region. BL-16 was completely upgraded as a soft X-ray spectroscopic beamline with fast polarization switching capabilities. Two tandem APPLE-II type undulators are installed to generate different

polarizations such as right- and left-hand circular polarizations, and the polarization is switched by modulating the electron orbit through the undulators. BL-13 was recently reconstructed as a VSX spectroscopic beamline for studying organic thin films adsorbed on well-defined surfaces using angle-resolved photoelectron spectroscopy and X-ray absorption spectroscopy. The detailed performance is described below.

In addition to the upgrade of the ID beamlines, competent bending-magnet stations are also being upgraded for supporting active users. The current status of SAXS stations at BL-6A and BL-10C, soft X-ray spectroscopy station at BL-11A, and X-ray topography and related X-ray diffraction station at BL-20B are also described in this section.

REFERENCES

- [1] *Photon Factory Activity Report 2010 #28*, (2012).
- [2] *Photon Factory Activity Report 2011 #29*, (2013).
- [3] *Photon Factory Activity Report 2012 #30*, (2014).

1-2 BL-15A, Dedicated to Semi-Microbeam XAFS/XRF/XRD and High-Brilliance SAXS/GI-SAXS Studies

As reported previously [1], a new beamline, BL-15A, was completed at the BL-15 section of the PF ring in FY2013. This new beamline has a short-gap undulator which produces high-brilliance X-rays ranging from 2.1 keV to 15 keV. The beamline will be dedicated to both XAFS/XRF/XRD studies using semi-micro focus beams (A1 station) and SAXS/GI-SAXS experiments using collimated soft and hard X-rays (A2 station).

In the XAFS/XRF/XRD studies, the semi-micro focus beam available in a wide range of photon energies allows analyzing the local structures of the elements and valence of inhomogeneous samples in the fields of environmental science and new energy source science. The soft X-rays up to 2.1 keV will provide access to the absorption edges of phosphorus and sulfur, which are very important targets for those fields.

The SAXS scientific programs include structural studies of functional membranes, time-resolved X-ray scattering and large hierarchical structure analysis. All three programs require a high-brilliance light source. In particular, grazing-incidence SAXS (GI-SAXS) using vertically small-size soft X-rays ranging between 2.1–3.0 keV will help to control the depth of the membrane

structure analysis and reduce the roughness defects of an imperfect membrane.

Furthermore, the combination of XAFS/XRF and SAXS experiments yields wide structural information from fine atomic structures to low and medium resolution. It is beneficial to build these instruments as two stations (A1 and A2) on the same beamline. BL-15A is oriented toward joint advanced studies using the two techniques.

The old BL-15 beamlines were scrapped and new construction work started in the spring of 2013. The construction was completed in the summer shutdown of 2013 (Fig. 1) and the first undulator beam was introduced on October 17, 2013 (Fig. 2). We subsequently started tuning the optics, and the first beams into the A1 and A2 stations were delivered on November 7, 2013

and February 19, 2014, respectively. After the optics tuning, preliminary beamline characterizations were carried out. The FWHM beam sizes at three focal points, 32.8 m, 36.75 m and 42.75 m from the source, were $20\ \mu\text{m}$ (H) \times $21\ \mu\text{m}$ (V), $289\ \mu\text{m}$ (H) \times $36\ \mu\text{m}$ (V) and $651\ \mu\text{m}$ (H) \times $44\ \mu\text{m}$ (V), respectively. The undulator spectra and the photon flux were measured and the results are consistent with the ray-tracing simulation. These beam performances are promising for both research activities.

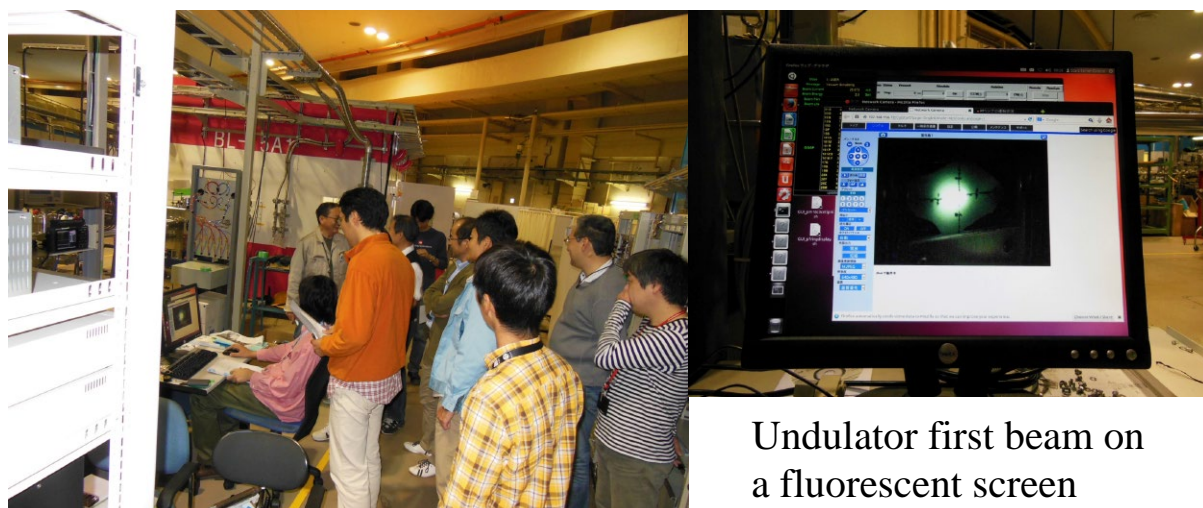
We will continue the optics tuning and commissioning experiments, and then start beamline operation for users in the autumn of 2014.

REFERENCE

- [1] *Photon Factory Activity Report 2012 #30*, A 73 (2013)



Figure 1: Bird's-eye view of the BL-15A.



Undulator first beam on a fluorescent screen

Figure 2: First beam introduction on October 17, 2013.

1-3 Construction of New Wide-Energy Range VUV & SX Beamline BL-2 “MUSASHI”

The new beamline BL-2 (MUSASHI: Multiple Undulator beamline for Spectroscopic Analysis on Surface and Hetero Interface) is designed for wide-energy-range spectroscopic analysis including X-ray photoelectron spectroscopy, angle-resolved photoemission spectroscopy, and X-ray absorption spectroscopy. The conceptual scheme of the new BL-2 is shown in Fig. 3. The new BL-2 has two types of undulators in tandem alignment; one is designed for the vacuum ultraviolet (VUV) region (30–300 eV), and the other for the soft X-ray (SX) region (250–2000 eV). Consequently, light with a relatively wide energy range while maintaining high brilliance and high energy resolution will be available in this beamline by the combination of the two undulators and a variable-included-angle varied-line-spacing plane-grating monochromator (VLS-PGM). Moreover, in BL-

2B, an additional double-crystal monochromator (DXM) is built into this branch beamline to make the energy range of 2000–4000 eV available using the wiggler mode of the SX undulator.

In the summer of 2013, the old BL-2A and BL-2C beamlines were scrapped and the new BL-2A and BL-2B beamlines were constructed (Fig. 4). Figure 5 shows a photoabsorption spectrum of N_2 molecules obtained using the new beamline optics with SX undulator. The fitting result by Voigt functions, Gaussian width of 31 meV with the Lorentzian width of 117 meV, indicates that the SX optics of the new BL-2 beamline achieve a resolving power of more than 13,000, which is much better than that of the old BL-2C beamline [1].

The installation of the new VUV undulator and the operation of VUV optics will start in the spring of 2014, and the completed version of the beamline will be opened for users in FY2015.

REFERENCE

- [1] M. Watanabe, A. Toyoshima, Y. Azuma, T. Hayaishi, Y. Yan and A. Yagishita, *Proc. SPIE*, **58**, 3150 (1997).

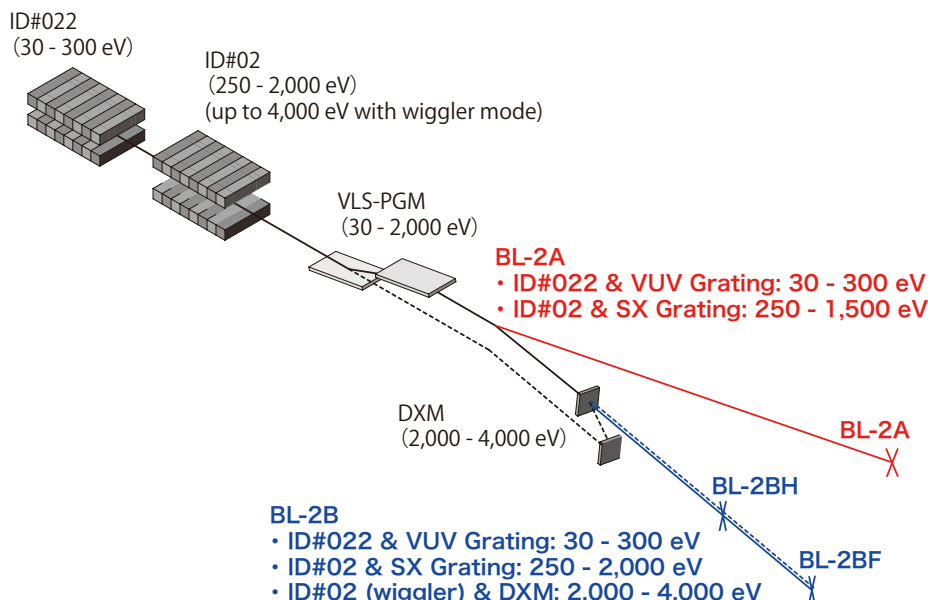


Figure 3: The conceptual scheme of the new BL-2 beamline.

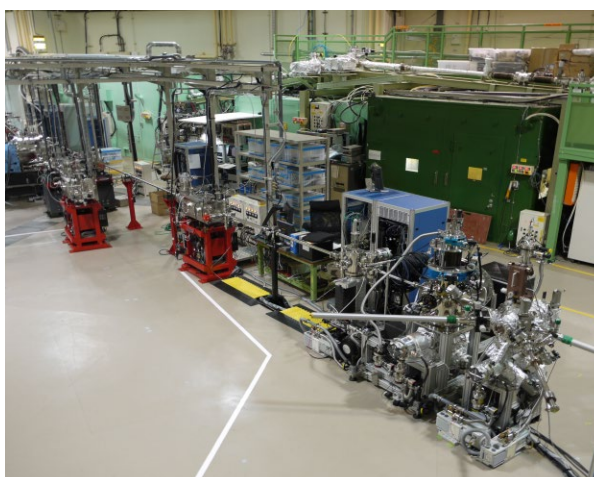


Figure 4: Photograph of the constructed BL-2A and BL-2B beamlines.

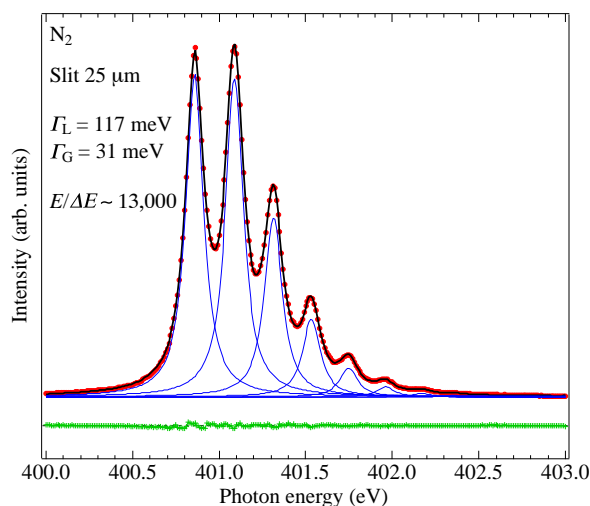


Figure 5: Photoabsorption spectrum of N_2 molecules.

1-4 Construction of BL13B, Optics for Photoelectron Spectroscopy

Optics for photoelectron spectroscopy for the study of surface chemistry (BL-13B) was opened for users in October, 2013. A typical photon intensity and photon energy resolution ($E/\Delta E$) of BL-13B are shown in Fig. 6. Carbon contamination on the Au-coated plane mirror (Mp) for suppressing higher harmonics was removed by using oxygen activated by non-monochromatized synchrotron radiation (SR) [1] as shown in Fig. 7. Since the removal of the carbon contamination, the photon intensity in the carbon K-edge region is improved while the change in intensity in the oxygen K-edge region is negligible.

REFERENCE

- [1] A. Toyoshima, T. Kikuchi, H. Tanaka, J. Adachi, K. Mase and K. Amemiya, *J. Synchrotron Rad.* **19**, 722 (2012).

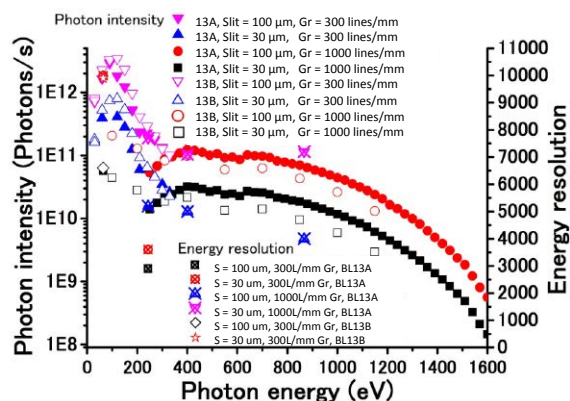


Figure 6: Typical photon intensity and photon energy resolution ($E/\Delta E$) of BL-13A and BL-13B in the photon energy region of 30–1600 eV.

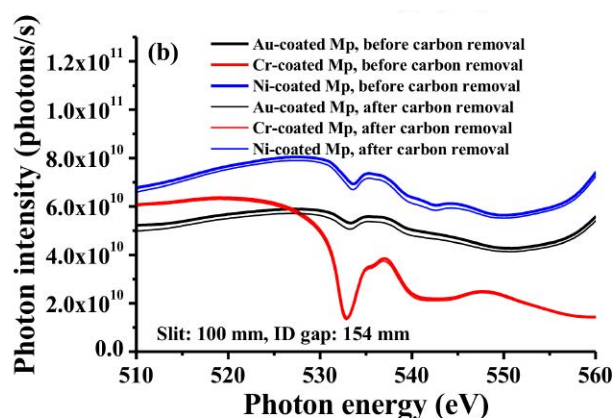
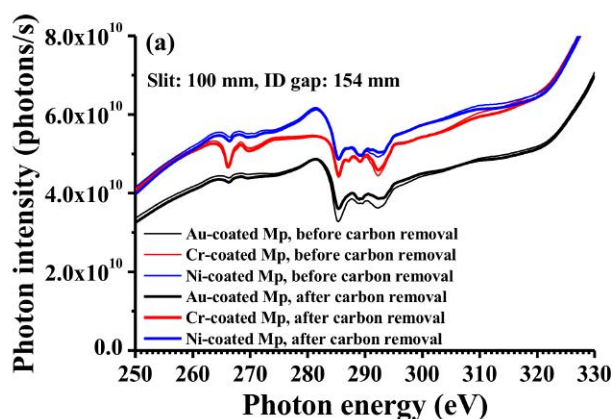


Figure 7: Photon intensity spectra of BL-13B in the (a) carbon and (b) oxygen K-edge regions measured with the 1000-lines/mm grating before and after in situ non-monochromatized-SR-activated oxygen cleaning of the Au-coated Mp.

1-5 Upgrade of PF SAXS Beamlines: Replacement of the Experimental Stage and the Detector at BL-6A, and Refurbishment of BL-10C

BL-6A is a small-angle X-ray scattering (SAXS) beamline for mainly the structural study of hard and soft materials. In BL-6A, the experimental stage and the SAXS detector were replaced in fiscal 2013 in order to improve the user operability and the detectable angle range (Fig. 8). The camera length can be changed semi-automatically from 0.25 to 2.5 m in this stage. The hybrid pixel detector, PILATUS 300K, had been used at BL-6A. However, its detectable area of $83.8 \times 106.5 \text{ mm}^2$ was narrow in order to enable structural analysis with large spatial resolution. PILATUS3 1M was newly installed as a SAXS detector, thus enabling measurement over a broad range of angle in combination with a WAXS detector, PILATUS 100K, since its area of $168.7 \times 179.4 \text{ mm}^2$ is sufficiently larger than that of the 300K. We also installed a downstream shutter (DSS) in BL-6A to improve the safety of BL-6A and BL-6C.

BL-10C is also a SAXS beamline and is one of the oldest beamlines at the Photon Factory. Therefore, in order to renew the optical components and the measurement system, scrap-and-rebuild of BL-10C was performed in fiscal 2013. The experimental hutch was enlarged in the summer of 2013 to prepare for the installation of the longer experimental stage. All other reconstruction work was conducted in March 2014. All the components from the end of the main hutch to the experimental hutch were removed first, then the main

components, the fixed-exit double-crystal monochromator, a two-dimensional focusing mirror (bent cylinder mirror), a long experimental stage, WAXD (Wide-angle X-ray diffraction) chambers and two hybrid pixel detectors, PILATUS3 2M for SAXS and 200K for WAXD, were newly installed in BL-10C (Fig. 9). As a result of these upgrades, users will be able to change the measurement energy from 6 to 14 keV and to use a higher-brilliance beam by changing the focusing ratio. The maximum camera length is extended from 2 m to 3 m in this experimental stage, and PILATUS3 2M

with a large area and high-speed readout will help to perform high-throughput structural analysis with a large spatial resolution. The simultaneous SAXS(GI-SAXS)/WAXD measurement system was newly constructed in BL-10C. In order to improve beamline safety, we also replaced the old electric wirings and distribution boards which had been used for over 30 years with new ones. A chain block and a cable ladder were also installed in the experimental hutch. The user time will restart from the end of May 2014 after commissioning.



Figure 8: New experimental stage and detector, PILATUS3 1M at BL-6A.

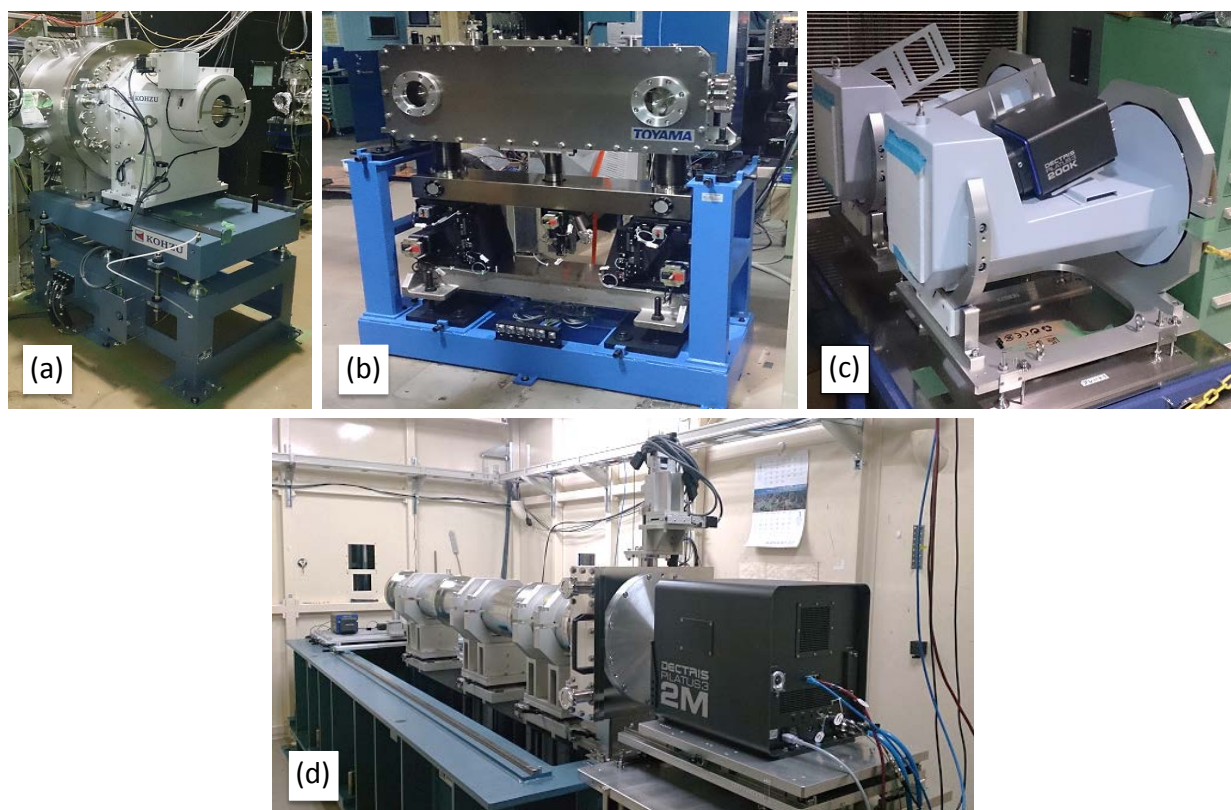


Figure 9: New beamline components at BL-10C. (a) A water-cooled fixed-exit Si(111) double-crystal monochromator. (b) A 1000-mm 2D-focusing mirror and a mirror bender. This mirror is coated with rhodium on the silicon substrate with a cylinder shape, and bent to focus the beam at the detector position with this bender. (c) Two kinds of chambers for WAXD experiments. One is for SAXS/WAXD, and the other is for GI-SAXS/WAXD. PILATUS3 200K can be exclusively installed in these chambers. (d) A new long experimental stage and a new PILATUS3 2M detector. Users can use the camera lengths of 0.25, 0.5, 1.0, 2.0 and 3.0 m, and change to these lengths semi-automatically.

1-6 Replacement of Main Optical Components of the Wide-Range Soft X-Ray Spectroscopy Station BL-11A

BL-11A provides soft X-rays in the energy range between 70 eV and 1900 eV with a grazing-incidence monochromator from a bending-magnet source, where all of the beamline components were reconstructed in 1996 [1-3]. After being used for 18 years, it was decided to replace the main part of the beamline optics to improve the performance. The purpose of this modification is to attain higher flux in the energy region higher than 1 keV and to provide a stable beam. To achieve this, the incident angle to the focusing mirrors (M0', M1 and

Mf) is changed from 2 degrees to 1 degree, except for the first mirror M0 in the shield wall, and a water-cooling system for the gratings is introduced. All the components have been set on the optical path and commissioning will start in May 2014. Details of the beamline optics and progress of the commissioning will be posted on the beamline website (http://pfwww.kek.jp/sxspec/sx/bl11a_e.html) together with the previous performance.

REFERENCES

- [1] K. Amemiya, Y. Kitajima, T. Ohta and K. Ito, *J. Synchrotron Rad.* **3**, 282 (1996).
- [2] Y. Kitajima, K. Amemiya, Y. Yonamoto, T. Ohta, T. Kikuchi, T. Kosuge, A. Toyoshima and K. Ito, *J. Synchrotron Rad.* **5**, 729 (1998).
- [3] Y. Kitajima, Y. Yonamoto, K. Amemiya, H. Tsukabayashi, T. Ohta and K. Ito, *J. Elec. Spectrosc. Relat. Phenom.* **927**, 101 (1999).

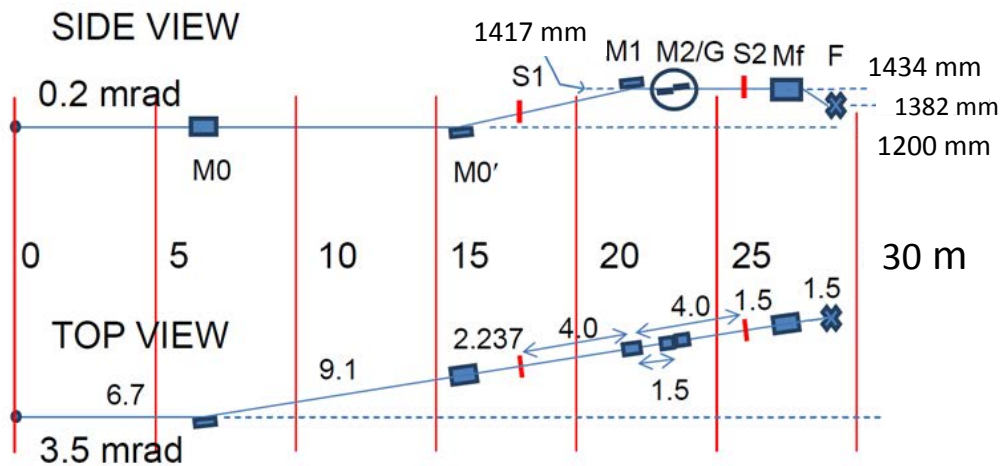


Figure 10: Schematic layout of BL-11A. Only M0 is left as before; the other components have been replaced.

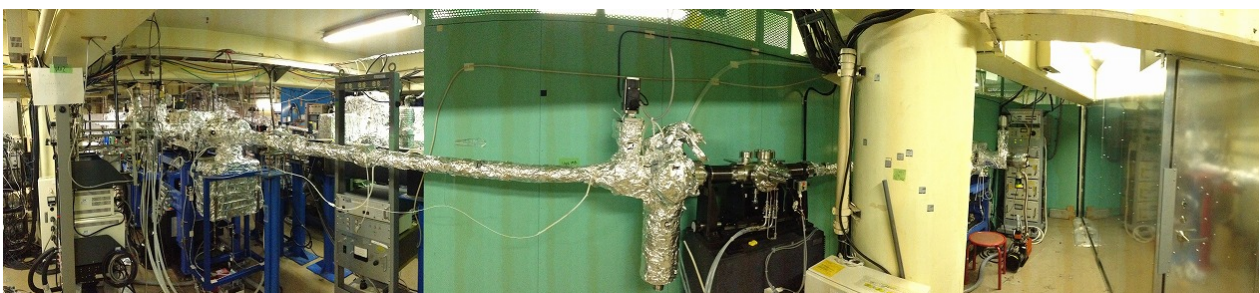


Figure 11: Photograph of M0', S1, M1 and M2/G chamber (from right to left).

1-7 Reconstruction of BL-20B for X-Ray Topography and Related X-Ray Diffraction Experiments

BL-20B, which was the former Australian beamline, had been reconstructed for X-ray diffraction topography and related X-ray diffraction experiments with SR from bending magnets. The Australian activity at BL-20B ceased at the end of February 2013. X-ray topography and related activities at the former BL-15B and 15C were transferred to the new BL-20B. Figure 12 shows a plan view of the beamline structure after the reconstruction. The main modified parts are as follows.

1. The cam-type double-crystal monochromator which was used at the old BL-6C was installed instead of the channel-cut monochromator system. The monochromator crystals have also been changed from CZ-Si (111) to FZ-Si (111).

2. All auxiliary vacuum pumps for turbo-molecular pumps were changed from oil rotary pumps to oil-free scroll pumps to prevent carbon contamination for the monochromator crystal.
3. A white SR beam is practically available with safety.
4. A γ -ray mask with water-cooled mask and one γ -ray stopper were additionally installed to strengthen safety for γ -rays.

The topography goniometer with vertical rotation axis for the former BL-15B and the topography goniometer with horizontal rotation axis for the former BL-15C were moved to the new BL-20B. The equivalent control system of the old BL-15C was employed for the beamline. The horizontal acceptance angle of SR is 1.6 mrad in spite of the designed value of 2.0 mrad. This seems to be caused by the difference of the actual SR axis and the designed axis.

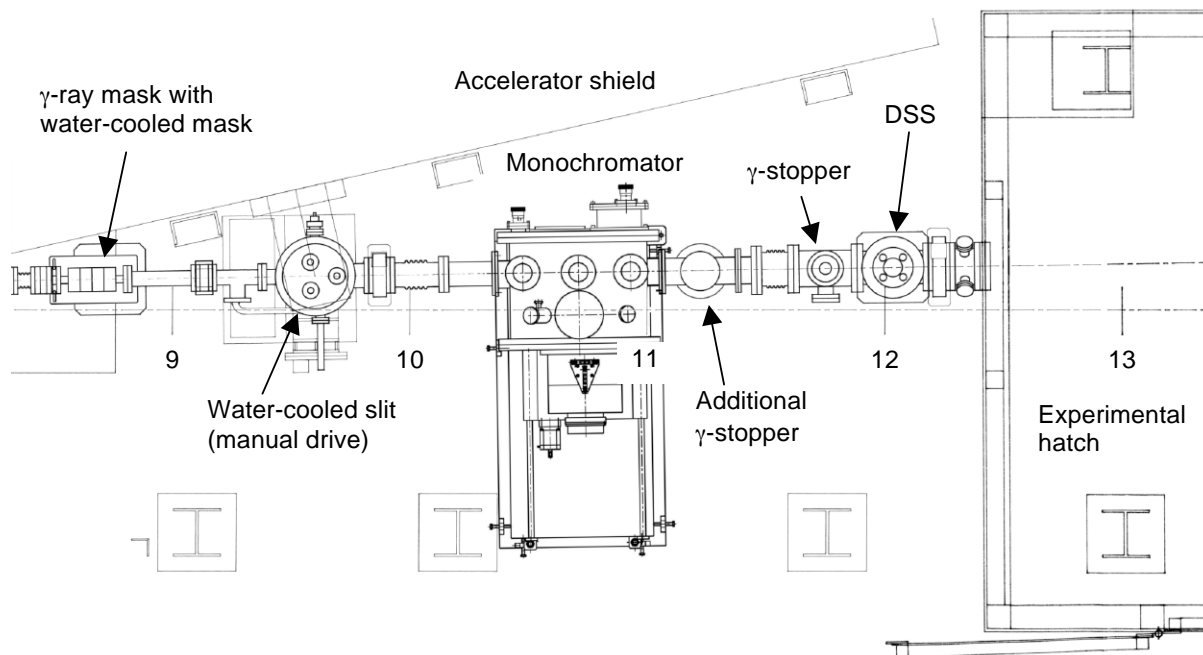


Figure 12: Plan view of the new BL-20B. The scale shows the distance from the light source along the BL-20A axis.

1-8 Upgrading of the BL-6C

BL-6C had been constructed as a double focusing X-ray beamline by means of a double-crystal X-ray monochromator and cylindrical bent X-ray mirror systems and used for almost ten years. The various scientific activities on material science used the beamline by means of resonant X-ray magnetic and non-magnetic Bragg scattering, X-ray MCD, X-ray fluorescent holography techniques, surface diffraction, and strain measurement systems. However, one of the problems was the limitation of relatively low energy usage for the focused X-ray beam because of the cut-off energy of the focusing mirror (~13 keV). The focusing mirror was located just upstream of the experimental hutch of BL-6C for geometrical reasons based on the interference of other beamlines.

In 2013, BL-15 was reconstructed based on the short-period undulator line, and the X-ray monochromator of the old BL-15C could be used for the present reconstruction of BL-6C. Figure 13 shows the plan views of the reconstruction. The upper and lower drawings

correspond to the new and old BL-6C, respectively. The mirror was located at 23.1 m from the light source before the reconstruction. After the reconstruction, the X-ray monochromator can be located beside the experimental hutch of BL-6A and the mirror can be shifted to the upstream of the beamline at the position of 19 m from the light source. Thus, the cut-off energy of the mirror can be increased up to about 20 keV.

The reconstruction was done during fiscal 2013. Figure 14 shows a photograph of the movement of the X-ray mirror. The focusing test of the beamline was successfully done in May 2014 and the FWHMs of the focused beam size are 0.5 mm (horizontal) and 0.3 mm (vertical), respectively. Figure 15 shows the energy spectra of the focused beam before and after reconstruction. It is possible for general users to use almost up to 19–20 keV monochromatic X-rays, enabling various atomic species such as Y, Zr, Nb, Mo and Ru to be examined by X-ray fluorescent holography and also resonant X-ray scattering techniques. Scientific results will emerge next fiscal year.

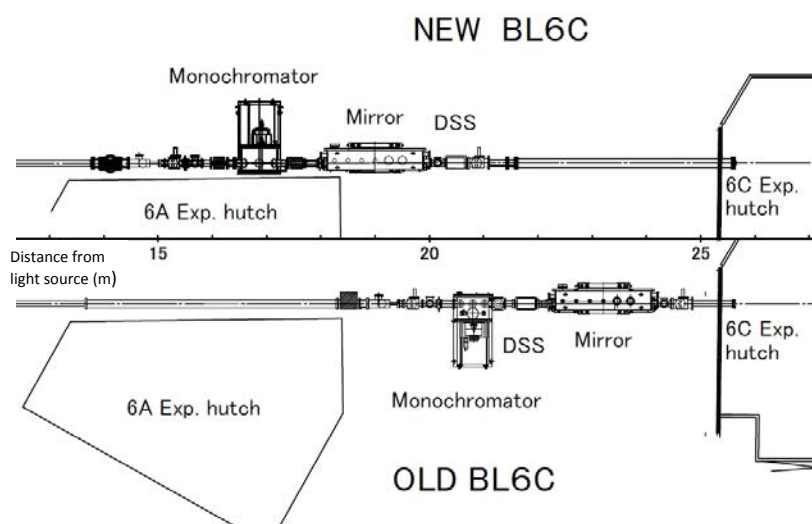


Figure 13: Plan views of the reconstruction. The upper and lower drawings correspond to the new and old BL-6C, respectively. The energy spectrum of the focused X-ray beam before (after) the reconstruction. It will be possible to use X-ray energy of up to 19 keV after the reconstruction.



Figure 14: Photograph of the movement of the X-ray mirror.

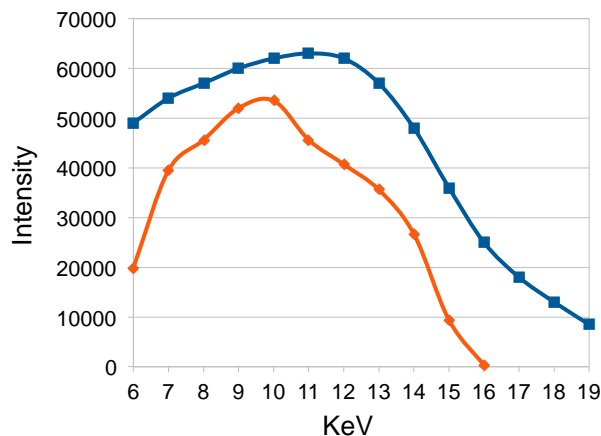


Figure 15: Energy spectra of the focused beam before and after reconstruction. The red (blue) line corresponds to the energy spectrum of the focused X-ray beam before (after) the reconstruction. It will be possible to use X-ray energy of up to 19 keV after the reconstruction.

2

Structural Biology Research Center

2-1 Overview

The Structural Biology Research Center (SBRC) was established in May 2000 at the Photon Factory (PF) located in the Institute of Material Structure Science (IMSS). The main tasks of the Center are to provide user support for X-ray synchrotron radiation studies of bio-macromolecules, encourage advanced technical development, and boost in-house structural biology research. The Center has approximately 40 members, including one professor (Dr. T. Senda), six associate professors (Drs. R. Kato, N. Igarashi, M. Kawasaki, N. Shimizu, N. Matsugaki, and F. Yumoto), and three assistant professors (Drs. Y. Yamada, N. Adachi, and M. Senda) as core members (Fig. 1). About half of the SBRC members are engaged in beamline operation and development. X-ray crystallography activities are carried out under the leadership of Drs. Matsugaki and Yamada. Drs. Shimizu and Igarashi are responsible for small-angle X-ray scattering (SAXS). In 2013, Dr. L. M. Chavas, who had contributed to the PX beamlines of the PF, moved to CFEL of DESY as a project leader.

The structural biology building was built in April 2001 (430 m²), and its area was later almost doubled to 765 m² (Fig. 2). About half of the SBRC members are involved in structural biology research in this building. All necessary structural biology experiments can be carried out in this laboratory. It has cell culture systems (bacteria, insect, and mammalian cells), liquid chromatography systems, a fully automated crystallization system, and equipment for physicochemical analyses such as Bi-

acore, dynamic light scattering, mass-spectroscopy and SEC-MALS. In-house biological research is carried out under the leadership of Drs. Senda, Kato, Kawasaki, and Adachi.

The SBRC has constructed five beamlines for protein crystallography: BL-1A, BL-5A, BL-17A, PF-AR NW12, and PF-AR NE3A. BL-5A was constructed using “Special Coordination Funds for Promoting Science and Technology” (FY2001–FY2003) from the Japan Science and Technology (JST) Agency. During the “Development of System and Technology for Advanced Measurement and Analysis” project, we developed a micro-beam beamline, BL-17A. BL-1A was constructed in the “Targeted Proteins Research Program” by MEXT/JST (FY2007–FY2011), and was designed for sulfur-SAD experiments (see below).

Under the PF Program Advisory Committee (PAC) system, the SBRC accepts many researchers from outside KEK who wish to collect diffraction data for their own macromolecular crystals. The number of academic proposals and users has reached 100–120/year in recent years. As a result of advances in structure-based drug design, pharmaceutical companies require a large amount of beam time. Many Japanese companies have been using the bio-macromolecular crystallography beamlines of KEK-PF. The Tsukuba Consortium, which is composed of seven companies (four from another Pharmaceutical Consortium for Structure Analysis and three other companies), uses our beamlines. Among them, Astellas Pharma, Inc. financed the construction of the beamline AR-NE3A for their research.



Figure 1: Members of the Structural Biology Research Center (SBRC).



Figure 2: Structural Biology Research Center.

2-2 Leading the National Project for Structural Life Science – PDIS Starting from FY2012

The SBRC plays a key role in a national project for structural life science, the Platform for Drug Discovery, Informatics, and Structural Life Science (PDIS). The PDIS, which was launched with the support of MEXT in FY2012, is an open platform providing comprehensive support for life-science researchers. The support includes protein production, bioinformatics, 3D-structure analysis, compound-library screening, etc. The PDIS is composed of three platforms: platforms of structural life science, drug discovery, and informatics. The SBRC is the head of the platform of structural life science. We plan to develop beamlines for protein crystallography and bio-SAXS and will provide services for researchers in biology fields to accelerate studies in structural life science. The SBRC also provides a high-throughput crystallization service using an automated crystallization and observation robot (PXS). In PDIS, the SBRC has accepted approximately 25 projects, and supports research ranging from crystallization to structure determination by X-ray crystallography; five crystal structures were determined in 2013. In addition, the SBRC has studied the sulfur-SAD method using low-energy X-rays, and has already succeeded in determining the crystal structures of some proteins by this method. In addition to the sulfur-SAD, BL-1A can be used to identify calcium ions in proteins. Prof. Miki's group in Kyoto University used BL-1A to identify calcium ions in the supramolecular complex between the photosynthetic reaction center and the light-harvesting antenna core [1]. They collected diffraction data of the supramolecular complex using two different wavelengths, 2.70Å and 3.15Å, and clearly showed the calcium ions bound to the supramolecular complex (Fig. 3).

2-3 Research Progresses under Several External Grants

In addition to the PDIS, the SBRC has obtained several external grants, such as CREST and PRESTO from JST, "Key strategic research for the use of X-ray free-electron lasers" from MEXT, "Photon and Quantum Basic Research Coordinated Development Program" from MEXT, and KAKEN-HI from MEXT/JSPS. One of the main projects of SBRC is to study the structural biology of chromatin related protein complexes. We have succeeded in purifying several protein complexes involved in chromatin transcription from budding yeast. Physicochemical analyses of these complexes are in progress for their structural study. This project is supported by PRESTO and KAKEN-HI. The second project is a study of the structural biology of the CagA oncoprotein derived from *Helicobacter pylori*, which causes some stomach diseases including stomach cancer. While the crystal structure of the N-terminal region of CagA has already been determined [2], the C-terminal region of CagA is considered to be an intrinsically disordered region. Our structural and biochemical analysis revealed that this region adopts a lariat-like loop structure by interacting with the N-terminal structured region. We are investigating the structural nature of the lariat-like loop region using CD and SAXS. In addition, we are working to reveal the tertiary structure of the CagA-PAR1-SHP2 complex. These CagA researches are supported by CREST/JST. The third project is the structural analysis of the redox-dependent affinity control of the electron transfer complex, which is supported by the Photon and Quantum Basic Research Coordinated Development Program. The SBRC is studying the detailed molecular mechanisms underlying the redox-dependent affinity control between ferredoxin BphA3 and ferredoxin reductase BphA4 on the basis of their crystal structures under various redox states at high resolution.

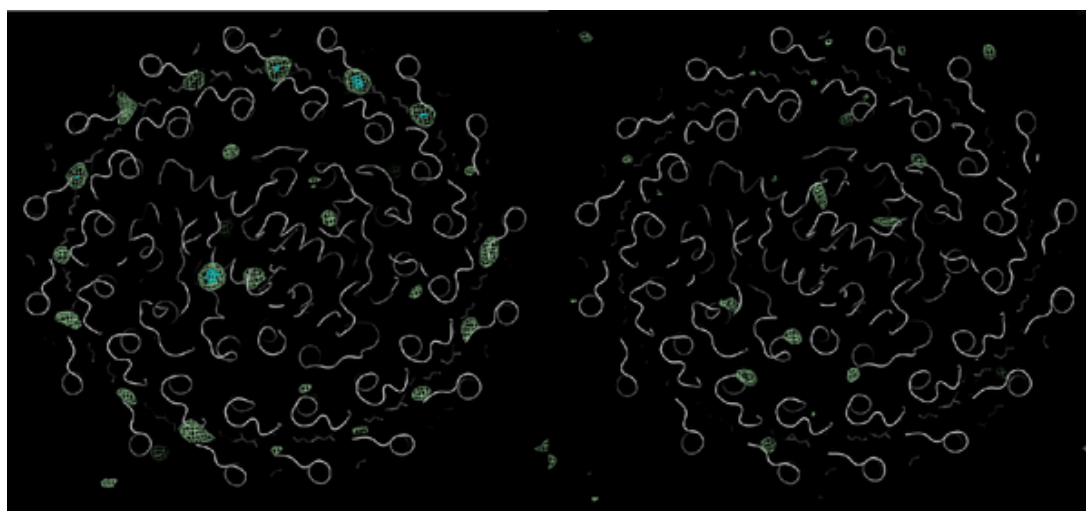


Figure 3: Determination of Ca^{2+} sites using long-wavelength X-rays in the supramolecular complex between the photosynthetic reaction center and the light-harvesting antenna core. Anomalous difference Fourier maps from datasets collected at 2.70 Å (left) and 3.15 Å (right), respectively. On the basis of these results, the positions of Ca^{2+} ions in the supramolecular complex were successfully determined. (Photo provided by Professor Kunio Miki, Graduate School of Science, Faculty of Science, Kyoto University)

In addition to these main projects, the SBRC has several other projects. In 2013, SBRC revealed the crystal structure of a reaction intermediate of an extradiol dioxygenase DesB. The crystal of the reaction intermediate was prepared under anaerobic conditions using an anaerobic chamber that was specially designed for anaerobic crystallization (Fig. 4). The crystal structure of DesB showed a large Fe ion shift in the catalytic reaction (Fig. 5). Biochemical studies revealed that this shift seemed to be related to the strict substrate specificity of this enzyme [3].

REFERENCES

- [1] S. Niwa, L.-J. Yu, K. Takeda, Y. Hirano, T. Kawakami, Z.-Y. Wang-Otomo and K. Miki, *Nature* **508**, 228 (2014).
- [2] T. Hayashi, M. Senda, H. Morohashi, H. Higashi, M. Horio, Y. Kashiba, L. Nagase, D. Sasaya, T. Shimizu, N. Venugopalan, H. Kumeta, N. N. Noda, F. Inagaki, T. Senda and M. Hatakeyama, *Cell Host & Microbe* **12**, 20 (2012).
- [3] K. Sugimoto, M. Senda, D. Kasai, M. Fukuda, E. Masai and T. Senda, *PLoS One* **9**, e92249 (2014).



Figure 4: Anaerobic chamber used to prepare crystals of reaction intermediates of DesB.

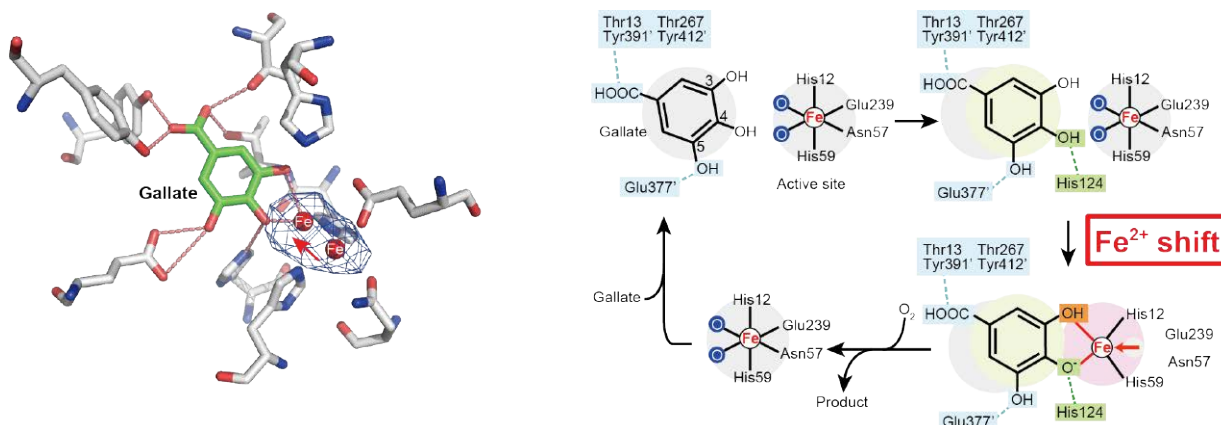


Figure 5: Active site of DesB (left) and its proposed catalytic reaction mechanism (right). In the catalytic reaction, the Fe^{2+} ion in the active site shifts by approximately 2 Å. In the left panel gallate (substrate) and Fe^{2+} ion are shown in green and red, respectively. This Fe^{2+} shift is critical to the catalytic reaction of DesB and contributes to the strict substrate specificity of this enzyme.

3

Condensed Matter Research Center

3-1 Overview

The Condensed Matter Research Center (CMRC) was established on April 1, 2009, in the Institute of Materials Structure Science (IMSS), KEK. The objective of the CMRC is to pursue cutting-edge research on condensed matter science through the comprehensive use of multi-probes supplied by the IMSS, such as synchrotron light, neutrons, muons, and slow positrons. The CMRC has four research groups: the correlated electron matter group, the surface/interface group, the matter under extreme conditions group, and the soft matter group. The members of these groups work closely with researchers at various universities and institutes around the world.

Through collaboration among these groups we are conducting nine bottom-up projects: 1. Hybridized Orbital Ordering, 2. Geometrical Correlation, 3. Molecular Crystals, 4. Oxide Hetero-structures, 5. Surface/interface Magnetism, 6. Extreme Conditions, 7. Soft Matter, 8. Hydrogen, and 9. Surface Structure and Electronic States. In addition, the CMRC is conducting two types of MEXT project: the Element Strategy Initiative to Form a Core Research Center, and the Photon and Quantum Basic Research Coordinated Development Program. In these national projects, the CMRC members are focusing on the Element Strategy Initiative for Electronic and Magnetic Materials, and Tribology with Muons and Neutrons.

(URL of CMRC: <http://cmrc.kek.jp>)

3-2 CMRC Projects

Hybridized Orbital Ordering Project [1-3]

Strong correlation among orbital, charge, and spin degrees of freedom often plays important roles in strongly correlated electron systems. The study of these electronic ordering states is essential to microscopically understand the phenomena in the systems. Resonant X-ray scattering (RXS) at the K -edge is a powerful tool for observing the spatial ordering of charge and orbital degrees of freedom in $3d$ transition metal oxides. The RXS signal at the K -edge ($1s \rightarrow 4p$ transition energy) reflects the $4p$ electronic state. On the other hand, the RXS signal at the $L_{2,3}$ -edge ($2p \rightarrow 3d$ transition energy) can probe the $3d$ electronic state directly. Moreover, signals at the K -edges of O, S, and P ions, which play a key role for the itinerancy through the orbital hybridization with the metal ion, are observable by using soft X-ray. In this project we have developed new diffractometers for resonant soft X-ray scattering depending on the experimental conditions.

Geometrical Correlation Project [4]

Geometrical frustration in the electronic degrees of freedom such as spin, charge, and orbital, which is often realized with highly symmetric crystals, has been one of the major topics in the field of condensed matter physics. The objective of this project is to determine a characteristic correlation time for fluctuations in itinerant

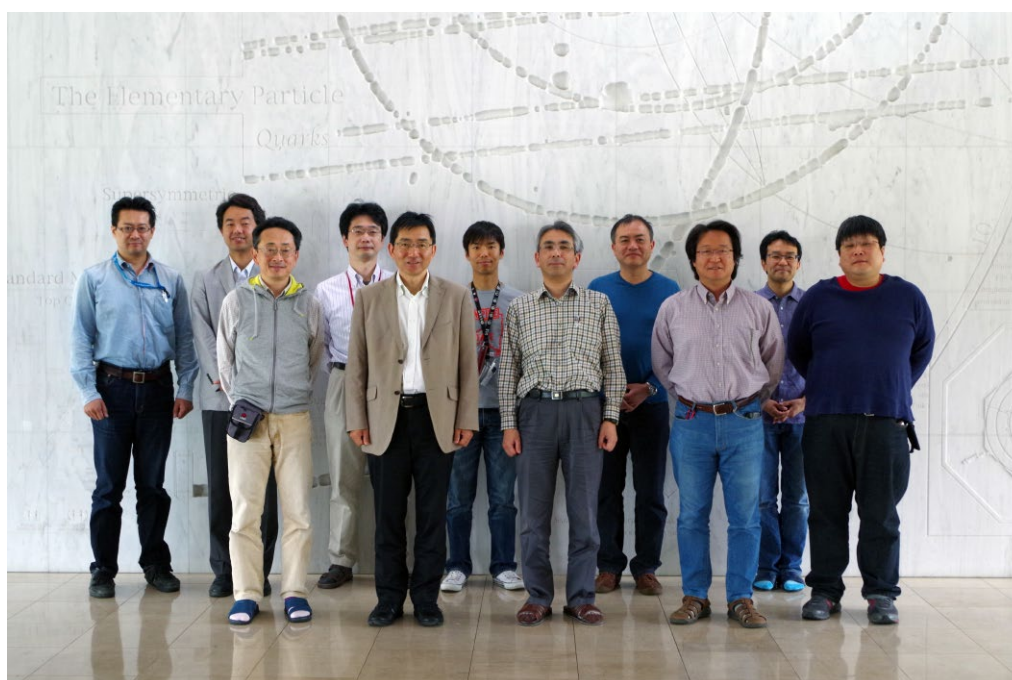


Figure 1: Project leaders of the Condensed Matter Research Center (CMRC).

systems with strong electron correlation under the influence of geometrical frustration using muons, neutrons, and synchrotron X-rays, which have different probing-time scales.

Molecular Crystals Project [5]

The electronic correlation in molecular crystal systems is being investigated to elucidate novel phenomena such as superconductivity and charge ordering. One topic in this project is the observation of a charge-cluster glass state in an organic conductor with triangular lattice. A combination of time-resolved transport measurements and X-ray diffraction revealed that the charge-liquid phase has two-dimensional charge clusters that fluctuate extremely slowly and heterogeneously.

Oxide Hetero-structures Project

The goal of this project is to design novel physical properties appearing at the heterointerface of strongly correlated oxides. The physical properties arise from strong mutual coupling among the spin, charge, and orbital degrees of freedom in the interface region between two different oxides. In order to control such properties, it is necessary to clarify the interfacial electronic, magnetic, and orbital structures. We are therefore using synchrotron radiation spectroscopic techniques having elemental selectivity to probe these structures in the nm-scale at the oxide heterointerface. For example, the electronic structure at the interface is determined by photoemission spectroscopy and X-ray absorption spectroscopy, the magnetic structure by magnetic circular dichroism of XAS, and the orbital structure by linear dichroism of XAS. We aim to design and create novel quantum materials by optimally combining sophisticated oxide growth techniques using laser molecular beam epitaxy and advanced analysis techniques using quantum beams.

Surface/Interface Magnetism Project [6]

The surface and interface of magnetic thin films play essential roles in the appearance of extraordinary magnetic properties such as perpendicular magnetic anisotropy and the giant magnetoresistance effect. We are investigating the crystalline, magnetic and electronic structures at the surface and interface of magnetic thin films and multilayers, in order to reveal the origin of fascinating magnetic properties that cannot be realized in bulk materials. For example, we have studied magnetic anisotropy of Fe/Ni multilayers, magnetic structures at the interface between antiferromagnetic FeMn and ferromagnetic Ni, effects of ion irradiation on ultrathin films, and a voltage-induced change in magnetic anisotropy of FeCo thin films grown on a ferroelectric substrate, by means of X-ray magnetic circular dichroism, extended X-ray absorption fine structure, and polarized neutron reflectivity techniques. We also plan to perform muon spin rotation experiments using an ultra-slow muon source.

Extreme Conditions Project

Materials under pressure and temperature show many interesting behaviors unlike those under ambient conditions. In this project, we are developing a new in-situ technique to investigate physical and chemical properties of the Earth and planetary materials including iron and hydrogen under extreme conditions.

Soft Matter Project [7]

Soft matter is a subfield of condensed matter comprising a variety of physical states that are easily deformed by thermal stresses or thermal fluctuations. They include liquids, colloids, polymers, liquid crystals, amphiphilic molecules, and a number of biological materials. These materials often self-organize into mesoscopic physical structures that are much larger than the microscopic scale (the arrangement of atoms and molecules), and yet are much smaller than the macroscopic scale of the material. The properties and interactions of these mesoscopic structures may determine the macroscopic behavior of the material. In spite of the various forms of these materials, many of their properties have common physicochemical origins, such as a large number of internal degrees of freedom, weak interactions between structural elements, and a delicate balance between entropic and enthalpic contributions to the free energy. These properties lead to large thermal fluctuations, a wide variety of forms, sensitivity of equilibrium structures to external conditions, macroscopic softness, and metastable states. From the above viewpoint, we are investigating the structural properties of soft matter such as liquids and amphiphilic molecules.

Hydrogen Project

Hydrogen plays important roles in material and life sciences and bridges fundamental science and engineering. There are many unsolved issues related to hydrogen: hydrogen bonding, hydrogen induced properties such as magnetism, superconductivity, embrittlement, thermal conductivity, hydrogen absorption/desorption mechanisms on material surfaces, activation of hydrogen near the surface of photo catalysts, and so on. Isotope effects and/or quantum effects are dominant for these properties, such as the effects of inverse isotopes on the superconductivity of palladium. This project involves neutron, synchrotron and muon beam specialists for observing hydrogen and aims to make observations to establish the quantum nature of hydrogen in materials.

Surface Structure and Electronic States Project [8]

Surface and near-surface structures have large effects on the properties of industrial materials especially those used for nanoelectronics devices and as catalysts. To develop those materials efficiently, definitive knowledge of the material surface and near-surface structures is essential. Recently, it has been revealed that reflection high-energy positron diffraction (RHEPD),

a positron counterpart of reflection high-energy electron diffraction (RHEED), is an ideal method for solid surface and near surface structure analysis. Emphasizing the advantage of using total reflection, we propose to rename the RHEPD method as total-reflection high-energy positron diffraction (TRHEPD). We have started a project "Surface structure and electronic state", which makes use of TRHEPD for surface structure analysis and other complementary methods for determining surface electronic states, e.g. angle-resolved photoemission spectroscopy (ARPES), to obtain complete information at and near the surface.

The Element Strategy Initiative Electronic Materials [9]

We are aiming to develop entirely new materials that do not use rare elements. In the Tokyo Institute of Technology for Element Strategy, we are developing materials based on successful experience far away from development policy, and are pioneering electronic materials to create new guidelines for material design using harmless elements to open up new fields of material science. We are researching the crystal, electronic, and magnetic structures of light elements such as hydrogen and oxygen in materials synthesized by the Material Creation Group by using synchrotron radiation, muon and neutron sources.

Magnetic Materials

The Elements Strategy Initiative Center for Magnetic Materials (ESICMM) at the National Institute of Material Science (NIMS) has set the goals of (1) laboratory-scale synthesis of mass-producible high-performance

next-generation permanent magnets that do not use critical scarce elements and (2) framework-building and the provision of basic science and technology that are needed in industrial R&D activities. In the CMRC, the "In situ analysis using neutrons and X-rays" project has been started as an analysis group member of ESICMM. The complementary use of neutrons at J-PARC/MLF and synchrotron X-rays at the Photon Factory is very useful for characterizing magnetic materials from the atomic scale to micrometer scale.

REFERENCES

- [1] T. Matsumura, H. Nakao and Y. Murakami, *J. Phys. Soc. Jpn.* **82**, 021007 (2013).
- [2] J. Fujioka, Y. Yamasaki, H. Nakao, R. Kumai, Y. Murakami, M. Nakamura, M. Kawasaki and Y. Tokura, *Phys. Rev. Lett.* **111**, 027206 (2013).
- [3] J. Okamoto, H. Nakao, Y. Yamasaki, H. Wadati, A. Tanaka, M. Kubota, K. Horigane, Y. Murakami and K. Yamada, *J. Phys. Soc. Jpn.* **83**, 044705 (2014).
- [4] K. M. Kojima, R. Kadono, M. Miyazaki, M. Hiraishi, I. Yamauchi, A. Koda, Y. Tsuchiya, H. S. Suzuki and H. Kitazawa, *Phys. Rev. Lett.* **112**, 087203 (2014).
- [5] F. Kagawa, T. Sato, K. Miyagawa, K. Kanoda, Y. Tokura, K. Kobayashi, R. Kumai and Y. Murakami, *Nature Physics* **9**, 419 (2013).
- [6] K. Amemiya, M. Sakamaki, M. Mizusawa and M. Takeda, *Phys. Rev. B* **89**, 054404 (2014).
- [7] K. Sadakane, M. Nagao, H. Endo and H. Seto, *J. Chem. Phys.* **139**, 234905 (2013).
- [8] K. Wada, T. Hyodo, A. Yagishita, M. Ikeda, S. Ohsawa, T. Shidara, K. Michishio, T. Tachibana, Y. Nagashima, Y. Fukaya, M. Maekawa and A. Kawasuso, *Eur. Phys. J. D* **66**, 37 (2012).
- [9] M. Hiraishi, S. Iimura, K. M. Kojima, J. Yamaura, H. Hiraka, K. Ikeda, P. Miao, Y. Ishikawa, S. Torii, M. Miyazaki, I. Yamauchi, A. Koda, K. Ishii, M. Yoshida, J. Mizuki, R. Kadono, R. Kumai, T. Kamiyama, T. Otomo, Y. Murakami, S. Matsuishi and H. Hosono, *Nature Physics* **10**, 300 (2014).

4 Slow Positron Facility

4-1 Overview

The Slow Positron Facility of the Photon Factory, equipped with a dedicated 55 MeV, 600 W linac, provides a high intensity, pulsed slow positron beam [1, 2]. The electrons accelerated by the linac are bombarded on a tantalum (Ta) converter plate, where Bremsstrahlung makes electron–positron pairs. The positrons so produced are moderated using a tungsten (W) foil moderator. The pulse width is determined by the pulse structure of the linac: it is 1 μ s (long-pulse mode) or 1–10 ns (variable, short-pulse mode) at frequencies of up to 50 Hz.

A variable high electrostatic tension (up to 35 kV) is applied to the slow positron production unit (Ta converter and W foil moderator); the obtained energy-tuned slow positron beam is magnetically guided to the experiment hall and then branched to experimental stations. The transportation of the beam with energy of up to 35 keV through a grounded beamline duct gives flexibility for experiments with grounded apparatus. The high-energy transport capability is unique among the world's high-intensity positron beam facilities.

The beam intensities are 5×10^7 slow- e^+ /s in the long-pulse mode and 5×10^6 slow- e^+ /s in the short-pulse mode.

The locations of the experimental stations were not changed in FY2013. The beamline branches currently available and the connected stations are summarized below:

[Test Hall]

SPF-A3: total-reflection high-energy positron diffraction (TRHEPD)

[Klystron Gallery Lab]

SPF-B1: photodetachment of positronium negative ion (Ps^-)

SPF-B2: positronium time-of-flight (Ps -TOF)

4-2 Projects

Two projects are running in connection with the activity of the Slow Positron Facility.

[1] Grant-in-Aid for Scientific Research (S) “Development of High-brightness and High-intensity Positron Diffraction and its Application to Surface Studies” (Project leader: Toshio Hyodo (KEK))

Low-energy positron diffraction (LEPD) and total-reflection high-energy positron diffraction (TRHEPD), the

positron counterpart of low-energy electron diffraction (LEED) and reflection high-energy electron diffraction (RHEED), respectively, are being developed for surface structure analysis. TRHEPD is a new name of the method formerly called reflection high-energy positron diffraction (RHEPD). Positron diffractions are easier to interpret than electron diffractions because: concerning LEPD, (1) the exchange interaction with material electrons is absent, (2) the surface sensitivity of the positron is higher owing to larger inelastic scattering cross section, and (3) the scattering factor for the positron falls off smoothly like that of X-rays and its angular dependence is also as simple as that of X-rays because a positron is repelled by the nuclei and does not have a bound state. Concerning TRHEPD, (4) the total reflection takes place owing to the positive electrostatic crystal potential of all the materials.

Since the positron is an antiparticle and so not found in everyday life, it is not easy to make a high-brightness and high-intensity beam for diffraction experiments in a laboratory. This project solves this problem by making use of a high-intensity slow-positron beam created by using the linac of the Slow Positron Facility and enhancing its brightness.

The extremely high sensitivity of the positron diffraction to the surface makes it possible to determine the details of the surface atomic configurations which are not easily done by X-ray or electron diffraction or a scanning tunneling microscope (STM). Direct determination of the surface atomic geometry will be attempted in two ways: by analyzing the TRHEPD patterns taken under total reflection conditions with the Patterson function, and by using the holographic reconstruction of the atomic arrangement using the LEPD spectra taken at various energies.

(Progress in FY2013) The structure of a silicene sheet on Ag(111) has been determined by using TRHEPD for the first time [3] by using the brightness enhanced beam on beamline SPF-A3. A new beamline branch for the LEPD station to be installed soon has been constructed; it will be called beamline SPF-A4. At the upstream of the beamline before the first branch, a pulse-stretch section has been planned. The purpose of this section is to address the following difficulties: the number of positrons within a single pulse is so large that the Doppler broadening of the annihilation γ -rays using a Ge detector cannot be measured because the signals pile up. Also, it is too large for the delay line detector for the planned LEPD measurements.

[2] Grant-in-Aid for Scientific Research (S) “The Evolution of Positronium Beam Science Using the Technique of Photodetachment of the Positronium Negative Ion” (Project leader: Yasuyuki Nagashima (Tokyo University of Science))

This project is being conducted in a laboratory at Tokyo University of Science and the Slow Positron Facility at KEK. Only a general introduction and the performance at KEK are described here.

The bound state of an electron and a positron is called positronium. It is the lightest “atom” which is metastable against self-annihilation into γ -rays with a lifetime of 125 ps or 142 ns. An energy-tunable beam of positronium will be a powerful tool in the investigation of material surfaces. However, the production of a beam with sufficient intensity and appropriate energy range was difficult to realize. The only beam of positronium produced before this project started was produced using charge exchange between positrons and gas molecules in the energy range below 400 eV.

This project aims to produce an energy-tunable positronium beam by employing photodetachment of the positronium negative ion (Ps^-), a bound state of two electrons and a positron, in an ultra-high-vacuum environment. Recently, Nagashima et al. found that the Ps^- is emitted efficiently from alkali metal-coated tungsten surfaces when bombarded with slow positrons [4]. Since the ion has a negative charge, it can be easily accelerated with an electric field. The photodetachment of Ps^- to neutral Ps after the acceleration makes an energy-tunable Ps beam [5,6]. In order to photodetach Ps^- , which has a short lifetime (479 ps), it must be irradiated with high-power pulsed YAG laser light. The linac-based beam at the Slow Positron Facility is suitable for the production of Ps^- synchronized to the laser pulses. The beam will demonstrate its power for analyzing the topmost layers of solids because positronium has negative affinity for most materials. Furthermore, the beam is not influenced by the charge-up of surfaces even if it is incident on insulators.

In the present project, investigation of the Ps^- photodetachment processes is also planned. The cross sections have been calculated and resonances for the Ps^- photodetachment have been predicted. Experimental studies on the photodetachment are important not only for basic science but also for efficient production of the energy-tunable Ps beam.

(Progress in FY2013) The energy-tunable Ps beam apparatus was completed and its spatial profile was measured in FY2012. In FY2013, the Ps beam apparatus was employed to investigate the Ps^- photodetachment resonances. Positrons generated in the short-pulse mode were transported in UHV and injected into a Na-coated polycrystalline tungsten target. The pulsed Ps^- ions emitted from the target were irradiated with UV pulses from a dye-laser and the Ps atoms formed through the Ps^- photodetachment were detected using a MCP. Preliminary data indicating the Ps^- resonance have been obtained.

In order to investigate the effect of alkali metal coating, time-of-flight of the Ps emitted from the Na-coated W surface was measured in FY2012. In FY2013, time-of-flight of the Ps emitted from Cs- and K-coated W was measured. The data show that the Ps yield increased drastically as in the case of Na coating. Furthermore, a low-energy component, which was not observed for the Na-coated surface, appeared by Cs and K coating. This is another interesting surface phenomenon waiting to be understood.

REFERENCES

- [1] K. Wada, T. Hyodo, A. Yagishita, M. Ikeda, S. Ohsawa, T. Shidara, K. Michishio, T. Tachibana, Y. Nagashima, Y. Fukaya, M. Maekawa and A. Kawasuso, *Eur. Phys. J. D* **66**, 37 (2012).
- [2] K. Wada, T. Hyodo, T. Kosuge, Y. Saito, M. Ikeda, S. Ohsawa, T. Shidara, K. Michishio, T. Tachibana, H. Terabe, R. H. Suzuki, Y. Nagashima, Y. Fukaya, M. Maekawa, I. Mochizuki and A. Kawasuso, *J. Phys. Conf. Ser.* **443**, 012082 (2013).
- [3] I. Mochizuki, Y. Fukaya, A. Kawasuso, K. Wada, T. Hyodo, K. Yaji, A. Harasawa and I. Matsuda, *Phys. Rev. B* **85**, 245438 (2012).
- [4] Y. Nagashima, T. Hakodate, A. Miyamoto and K. Michishio, *New J. Phys.* **10**, 123029 (2008).
- [5] K. Michishio, T. Tachibana, H. Terabe, A. Igarashi, K. Wada, T. Kuga, A. Yagishita, T. Hyodo and Y. Nagashima, *Phys. Rev. Lett.* **106**, 153401 (2011).
- [6] *Photon Factory Activity Report 2010 #28*, A 68 (2012).
- [7] K. Michishio, T. Tachibana, R. H. Suzuki, K. Wada, A. Yagishita, T. Hyodo and Y. Nagashima, *Appl. Phys. Lett.* **100**, 254102 (2012).
- [8] *Photon Factory Activity Report 2011 #29*, A 60 (2013).
- [9] H. Terabe, S. Iida, K. Wada, T. Hyodo, A. Yagishita and Y. Nagashima, *J. Phys. Conf. Ser.* **443**, 012075 (2013).
- [10] Y. Nagashima, K. Michishio, H. Terabe, R. H. Suzuki, S. Iida, T. Yamashita, R. Kimura, T. Tachibana, I. Mochizuki, K. Wada, A. Yagishita and T. Hyodo, *J. Phys.: Conf. Ser.* **505**, 012037 (2014).
- [11] Y. Nagashima, K. Michishio, and H. Terabe, *AIP Conf. Proc.* **27**, 1588 (2014).

5

IMSS Instrument R&D Team

The IMSS Instrument R&D team has been developing new detector systems for material science and biology since May 2010. Here we introduce R&D projects ongoing in the Photon Factory and the results obtained in FY2013.

5-1 X-Ray Imaging Using Synchrotron Radiation for Studies on Hierarchic Structure and Dynamics in Materials

A new project for developing a high-performance Silicon-On-Insulator (SOI) area detector is just starting for studies on hierarchic structure and dynamics in new materials. SOI technology is suitable for developing a good pixelated monolithic detector for X-ray imaging experiments using synchrotron radiation. The SOI device has no mechanical bump bonding and so a smaller pixel size can be achieved. A large gain and low-noise operation can be expected because the parasitic capacitances of sensing nodes are very small. The new SOI detector with a high space resolution of $30 \times 30 \mu\text{m}^2$ pixel will be valuable for investigating new ferroelectric materials for electronics applications. Utilizing the fine pixels of the new detector, we aim to determine the precise positions of hydrogen atoms, which are related to the mechanism of the large polarization of a ferroelectric, found in an organic complex. We also aim to determine the time response of the domain structure in such a sample to the application of an external electric field by using the 1 kHz to 1 MHz framing rate of a new detector system, as shown in Fig. 1. To study non-crystallized bio-molecules and structural changes of

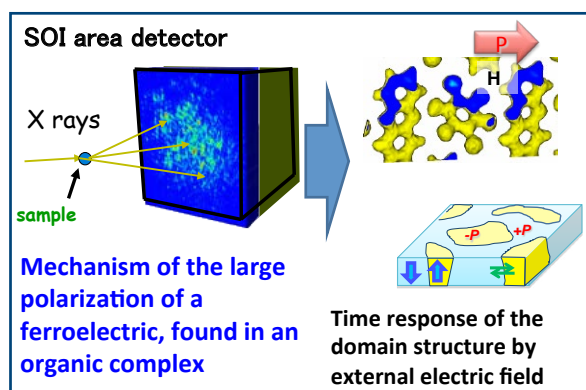


Figure 1: X-ray imaging using SOI area detector for studies on hierarchic structure and dynamics in materials.

cell membranes, the fine pixels and high frame rate of the SOI detector will be effective for grazing-incidence small-angle X-ray scattering (GI-SAXS) measurement. The detector's high sensitivity to soft X-rays of around 2 keV is also attractive for studies using X-ray absorption of phosphor or sulfur. GI-SAXS measurements will be conducted with the new SOI area detector at BL-15A.

5-2 Ultra-Fast Signal Processing System for a Si-APD Array X-Ray Detector

The project team has been developing an X-ray detector system using a 64-pixel Si-APD linear array (pixel size: $100 \mu\text{m} \times 200 \mu\text{m}$) and pulse counting electronics for multi-channel scaling (MCS). In FY2013, the team applied the detector system to nuclear resonant scattering experiments on ^{57}Fe (first excited level: 14.4 keV, half-life: 98 ns) using synchrotron radiation. The experiment was carried out at beamline BL09XU of SPring-8. A sample including ^{57}Fe and the detector were arranged along the incident beam axis for nuclear forward scattering. The detector counted the resonant γ -ray photons emitted from hyperfine splitting levels which were generated by surrounding electronic states. By using this system with MCS, information on material properties of the sample was successfully obtained from data recorded at each pixel of the detector as the time distribution of the γ -ray counts using 1 ns sampling.

5-3 Auger-Electron Detector System for Depth-Resolved X-Ray Magnetic Circular Dichroism (XMCD)

The group working for beamline BL-16A has been preparing a multi-anode MCP detector system, which has an angle-resolution and a fast digital data read-out of 30 channels, instead of the system consisting of a CCD and a fluorescence screen. In 10-Hz polarization switching of the insertion devices installed in BL-16A, the new MCP system improved the S/N ratio and the dynamic range of output counts in XMCD measurements. In FY2013, tests of data acquisition at a count rate of more than 10^7 s^{-1} per channel were conducted using an improved frontend board.

6 Summary of Experimental Stations

About 54 experimental stations are operated at the PF storage ring, the PF-AR and the slow positron facility (SPF), as shown in Figs. 1, 2 and 3. 35 stations are dedicated to research using hard X-rays, 16 stations for studies in the VUV and soft X-ray energy regions, and 3 stations for studies using slow positrons. Tables 1, 2 and 3 summarize the areas of research carried out at the experimental stations at the PF storage ring, PF-AR and SPF. The specifications in terms of the optics and performance of each experimen-

tal station differ according to experimental requirements and methodology. Tables 4, 5 and 6 list the details of the optics of the hard X-ray stations, the soft X-ray / VUV stations and slow positron stations. The principal performance parameters, including energy range, energy resolution, beam-spot size, and photon flux at the sample position for PF and PF-AR, and energy range, pulse width, frequency, and positron flux for SPF are shown.

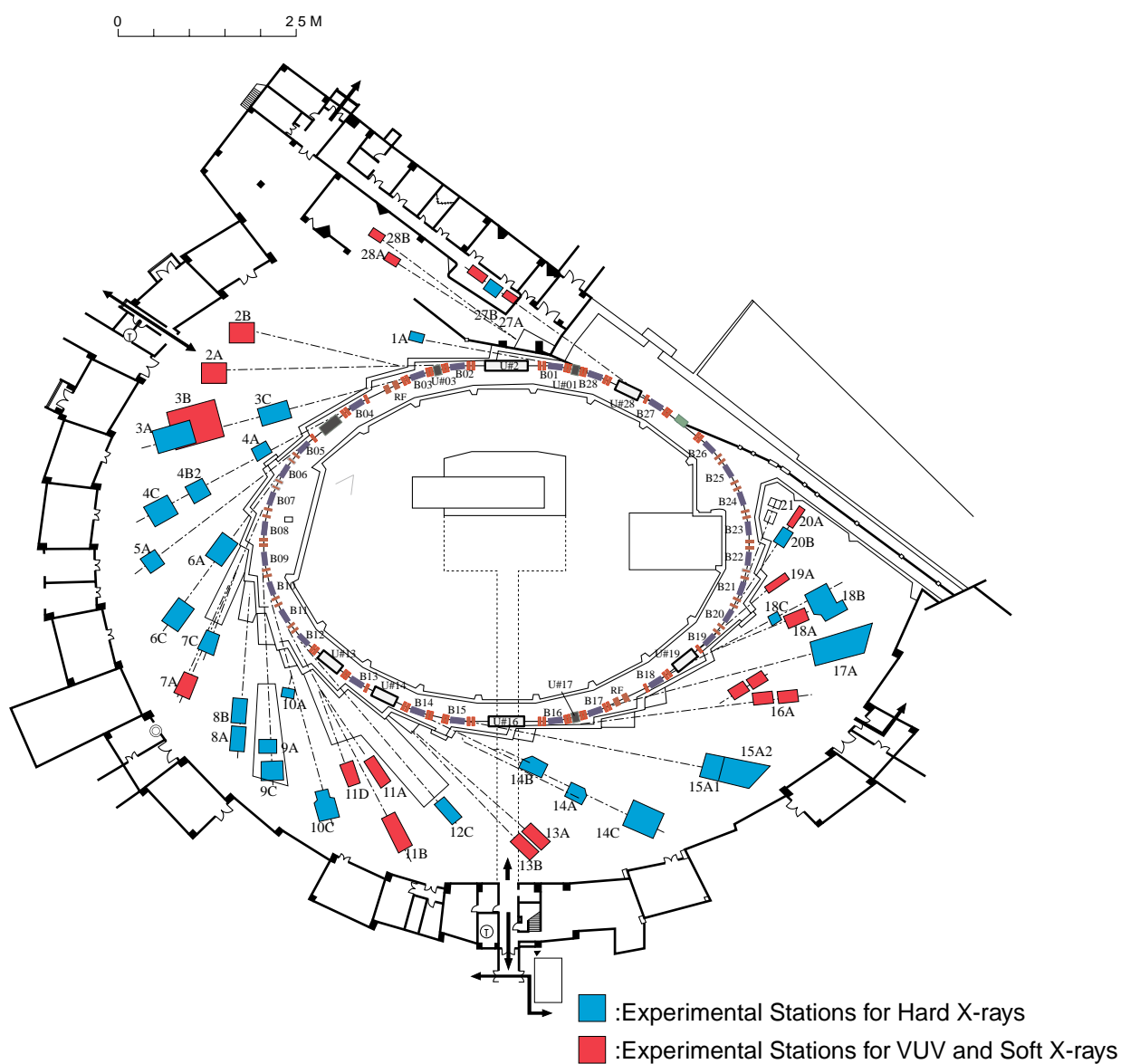


Table 1: List of experimental stations at the PF storage ring.

Experimental Station		Person in Charge
BL-1 A	(Short Gap Undulator) Macromolecular crystallography	N. Matsugaki
BL-2 A* B*	(Undulator) Soft X-ray spectroscopy Soft X-ray spectroscopy	K. Amemiya K. Amemiya
BL-3 A B C	(A: Short Gap Undulator) X-ray diffraction and scattering station for materials science VUV and soft X-ray spectroscopy(◇) Characterization of X-ray optical elements/White X-ray magnetic diffraction	H. Nakao H. Kato [Hirosaki Univ.], A. Yagishita K. Hirano
BL-4 A B2 C	Trace element analysis, X-ray microprobe High resolution powder diffraction(♣) X-ray diffraction and scattering	A. Iida T. Ida [Nagoya Inst. Tech.], H. Nakao Y. Yamasaki
BL-5 A	(Multipole Wiggler) Macromolecular crystallography	N. Matsugaki
BL-6 A C	Small-angle X-ray scattering X-ray diffraction and scattering(♣)	N. Igarashi S. Sasaki [Tokyo Inst. Tech.], H. Kawata
BL-7 A C	Soft X-ray spectroscopy(◇) X-ray spectroscopy and diffraction	J. Okabayashi [RCS], K. Amemiya H. Sugiyama
BL-8 A B	Weissenberg camera for powder/Single-crystal measurements under extreme conditions Weissenberg camera for powder/Single-crystal measurements under extreme conditions	R. Kumai R. Kumai
BL-9 A C	XAFS XAFS	H. Abe H. Abe
BL-10 A C	X-ray diffraction and scattering(♣) Small-angle X-ray scattering	A. Yoshiasa [Kumamoto Univ.], Y. Yamasaki N. Shimizu
BL-11 A B D	Soft X-ray spectroscopy Surface EXAFS, soft X-ray spectroscopy Characterization of optical elements used in the VSX region	Y. Kitajima Y. Kitajima K. Mase
BL-12 C	XAFS	H. Nitani

Experimental Station		Person in Charge
BL-13 A/B	(Undulator) Scanning transmission soft X-ray microscopy and microspectroscopy	K. Mase
BL-14 A B C	(Vertical Wiggler) Crystal structure analysis and detector development High-precision X-ray optics Medical applications and general purpose (X-ray)	S. Kishimoto K. Hirano K. Hyodo
BL-15 A1* A2*	Semi-microbeam XAFS High brilliance small-angle X-ray scattering	H. Nitani N. Shimizu
BL-16 A	(Variable Polarization Undulator) Soft X-ray spectroscopies with circular and linear polarization	K. Amemiya
BL-17 A	(Short Gap Undulator) Macromolecular crystallography	Y. Yamada
BL-18 A B* C	Angle-resolved photoelectron spectroscopy of surfaces and interfaces(◆) Multipurpose monochromatic hard X-ray station(◆) High pressure X-ray powder diffraction (DAC)(♠)	K. Yaji [ISSP], A. Yagishita S. Velaga [India, Saha Institute], R. Kumai S. Nakano [NIMS], T. Kikegawa
BL-19 A	(Revolver Undulator) Spin-resolved photoelectron spectroscopy (Mott detector)(◆)	K. Yaji [ISSP], A. Yagishita
BL-20 A B	VUV spectroscopy(◇) White & monochromatic X-ray topography and X-ray diffraction experiment	N. Kouchi [Tokyo Inst. Tech], J. Adachi H. Sugiyama
BL-27 A B	(Beamline for experiments using radioisotopes) Radiation biology, soft X-ray photoelectron spectroscopy Radiation biology, XAFS, X-ray diffuse scattering	N. Usami N. Usami
BL-28 A/B	(Elliptical / Helical Undulator) High-resolution VUV-SX beamline for angle-resolved photoemission High-resolution VUV-SX spectroscopy	K. Ono

♠ User group operated beamline

◆ External beamline

◇ Operated by University

* Under reconstruction

RCS: Research Center for Spectrochemistry, the University of Tokyo

ISSP: Institute for Solid State Physics, the University of Tokyo

Table 2: List of experimental stations at the PF-AR.

Experimental Station		Person in Charge
AR-NE1 A	(Multipole Wiggler) Laser-heating high pressure X-ray diffraction and nuclear resonant scattering (DAC)	T. Kikegawa
AR-NE3 A	(Undulator) Macromolecular crystallography	Y. Yamada
AR-NE5 C	High pressure and high temperature X-ray diffraction (MAX-80)	T. Kikegawa
AR-NE7 A	High pressure and high temperature X-ray diffraction (MAX-III), X-ray imaging	K. Hyodo
AR-NW2 A	(Undulator) XAFS/Dispersive XAFS/Time-resolved-X-ray diffraction	H. Abe
AR-NW10 A	XAFS	H. Nitani
AR-NW12 A	(Undulator) Macromolecular crystallography	Y. Yamada
AR-NW14 A	(Undulator) Time-resolved X-ray diffraction, scattering and absorption	S. Nozawa

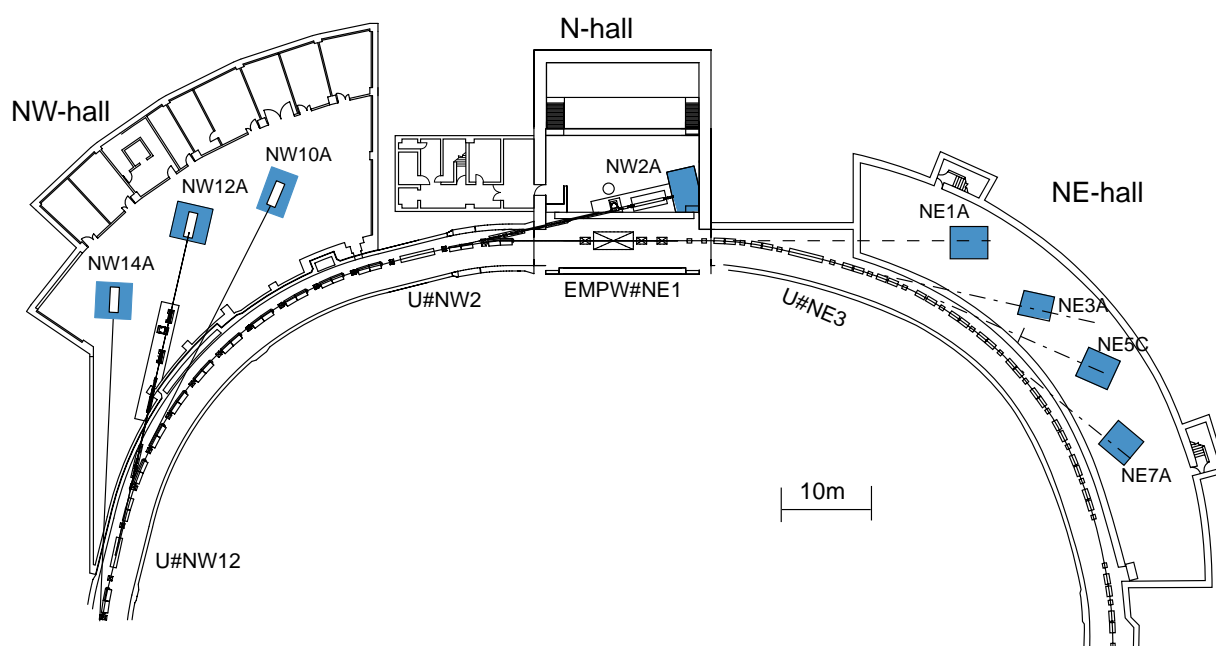


Figure 2: Plan view of beamlines in the PF-AR north-east, north, and north-west experimental halls.

Table 3: List of experimental stations at the Slow Positron Facility.

Experimental Station		Person in Charge
SPF-A3*	Total-reflection high-energy positron diffraction	T. Hyodo
SPF-B1	General purpose (Positronium negative ion)	T. Hyodo
SPF-B2	Positronium time-of-flight	T. Hyodo

* Under reconstruction

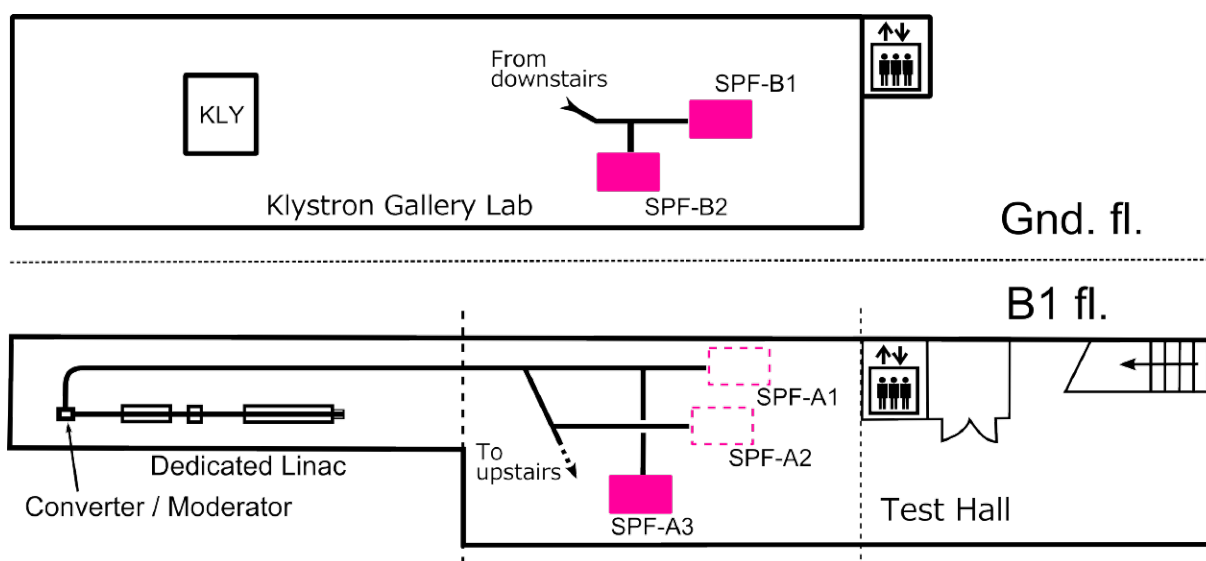


Figure 3: View of beamlines in the Slow Positron Facility.

Table 4: Specifications of X-ray beamline optics.

Branch Beamline	Horizontal Acceptance (mrad)	Type of Monochromator	Mirror	Photon Energy (keV)	Beam Size (H×V) (mm)	Photon Flux at Sample Position (/s)	Energy Resolution ($\Delta E/E$)×10 ⁻⁴	Reference
BL-1A	0.15	Channel-Cut Si(111) Liquid N ₂ Cooling	Bimorph Si Rh-Coated Si Rh-Coated	3.7 ~ 4.5 11.2 ~ 12.9	0.05×0.01	4×10 ¹¹ @11.2 keV (0.025×0.01mm ²)	~2	
BL-3A	1	Flat Double Crystal Si(111)	Bent Cylinder	4 ~ 14	0.7×0.2	6×10 ¹²	~5	1, 2
BL-3C	1.75	Double Crystal Si(111)	None	4 ~ 20 or white	20×6(mono) 0.1×0.1(white)		~2	
BL-4A	6	Double Crystal Si(111)	Vertical Focusing Mirror	4 ~ 20	50×4		~2	3
BL-4B2	4.5	Flat Double Crystal Si(111)	Bent Cylinder	6 ~ 20	13×2		~2	4, 5
BL-4C	2	Flat Double Crystal Si(111)	Bent Cylinder	5 ~ 19	0.7×0.5		~5	6, 7
BL-5A	0.5	Micro-Channel Double Crystal Si(111)	Bent Plane Si Rh-Coated Bent Cylinder Si Rh-Coated	6.5 ~ 17	1.2×0.4	3×10 ¹¹ (0.2×0.2 mm ²)	~2	
BL-6A	2	Bent Crystal Ge(111) ($\alpha = 8.0^\circ$)	Bent Plane ULE	8.3 (fixed)	0.5×0.2	1.0×10 ¹² /mm ² (Slit full-open)	~10	8
BL-6C	2	Flat Double Crystal Si(111)	Bent Cylinder	5 ~ 20 (~25 non-Focus)	0.5×0.3			
BL-7C	4	Double Crystal Si(111) Sagittal Focusing	Double Mirror Fused Quartz Focusing	4 ~ 20 (4 ~ 13)	5×1	1×10 ¹⁰ /6mm ² (8 keV, 300 mA) (1×10 ¹¹ when focused)	~2	9 - 11
BL-8A	2.22	Flat Double Crystal Si(111)	Bent Cylinder	5 ~ 19	0.82×0.52	3.2×10 ¹¹ (12.4keV, 400mA)	~5	12
BL-8B	2.21	Flat Double Crystal Si(111)	Bent Cylinder	5 ~ 19	0.75×0.45	2.2×10 ¹¹ (12.4keV, 400mA)	~5	12
BL-9A	3	Double Crystal Si (111)	Collimating and Focusing Bent Conical Mirrors Rh-Coated Double Flat Mirror Ni-Coated	2.1 ~ 15	0.5×0.3	6×10 ¹¹ (7keV, 450 mA)	2	13, 14
BL-9C	3.5	Double Crystal Si(111)	Bent Cylinder Rh-Coated Si	4 ~ 23	0.8×0.6	1×10 ¹¹ (8keV, 450 mA)	~2	

Branch Beamline	Horizontal Acceptance (mrad)	Type of Monochromator	Mirror	Photon Energy (keV)	Beam Size (HxV) (mm)	Photon Flux at Sample Position (/s)	Energy Resolution ($\Delta E/E$) $\times 10^{-4}$	Reference
BL-10A	1	Si(111), Si(311) Quartz(100) PG(002) Curved Si(111) ($\alpha \sim 4^\circ, 8^\circ$)	Plane Pt Coated Fused Quartz	5 ~ 25	10x3		10 ~5	15
BL-10C	2.1	Fix-Exit Double Crystal Si(111)	Bent Cylinder Rh-Coated	6 ~ 14	0.63x0.18	1.5×10^{11} (8 keV)	2	
BL-12C	2	Double Crystal Si(111)	Bent Cylinder Double Flat Mirror Ni-Coated	4 ~ 23	0.6x0.6	9×10^{10} (8 keV, 450mA)	~2	16
BL-14A	1.28 (Vertical)	Double Crystal Si (111) Si (311) Si (553)	Bent Cylinder Rh-Coated Fused Quartz	5.1 ~ 19.1 9.9 ~ 35.6 22.7 ~ 84.5	2x1 at focus 5x38		2	17
BL-14B	2.2 (Vertical)	Flat Double Crystal Si(111)	None	10 ~ 57	5x14		2	18
BL-14C	1.96 (Vertical)	Double Crystal Si(111), Si(220)	None	5 ~ 100 or white	6x70		2	19, 20
BL-15A1*	0.2	Double Crystal Si(111) Liquid N ₂ Cooling	Horizontal: Bent Plane Si Rh-Coated Bimorph Silica Rh-Coated Vertical: Bent Plane Si Rh-Coated Double Flat Si Ni-Coated	2.1 ~ 15	0.02x0.02 0.6x0.04	3.5×10^{11} (7.5 keV, 450mA)	~2	21
BL-15A2*								
BL-17A	0.1 ~ 0.2	Double Crystal Si(111) Liquid N ₂ Cooling	Bent Plane Si Rh-Coated Bent Plane Si Rh-Coated	6 ~ 13	0.25x0.04	10^{10} (12.4 keV, 450mA, 0.02x0.02mm ²)	~2	22 - 24
BL-18B [India, DST]	2	Double Crystal Si(111)	Plane and Bent Cylinder	6 ~ 20			~2	
BL-18C	1	Double Crystal Si(111)	Cylinder Fused Quartz Pt-Coated	6 ~ 25	0.07x0.04		~2	
BL-20B	1.6	Double Crystal Si(111)	None	5 ~ 25 or white	20x5	1×10^{11} (12 keV, 450mA)	~2	
BL-27B	4	Double Crystal Si(111)	None	4 ~ 20	100x6		~2	25

Branch Beamline	Horizontal Acceptance (mrad)	Type of Monochromator	Mirror	Photon Energy (keV)	Beam Size (H×V) (mm)	Photon Flux at Sample Position (/s)	Energy Resolution ($\Delta E/E$)×10 ⁻⁴	Reference
AR-NE1A	0.28	Micro-Channel Double Crystal Si(111), High-Resolution Channel Cut Si(4,2,2)&(12,2,2)	Bent Plane W/C Multilayer Coated Si	6 ~ 50	0.8×0.2	8×10 ¹¹ (0.2×0.2mm ²)	~2	
AR-NE3A	H:0.2 V:0.1	Double Crystal Si(111) Liquid N ₂ Cooling	Pre-Mirror Bent Flat Si Rh-Coated Post-Mirror Bent Cylinder Fused Quartz Rh-Coated	6.5 ~ 17	0.8×0.2	8×10 ¹¹ (0.2×0.2mm ²)	~2	26, 27
AR-NE5C	3	Double Crystal Si(111)	None	30 ~ 100 or white	60×5		5	28
AR-NE7A	4	Double Crystal Si(111)		25 ~ 50 or white	80×3		5	
AR-NW2A	H:1.0 V:0.2	Double Crystal Si(111) Liquid N ₂ Cooling	Bent Cylinder Si Rh-Coated Bent Flat Si Rh-Coated	5 ~ 25	0.6×0.2 ~10×0.06	6×10 ¹² (12keV, 60mA)	~2	29 - 31
AR-NW10A	1.2	Si(311)	Pt-Coated Bent Cylinder Double Flat Mirror Rh-Coated	8 ~ 42	2.2×0.5	1×10 ¹⁰ (22 keV, 60mA)	~1	32
AR-NW12A	H:0.3 V:0.1	Double Crystal Si(111) Liquid N ₂ Cooling	Pre-Mirror Bent Flat Si Rh-Coated Post-Mirror Bent Cylinder Si Rh-Coated	6.5 ~ 17	1.3×0.3	2×10 ¹¹ (0.2×0.2 mm ²)	~2	33 - 35
AR-NW14A	H:0.3 V:0.1	Double Crystal Si(111) Liquid N ₂ Cooling	Bent Cylinder Rh-Coated Bent Flat Rh-Coated	4.9 ~ 25	0.45×0.25	5×10 ¹²	~2	36

* Under reconstruction

India DST: Department of Science & Technology

REFERENCES

- [1] *Photon Factory Activity Report 2006*, #24, A 64 (2008).
- [2] *Photon Factory Activity Report 2006*, #24, A 104 (2008).
- [3] A. Iida *et al.*, *Rev. Sci. Instrum.* **66**, 1373 (1995).
- [4] Powder Diffraction User Group, *KEK Report 94-11* (1995).
- [5] H. Toraya, H. Hibino and K. Ohsumi, *J. Synchrotron Rad.* **3**, 75 (1996).
- [6] H. Iwasaki *et al.*, *Rev. Sci. Instrum.* **60**, 2406 (1989).
- [7] *Photon Factory Activity Report 1995* #13, E-1 (1996).
- [8] N. Shimizu *et al.*, *J. Phys.: Conf. Ser.* **425**, 202008 (2013).
- [9] M. Nomura and A. Koyama, *KEK Internal*, **93-1** (1993).
- [10] M. Nomura *et al.*, *KEK Report*, **91-1** (1991).
- [11] M. Nomura and A. Koyama, in "X-ray Absorption Fine Structure", ed. by S. S. Hasnain, Ellis Horwood, Chichester, **667** (1991).
- [12] A. Nakao *et al.*, *AIP Conf. Proc.* **1234**, 367 (2010).
- [13] M. Nomura and A. Koyama, *J. Synchrotron Rad.* **6**, 182 (1999).
- [14] M. Nomura and A. Koyama, *Nucl. Instrum. Meth.* **A467-468**, 733 (2001).
- [15] S. Sasaki, *Rev. Sci. Instrum.* **60**, 2417 (1989).
- [16] M. Nomura and A. Koyama, *KEK Report*, **95-15** (1996).
- [17] Y. Satow and Y. Iitaka, *Rev. Sci. Instrum.* **60**, 2390 (1989).
- [18] M. Ando *et al.*, *Nucl. Instrum. Meth.* **A246**, 144 (1986).
- [19] *Photon Factory Activity Report 1999*, #17, A 92 (2000).
- [20] *Photon Factory Activity Report 1999*, #17, A 103 (2000).
- [21] N. Igarashi *et al.*, *J. Phys.: Conf. Ser.* **425**, 072016 (2013).
- [22] N. Igarashi *et al.*, *AIP Conf. Proc.* **879**, 812 (2007).
- [23] N. Igarashi *et al.*, *J. Synchrotron Rad.* **15**, 292 (2008).
- [24] Y. Yamada *et al.*, *J. Synchrotron Rad.* **20**, 938 (2013).
- [25] H. Konishi *et al.*, *Nucl. Instrum. Meth.* **A372**, 322 (1996).
- [26] Y. Yamada *et al.*, *AIP Conf. Proc.* **1234**, 415 (2010).
- [27] M. Hiraki *et al.*, *AIP Conf. Proc.* **1234**, 673 (2010).
- [28] T. Kikegawa *et al.*, *Rev. Sci. Instrum.* **66**, 1335 (1995).
- [29] T. Mori *et al.*, *AIP Conf. Proc.* **705**, 255 (2004).
- [30] H. Kawata *et al.*, *AIP Conf. Proc.* **705**, 663 (2004).
- [31] Y. Inada *et al.* *AIP Conf. Proc.* **879**, 1230 (2007).
- [32] M. Nomura *et al.*, *AIP Conf. Proc.* **882**, 896 (2007).
- [33] L.M.G. Chavas *et al.*, *J. Synchrotron Rad.* **19**, 450 (2012).
- [34] L.M.G. Chavas *et al.*, *J. Phys.: Conf. Ser.* **425**, 012008 (2013).
- [35] L.M.G. Chavas *et al.*, *J. Synchrotron Rad.* **20**, 838 (2013).
- [36] S. Nozawa *et al.*, *J. Synchrotron Rad.* **14**, 313 (2007).

Table 5: Specifications of VUV and soft X-ray beamline optics.

Beamline	Acceptance H × V (mrad) or Undulator Parameters	Type of Monochromator	Groove Density (#/mm)	Energy Range (eV)	Beam Size H × V (mm)	Resolving Power (E/ΔE) Photon Flux (photons/s)	Reference
BL-2A* Undulator	ID02: $K_{\max} = 2.3$, $\lambda_u = 6$ cm ID022: $K_{\max} = 5.0$, $\lambda_u = 16$ cm	Variable-Included-Angle Varied-Line-Spacing Plane Grating	400 600 1000	30 ~ 2000	~0.5 × 0.1	2000 ~ 20000 $10^{13} \sim 10^{11}$	1
BL-2B* Undulator	ID02: $K_{\max} = 2.3$, $\lambda_u = 6$ cm ID022: $K_{\max} = 5.0$, $\lambda_u = 16$ cm	Variable-Included-Angle Varied-Line-Spacing Plane Grating Double Crystal InSb(111), Ge(111), Si(111)	400 600 1000	30 ~ 4000	~0.5 × 0.1	2000 ~ 20000 $10^{13} \sim 10^{11}$	1
BL-3B	10 × 2	Grazing Incidence R = 24 m $\alpha + \beta = 165^\circ$ 1800	200 600	10 ~ 280	< 2φ	200 ~ 3000 $10^{12} \sim 10^9$	2, 3
BL-7A [RCS]	6 × 1	Varied-Line-Space Plane Grating	300 650	50 ~ 1300	2.5 × 0.5	1000 ~ 9000 $10^{12} \sim 10^9$	4
BL-11A	5 × 1	Varied-Line-Space Plane Grating	300 800 1200	70 ~ 1900	2 × 1	500 ~ 5000 $10^{12} \sim 10^9$	5 - 8
BL-11B	4 × 0.6	Double Crystal InSb (111), Si (111)		1724 ~ 5000	5 × 2	2000 10^{10}	9 - 11
BL-11D	4 × 2	Grazing Incidence Varied Deviation-Angle On-Blaze Mount R ₁ = 52.5 m R ₃ = 22.5 m	2400	60 ~ 245 200 ~ 900	1 × 0.1	2000 10^{11}	12, 13
BL-13A/B Undulator	$K_{\max} = 8$ $\lambda_u = 18$ cm	Variable-Included-Angle Varied-Line-Spacing Plane Grating	300 1000	30 ~ 330 100 ~ 1600	~0.2 × 0.04	4000 ~ 10000 $10^{12} \sim 10^9$	14 - 16
BL-16A Undulator	$K_{\max} = 2.37$ (Circular Polarization) $K_{\max} = 3.12$ (Horizontal Linear Polarization) $K_{\max} = 1.98$ (Vertical Linear Polarization) $K_{\max} = 1.73$ (45-deg Linear Polarization) $\lambda_u = 5.6$ cm	Variable-Included-Angle Varied-Line-Spacing Plane Grating	500 1000	250 ~ 1500	~0.2 × 0.1	4000 ~ 8000 $10^{12} \sim 10^{11}$	17, 18
BL-18A [ISSP]	2 × 2	Grazing Incidence R = 3 m $\alpha + \beta = 160^\circ$ R = 6.65 m $\alpha + \beta = 167.5^\circ$	300 600 1000	15 ~ 150	< 1φ	1000~2000 $10^{11} \sim 10^9$	19
BL-19A Revolver Undulator [ISSP]	[K = 1.0 ~ 9.0 $\lambda_u = 16.4$ cm K = 0.5 ~ 1.25 $\lambda_u = 5$ cm K = 0.5 ~ 2.5 $\lambda_u = 7.2$ cm K = 1.0 ~ 5.0 $\lambda_u = 10$ cm	Grazing Incidence R = 2 m $\alpha + \beta = 160^\circ$ R = 4 m $\alpha + \beta = 170^\circ$	600 1200 600 1200	12 ~ 250	< 0.7φ	1000 10^{12}	20, 21

Beamline	Acceptance H × V (mrad) or Undulator Parameters	Type of Monochromator	Groove Density (#/mm)	Energy Range (eV)	Beam Size H × V (mm)	Resolving Power (E/ΔE) Photon Flux (photons/s)	Reference
BL-20A	28 × 5	3m Normal Incidence	1200 2400	5 ~ 40	2 × 1	300 ~ 30000 10 ¹² ~ 10 ⁸	22
BL-27A	5 × 0.5	Double Crystal InSb (111)		1800 ~ 4000		2000	23
BL-28A/B Helical Undulator	K _x = 0.23 ~ 3 K _y = 0.23 ~ 6 K _y = 0.23 ~ 6	Varied-Line-Space Plane Grating	400	30 ~ 300	0.15 × 0.05	30000 10 ¹²	1

* Under reconstruction
RCS: Research Center for Spectrochemistry, the University of Tokyo
ISSP: Institute for Solid State Physics, the University of Tokyo

REFERENCES

- [1] K. Amemiya and T. Ohta, *J. Synchrotron Rad.* **11**, 171 (2004).
[2] A. Yagishita *et al.*, *Nucl. Instrum. Meth.* **A306**, 578 (1991).
[3] S. Masui *et al.*, *Rev. Sci. Instrum.* **63**, 1330 (1992).
[4] K. Amemiya *et al.*, *J. Elec. Spectrosc. Relat. Phenom.* **124**, 151 (2002).
[5] K. Amemiya *et al.*, *J. Synchrotron Rad.* **3**, 282 (1996).
[6] K. Amemiya *et al.*, *Proc. SPIE Proceedings* **3150**, 171 (1997).
[7] Y. Kitajima *et al.*, *J. Synchrotron Rad.* **5**, 729 (1998).
[8] Y. Kitajima *et al.*, *J. Elec. Spectrosc. Relat. Phenom.* **101-103**, 927 (1999).
[9] T. Ohta *et al.*, *Nucl. Instrum. Meth.* **A246**, 373 (1986).
[10] M. Funabashi *et al.*, *Rev. Sci. Instrum.* **60**, 1983 (1989).
[11] T. Iwazumi *et al.*, *Rev. Sci. Instrum.* **66**, 1691 (1995).
[12] *Photon Factory Activity Report 1997 #15*, A 101 (1998).
[13] T. Hatano and S. Aihara, *J. Phys.: Conf. Ser.* **425**, 152018 (2013).
[14] K. Mase *et al.*, *AIP Conf. Proc.* **1234**, 709 (2010).
[15] A. Toyoshima *et al.*, *J. Vac. Soc. Jpn.* **54**, 580 (2011).
[16] A. Toyoshima *et al.*, *J. Phys.: Conf. Ser.* **425**, 152019 (2013).
[17] K. Amemiya *et al.*, *AIP Conf. Proc.* **1234**, 295 (2010).
[18] K. Amemiya *et al.*, *J. Phys.: Conf. Ser.* **425**, 152015 (2013).
[19] S. Suzuki *et al.*, *Activity Report of SRL-ISSP* **60**, (1989).
[20] A. Kakizaki *et al.*, *Rev. Sci. Instrum.* **60**, 1893 (1989).
[21] A. Kakizaki *et al.*, *Rev. Sci. Instrum.* **63**, 367 (1992).
[22] K. Ito *et al.*, *Rev. Sci. Instrum.* **66**, 2119 (1995).
[23] H. Konishi *et al.*, *Nucl. Instrum. Meth.* **A372**, 322 (1996).

Table 6: Specifications of the beamlines at Slow Positron Facility.

Beamline	Beam Energy	Pulse Width	Frequency	Intensity	Reference
SPF-A3*	100eV - 35keV	1μs	≤ 50Hz	5×10 ⁷ e+/s (5×10 ⁶ e+/s after brightness enhancement)	3,4
SPF-B1	100eV - 35keV	1-10ns	≤ 50Hz	5×10 ⁶ e+/s	1,2,3,4
SPF-B2	100eV - 35keV	1-10ns	≤ 50Hz	5×10 ⁶ e+/s	5,6

* Under reconstruction

REFERENCES

- [1] T. Tachibana, *et al.*, *Nucl. Instrum. Methods Phys. Res., Sect. A* **621**, 670 (2010).
[2] K. Michishio, *et al.*, *Phys. Rev. Lett.* **106**, 153401 (2011).
[3] K. Wada, *et al.*, *Eur. Phys. J. D* **66**, 37 (2012).
[4] K. Michishio, *et al.*, *Appl. Phys. Lett.* **100**, 254102 (2012).
[5] K. Wada, *et al.*, *J. Phys.: Conf. Ser.* **443**, 012082 (2013).
[6] H. Terabe, S. Iida, K. Wada, T. Hyodo, A. Yagishita and Y. Nagashima, *J. Phys.: Conf. Ser.* **443**, 012075 (2013).

Accelerators



Accelerators

1. Outline of the Accelerators	97
2. PF Ring	100
2-1 Operation Summary	
2-2 Project to Renew the Insertion Devices at the PF Ring	
3. PF-AR	103
3-1 Operation Summary	
3-2 New PF-AR Transport Line	

Two electron storage rings which are the PF-ring and the PF-AR as the dedicated light sources were stably operated at the Photon Factory. The KEK linear accelerator with maximum electron energy of 8 GeV is employed to inject electron beam into the rings. The full energy injection of 2.5 GeV is carried out at the PF-ring, while it is required to increase from the injection energy of 3 GeV to the operation energy of 6.5 GeV at the PF-AR.

The machine parameters of the rings and the calculated spectral performances are listed in Table 1 and Table 2, respectively. The spectral distributions of synchrotron radiation (SR) from the bending magnets and the insertion devices are shown in Fig. 1.

Table 1: Principal beam parameters of the PF ring and PF-AR.

	PF	PF-AR
Energy	2.5 GeV	6.5 GeV
Natural emittance	34.6 nm rad	293 nm rad
Circumference	187 m	377 m
RF frequency	500.1 MHz	508.6 MHz
Bending radius	8.66 m	23.2 m
Energy loss per turn	0.4 MeV	6.66 MeV
Damping time		
Vertical	7.8 ms	2.5 ms
Longitudinal	3.9 ms	1.2 ms
Natural bunch length	10 mm	18.6 mm
Momentum compaction factor	0.00644	0.0129
Natural chromaticity		
Horizontal	-12.9	-14.3
Vertical	-17.3	-13.1
Stored current	450 mA	60 mA
Number of bunches	252	1
Beam lifetime	20-25 h (at 450 mA)	20-25 h (at 60 mA)

Table 2: Calculated spectral performances of the bend source and all the insertion devices at the PF ring (2.5 GeV, 450 mA) and the PF-AR (6.5 GeV, 60 mA). λ_u : period length, M : number of the periods, L : length of undulator or wiggler, $G_y(G_x)$: minimum vertical (horizontal) gap height, $B_y(B_x)$: maximum vertical (horizontal) magnetic field, Type of magnet, H: hybrid configuration, S.C.: super conducting magnet, σ_x, σ_y : horizontal or vertical beam size, σ'_x, σ'_y : horizontal or vertical beam divergence, $K_x(K_y)$: vertical (horizontal) deflection parameter, D : photon flux density (photons/sec/mrad²/0.1%b.w.), B : brilliance (photons/sec/mm²/mrad²/0.1%b.w.), P_r : total radiated power. Different operating modes of undulator and wiggler are denoted by -U and -W, respectively.

Name	E/I GeV/mA	λ_u cm	N	L m	$G_y(G_x)$ cm	$B_y(B_x)$ T	Type of magnet	σ_x mm	σ_y mm	σ'_x mrad	σ'_y mrad	$K_x(K_y)$	ϵ_r/ϵ_e keV	D	B	P_r kW
PF 2.5/450																
Bend								0.41	0.059	0.178	0.012		4	5.38E+13	3.48E+14	
SGU#01		1.2	39	0.5	0.4	0.7	P(NdFeB)	0.6	0.012	0.088	0.029	0.78		4.56E+16	9.90E+17	0.4
U#02-1		6	60	3.6	2.8	0.4	H(NdFeB)	0.65	0.042	0.054	0.008	2.3		2.73E+17	1.55E+18	1.07
U#02-2		16	17	2.72	2.6	0.33(0.33)	P(NdFeB)	0.65	0.042	0.054	0.008	4.93(4.93)		9.53E+15	4.58E+16	0.53
SGU#03		1.8	26	0.5	0.4	1	P(NdFeB)	0.6	0.012	0.088	0.029	1.68		2.50E+16	5.44E+17	0.82
MPW#05-W		12	21	2.5	2.64	1.4	H(NdFeB)	0.71	0.045	0.078	0.009	16	5.9	2.22E+15	1.10E+16	8.83
MPW#13-U		18	13	2.5	2.71	1.5	H(NdFeB)	0.74	0.02	0.094	0.019	2		1.70E+16	1.57E+17	0.06
VW#14					5	5	S.C.	0.53	0.045	0.128	0.008		20.8	5.42E+13	3.59E+14	
SGU#15		1.76	27	0.5	0.4	0.97	P(NdFeB)	0.6	0.012	0.088	0.029	1.37		4.38E+15	9.44E+16	0.75
U#16-1 & 16-2		5.6	44	2.5	2.1	0.6(0.38)	P(NdFeB)	0.654	0.042	0.055	0.008	3(2)		1.03E+18	1.82E+17	0.88
SGU#17		1.6	29	0.5	0.4	0.92	P(NdFeB)	0.6	0.012	0.088	0.029	1.37		7.88E+15	1.71E+17	0.69
Revolver#19B		7.2	32	3.6	2.8	0.4	H(NdFeB)	0.7	0.045	0.078	0.009	2.7		7.17E+16	3.52E+17	0.63
EMPW#28-U		16	12	1.92	3(11)		P(NdFeB)	0.53	0.045	0.127	0.008	3(3)		1.55E+16	1.00E+16	0.26
PF-AR 6.5/60																
Bend								1	0.2	0.593	0.036		26	3.90E+13	3.11E+13	
EMPW#NE1W		16	21	3.36	3(11)	1(0.2)	P(NdFeB)	1.07	1.07	0.268	0.032	15(3)	28(90%)	1.84E+15	2.54E+15	5.52
U#NE3		4	90	3.6	1	0.8	P(NdFeB)	1.57	0.17	0.312	0.029	3		1.29E+16	7.66E+15	3.708
U#NW2		4	90	3.6	1	0.8	P(NdFeB)	1.57	0.17	0.312	0.029	3		1.29E+16	7.66E+15	3.708
U#NW12		4	95	3.8	1	0.8	P(NdFeB)	1.57	0.17	0.312	0.029	3		1.29E+16	7.66E+15	3.912
U#NW14-36		3.6	79	2.8	1	0.8	P(NdFeB)	1.35	0.14	0.338	0.036	2.8		7.69E+15	6.49E+15	3.12
U#NW14-20		2	75	1.5	0.8	0.63	P(NdFeB)	0.75	0.07	0.383	0.038	1.17		7.69E+15	6.49E+15	0.936

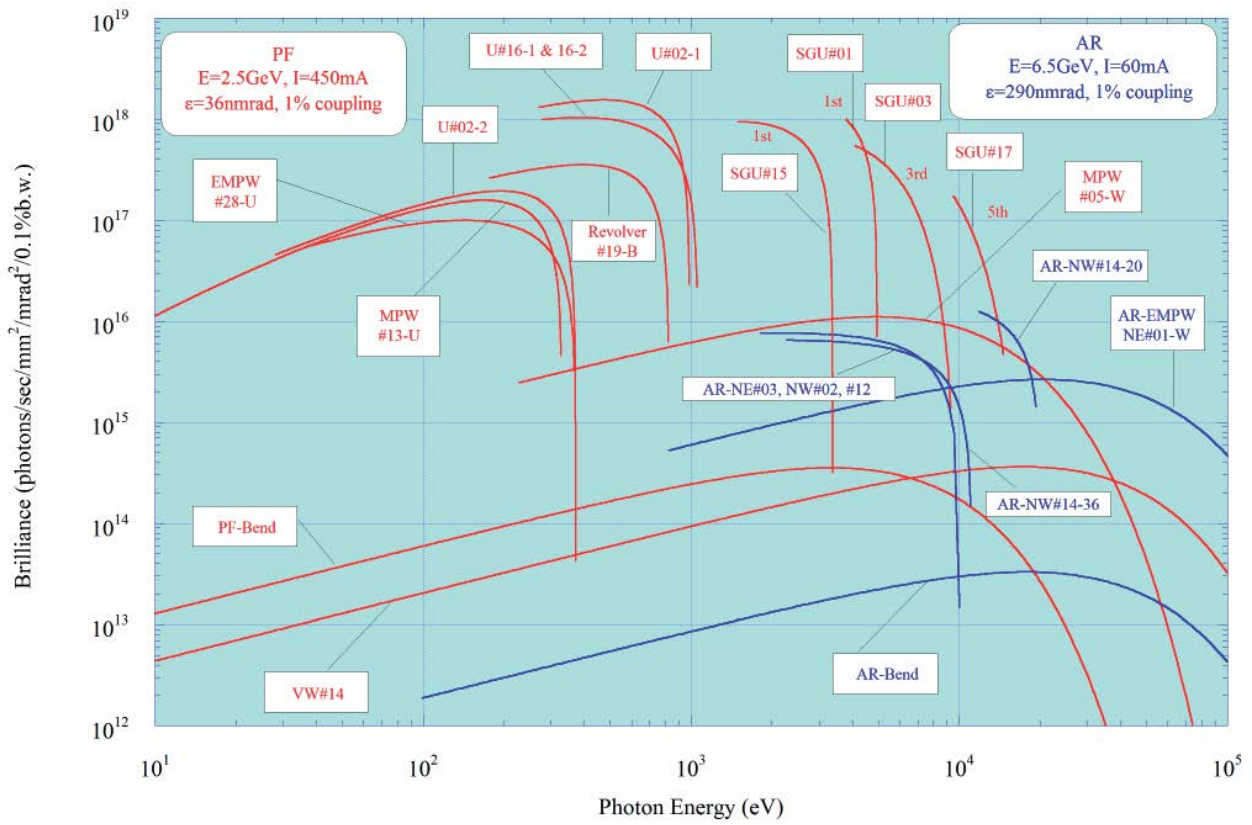
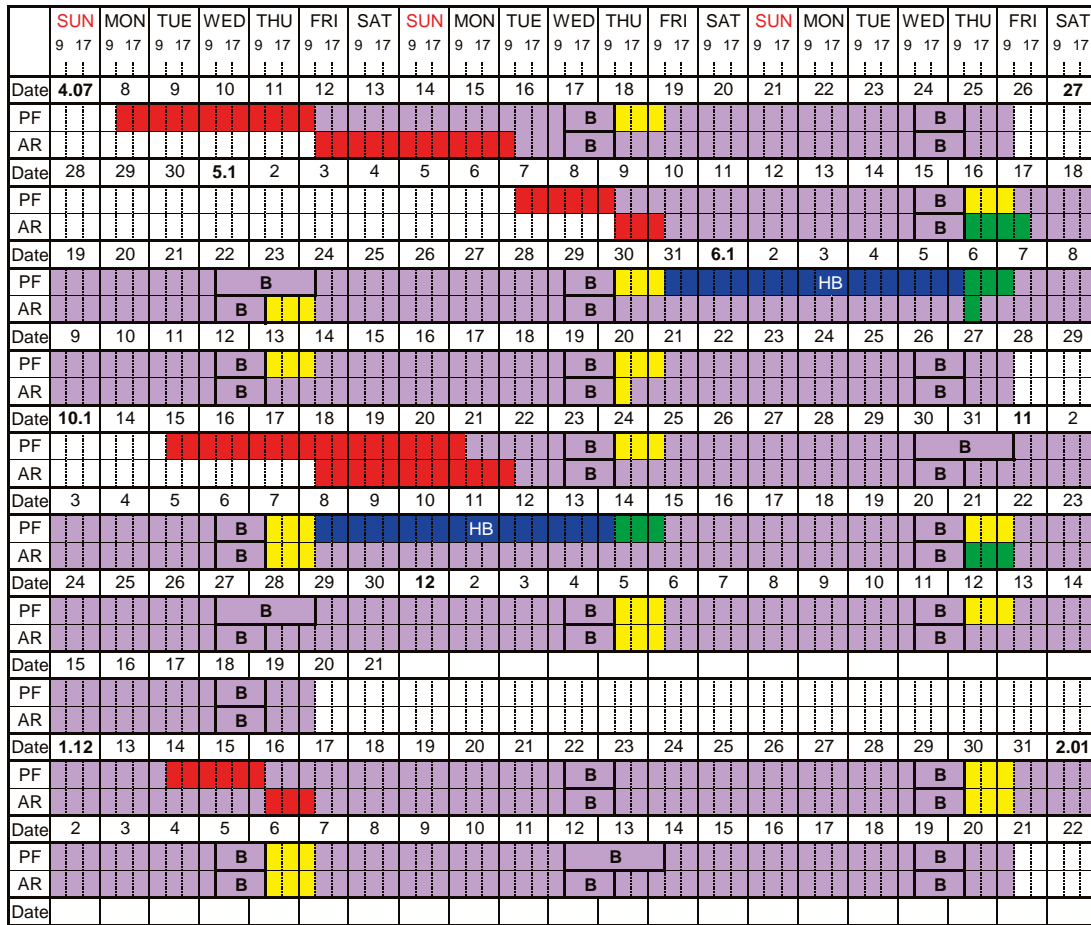


Figure 1: Synchrotron radiation spectra available at the PF Storage Ring (2.5 GeV) and the PF-AR (6.5 GeV). Brilliance of the radiation vs. photon energy are denoted by red curves for the insertion devices, SGU#01, U#02-1 & 02-2, SGU#03, MPW#05, MPW#13, VW#14, SGU#15, U#16-1 & 16-2, SGU#17, Revolver#19-B and EMPW#28, and bending magnets (PF-Bend) at the PF Storage Ring. Blue curves denote those for the insertion devices, EMPW#NE01, U#NE03, U#NW02, U#NW12, U#NW14-36 and U#NW14-20, and the bending magnets (AR-Bend) at the PF-AR. The name of each source is assigned in Table 2. Several insertion devices have both undulator and wiggler modes, which are denoted by U and W, respectively. The spectral curve of each undulator (or undulator mode of multipole wiggler) is a locus of the peak of the first harmonic within the allowance range of K parameter. For SGU#01 and SGU#15, the first harmonic regions are shown. For SGU#03, the third harmonic region is shown. For SGU#17, the fifth harmonic region is shown. Spectra of Revolver#19 for surface B are shown.

2-1 Operation Summary

A timetable of the PF ring and PF-AR operations in FY2013 is shown in Fig. 1. The operational statistics for the PF ring are summarized in Table 1. The statistics for each fiscal year since the commencement of the accelerator's operation are shown in Fig. 2. In FY2013, the

total operation time and actual user time were 4176.0 h and 3451.4 h, respectively. The actual user operation time was less than 4000 h because it was difficult to obtain the sufficient total operation time, owing to an increase in electrical charges, among other factors. The failure time for this year was 52.6 h, which is shown in Fig. 3 as a percentage of the total operation time.



- PF: PF ring
- AR: PF-AR
- Tuning and ring machine study
- Ring machine study
- Hybrid operation
- Short maintenance and /or machine study
- Experiment using SR

Figure 1: Timetable for the PF ring and PF-AR operation in FY2013.

Table 1: Operation statistics for PF ring in FY2013.

	Total
Ring operation time (h)	4176.0
Actual user time (h)	3451.4
Machine adjustment time (h)	672.0
Failure time (h)	52.6

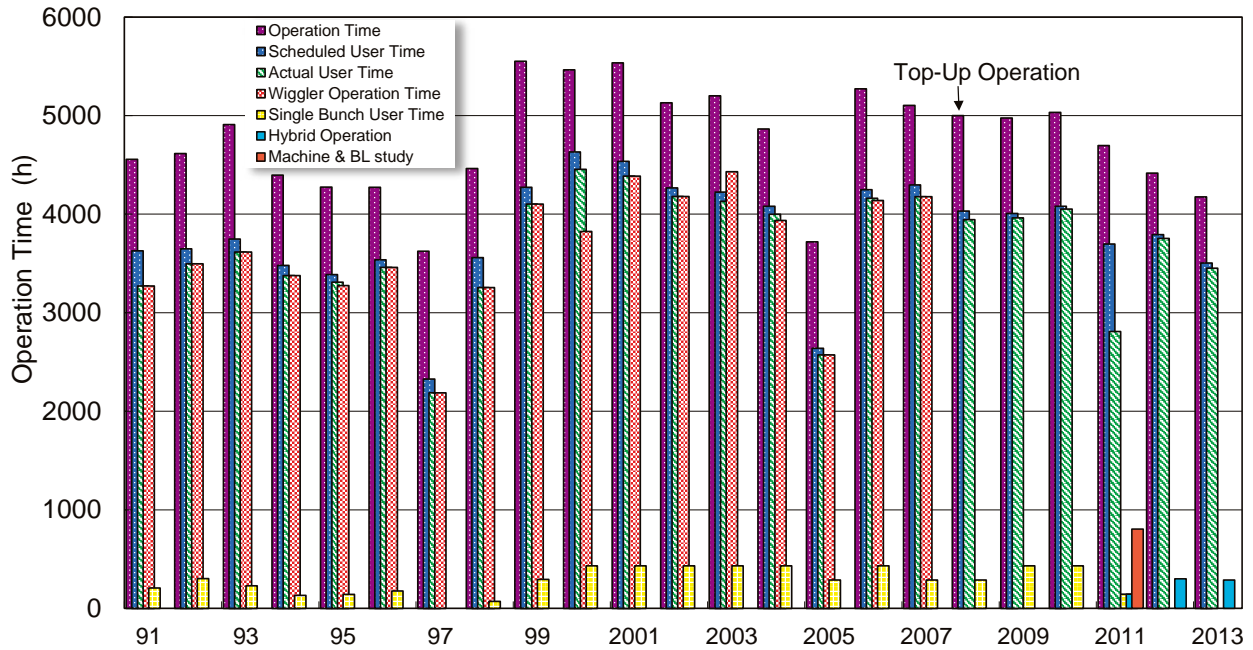


Figure 2: Total operation time, scheduled user time, actual user time, and single-bunch user time for the PF ring in each fiscal year since the commencement of accelerator operation.

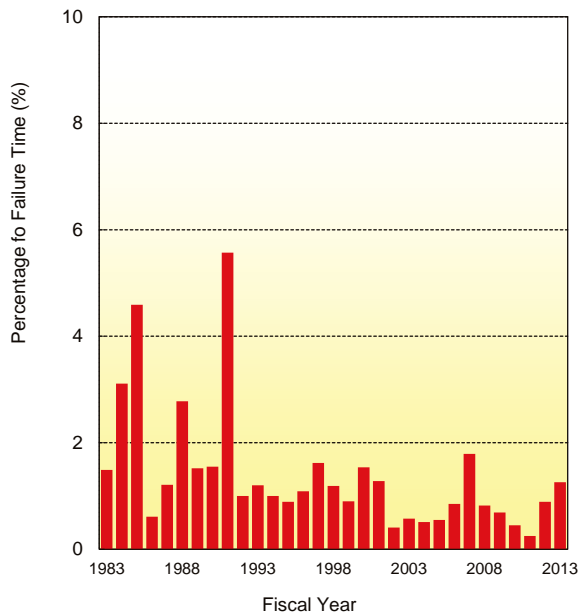


Figure 3: Percentage of failure time with respect to total operation time in the PF ring.

2-2 Project to Renew the Insertion Devices at the PF Ring

2-2-1. Installation of a new short gap undulator (SGU#15)

A new short gap undulator (SGU), SGU#15, was installed at the straight section of B14-15 during the summer shutdown of the PF ring. In the PF storage ring, there are four 1.4m-long straight sections for SGU in an in-vacuum configuration for the X-ray light source with energy of around 10 keV. We have constructed three SGUs with a period length of less than 20 mm step by step over the last eight years. SGU#15 is the fourth SGU with a period length of 17.6 mm as a light source for both small-angle X-ray scattering experiments and XAFS experiments. Table 2 compares the basic parameters of the SGUs.

We installed SGU#15 in the PF ring in August 2013 after commissioning of the vacuum system. Figure 4 shows a photograph of the baking of SGU#15 and Figure 5 shows a photograph of the installation of SGU#15. User operation of SGU#15 started steadily following the autumn operation of the PF ring. During the commissioning study, we confirmed the operation with the minimum gap of 4 mm and tuned the correction magnets at both ends of the SGU for the independent tuning operation of SGU#15.

Table 2: Basic parameters of SGUs in the PF ring.

Name	Period length (mm)	Number of periods	Maximum By (T)	Minimum gap (mm)	Target photon energy region (KeV)	Year of construction
SGU#17	16	29	0.92	4	6-13	2005
SGU#03	18	26	1.0	4	4-14	2006
SGU#01	12	39	0.7	4	4-13	2009
SGU#15	17.6	29	0.96	4	2-15	2013

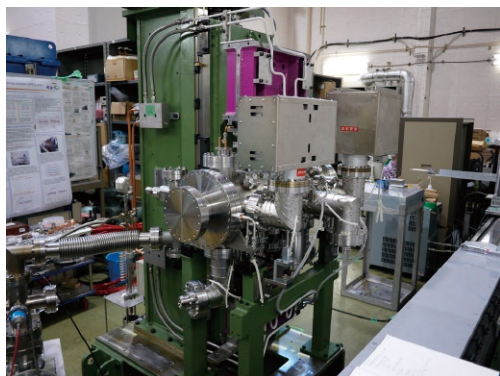


Figure 4: SGU#15 during vacuum commissioning.



Figure 5: SGU#15 during installation.

2-2-2. Construction of the new undulator (U#02-2) for BL02

At the PF ring, a project to renew the insertion devices for BL02, BL13 and BL28 is under way. These three insertion devices are all elliptically polarizing undulators (EPU) to obtain various polarization states. As the first step, we constructed U#02-2 for BL02 this year.

U#02-2 has a period length of 160 mm to obtain photons in the VUV energy region from 30 eV to 300 eV with the first harmonic radiation. The periodicity number of U#02-2 is 17 and the maximum K value is 5. U#02-2 has the same magnetic arrangement of the SPring-8 circular undulator as the EPU. U#02-2 has six variable rows of magnetic arrays to control the various polarization states of radiation. The two center arrays produce a vertical magnetic field and the four side arrays produce a horizontal field. The polarization states are selected by controlling the longitudinal positions of these rows individually. The available polarization modes of U#02-2 are linear polarization in the horizontal and vertical directions, circular polarization ($B_x/B_y = 1$) and elliptical polarization ($B_x/B_y = 1/2$).

The magnetic adjustment of U#02-2 was finished as scheduled. First, we adjusted the vertical magnetic field produced by the center arrays in December 2013. After magnetic measurements of the vertical magnetic field, we assembled and adjusted the four side magnet arrays for the horizontal magnetic field in February 2014. Figure 6 shows a photograph of U#02-2 during the magnetic adjustment.

We installed U#02-2 at the straight section of B01-B02 of the PF ring in March 2014. We moved the existing undulator (U#02-1) to the downstream of the straight section, and installed U#02-2 in tandem at the upstream of U#02-1. Figure 7 shows a photograph of U#02-1 and U#02-2 during installation in the PF ring. The right-side undulator is the new U#02-2. We use U#02-1 and U#02-2 exclusively to obtain photons over a wide energy region at the single beamline. U#02-2 became operational for user experiments after commissioning in the PF ring. User operation of U#02-2 started in linear polarization mode along the horizontal and vertical directions in May 2014. The other operation modes will soon become available in turn.



Figure 6: U#02-2 during the magnetic adjustment.



Figure 7: U#02-1 and U#02-2 during installation.

3-1 Operation summary

In FY2013, the construction of the tunnel for the direct beam transport (BT) line was almost completed. The lattice design of the 6.5-GeV BT line has been finished, and the production of DC magnets, kicker and septum magnets, pulsed bending magnets, and vacuum ducts was started. Details of the project to realize the full-energy top-up injection will be described in the next section.

In summer 2013, 16 power supplies of the quadrupole magnets were updated. We have continued to update aged power supplies year by year. There are eight power supplies still waiting to be updated, while there are a total of 28 quadrupole power supplies operating in the PF-AR.

Figure 1 shows the full history of the operation time. The operation statistics are summarized in Table 1. The total operation time has remained at about 4000 h and the user time was much less than the required 4000 h in these three years. The insufficient operation time was due to the unavoidable factors of budget circumstances and higher electricity bills. The accelerator group made an effort to reduce the time for accelerator conditioning and to keep a high user time ratio at around 90%.

The numbers of failures by source are summarized in Table 2 for recent years, and are classified by down

time as a pie chart in Fig. 2. In FY2013, failures in beam injection including ramping up and those in beam instrumentation (control/monitor) increased.

The 30-year-old analog detection circuits of the beam position monitor (BPM) caused repeated troubles for COD measurement and emergency repair was necessary. To improve the BPM system, new signal transmission cables are being prepared, and the detection circuits are planned to be renovated by the end of FY2014.

Construction of the new BT tunnel near the present BT line might disturb the condition of the beam injection. When the full-energy injection is realized in future, most of the beam instabilities affecting the injection will be resolved, and stable, efficient injection is expected. The dust-trapping decreased drastically in FY2013. This is thought to be a side effect of the reduced stored current due to the insufficient injection condition.

The total down time in FY2013 amounted to about 100 h, which is unfortunately the worst result in recent years. The longest down time was a 24-hour cancellation of user time in order to secure radiation safety for the construction site of the BT tunnel. The other long down time was a 20-hour interruption because of an initial defect in a quadrupole power supply installed in summer 2003.

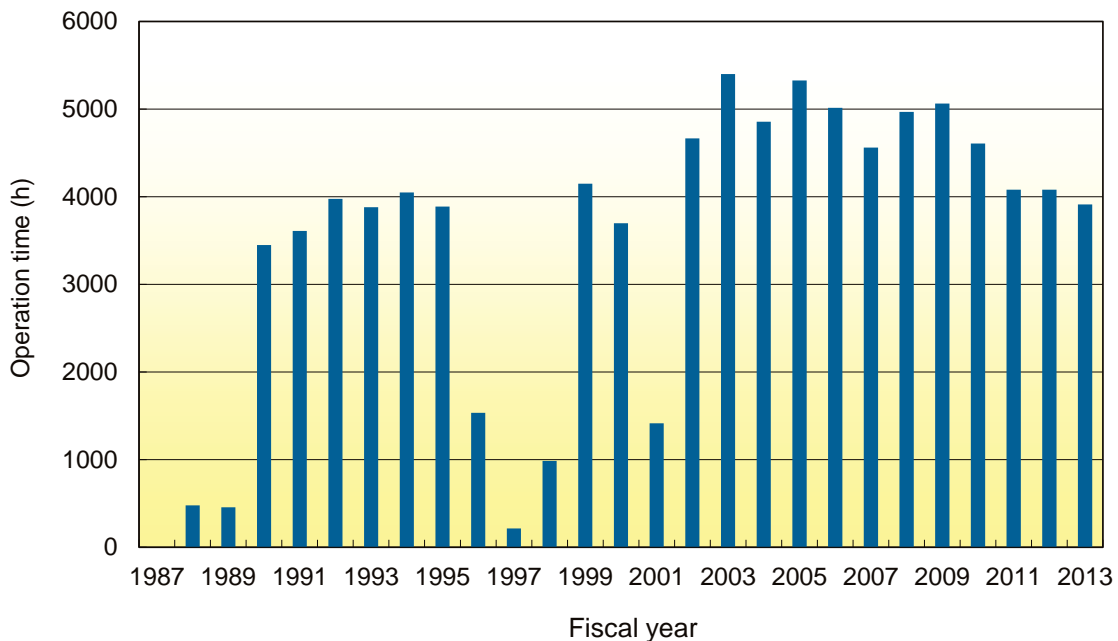


Figure 1: Full history of the operation time of the PF-AR.

Table 1: Operation statistics and mean time between failures (MTBF) during FY2005 – FY2013.

Fiscal year	2005	2006	2007	2008	2009	2010	2011	2012	2013
Total operation time (h)	5313	5016	4561	4969	5063	4608	4080	4080	3912
Scheduled user time (h)	4456	4032	3624	4344	4392	4032	2904	3672	3478
Ratio of user time (%)	83.9	80.4	79.5	87.4	86.7	87.5	71.2	90.0	88.9
Number of failures	79	51	60	40	41	74	49	33	47
Total down time (h)	69.3	55.1	45.2	41.7	91.0	73.7	38.7	29.7	99.6
Failure rate (%)	1.6	1.4	1.2	1.0	2.1	1.8	1.3	0.8	2.9
MTBF (h)	56.4	79.1	60.4	108.6	107.1	54.5	59.3	111.3	74.0
Mean down time (h)	0.9	1.1	0.8	1.0	2.2	1.0	0.8	0.9	2.1

Table 2: Classification of failures by source of trouble.

Fiscal year	2005	2006	2007	2008	2009	2010	2011	2012	2013
RF	12	10	1	4	8	10	5	4	5
Magnet	4	1	1	2	2	10	8	3	4
Injection	4	3	8	9	1	6	4	3	18
Vacuum	2	6	2	0	2	1	0	1	0
Dust trap	37	24	39	15	16	24	20	13	3
Insertion devices	0	1	0	0	0	0	0	0	0
Control / Monitor	4	0	1	1	1	2	1	2	8
Cooling water	5	1	0	3	4	4	1	0	2
Safety / Beamline	9	4	5	5	7	17	3	4	3
Earthquake	2	0	1	0	0	0	5	3	1
Electricity	0	1	2	1	0	0	2	0	3
Total	79	51	60	40	41	74	49	33	47

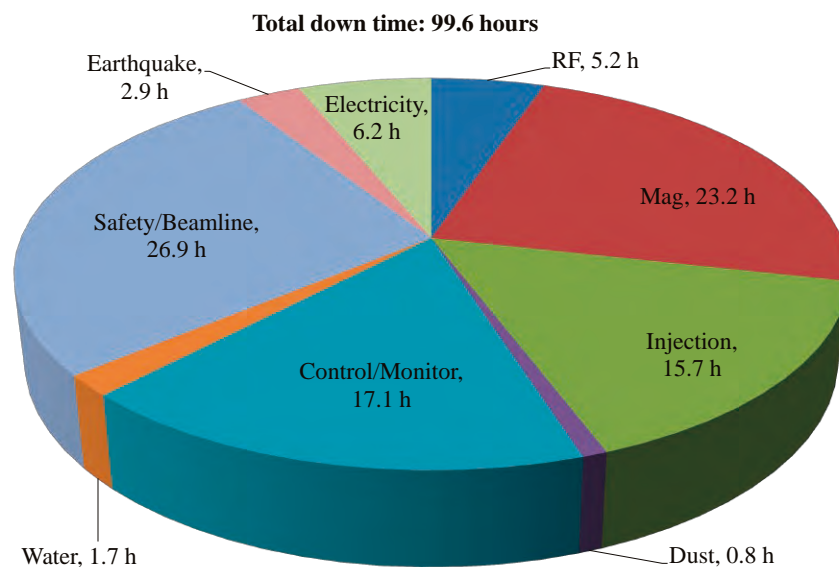


Figure 2: Pie chart of the down time in FY2013.

3-2 New PF-AR Transport Line

Construction of a new beam transport line (BT) for the Photon Factory Advanced Ring (PF-AR) started at KEK's Tsukuba campus in April 2013. This new BT will enable 6.5-GeV full energy injection and top-up operation for the PF-AR. At present, the beam injection is carried out with beam energy of 3 GeV, and the accumulated beam with a beam current of 60 mA is ramped up to 6.5 GeV. Then, the user operation starts. Beam injection is done twice a day and it takes about 15 minutes for each injection. So far, the PF-AR has used the common BT with the KEKB (8-GeV electrons) as shown in Figure 3. During the PF-AR beam injection, the BT was optimized for the PF-AR and the KEKB beam injection was pending.

Fast switching injection with 50 Hz from the KEK LINAC to the three rings, the PF-ring (2.5 GeV) and the KEKB LER (3.5 GeV) / HER (8 GeV), has already been achieved. In the upcoming SuperKEKB project, the estimated beam lifetime is as short as 10 minutes, so fast switching injection to the PF-AR is required by the start of the physics run at SuperKEKB in January 2016. Therefore, the new BT is separated from the SuperKEKB BT at the end of the KEK LINAC using a pulsed bending magnet as shown in Figure 3. The separated beam for the PF-AR passes through a new tunnel, about 200 m long, and injected the PF-AR.

Construction of the tunnel was started in April 2013, and will be completed in FY2013. Figure 4 shows the precursor tunnel and the inside of the tunnel. The construction of infrastructure (cooling water, etc.) will begin in April 2014 and end in September 2014. The accelerator components such as the magnet, vacuum and monitor systems were fabricated in FY2013 (Figure 5). The components will be adjusted and the infrastructure of electric devices and the cooling water system will be constructed in FY2014. Installation of the accelerator components and beam commissioning of the direct BT are scheduled for FY2015. Optical parameters from the end of the injector linac to the injection point of the PF-AR are shown in Figure 6.



Figure 4: Upper photograph: the precursor tunnel in November 2013. Lower photograph: the inside of the tunnel before painting.



Figure 5: Fabricated magnets.

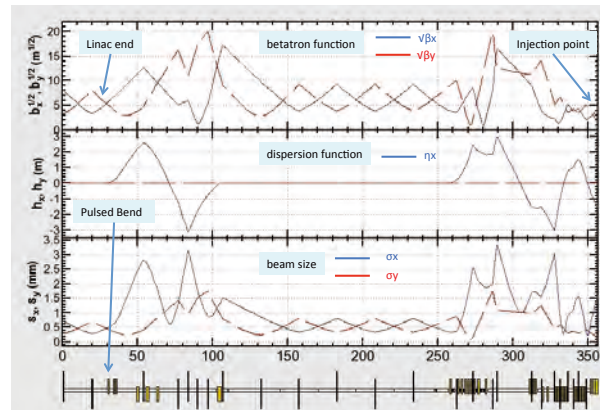


Figure 6: Optical functions from the end of the injector linac to the injection point of the PF-AR. Blue and red lines represent the horizontal and vertical parameters, respectively.

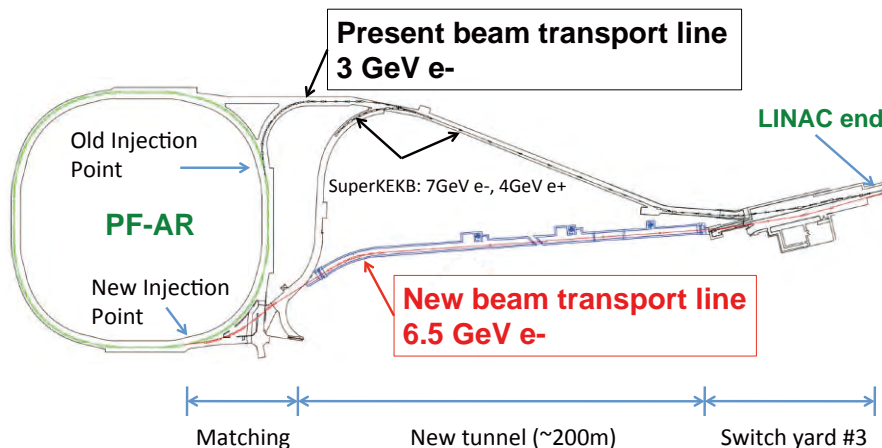
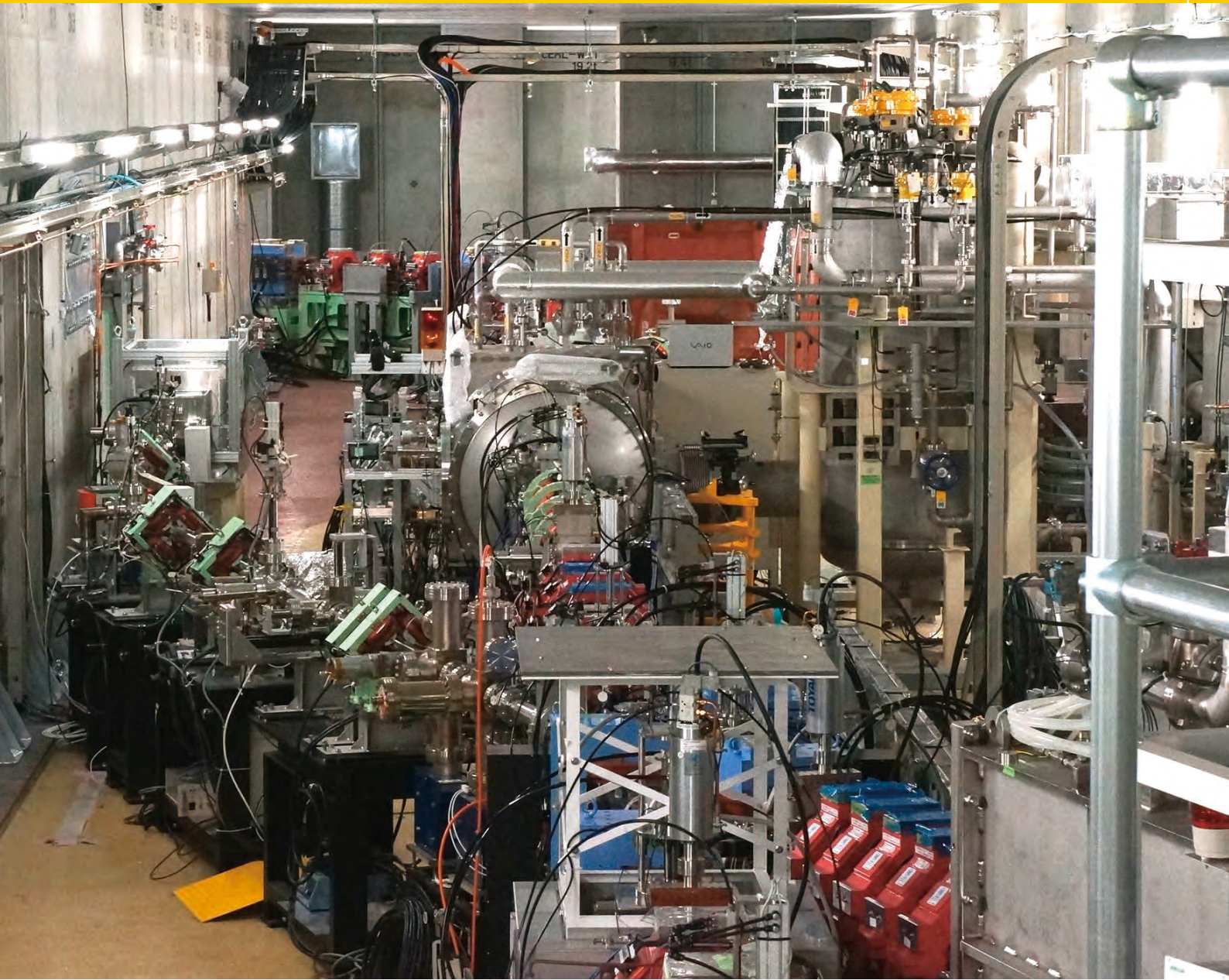


Figure 3: New beam transport line (red) for the PF-AR. The black line shows the present beam transport line; the blue area is the new tunnel.

Future Light Source



Future Light Source

1. ERL Project Overview	109
2. cERL	110
2-1 cERL Overview	
2-2 Commissioning of cERL	

1

ERL Project Overview

KEK established the ERL (Energy Recovery Linac) Project Office in April 2006. Because a GeV-class ERL machine had not been constructed anywhere in the world, it was necessary to first construct a compact ERL (cERL) with an energy of 35 MeV that could be used for the development of several critical accelerator components such as a high-brilliance DC photocathode electron gun and superconducting cavities for the injector and main accelerator. In the 2013 fiscal year, the cERL were successfully installed in an ERL test facility and the energy recovery beam operation has been successfully demonstrated.

In 2013 fiscal year, the commissioning of the cERL has been done by two-steps. The first step is the commissioning of the injector part; the high-brightness DC electron gun and superconducting cavity for injector and other component to examine the electron beam qualities. The beam test successfully has been completed from April to end of June. Then, during the period of July

to November, the recirculation loop; electric magnets, beam monitors and vacuum components, has been installed, and we could start the commissioning of the whole energy recovery Linac from the end of December. The commissioning has successfully progressed and the ERL operation as shown in Fig. 1 has been confirmed at 12th of March with the following machine parameters. The electron beams are accelerated up to 390 keV by the DC electron gun accelerates, then up to 2.9 MeV by the injector super-conducting cavity, and finally up to 20 MeV by the main linac super-conducting-cavity. Then, the return electron beams are decelerated by the superconducting cavity down to 2.9 MeV and go to a beam dump. The beam current is 6 μA . The beam current will be increased up to 10 mA at least in a step-by-step manner for several years and also we will install laser-Compton-Scattering (LCS) X-ray beamline at next fiscal year 2014.

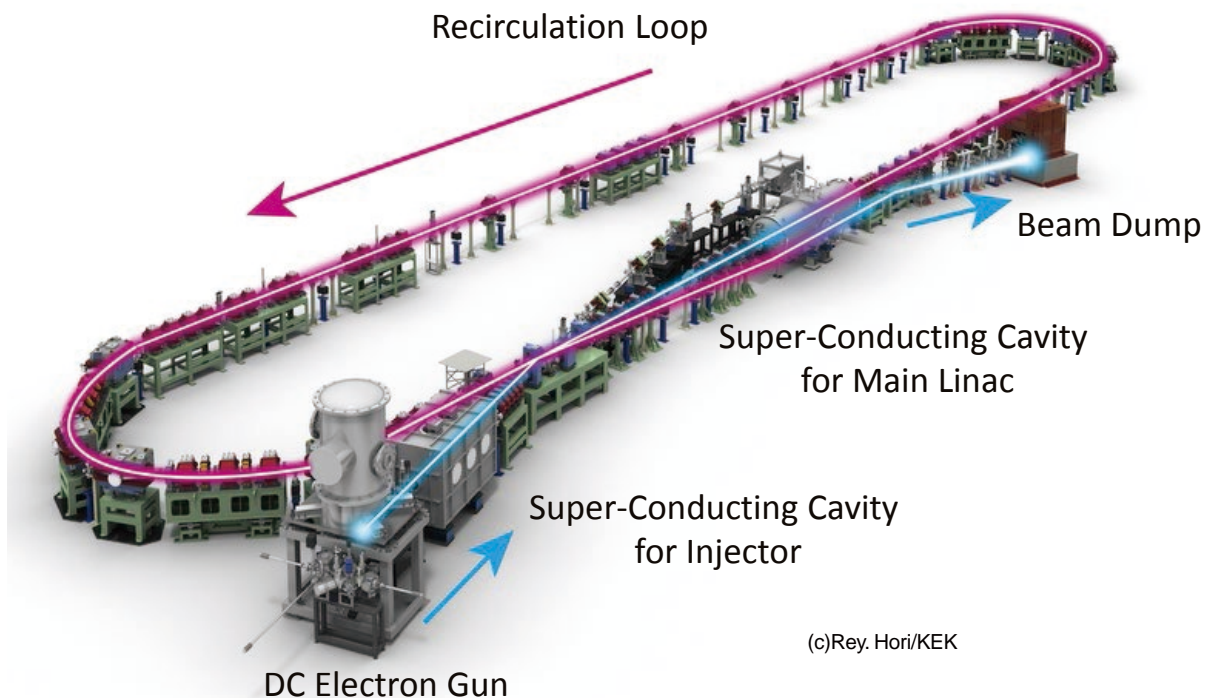


Figure1: Bird view (CG) of the cERL. The energy of the electron beam from the injector to main linac is 2.9 MeV (blue color), then the electron beams are accelerated up to 20 MeV (red color) by the super conducting cavity for main linac. The electron beams return back to the cavity with energy of 20 MeV and are decelerated down to 2.9 MeV, then go to a beam dump.

2

cERL

2-1 cERL Overview

To demonstrate the generation and recirculation of low-emittance and high-current beams that are required for the 3-GeV ERL project (PEARL) [1], the Compact ERL (cERL) [2] has been constructed at KEK. The cERL consists of a 5-MeV injector, a 30-MeV main linac, and a recirculation loop. The principal parameters of the cERL are given in Table 1.

High-brightness electron beams are produced in the photocathode DC electron gun of the injector. The beams are accelerated up to a nominal energy of 5 MeV using a superconducting (SC) injector cryomodule. The beams are merged with the SC main linac where they are accelerated to a nominal energy of 35 MeV, and then are transported through the recirculation loop. The beams are then decelerated in the main linac, and are dumped. The beams from the injector can also be transported through the injector-diagnostic beamline where various beam properties can be measured.

The injector was constructed in FY2012, and was completed in April, 2013. Commissioning of the injector was carried out from April to June, 2013 [3]. During this period, we demonstrated the production and acceleration of low-emittance beams, which is described in the next section. We also demonstrated stable operation of the injector including the photocathode DC gun under a cathode voltage of 390 kV as well as the SC cavities of the injector with a typical accelerating gradient of 7 MV/m. The total beam-operation time during the injector commissioning was approximately 202 hours.

From July to November, 2013, we constructed the recirculation loop of the cERL [4]. First, base plates for the magnets were installed in the cERL accelerator room (radiation shielding). Next, the magnets including eight bending magnets and 60 quadrupole magnets with their girders were installed. The magnets were then precisely aligned using both a laser tracker and a tilting level; 40 surveying references, which were located at the inner walls of the accelerator room, were used as references. In this installation process, the magnets were aligned within ± 0.1 mm in position and within ± 0.1 mrad in angle. The upper parts of the magnets were then removed, and all vacuum chambers were

installed. Thirty screen monitors and 45 stripline beam-position monitors (BPMs) were also installed. After the magnets were reassembled, it was found that the magnets were aligned less accurately (mostly, ± 0.5 mm in position and ± 0.5 mrad in angle), however, we did not realign the magnets due to limited time.

The main-linac cryomodule having two nine-cell SC cavities was installed in FY2012. During the high-power test, the two cavities achieved accelerating voltages of 14.2 MV and 13.5 MV, respectively, for more than 1 hour. However, field emissions emerged at an accelerating voltage of about 8 MV. Then, we decided to start commissioning of the entire cERL with an accelerating voltage of 8.5 MV/cavity, by which the beam energy in the recirculation loop was determined to be 20 MeV.

We also installed power supplies for the magnets, as well as the electronics for the beam diagnostic system, vacuum system, and so on, outside the accelerator room. The construction of the cERL was completed in November 2013. The present (at the end of FY2013) layout of the cERL is shown in Fig. 1. Figures 2 and 3 show photographs of the cERL.

From December 2013 to March 2014, we commissioned the entire cERL. During this period, electron beams were successfully recirculated through the recirculation loop, and were decelerated and transported to the beam dump with small beam losses. The maximum beam current of about $6.5 \mu\text{A}$ was achieved under continuous-wave (CW) operation. The principal parameters achieved during this period are given in Table 2. In the next section, the commissioning of the cERL is reported in detail. With these achievements, we are going to the next stage with high-bunch-charge or high-current operations which are needed to construct the 3-GeV ERL.

REFERENCES

- [1] "Energy Recovery Linac Conceptual Design Report", *KEK Report 2012-4* (2012)
<http://ccdb5fs.kek.jp/tiff/2012/1224/1224004.pdf>
- [2] S. Sakanaka *et al.*, *Proc. of IPAC13* (2013) 2159.
<http://accelconf.web.cern.ch/AccelConf/IPAC2013/index.htm>
- [3] S. Sakanaka *et al.*, *Proc. of ERL2013* (2013)16.
<http://accelconf.web.cern.ch/AccelConf/ERL2013/index.htm>
- [4] N. Nakamura *et al.*, *Proc. of IPAC14* (2014) 353.
<http://inspirehep.net/record/1314288?ln=ja>

2-2 Commissioning of cERL

2-2-1. Commissioning of Injector beam line

The beam commissioning of the cERL was carried out in two steps. First, the injector beamline, which consists of a photocathode DC gun, two solenoid magnets, a bunching cavity, superconducting injector cavities, five quadrupole magnets, and a beam diagnostic line to measure the injector beam performance, was placed into operation. The maximum beam energy and current were limited to 6 MeV and 1 μA , respectively. In the second step, we constructed a merger section and a recirculation loop with main superconducting cavities, and operated the whole ERL to demonstrate energy recovery without beam loss. In the second step, the maximum beam energy and current were increased to 35 MeV and 10 μA , respectively.

From 22 April 2013 to 28 June 2013, we carried out the beam commissioning of the cERL injector beamline to demonstrate high-quality beam generation from the photocathode gun, beam acceleration by the injector superconducting cavities, and beam transportation without degradation of beam quality. The photocathode gun, which was developed by JAEA, was operated at 390 kV. Although the maximum gun voltage was 500 kV, which was demonstrated at JAEA, it was reduced to 390 kV to avoid the discharge around the ceramic insulator. As a photocathode material, we employed a GaAs photocathode with NEA surface to generate a low-emittance beam. In order to confirm the low-emittance beam generation from the photocathode gun, we measured the transverse emittance using the solenoid scan method for very low bunch charge operation with 10 fC. The measured normalized emittance was 0.07 mm mrad, which was almost the same as the expected value from the GaAs photocathode.

The 390-keV electron beam was accelerated by the

injector superconducting cavities. After phase tuning of the cavities, we succeeded in accelerating the beam to 5.6 MeV with the acceleration field gradient of 7 MV/m. It only took 5 days to generate, accelerate and transport the electron beam to the beam dump without beam loss. On 23 May 2013, a radiation safety inspection of the injector beamline was performed with the average current of 200 nA, and we received a certificate of passing the inspection on 27 May 2013.

After the radiation safety inspection, we continued the beam operation for hardware performance tests, beam quality measurements, and fine beam tuning. The summaries of these are as follows. The photocathode gun operation was very stable, and there was no discharge during the injector commissioning. The injector superconducting cavities were also very stable with the acceleration gradient of 7 MV/m. The refrigerator for superconducting cavities had a few troubles, but these were not serious and the downtime was less than several hours.

The beam emittance after the injector cavities was measured for low bunch charge and for high bunch charge. For low bunch charge operation with 10 fC, the transverse normalized emittance was 0.17 mm mrad. This was slightly larger than the expected value of 0.1 mm mrad by particle tracking simulation without space charge effect. Figure 4 shows that the beam profiles for low bunch charge operation. For high bunch charge operation with 7.7 pC, the emittance was less than 0.8 mm mrad, which depends on the condition of the beam transportation; this was larger than the expected value of 0.3 mm mrad by particle tracking simulation with space charge effect. For high bunch charge operation, we did not allow enough time for fine beam tuning. In the next beam operation, we plan to perform fine beam tuning around the injector superconducting cavities to reduce the emittance growth.

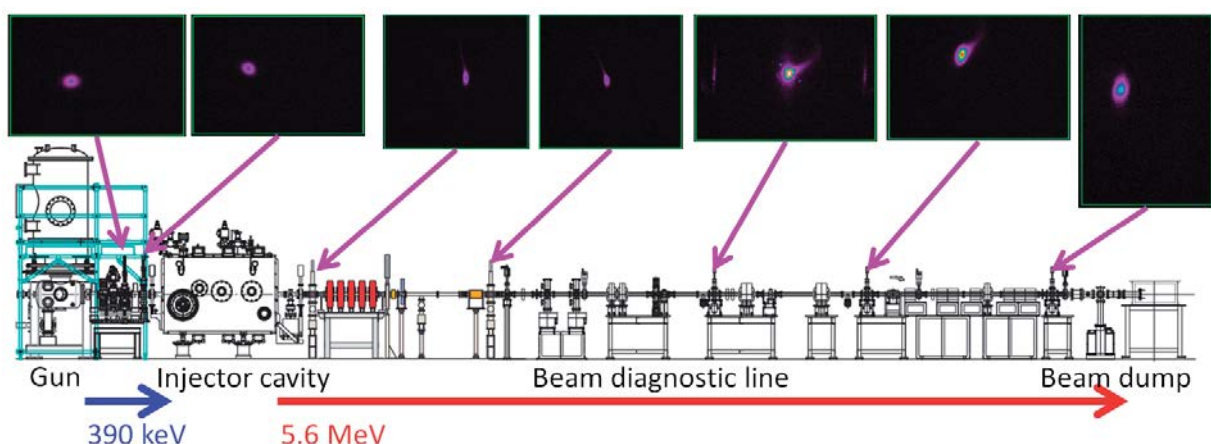


Figure 4: Transverse beam profiles in beam commissioning of cERL injector. The profiles were measured at screen monitors. Average beam current and bunch charge were 150 pA and 20 fC, respectively.

2-2-2. Commissioning of Recirculation Loop

The arc section of the recirculation loop consists of four 45-degree bending magnets and two quadrupole triplets, in which the beam optics are designed to make it isochronous and achromatic. The layout of the recirculation loop is shown in Fig. 5. A straight section between the two arc sections includes a pathlength control chicane and an interaction point of laser inverse Compton scattering. The injection beam is transported to the main linac through the injection chicane and merges with the recirculation beam. The recirculation beam is decelerated down to the injection energy, and then led to the main dump through the dump chicane.

The beam commissioning of the recirculating loop was performed for almost two months from Dec. 2013 to Mar. 2014 (including a one-month shutdown). The applied voltage of the DC electron gun is 390 kV, the same as was used during injector commissioning. During beam tuning, the average beam current is kept at less than 1 nA with a bunch charge of 10–100 fC and a pulse duration of 1 μ s. The acceleration field of the main cavity is limited to 8.5 MV per cavity to avoid increasing the radiation dose outside the accelerator room due

to field emission. Concerning the kinetic momentum of the electron beams, the ratio of the injection to the recirculation beam should be less than seven because the physical aperture is limited by the vacuum chamber of the chicanes. Accordingly, the injection and recirculation energy are set to 2.9 MeV and 20 MeV, respectively.

In the first week, we succeeded in accelerating the electron beam up to 20 MeV with the two cavities, which was confirmed at the 45-degree bending magnet. Stability factors of the low-level RF during beam operation were less than 0.02% in amplitude and 0.02 degree in phase, which satisfy the requirements of cERL. However, the decelerated beam failed to reach the main dump because the leakage magnetic field of BMAG05 in Fig. 6 kicked the injection beam during the orbit tuning of the recirculation beam. In addition, it was found that the magnet of the cold cathode gauges (CCGs) kicked and distorted the low-energy injection/dump beam (Fig. 7). To remove such an unwanted magnetic field, a magnetic shield was added in the injection/merger chicane during the beam shutdown in Jan. 2014 and some CCGs were removed without serious effect on vacuum monitoring.

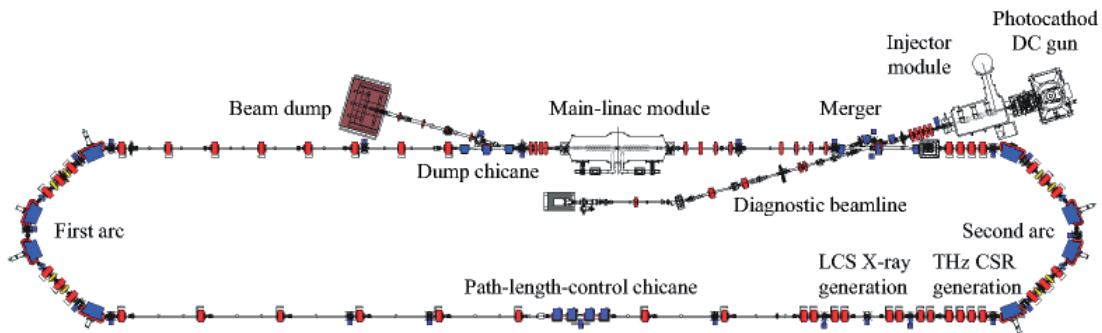


Figure 5: Illustration of the cERL.

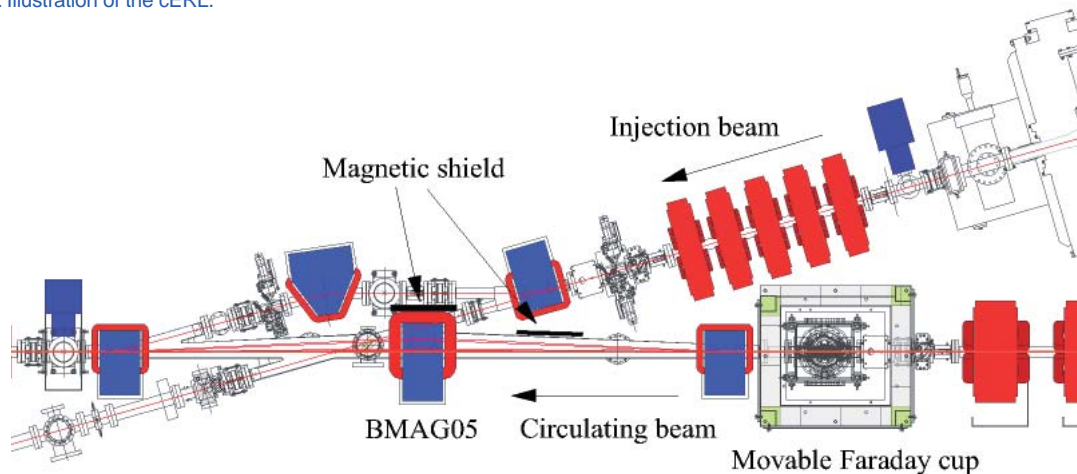


Figure 6: Effects of magnetic field of BMAG05 on the 2.9-MeV injection beam. Iron plates are effective as a magnetic shield.

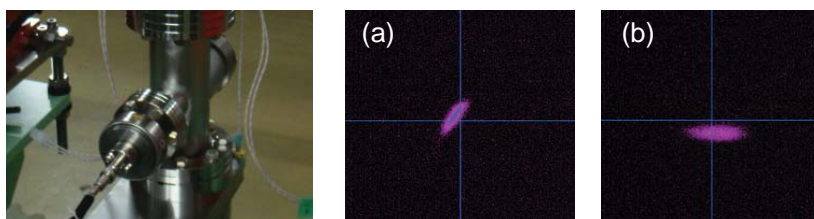


Figure 7: Left: Magnet of CCG (20 cm from chamber) Right: Beam profile (a) before and (b) after removing CCG and optics matching.

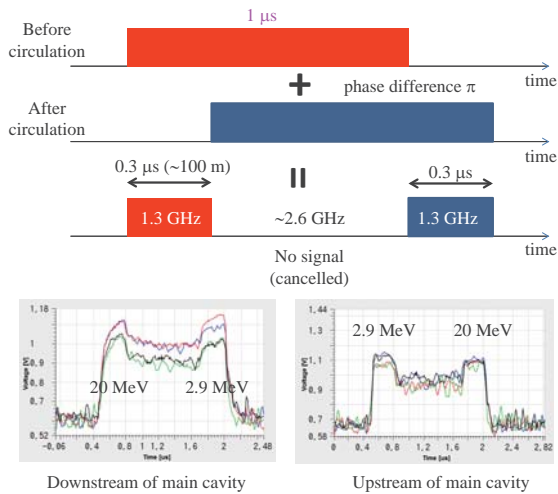


Figure 8: BPM signal of two accelerated and decelerated beams during burst operation. The signal is not completely cancelled even during the time period when both beams exist because the velocity of 2.9-MeV electrons is slightly different from the velocity of light.

In the region from the merger chicane to the dump chicane, it is impossible to monitor the circulation beam with an invasive beam diagnostics tool such as a screen monitor. Therefore, to distinguish the recirculation beam from the injection beam, a strip-line BPM as a non-invasive monitor was utilized in a burst mode operation. In principle, BPM with a 1.3-GHz bandpass filter is insensitive to the 2.6-GHz beam signal, in which the recirculating beam is out of phase with the injection beam by π . However, the head (tail) of the rectangular burst pulse transports the main linac without accompanying the recirculating (injection) beam as shown in Fig. 8. The temporal duration of the head (tail) is almost 300 ns with the recirculation loop of 92 m. This duration is long enough to distinguish the two beam position signals. Orbit tuning of the two beams is enabled by the simultaneous measurement with BPM and the decelerated beam was successfully observed at the main dump in a week. Figure 9 shows the beam profiles on the screen monitors and signals of Faraday cups in Feb. 2014. There is no significant beam loss in the recirculation loop according to the beam current measured by three Faraday cups, which are located at the DC electron gun, the exit of the second arc (Fig. 6) and the main dump. The en-

ergy of the dump beam is close to that of the injection beam, which is assumed from the bending radius of the BMAD01 (in Fig. 11).

To increase the efficiency of the energy recovery, the recirculation beam needs to match the deceleration RF phase of the main cavity. Therefore, fine tuning of the pathlength of the recirculation loop (recirculation time) is demonstrated with (a) a path-length chicane and (b) steering magnets of the second arc in Fig. 10. The pathlength was optimized to minimize the dump energy because the average beam current at the beam tuning is too low to observe the beam loading at the main cavity. The results are shown in Fig. 11. The bending angle of BMAD01 has a maximum value, in which the dump energy is assumed to be close to a minimum value.

After completing the beam tuning, 6.5 μA CW operation was demonstrated to observe the beam loading of the main cavity. The results are shown in Fig. 12. “Energy recovery test” means the normal operation of ERL. “Beam loading test” is another test, in which the electron beam is accelerated with the upstream cavity and then decelerated with the downstream cavity to lead into the main dump. There is no energy recovery in the latter test, which is performed as a reference. The difference between the input and reflection RF power, $\Delta(\text{Pin-Pref})$, in both tests is compared in Fig. 12. In the beam loading test, $\Delta(\text{Pin-Pref})$ of the upstream cavity has a positive value when the beam current exists. This means that input RF power is necessary in order to accelerate the electron beam without energy recovery. The downstream cavity receives the power from the decelerated electron beam, and vice versa. In contrast, $\Delta(\text{Pin-Pref})$ is constant regardless of the electron current in the energy recovery test. This proves that the power of the decelerated beam is recovered at the main cavity.

There are still problems concerning optics tuning and matching. We found that the beam response of some quadrupole magnets did not match the magnetic field measurements. In addition, unknown xy coupling appeared. Therefore, the single-kick response and the dispersion function of the two arc sections are slightly different from the design optics. These problems are now being investigated.

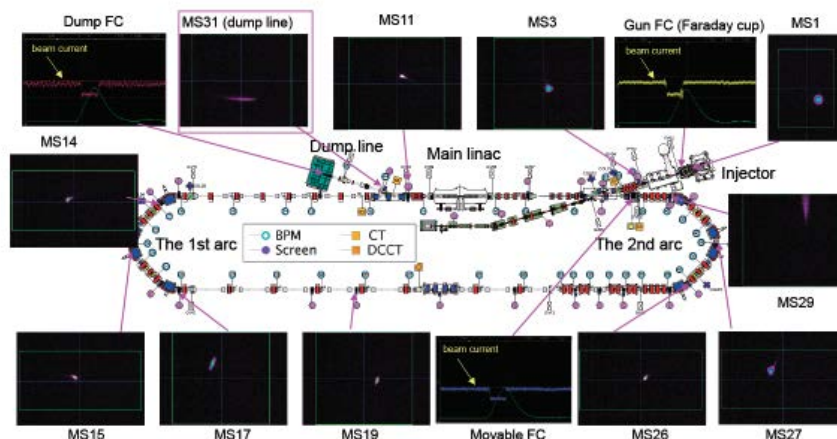


Figure 9: Beam profiles on the screen monitor and signals of Faraday cups (Feb. 2014).

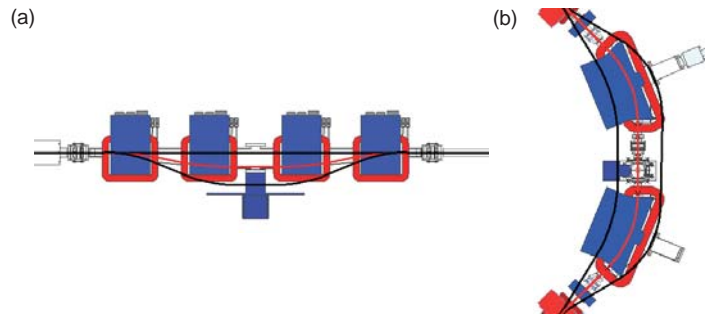


Figure 10: Magnetic pathlength control. (a) Chicane in the recirculation loop, (b) Combination of the steering magnet at the top of the second arc.

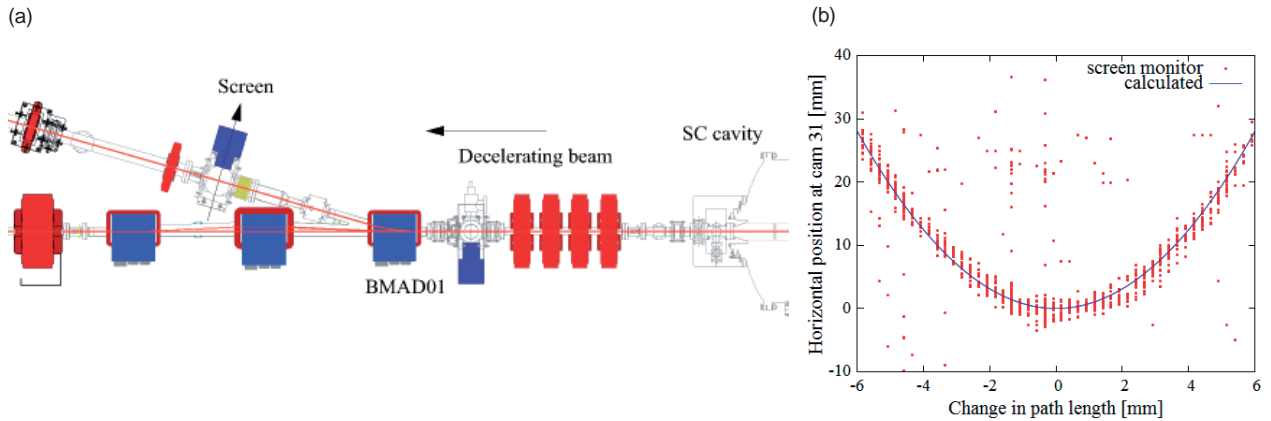


Figure 11: (a) Schematic of lattice layout at the dump chicane. (b) Plot of horizontal beam position at the screen (cam31) vs. pathlength of recirculation loop.

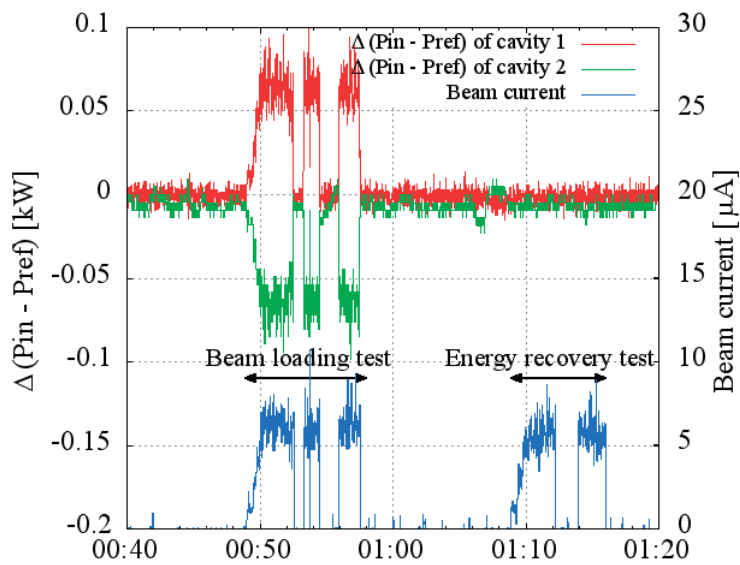


Figure 12: Plot of difference between the input and reflection RF power of the main linac, $\Delta(P_{in}-P_{ref})$ in the energy recovery test and the beam loading test. Cavity 1 and 2 mean the upstream and downstream cavity, respectively.

Users Program & Outreach Activities



Users Program and Outreach Activities

1. Experimental Proposals	119
1-1 Scientific Proposals	
1-2 Industrial Proposals	
1-3 Statistics of the Proposals	
2. Workshops and Seminars	122
2-1 IMSS Science Festa	
2-2 PF Workshops	
2-3 Seminars	
3. Graduate School Education	123
4. International Collaboration	124
4-1 Overview	
4-2 Indian Beamline	
4-3 Cooperation with the SESAME Project	

1 Experimental Proposals

1-1 Scientific Proposals

The Photon Factory accepts experimental proposals submitted by researchers mainly at universities and research institutes inside and outside Japan. The proposals are reviewed by the PF Program Advisory Committee (PF-PAC), and those that are favorably recommended are formally approved by the Advisory Committee for the Institute of Materials Structure Science. The number of accepted proposals over the period 2002-2013 is shown in Table 1, where S1/S2, U, G, and P denote Special, Urgent, General and Preliminary proposals, respectively. The number of current G-type proposals each year has exceeded 800 for the past few

years. A full list of the proposals effective in FY2013 and their scientific output can be found in Part B of this volume.

S-type proposals are divided into two categories, S1 and S2. S1 proposals are self-contained projects of excellent scientific quality, and include projects such as the construction and improvement of beamlines and experimental stations which will be available for general users after the completion of the project. S2 proposals are superior-grade projects that require the full use of synchrotron radiation or a large amount of beam time. Table 2 lists the S-type projects effective in FY2013. The current status and results to date of S1 and S2 proposals must be reported at the PF Symposium held

Table 1: Number of proposals accepted for the period 2002-2013.

Category	FY2002	2003	2004	2005	2006	2007	2008	2009	2010	2011	2012	2013
S1	0	1	1	0	1	0	0	0	0	0	0	0
S2	3	2	0	3	6	1	4	6	3	2	4	5
U	3	2	4	0	1	7	3	2	2	0	4	1
G	321	318	382	310	386	403	402	397	407	415	454	447
P	16	9	13	10	22	14	14	14	16	11	18	18

Table 2: List of S-type proposals effective in FY2013.

Proposal No.	Spokesperson	Title
2013S2-001	T. Matsushita KEK-PF	Development of time-resolved X-ray reflectometry and its applications
2013S2-002	Y. Murakami KEK-PF	Synchrotron radiation research on element strategy project_electronic materials: The study of functionalities in lightelement anion systems
2013S2-003	Y. Takahashi Hiroshima Univ.	Development of sustainable science by scanning transmission X-ray microscopy (STXM)
2013S2-004	K. Amemiya KEK-PF	Exploration of spintronics materials by soft X-ray polarization switching
2013S2-005	Y. Nagashima Tokyo Univ. of Sci	Laser spectroscopy of positronium negative ions and its applications
2012S2-001	T. Takahashi Tohoku Univ.	Quantum phenomena of Dirac fermion systems studied by high-resolution angle-resolved photoemission spectroscopy
2012S2-004	A. Waseda AIST	Crystal evaluation of silicon crystals for the determination of the Avogadro constant
2012S2-005	H. Nakao KEK-PF	Materials structure science by resonant soft X-ray scattering under external field
2012S2-006	J. Yoshinobu Univ. of Tokyo	Physical chemistry at surface and interface of energy-conversion materials using VUV/SX SR spectroscopies
2011S2-003	M. Oshima Univ. of Tokyo	Operando analysis of green nano-device structures by high-resolution electron spectroscopy

at the end of every Japanese fiscal year. The scientific output of S1 and S2 proposals is presented in the Highlights of Part A and in the Users' Reports of Part B of this volume.

Proposals are categorized into five scientific disciplines, and reviewed by the five subcommittees of PF-PAC: 1) electronic structure, 2) structural science, 3) chemistry and new materials, 4) life science I (protein crystallography), and 5) life science II (including soft matter science). Figure 1 shows the distribution by research field of the proposals accepted by the subcommittees in FY2013.

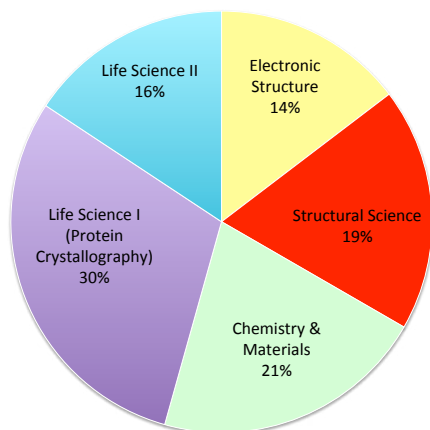


Figure 1: Distribution by scientific field of experimental proposals accepted in FY2013.

1-2 Industrial Proposals

The S, U, G, and P-type proposals are opened for nonproprietary industrial research by limited companies that can apply for the Grant-in-Aid for Scientific Research. Besides these, 41 proprietary industrial projects (Y-type) and 27 nonproprietary collaborative studies with private companies (C-type) were conducted.

Thirteen trial-use programs for industrial applications are carried out with the financial support of a MEXT project, the Open Advanced Research Facilities Initiative. Among these, nine are newly approved and four are continued from FY2012.

1-3 Statistics of the Proposals

The number of users, for all types of proposals, has reached 3,391. Although the number of experimental stations has decreased, the approved scientific proposals and number of users have increased annually, as shown in Fig. 2. This indicates a high and increasing demand for synchrotron radiation and can be attributed to continuous improvements in the storage rings, beamlines, and experimental stations. The synchrotron has become one of the most important research tools for carrying out advanced science experiments and developments. About 20% of the proposals are conducted by new spokespersons, which indicates that the Photon

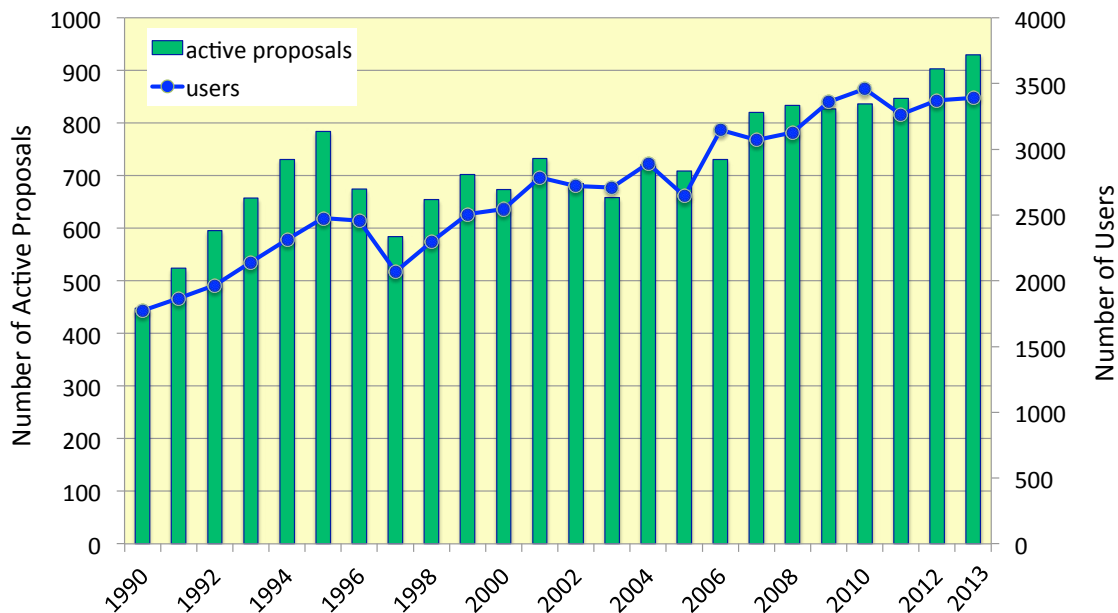


Figure 2: Number of registered PF users and scientific proposals over the period 1990-2013.

Factory is open to public academic scientists. Figure 3 shows the distribution of users by institution and position. Over two-thirds of the users belong to universities, with approximately 75% of the users associated with national universities. Over half of the university users are graduate and undergraduate students; this indicates that the Photon Factory plays an important role in both research and education. The geographical distribution

of the Photon Factory users is shown in Fig. 4 and Fig. 5, which also indicates the immense contribution of the Photon Factory to research and education throughout Japan. The registered number of papers published in 2013 based on experiments at the PF was 622 at the time of this writing and is expected to exceed 680. In addition, 21 doctoral and 87 master theses have been presented.

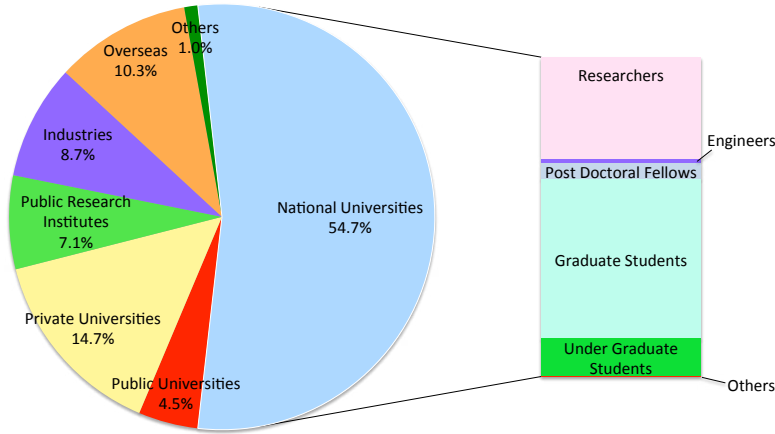


Figure 3: Distribution of users by institution and position.

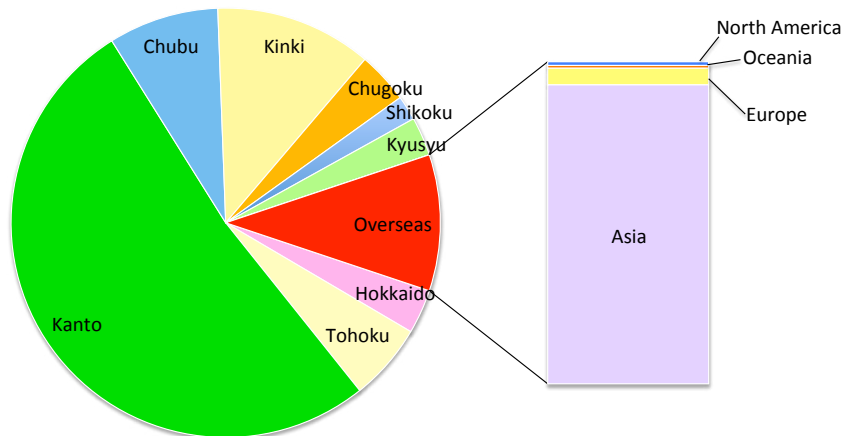


Figure 4: Regional distribution of the spokespersons of proposals accepted in FY2013.

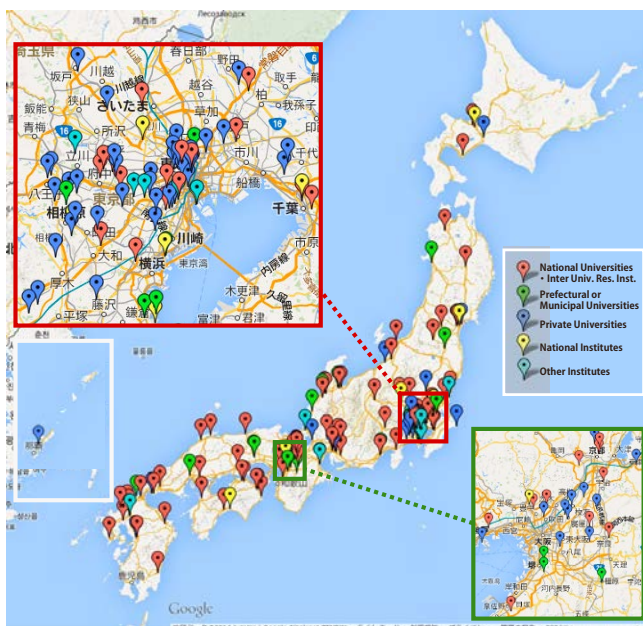


Figure 5: Geographical distribution of Photon Factory users in FY 2013 (domestic users only).

2 Workshops and Seminars

2-1 IMSS Science Festa

The IMSS (Institute of Materials Structure Science) Science Festa was held on March 18-19, 2014 at the EPOCHAL Tsukuba with the support of user community and KEK.

Following two Scientific Sessions with invited speakers—one concerning material science involving hydrogen, and the other concerning research on the surface structure of TiO₂, steels and artificial photosynthesis for contributing to a sustainable society—a Poster Session was held on the first day of the Festa. There were 219 user poster presentations, with research results presented from 11 S-type and 3 U-type proposals. There were more than 72 presentations from the staff of the Accelerator Laboratory of KEK, Neutron Science Division and Muon Science Division of IMSS, MLF (J-PARC Materials and Life Science Experimental Facility) and the PF staff, resulting in a total of more than 291 poster presentations. Following the Poster Session, another Scientific Session with invited speakers concerning structural biology by synchrotron radiation and neutrons was held.

The 31st PF symposium, the annual users' meeting, the 5th MLF symposium and the MSL (Muon Science Laboratory) workshop were held simultaneously on March 19, the second day of the IMSS Science Festa. The Festa provided an excellent opportunity to exchange a broad range of knowledge in such fields as synchrotron, neutron, muon, materials and life sciences, and was attended by more than 490 users and IMSS staff.

The main purpose of the PF symposium is to discuss the present status and future projects of the PF, and to encourage networking among users and PF staff through scientific presentations and discussions. At the start of the PF symposium, PF staff reported on the recent progress of the facility, including rearrangement of beamlines. We also had a discussion session on PF operation, especially regarding beamtime for users and future light sources.

2-2 PF Workshops

Two PF workshops were held in FY2013. Anyone can propose such a workshop, which then freely discusses a specific scientific topic in synchrotron-radiation research and its related application fields. The proceedings of the workshops can be found in the KEK proceedings, which are available at the KEK Library.

- (1) "Development of Novel Light Sources Based on Very Short Period Undulators" held on September 18-19, 2013. KEK Proceedings 2013-5 (in Japanese).
- (2) "The 2nd Workshop on Advanced Observational Techniques - Local Structure Analysis and Time-Resolved Measurement" held on February 21, 2014.

2-3 Seminars

The seminars hosted by each scientific project in IMSS were arranged as seminars hosted by IMSS, called "IMSS Colloquium" and "IMSS Danwakai". These seminars provide an opportunity to exchange a broad range of knowledge in such fields as synchrotron, neutron and muon science. IMSS Colloquium invites leading scientists in each scientific field. Please refer to the following URLs for more details.

URL of IMSS Colloquium (in Japanese):

http://imss.kek.jp/event/for_researchers/imss_colloquium/

URL of IMSS Danwakai (in Japanese):

http://imss.kek.jp/event/for_researchers/imss_danwakai/

3 Graduate School Education

KEK is one of the basic organizations of the Graduate University for Advanced Studies (SOKENDAI), and has the School of High Energy Accelerator Science, which consists of three departments: Accelerator Science, Materials Structure Science, and Particle and Nuclear Physics. The majority of the PF staff members are in charge of giving lectures and supervising graduate students of the Department of Materials Structure Science. SOKENDAI offers a five-year PhD course for undergraduate students and a three-year PhD course for master's degree holders. The School of High Energy Accelerator Science held its "open campus day" for young researchers and undergraduate students at the Tsukuba campus on July 9, 2013 and half-day guidance meetings for potential young candidates in June 22, 2013 and March 8, 2014 at Tokyo. Figure 1 is a photo of Prof. Toshiya Senda of the PF, who explains what is "Structural Biology" by using synchrotron radiation at the guidance meeting in March 8, 2014. The PF has also a system for Joint PhD (JPHD) students, who are accepted by the PF to pursue advanced studies under the supervision of PF staff members towards their PhD degrees in collaboration with their home universities. The numbers of graduate students of SOKENDAI and JPHD during the past fifteen years are listed in Table 1.

In addition to the SOKENDAI and JPHD graduate students, a number of doctoral theses were written based on research carried out at the PF. Figure 2 shows the statistics of such graduate students.



Figure 1: A snapshot of the guidance.

Table 1: Number of SOKENDAI and JPHD students at the PF over the period 1999-2013.

FY	SOKENDAI	JPHD
1999	6	11
2000	8	12
2001	10	8
2002	12	13
2003	12	7
2004	14	5
2005	14	6
2006	9	10
2007	6	13
2008	6	10
2009	6	9
2010	5	10
2011	4	5
2012	6	6
2013	6	7

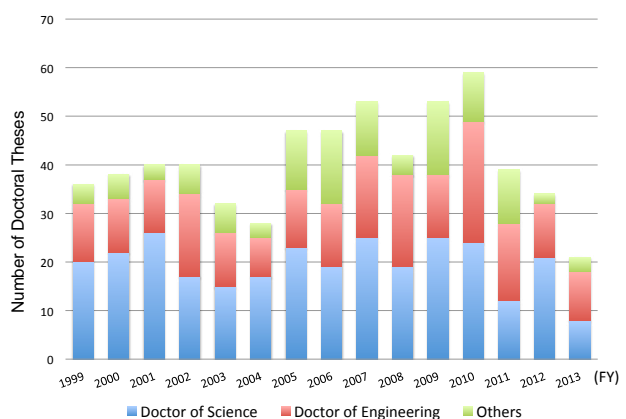


Figure 2: Number of students who obtained doctoral degrees based on scientific activities at the PF.

4 International Collaboration

4-1. Overview

The Photon Factory has been collaborating internationally. The Indian beamline BL-18B started operation in 2009, and part of the beamtime is open for domestic users as well. The Photon Factory is also collaborating with the international synchrotron radiation community through meetings, workshops, and schools. The SESAME-JSPS school (Trunc, Turkey) and Cheiron school (Nishi-harima, Japan) were partly supported by PF.

4-2. Indian Beamline

The Department of Science and Technology (DST), Government of India and KEK agreed to set up an Indian beamline at the Photon Factory in 2008 with the Saha Institute of Nuclear Physics (SINP) as a nodal institute of India. Beamline 18B is leased to DST, and SINP set up two diffractometers and related detection systems. Twenty-seven experiments were carried out at BL-18B, and six papers based on BL-18B experiments were published in FY2013. The beamline is fully operational, and is open not only for Indian scientists but also general users.

4-3. Cooperation with the SESAME Project

SESAME (Synchrotron-light for Experimental Science and Applications in the Middle East) is a synchrotron light source under construction in Jordan. The SESAME facility is expected to enter full operation in late 2015, which will be the first major international research center in the Middle East. It is a unique and cooperative venture by scientists and governments of the region set up on the model of CERN (European Organization for Nuclear Research). It is being developed under the auspices of UNESCO (United Nations Educational, Scientific and Cultural Organization) following formal approval at the Organization's Executive Board Meeting (164th



Figure 1: Group photograph at the 4th SESAME-JSPS school.

session, May 2002). The current members of SESAME are Bahrain, Cyprus, Egypt, Iran, Israel, Jordan, Pakistan, the Palestinian Authority, and Turkey. Japan has been supporting the SESAME project from the outset in 2000, and formally joined as an Observer in 2009. (Current Observers as of 2013 are France, Germany, Greece, Italy, Japan, Kuwait, Portugal, Russian Federation, Sweden, Switzerland, the United Kingdom, and the United States of America.) According to the cooperation framework between SESAME and Japan, researchers in Japan have held a series of schools concerning synchrotron radiation instrumentation and science in Cairo (2008), Antalya (2010), Amman (2011), and Trunc (2013) under the Asia and Africa Science Platform Program supported by the Japan Society of Promotion of Science (JSPS).

The 4th SESAME-JSPS School was held from June 13 to 22, 2013 at the Institute for Theoretical and Applied Physics (ITAP), Trunc, Turkey, which was a joint school with the 2nd Henry Moseley X-ray School. The school consisted of six days of lectures and two days of hands-on practice sessions, in which Japanese lecturers took charge of three lectures and all practice sessions. The 35 students from SESAME countries joined the school and eagerly learned about state-of-the-art techniques and science using synchrotron radiation. The hands-on practice session mainly focused on data analysis of five types of typical synchrotron measurement: X-ray photoelectron spectroscopy (XPS), X-ray absorption fine structure (XAFS), macromolecular crystallography, powder diffraction, and X-ray fluorescence analysis, using portable PCs. The students were separated into five groups, learned the principles of each technique, studied how to process the data, and finally gave presentations on what they had learned during the practice sessions. The SESAME-JSPS school has been highly evaluated by the participants due to the comprehensive hands-on practice, and has provided valuable opportunities to enlarge the synchrotron user community in the Middle East.



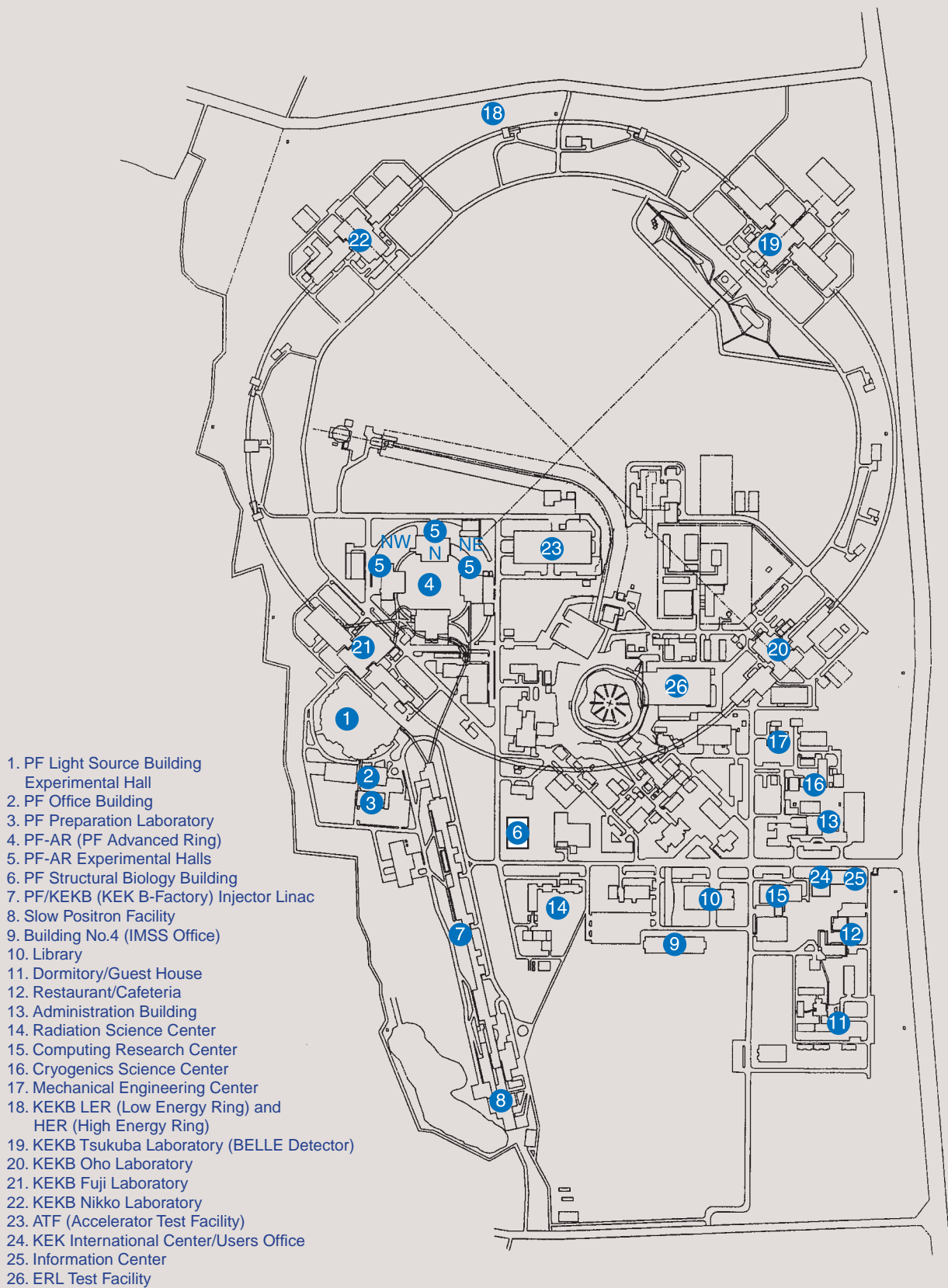
Figure 2: Presentation session to summarize the practice sessions.

Appendices



1. Site and Organization





KEK consists of four research institutions, i.e., the Institute of Materials Structure Science (IMSS), the Institute of Particle and Nuclear Studies (IPNS), the Accelerator Laboratory (AL), and the Applied Research Laboratory. As shown in Fig. 1, the IMSS constitutes the Synchrotron Radiation Divisions I and II, the Neutron Science Division, the Muon Science Division, the Structural Biology Research Center, and the Condensed Matter Research Center. Table I shows a list of the members of the Advisory Committee of the IMSS.

Photon Factory (PF) consists of two divisions of the IMSS (the Synchrotron Radiation Divisions I and II) and the Accelerator Division VII of the AL as shown in the organization chart of Fig. 2. The staff members of the PF list in Table 2. Synchrotron Radiation Science Divi-

sions I and II consist of five beamline groups (electronic structure group, condensed matter group, materials chemistry group, life sciences group and slow positron group), two engineering and administration groups (beamline engineering, technical services & safety group and user support & dissemination group) and two working groups (ultrafast dynamics group and advanced detector R&D group). The Accelerator Division VII has six groups, which are named Light Source Group I to VI. The missions of each group are as follows: Group I is in charge of orbits, magnets, and insertion devices, Group II of RF, SC cavities and so on, Group III mainly of vacuum, Group IV mainly of beam diagnostics and accelerator control, Group V of front-end, safety and so on, and Group VI mainly of electron guns.

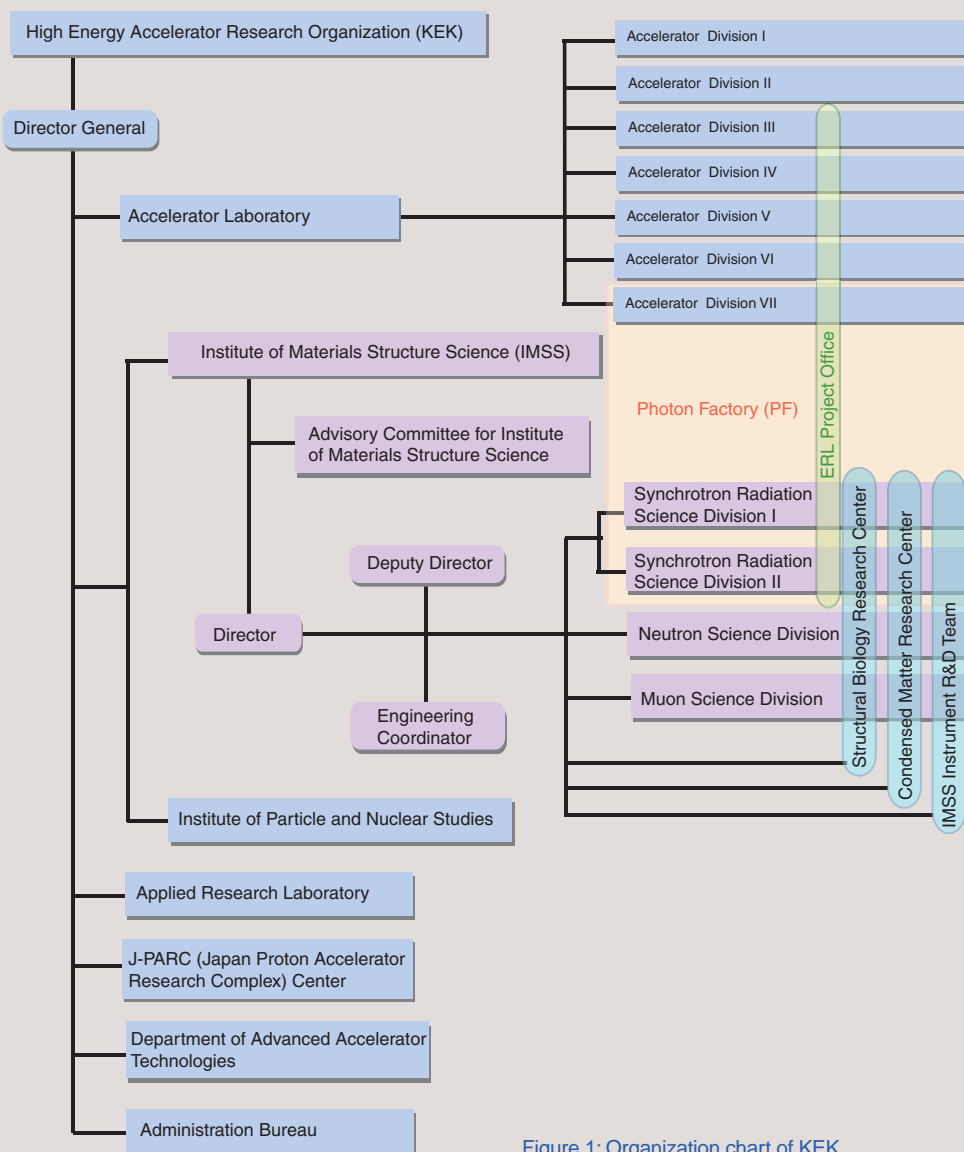


Figure 1: Organization chart of KEK.

Table 1: The members of the Advisory Committee for Institute of Materials Structure Science.

ADACHI, Shin-ichi	Photon Factory, IMSS, KEK
AKIMITSU, Jun	Aoyama Gakuin University
AMEMIYA, Yoshiyuki**	The University of Tokyo
FUJII, Yasuhiko	Comprehensive Research Organization for Science and Society
KADONO, Ryosuke	Muon Science Division, IMSS, KEK
KANAYA, Toshiji	Kyoto University
KATAOKA, Mikio	Nara Institute of Science and Technology
KAWATA, Hiroshi	Photon Factory, IMSS, KEK
KOBAYASHI, Yukinori	Photon Factory, Accelerator Laboratory, KEK
KUMAI, Reiji	Photon Factory, IMSS, KEK
KUMIGASHIRA, Hiroshi	Photon Factory, IMSS, KEK
MIYAKE, Yasuhiro	Muon Science Division, IMSS, KEK
MIZUKI, Jun'ichiro	Kwansei Gakuin University
MURAKAMI, Youichi	Photon Factory, IMSS, KEK
OSHIMA, Masaharu	The University of Tokyo
OTOMO, Toshiya	Neutron Science Division, IMSS, KEK
SAITO, Naohito	Institute of Particle and Nuclear Studies, KEK
SASAKI, Shinichi	Applied Research Laboratory, KEK
SATO, Mamoru	Yokohama City University
SETO, Hideki*	Neutron Science Division, IMSS, KEK
SENDA, Toshiya	Photon Factory, IMSS, KEK
TAKATA, Masaki	RIKEN/SPring-8
TORIKAI, Eiko	University of Yamanashi
YAMAGUCHI, Seiya	Accelerator Laboratory, KEK

* Chairperson ** Vice-Chairperson

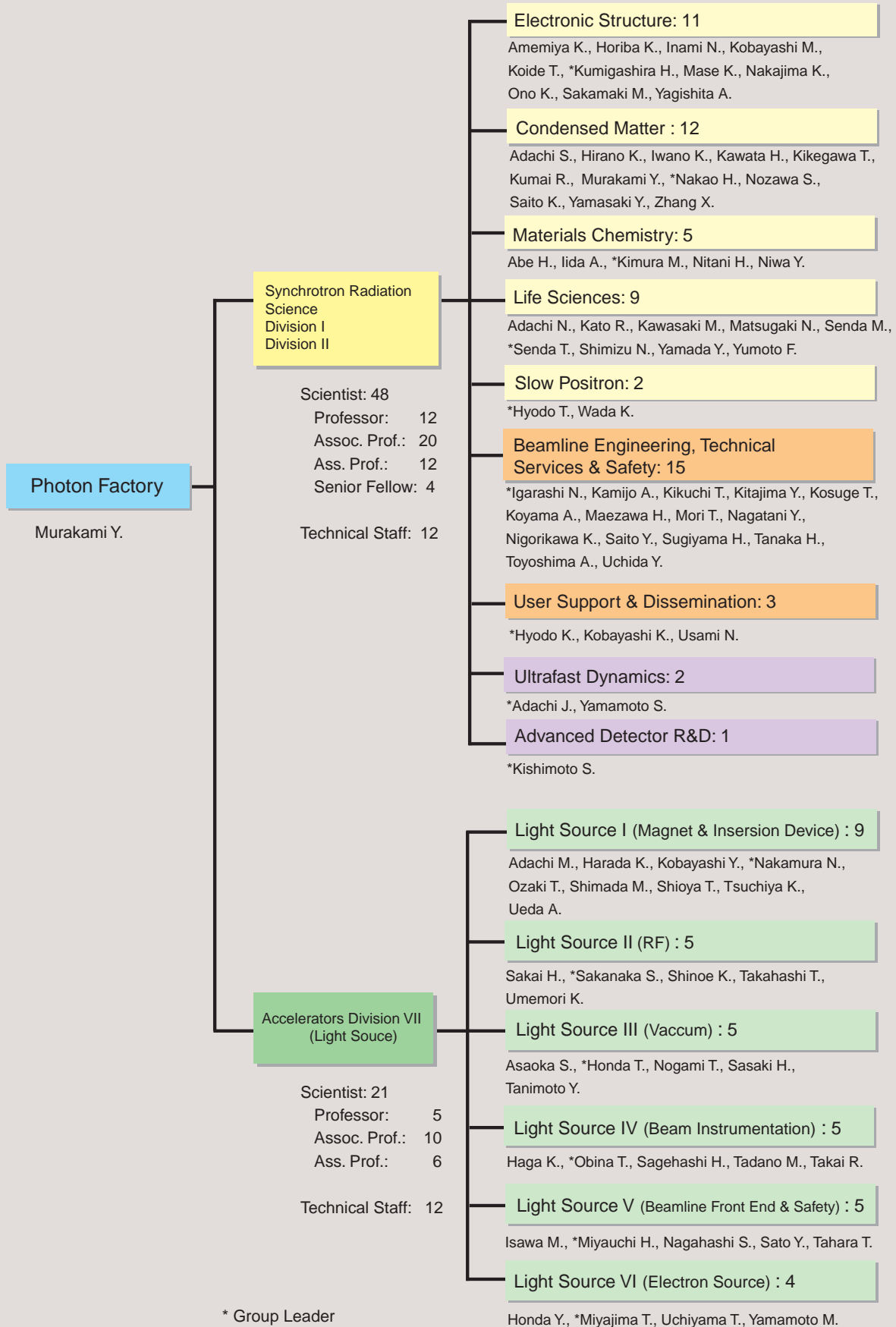


Figure 2: Organization chart of PF (as of March 31, 2014) .

Table 2: Staff members of the Photon Factory.

Name	Group*
Research Staff	
Director	
MURAKAMI, Youichi	CM
Synchrotron Radiation Science Division I & II	
ABE, Hitoshi	MC
ADACHI, Jun-ichi	UD (<i>ES</i>)
ADACHI, Naruhiko	LS
ADACHI, Shinichi	CM (<i>UD, AD</i>)
AMEMIYA, Kenta	ES (<i>BETSS, AD, UD</i>)
HIRANO, Keiichi	CM
HORIBA, Koji	ES
HYODO, Kazuyuki	USD (<i>LS</i>)
HYODO, Toshio	SPF
IGARASHI, Noriyuki	BETSS (<i>LS, AD</i>)
IIDA, Atsuo	MC
INAMI, Nobuhito	ES (<i>AD</i>)
IWANO, Kaoru	CM
KAMIJO, Ai	BETSS
KATO, Ryuichi	LS
KAWASAKI, Masato	LS
KAWATA, Hiroshi	CM
KIKEGAWA, Takumi	CM
KIKUCHI, Takashi	BETSS (<i>UD</i>)
KIMURA, Masao	MC
KISHIMOTO, Shunji	AD, CM (<i>UD</i>)
KITAJIMA, Yoshinori	BETSS (<i>ES</i>)
KOBAYASHI, Katsumi	USD
KOBAYASHI, Masaki	ES
KOIDE, Tsuneharu	ES
KOSUGE, Takashi	BETSS (<i>AD</i>)
KOYAMA, Atsushi	BETSS
KUMAI, Reiji	CM (<i>AD</i>)
KUMIGASHIRA, Hiroshi	ES
MAEZAWA, Hideki	BETSS
MASE, Kazuhiko	ES
MATSUGAKI, Naohiro	LS
MORI, Takeharu	BETSS
NAGATANI, Yasuko	BETSS
NAKAJIMA, Kyo	ES
NAKAO, Hironori	CM (<i>UD</i>)
NIGORIKAWA, Kazuyuki	BETSS (<i>AD</i>)
NITANI, Hiroaki	MC
NIWA, Yasuhiro	MC (<i>BETSS, UD</i>)
NOZAWA, Shunsuke	CM (<i>UD</i>)
ONO, Kanta	ES (<i>AD</i>)
SAITO, Kotaro	CM
SAITO, Yuuki	BETSS
SAKAMAKI, Masako	ES (<i>AD</i>)
SENDA, Miki	LS
SENDA, Toshiya	LS
SHIMIZU, Nobutaka	LS (<i>BETSS</i>)
SUGIYAMA, Hiroshi	BETSS (<i>CM</i>)

Name	Group*
TANAKA, Hirokazu	BETSS (UD)
TOYOSHIMA, Akio	BETSS (UD)
UCHIDA, Yoshinori	BETSS
USAMI, Noriko	USD (LS)
WADA, Ken	SPF
YAGISHITA, Akira	ES
YAMADA, Yusuke	LS
YAMAMOTO, Shigeru	UD
YAMASAKI, Yuichi	CM (UD)
YUMOTO, Fumiaki	LS
ZHANG, Xiaowei	CM

Accelerator Division VII

ADACHI, Masahiro	Light Source I
ASAOKA, Seiji	Light Source III
HAGA, Kaiichi	Light Source IV
HARADA, Kentaro	Light Source I
HONDA, Tohru	Light Source III
HONDA, Yosuke	Light Source VI
ISAWA, Masaaki	Light Source V
KOBAYASHI, Yukinori	Light Source I
MIYAJIMA, Tsukasa	Light Source VI
MIYAUCHI, Hiroshi	Light Source V
NAGAHASHI, Shinya	Light Source V
NAKAMURA, Norio	Light Source I
NOGAMI, Takashi	Light Source III
OBINA, Takashi	Light Source IV
OZAKI, Toshiyuki	Light Source I
SAGEHASHI, Hidenori	Light Source IV
SAKAI, Hiroshi	Light Source II
SAKANAKA, Shogo	Light Source II
SASAKI, Hiroyuki	Light Source III
SATO, Yoshihiro	Light Source V
SHIMADA, Miho	Light Source I
SHINOE, Kenji	Light Source II
SHIOYA, Tatsuro	Light Source I
TADANO, Mikito	Light Source IV
TAHARA, Toshihiro	Light Source V
TAKAHASHI, Takeshi	Light Source II
TAKAI, Ryota	Light Source IV
TANIMOTO, Yasunori	Light Source III
TSUCHIYA, Kimichika	Light Source I
UCHIYAMA, Takashi	Light Source VI
UEDA, Akira	Light Source I
UMEMORI, Kensei	Light Source II
YAMAMOTO, Masahiro	Light Source VI

Guest Professor

ASAKURA, Kiyotaka	(Hokkaido Univ.)
HAJIMA, Ryoichi	(JAEA)
ISHIHARA, Sumio	(Tohoku Univ.)
KAMIKUBO, Hironari	(Nara Institute of Science and Technology)
KATOH, Masahiro	(UVSOR)

Name	Group*
KONDO, Tadashi	(Osaka Univ.)
KOSHIHARA, Shinya	(Tokyo Institute of Technology)
MORITOMO, Yutaka	(Univ. of Tsukuba)
OHKUMA, Haruo	(SPring-8)
TAKAHASHI, Yoshio	(Hiroshima Univ.)
YAO, Min	(Hokkaido Univ.)

Postdoctoral Fellow

SAKAI, Enju
TAKEICHI, Yasuo

The Graduate University for Advanced Studies

HARADA, Ayaka
INOUE, Keisuke
MATSUBARA, Haruki
WU, Yanlin

* Synchrotron Radiation Science Division

ES	Electronic Structure
CM	Condensed Matter
MC	Materials Chemistry
LS	Life Sciences
SPF	Slow Positron Facility
BETSS	Beamline Engineering, Technical Services and Safety
USD	User Support and Dissemination
UD	Ultrafast Dynamics
AD	Advanced Detector R&D

Italic: the additional post

2. Awards

Medal with Purple Ribbon

NISHIKAWA, Keiko (Chiba Univ.)

“Achievement in Physical Chemistry Research”

Humboldt Prize

KOSHIHARA, Shinya (Tokyo Inst. of Tech.)

“Photoinduced Phase Transition”

The Commendation for Science and Technology by the Minister of Education, Culture, Sports, Science and Technology, The Young Scientists’ Prize

WAKABAYASHI, Yuusuke (Osaka Univ.)

“Microscopic Structural Study of Surface Functionality”

The Commendation for Science and Technology by the Minister of Education, Culture, Sports, Science and Technology, The Young Scientists’ Prize

NUMATA, Tomoyuki (AIST)

“Structural and Functional Studies of tRNA Modification Enzymes”

The Commendation for Science and Technology by the Minister of Education, Culture, Sports, Science and Technology, The Young Scientists’ Prize

NIHEI, Masayuki (Univ. of Tsukuba)

“Research on the Creation of External Stimuli-Responsive Metal Complexes and their Functions”

The Commendation for Science and Technology by the Minister of Education, Culture, Sports, Science and Technology, The Young Scientists’ Prize

SOUMA, Seigo (Tohoku Univ.)

“Development of an Instrument for Angle-Resolved Photoemission Spectroscopy and Investigation of the Electronic Structures of Functional Materials”

American Chemical Society, Arthur C. Cope Scholar Award

FUJITA, Makoto (The Univ. of Tokyo)

“Pioneering a Novel Principle of Metal-Directed Self-Assembly for Constructing Nanoscale Discrete Structures and Developing Functions and Properties in their Cavities”

MIT Lectureship Prize

FUJITA, Makoto (The Univ. of Tokyo)

“Coordination Self-Assembly: Structure and Function”

MPGD2013 Georges Charpak’s Young Scientist Award

FUJIWARA, Takeshi (The Univ. of Tokyo)

“Development of Innovative Gaseous Radiation Detector with Photo-Etchable Glass”

New Products & Novel Technology Award, The 11th International Conference on Ferrites

ICHIYANAGI, Yuko (Yokohama National Univ.)

“Optimization of Ferrite Nanoparticles as an Agent for Hyperthermia Treatment”

The Crystallographic Society of Japan, Progress Prize

HOSHINO, Manabu (Tokyo Inst. of Tech.)

“Structure Visualization of Short-Lived Photoexcited Molecule by Single Crystal X-Ray Structure Analysis”

Japanese Association of Forensic Science and Technology, Encouragement Prize

NISHIWAKI, Yoshinori (Kochi Univ.)

“Nondestructive Discrimination of White Polyester Monofilament using Synchrotron Radiation X-Ray Fluorescence Spectrometry”

The Japan Society of High Pressure Science and Technology, Encouragement Prize
SATO, Tomoko (Hiroshima Univ.)
“High-Pressure Behavior of SiO₂ Glass”

The Atomic Collision Society of Japan, Young Scientist Award
MICHISHIO, Koji (Tokyo Univ. of Sci.)
“Photodetachment of Positronium Negative Ions and its Application to Positronium Beam Production”

Japanese Society for Synchrotron Radiation Research, Encouragement Prize
YOSHIMATSU, Kohei (Tokyo Inst. of Tech.)
“Metallic Quantum Well States of Strongly Correlated Oxide Studied by Synchrotron Radiation Photoemission Spectroscopy”

Japanese Positron Science Society, Encouragement Prize
WADA, Ken (KEK-PF)
“Increase in the Beam Intensity of the Slow-Positron Beam at the KEK Slow Positron Facility”

Japan Association of Mineralogical Sciences Award
MIYAWAKI, Ritsuro (Natl. Mus. of Nature and Sci.)
“Crystal Chemistry of Rare Earth Minerals”

Japan Association of Mineralogical Sciences Award for Applied Mineralogy
KIMURA, Masao (Nippon Steel & Sumitomo Metal)
“Research on Dynamic Observation of Mineralogical Structures and its Application to Steel-Relating Materials and Processes”

Japan Association of Mineralogical Sciences, Sakurai Medal
NAGASE, Toshiro (Tohoku Univ. Mus.)
“Tanohataite, LiMn₂Si₃O₈(OH): a New Mineral from the Tanohata Mine, Iwate Prefecture, Japan”

The Japanese Liquid Crystal Society, Paper Award
OKOSHI, Kento (Chitose Inst. of Sci. and Tech.)
“Liquid Crystal Phases Observed in Rigid-Rod Polymers”

The Ceramic Society of Japan, Science Prize
IDEMOTO, Yasushi (Tokyo Univ. of Sci.)
“Investigation into Properties of Highly Functional Oxides using Quantum Beam and Thermodynamic Measurement”

Young Scientist Award of the Physical Society of Japan
SHIRASAWA, Tetsuro (The Univ. of Tokyo)
“Structural Science Based on the Determination of Atomic Arrangement of Buried Interface”

The Institute of Electronics, Information and Communication Engineers, MI Research Encouragement Prize
SUNAGUCHI, Naoki (Gunma Univ.)
“Principle Experiment of 3D X-Ray Fluorescent CT using Pinholes”

The Society of Instrument and Control Engineers, Paper Award
SUNAGUCHI, Naoki (Gunma Univ.)
“Refraction-Contrast X-Ray CT Based on Dark-Field Imaging for Biological Tissues”

Radiation Effects Association, Encouragement Award for Radiation Research
TOMITA, Masanori (Central Res. Inst. of Electric Power Ind.)
“Mechanisms of X-Ray-Induced Bystander Responses”

The Society of Polymer Science, Award for Encouragement of Research in Polymer Science
NORO, Atsushi (Nagoya Univ.)
“Studies on Creation of Multi-Component Polymer Materials by Controlling Noncovalent Interactions”

Fellow of The Surface Science Society of Japan
KONDOH, Hiroshi (Keio Univ.)
“Operando Direct Observations of Surface Chemical Processes”

The Foundation for High Energy Accelerator Science, Nishikawa Prize, 2013
HARADA, Kentaro (KEK-Accl)
“Development of New Injection Scheme using a Pulsed Quadrupole Magnet in Electron Storage Rings”

3. Theses

Lists of doctoral theses, which were written based on the PF experiments.

Doctor of Engineering

ZHAO, Yunfeng (Yamagata Univ.)

“Structural Formation under Polymer Processing Relevant Conditions” (15A, 6A and 10C)

Doctor of Science

YANG, Cuiping (Ehime Univ.)

“Phase Relations and Melt Compositions in Hydrous Pyrolite under High Temperature and High Pressure and the Equation of State of Hydrous Minerals” (NE5C and NE7A)

Doctor of Engineering

KIM, Dongyoung (The Univ. of Tokyo)

“Bond Percolation Conductivity in Heavily Fe-doped BaZrO₃ and its Application in H⁺-SOFC” (19B)

Doctor of Science

NAKADA, Ryoichi (Hiroshima Univ.)

“Stable Isotopic and Speciation Studies on Neo-Rare Earth Element Geochemistry and Paleoenvironmental Analysis” (9A and 12C)

Doctor of Philosophy

BISWAS, Nupur (Univ. of Calcutta)

“Studies on Confined Polymers” (18B)

Doctor of Philosophy

LIU, Liang (The Univ. of Tokyo)

“Electronic Transport and Angle-Resolved Photoemission Studies of Iron-Based Superconductors” (28A)

Doctor of Philosophy

AMBOLO DE, Leo Cristobal II Castro (The Univ. of Tokyo)

“Photoemission Study of the Iron-Based Superconductor FeTe_{1-x}Se_x” (28A)

Doctor of Science

SHINOHARA, Yuji (Tokyo Inst. of Tech.)

“Study on the Biosynthetic Pathway for the Beta-Amino Acid Starter Unit of Macrolactam Polyketide Antibiotic Vicenistatin” (5A, NW12A)

Doctor of Engineering

IKITAMURA, Shingo (Nagoya Univ.)

“Structural Study of Human APOBEC3 Family Proteins including HIV-1 Vif-Binding Interface” (17A)

Doctor of Science

OKA, Kazuki (Chiba Univ.)

“Molecular Approach of the Interfacial Design for Platinum, Carbon, and Polymer Electrolyte in Polymer Electrolyte Fuel Cells” (7C, 9C and 12C)

Doctor of Science

IMAI, Yosuke (Kyushu Univ.)

“Specific Ion Effects on Counterion Distribution in Surfactant Adsorbed Films Studied through Surface Tensiometry and Total Reflection XAFS” (7C)

Doctor of Science

KUMAGAI, Yoshiaki (Tokyo Inst. of Tech.)

“Investigation of Doubly Excited Molecules by Measuring Cross Sections for the Formation of H(2s) Fragment Atoms” (20A and 28B)

Doctor of Engineering

KOIDE, Yuichiro (Nihon Univ.)

“Effect of Cast-Solvent on the Morphology of Mixtures of Stereoisomeric Poly(lactic acid)s” (10C)

Doctor of Philosophy

MONTASIR, Elahi (Tokyo Univ. of Agri. & Tech.)

“Structural and Thermodynamic Analysis of Dengue Envelope Protein Domain III: Insights into Dengue's Serospecificity and Molecular Evolution” (5A and 17A)

Doctor of Philosophy

WANG, Doudou (The Univ. of Tokyo)

“Structural and Functional Analysis of Kinesin Superfamily Protein KIF19A” (1A, 5A and NW12A)

4. Publication List

1A

S.Arai, S.Saijo, K.Suzuki, K.Mizutani, Y.Kakinuma, Y.Ishizuka-Katsura, N.Ohsawa, T.Terada, M.Shirouzu, S.Yokoyama, S.Iwata, I.Yamato and T.Murata
Rotation Mechanism of *Enterococcus hirae* V₁-ATPase Based on Asymmetric Crystal Structures
Nature, **493** (2013) 703.

D.Kim, J.Park, S.J.Kim, Y.-M.Soh, H.M.Kim, B.-H.Oh and J.-J.Song
Brucella Immunogenic BP26 Forms a Channel-Like Structure.
J. Mol. Biol., **425** (2013) 1119.

J.Y.Yoon, J.Kim, D.R.An, S.J.Lee, H.S.Kim, H.N.Im H.J.Yoon, J.Y.Kim, S.J.Kim, B.W.Han and S.W.Suh
Structural and Functional Characterization of HP0377, a Thioredoxin-Fold Protein from *Helicobacter pylori*
Acta Cryst. D, **69** (2013) 735.

N.Numoto, K.Shimizu, K.Matsumoto, K.Miki and A.Kita
Observation of the Orientation of Membrane Protein Crystals Grown in High Magnetic Force Fields
J. Cryst. Growth, **367** (2013) 53.

T.Arimori, N.Kawamoto, S.Shinya, N.Okazaki, M.Nakazawa, K.Miyatake, T.Fukamizo, M.Ueda and T.Tamada
Crystal Structures of the Catalytic Domain of a Novel Glycohydrolase Family 23 Chitinase from *Ralstonia* sp. A-471 Reveals a Unique Arrangement of the Catalytic Residues for Inverting Chitin Hydrolysis
J. Biol. Chem., **288** (2013) 18696.

K.J.Cho, J.-H.Lee, K.W.Hong, S.-H.Kim, Y.Park, J.Y.Lee, S.Kang, S.Kim, J.H.Yang, E.-K.Kim, J.H.Seok, S.Unzai, S.Y.Park, X.Saelens, C.-J.Kim, J.-Y.Lee, C.Kang, H.-B.Oh, M.S.Chung and K.H.Kim
Insight into Structural Diversity of Influenza Virus Haemagglutinin
J. General Virology, **94** (2013) 1712.

S.Okazaki, S.Nakano, D.Matsui, S.Akaji, K.Inagaki and Y.Asano
X-Ray Crystallographic Evidence for the Presence of the Cysteine Tryptophylquinone Cofactor in L-Lysine ϵ -Oxidase from *Marinomonas mediterranea*
J. Biochem., **154** (2013) 233.

Y.Yagita, N.Kuse, K.Kuroki, H.Gatanaga, J.M.Carlson, T.Chikata, Z.L.Brumme, H.Murakoshi, T.Akahoshi, N.Pfeifer, S.Mallal, M.John, T.Ose, H.Matsubara, R.Kanda, Y.Fukunaga, K.Honda, Y.Kawashima, Y.Ariumi, S.Oka, K.Maenaka and M.Takiguchi
Distinct HIV-1 Escape Patterns Selected by Cytotoxic T Cells with Identical Epitope Specificity
J. Virol., **87** (2013) 2253.

S.Matsumoto, A.Shimada, J.Nyirenda, M.Igura, Y.Kawano and D.Kohda
Crystal Structures of an Archaeal Oligosaccharyltransferase Provide Insights into the Catalytic Cycle of N-Linked Protein Glycosylation
Proc. Natl. Acad. Sci. USA, **110** (2013) 17868.

A.Nakamura, T.Ishida, S.Fushinobu, K.Kusaka, I.Tanaka, K.Inaka, Y.Higuchi, M.Masaki, K.Ohta, S.Kaneko, N.Niimura, K.Igarashi and M.Samajima
Phase-Diagram-Guided Method for Growth of a Large Crystal of Glycoside Hydrolase Family 45 Inverting Cellulase Suitable for Neutron Structural Analysis
J. Synchrotron Rad., **20** (2013) 859.

S.Fushinobu, V.D.Alves and P.M.Coutinho
Multiple Rewards from a Treasure Trove of Novel Glycoside Hydrolase and Polysaccharide Lyase Structures: New Folds, Mechanistic Details, and Evolutionary Relationships
Curr. Opin. Struct. Biol., **23** (2013) 652.

K.Matsumoto, Y.Tanaka, T.Watanabe, R.Motohashi, K.Ikeda, K.Tobitani, M.Yao, I.Tanaka and S.Taguchi
Directed Evolution and Structural Analysis of NADPH-Dependent Acetoacetyl Coenzyme A (Acetoacetyl-CoA) Reductase from *Ralstonia eutropha* Reveals Two Mutations Responsible for Enhanced Kinetics
Appl. Environ. Microbiol., **79** (2013) 6134.

M.Momma and Z.Fujimoto
Expression, Crystallization and Preliminary X-Ray Analysis of Rice L-Galactose Dehydrogenase
Acta Cryst. F, **69** (2013) 809.

T.Arimori, A.Ito, M.Nakazawa, M.Ueda and T.Tamada
Crystal Structure of Endo-1,4- β -Glucanase from *Eisenia fetida*
J. Synchrotron Rad., **20** (2013) 884.

J.-K.Li, J.-H.Liao, H.Li, C.-I.Kuo, K.-F.Huang, L.-W.Yang, S.-H.Wu and C.-I.Chang
The N-Terminal Substrate-Recognition Domain of a LonC Protease Exhibits Structural and Functional Similarity to Cytosolic Chaperones
Acta Cryst. D, **69** (2013) 1789.

J.-H.Ha, Y.Eo, A.Grishaev, M.Guo, J.A.I.Smith, H.O.Sintim, E.-H.Kim, H.-K.Cheong, W.E.Bentley and K.-S.Ryu
Crystal Structures of the LsrR Proteins Complexed with Phospho-AI-2 and Two Signal-Interrupting Analogues Reveal Distinct Mechanisms for Ligand Recognition
J. Am. Chem. Soc., **135** (2013) 15526.

Y.Saito, H.Yuki, M.Kuratani, Y.Hashizume, S.Takagi, T.Honma, A.Tanaka, M.Shirouzu, J.Mikuni, N.Handa, I.Ogahara, A.Sone, Y.Najima, Y.Tomabechi, M.Wakiyama, N.Uchida, M.Tomizawa-Murasawa, A.Kaneko, S.Tanaka, N.Suzuki, H.Kajita, Y.Aoki, O.Ohara, L.D.Shultz, T.Fukami, T.Goto, S.Taniguchi, S.Yokoyama and F.Ishikawa

A Pyrrolo-Pyrimidine Derivative Targets Human Primary AML Stem Cells in Vivo
Science Translational Medicine, **5** (2013) 181ra52.

J.Fujita, Y.Miyazaki, M.Hirose, C.Nagao, E.Mizohata, Y.Matsumoto, K.Mizuguchi, T.Inoue and H.Matsumura
Expression, Purification, Crystallization and Preliminary Crystallographic Study of FtsA from Methicillin-Resistant *Staphylococcus aureus*
Acta Cryst. F, **69** (2013) 895.

K.Komoda, M.Narita, I.Tanaka and M.Yao
Expression, Purification, Crystallization and Preliminary X-Ray Crystallographic Study of the Nucleocapsid Protein of *Tomato spotted wilt virus*
Acta Cryst. F, **69** (2013) 700.

A.Shimizu, A.Kawana-Tachikawa, A.Yamagata, C.Han, D.Zhu, Y.Sato, H.Nakamura, T.Koibuchi, J.Carlson, E.Martin, C.J.Brumme, Y.Shi, G.F.Gao, Z.L.Brumme, S.Fukai and A.Iwamoto
Structure of TCR and Antigen Complexes at an Immunodominant CTL Epitope in HIV-1 Infection
Sci. Rep., **3** (2013) 3097.

A.Nakamura, T.Nemoto, I.U.Heinemann, K.Yamashita, T.Sonoda, K.Komoda, I.Tanaka, D.Söll and M.Yao
Structural Basis of Reverse Nucleotide Polymerization
Proc. Natl. Acad. Sci. USA, **110** (2013) 20970.

J.Y.Yoon, D.R.An, H.-J.Yoon, H.S.Kim, S.J.Lee, H.N.Im, J.Y.Jang and S.W.Suh
High-Resolution Crystal Structure of *Streptococcus pyogenes* β -NAD⁺ Glycohydrolase in Complex with its Endogenous Inhibitor IFS Reveals a Highly Water-Rich Interface
J. Synchrotron Rad., **20** (2013) 962.

K.Murayama, K.Kano, Y.Matsumoto and D.Sugimori
Crystal Structure of Phospholipase A₁ from *Streptomyces albidoflavus* NA297
Journal of Structural Biology, **182** (2013) 192.

T.Tominaga, S.Watanabe, R.Matsumi, H.Atomi, T.Imanaka and K.Miki
Crystal Structures of the Carbamoylated and Cyanated Forms of HypE for [NiFe] Hydrogenase Maturation
Proc. Natl. Acad. Sci. USA, **110** (2013) 20485.

J.S.Park, W.C.Lee, J.H.Song, S.I.Kim, J.C.Lee, C.Cheong and H.-Y.Kim
Purification, Crystallization and Preliminary X-Ray Crystallographic Analysis of Diaminopimelate Epimerase from *Acinetobacter baumannii*
Acta Cryst. F, **69** (2013) 42.

Y.Sun, X.Wang, S.Yuan, M.Dang, X.Li, X.C.Zhang and Z.Rao

An Open Conformation Determined by a Structural Switch for 2A Protease from Coxsackievirus A16
Protein Cell, **4** (2013) 782.

D.Liu, K.-S.Ryu, J.Ko, D.Sun, K.Lim, J.-O.Lee, J.Hwang, Z.-W.Lee and B.-S.Choi
Insights into the Regulation of Human Rev1 for Translesion Synthesis Polymerases Revealed by the Structural Studies on its Polymerase-Interacting Domain
J. Molecular Cell Biology, **5** (2013) 204.

1B

N.J.O.Silva, S.Saisho, M.Mito, A.Millan, F.Palacio, A.Cabot, O.Iglesias and A.Labarta
Pressure Effects in Hollow and Solid Iron Oxide Nanoparticles
J. Magn. Magn. Mater., **335** (2013) 1.

1C

K.Mase, E.Kobayashi, A.Nambu, T.Kakiuchi, O.Takahashi, K.Tabayashi, J.Ohshita, S.Hashimoto, M.Tanaka and S.Nagaoka
Site-Specific Ion Desorption from Condensed F₃SiCD₂CH₂Si(CH₃)₃ Induced by Si-2p Core-Level Ionizations Studied with Photoelectron Photoion Coincidence (PEPICO) Spectroscopy, Auger Photoelectron Coincidence Spectroscopy (APECS) and Auger Electron Photoion Coincidence (AEPICO) Spectroscopy
Surf. Sci., **607** (2013) 174.

K.Edamoto
The Electronic Properties of Nickel Phosphide Surfaces: Angle-Resolved and Resonant Photoemission Studies
Appl. Surf. Sci., **269** (2013) 7.

2C

T.Kinoshita, K.Arai, K.Fukumoto, T.Ohkochi, M.Kotsugi, F.Guo, T.Muro, T.Nakamura, H.Osawa, T.Matsushita and T.Okuda
Observation of Micro-Magnetic Structures by Synchrotron Radiation Photoelectron Emission Microscopy
J. Phys. Soc. Jpn., **82** (2013) 021005.

S.Kurosumi, K.Horiba, N.Nagamura, S.Toyoda, H.Kumigashira, M.Oshima, S.Furutsuki, S.Nishimura, A.Yamada and N.Mizuno
Resonant Photoemission Spectroscopy of the Cathode Material Li_xMn_{0.5}Fe_{0.5}PO₄ for Lithium-Ion Battery
J. Power Sources, **226** (2013) 42.

T.Mizuno, J.Adachi, M.Kazama, M.Stener, P.Decleva and A.Yagishita

Angular Correlation between B K-VV Auger Electrons of BF_3 Molecules and Coincident Fragment Ions: Manifestation of Difference between the Angular Correlation and Molecular Frame Auger Electron Angular Distribution
Phys. Rev. Lett., **110** (2013) 043001.

E.Sakai, M.Tamamitsu, K.Yoshimatsu, S.Okamoto, K.Horiba, M.Oshima and H.Kumigashira
Gradual Localization of Ni 3d States in LaNiO_3 Ultrathin Films Induced by Dimensional Crossover
Phys. Rev. B, **87** (2013) 075132.

T.Okuda, R.Kajimoto, M.Okawa and T.Saitoh
Effects of Hole-Doping and Disorder on the Magnetic States of Delafossite CuCrO_2 Having a Spin-3/2 Antiferromagnetic Triangular Sublattice
Int. J. Mod. Phys. B, **27** (2013) 1330002.

S.Kawakami, N.Nakajima, T.Takigawa, M.Nakatake, H.Maruyama, Y.Tezuka and T.Iwazumi
UV-Induced Change in the Electronic Structure of SrTiO_3 at Low Temperature Probed by Resonant X-Ray Emission Spectroscopy
J. Phys. Soc. Jpn., **82** (2013) 053701.

T.Yokobori, M.Okawa, K.Konishi, R.Takei, K.Katayama, S.Oozono, T.Shinmura, T.Okuda, H.Wadati, E.Sakai, K.Ono, H.Kumigashira, M.Oshima, T.Sugiyama, E.Ikenaga, N.Hamada and T.Saitoh
Electronic Structure of Hole-Doped Delafossite Oxides $\text{CuCr}_{1-x}\text{Mg}_x\text{O}_2$
Phys. Rev. B, **87** (2013) 195124.

K.Tsubota, T.Wakita, H.Nagao, C.Hiramatsu, T.Ishiga, M.Sunagawa, K.Ono, H.Kumigashira, M.Danura, K.Kudo, M.Nohara, Y.Muraoka and T.Yokoya
Collapsed Tetragonal Phase Transition of $\text{Ca}(\text{Fe}_{1-x}\text{Rh}_x)_2\text{As}_2$ Studied by Photoemission Spectroscopy
J. Phys. Soc. Jpn., **82** (2013) 073705.

A.Chikamatsu, T.Matsuyama, T.Katayama, Y.Hirose, H.Kumigashira, M.Oshima, T.Fukumura and T.Hasegawa
Electronic and Transport Properties of Eu-Substituted Infinite-Layer Strontium Ferrite Thin Films
J. Cryst. Growth, **378** (2013) 165.

K.Nogami, K.Yoshimatsu, H.Mashiko, E.Sakai, H.Kumigashira, O.Sakata, T.Oshima and A.Ohtomo
Epitaxial Synthesis and Electronic Properties of Double-Perovskite $\text{Sr}_2\text{TiRuO}_6$ Films
Appl. Phys. Express, **6** (2013) 105502.

K.Yoshimatsu, E.Sakai, M.Kobayashi, K.Horiba, T.Yoshida, A.Fujimori, M.Oshima and H.Kumigashira
Determination of the Surface and Interface Phase Shifts in Metallic Quantum Well Structures of Perovskite Oxides
Phys. Rev. B, **88** (2013) 115308.

H.Suzuki, T.Yoshida, S.Ideta, G.Shibata, K.Ishigami, T.Kadono, A.Fujimori, M.Hashimoto, D.H.Lu, Z.-X.Shen, K.Ono, E.Sakai, H.Kumigashira, M.Matsuo and T.Sasagawa
Absence of Superconductivity in the Hole-Doped Fe Pnictide $\text{Ba}(\text{Fe}_{1-x}\text{Mn}_x)_2\text{As}_2$: Photoemission and X-Ray Absorption Spectroscopy Studies
Phys. Rev. B, **88** (2013) 100501.

K.Yoshimatsu, H.Wadati, E.Sakai, T.Harada, Y.Takahashi, T.Harano, G.Shibata, K.Ishigami, T.Kadono, T.Koide, T.Sugiyama, E.Ikenaga, H.Kumigashira, M.Lippmaa, M.Oshima and A.Fujimori
Spectroscopic Studies on the Electronic and Magnetic States of Co-Doped Perovskite Manganite $\text{Pr}_{0.8}\text{Ca}_{0.2}\text{Mn}_{1-y}\text{Co}_y\text{O}_3$ Thin Films
Phys. Rev. B, **88** (2013) 174423.

S.Toyoda, T.Namiki, E.Sakai, K.Nakata, M.Oshima and H.Kumigashira
Chemical-State-Resolved Depth Profiles of $\text{Al}/\text{Pr}_{0.7}\text{Ca}_{0.3}\text{MnO}_3$ Stacked Structures for Application in Resistive Switching Devices
J. Appl. Phys., **114** (2013) 243711.

M.Sakaki, N.Nakajima, F.Nakamura, Y.Tezuka and T.Suzuki
Electric-Field-Induced Insulator-Metal Transition in Ca_2RuO_4 Probed by X-Ray Absorption and Emission Spectroscopy
J. Phys. Soc. Jpn., **82** (2013) 093707.

M.Yamazaki, J.Adachi, T.Teramoto and A.Yagishita
Interatomic Resonant Auger Effects in Core-Level Photoemission from NO and CS_2 Molecules
J. Phys. B, **46** (2013) 115101.

M.Kazama, T.Fujikawa, N.Kishimoto, T.Mizuno, J.Adachi and A.Yagishita
Photoelectron Diffraction from Single Oriented Molecules: Towards Ultrafast Structure Determination of Molecules using X-Ray Free-Electron Lasers
Phys. Rev. A, **87** (2013) 063417.

3A

H.Wadati
Report on JSSRR Scientific Awards Resonant Soft X-Ray Scattering Studies of Transition-Metal-Oxide Thin Films
J. Jpn. Soc. Synchrotron Rad. Res., **26** (2013) 118. (*in Japanese*).

H.Maeda, Y.Ishiguro, T.Honda, J.-S.Jung, S.Michimura, T.Inami, T.Kimura and Y.Wakabayashi
Structural Investigation of Magnetocapacitive SmMnO_3
J. Ceram. Soc. Jpn., **121** (2013) 265.

- H.Sagayama, D.Uematsu, T.Arima, K.Sugimoto, J.J.Ishikawa, E.O'Farrell and S.Nakatsuji
Determination of Long-Range All-In-All-Out Ordering of Ir⁴⁺ Moments in a Pyrochlore Iridate Eu₂Ir₂O₇ by Resonant X-Ray Diffraction
Phys. Rev. B, **87** (2013) 100403.
- Y.Yamaki, Y.Yamasaki, H.Nakao, Y.Murakami, Y.Kaneko, and Y.Tokura
X-Ray Photoinduced Persistent and Bidirectional Phase Transition Enabled by Impurity Doping in Layered Manganite
Phys. Rev. B, **87** (2013) 081107.
- Y.Nii, H.Sagayama, H.Uemetsu, N.Abe, K.Taniguchi and T.Arima
Interplay among Spin, Orbital, and Lattice Degrees of Freedom in a Frustrated Spinel Mn₃O₄
Phys. Rev. B, **87** (2013) 195115.
- K.Tomiyasu, Y.Kubota, S.Shimomura, M.Onodera, S.Koyama, T.Nojima, S.Ishihara, H.Nakao and Y.Murakami
Spin-State Responses to Light Impurity Substitution in Low-Spin Perovskite LaCoO₃
Phys. Rev. B, **87** (2013) 224409.
- Y.Ishiguro, K.Kimura, S.Nakatsuji, S.Tsutsui, A.Q.R. Baron T.Kimura and Y.Wakabayashi
Dynamical Spin-Orbital Correlation in the Frustrated Magnet Ba₃CuSb₂O₉
Nature Communications, **4** (2013) 3022.
- J.Fujioka, Y.Yamasaki, H.Nakao, R.Kumai, Y.Murakami, M.Nakamura, M.Kawasaki and Y.Tokura
Spin-Orbital Superstructure in Strained Ferrimagnetic Perovskite Cobalt Oxide
Phys. Rev. Lett., **111** (2013) 027206.
- N.S.Sokolov, S.M.Suturin, B.B.Krichevtsov, V.G.Dubrovskii, S.V.Gastev, N.V.Sibirev, D.A.Baranov, V.V.Fedorov, A.A.Sitnikova, A.V.Nashchekin, V.I.Sakharov, I.T.Serenkov, T.Shimada, T.Yanase and M.Tabuchi
Cobalt Epitaxial Nanoparticles on CaF₂/Si(111): Growth Process, Morphology, Crystal Structure, and Magnetic Properties
Phys. Rev. B, **87** (2013) 125407.
- S.M.Suturin, V.V.Fedorov, A.M.Korovin, G.A.Valkovskiy, S.G.Konnikov, M.Tabuchi and N.S.Sokolov
A Look Inside Epitaxial Cobalt-on-Fluorite Nanoparticles with Three-Dimensional Reciprocal Space Mapping using GIXD, RHEED and GISAXS
J. Appl. Cryst., **46** (2013) 874.
- T.Nakajima, Y.Iguchi, H.Tamatsukuri, S.Mitsuda, Y.Yamasaki, H.Nakao and N.Terada
Uniaxial-Pressure Effects on Spin-Driven Lattice Distortions in Geometrically Frustrated Magnets CuFe_{1-x}Ga_xO₂ ($x = 0, 0.035$)
J. Phys. Soc. Jpn., **82** (2013) 114711.
- K.M.Papp-Wallace, M.A.Taracila, J.A.Gatta, N.Ohuchi, R.A.Bonomo and M.Nukaga
Insights into β -Lactamases from *Burkholderia* Species, Two Phylogenetically Related Yet Distinct Resistance Determinants
J. Biol. Chem., **288** (2013) 19090.
- K.Jogo, K.Nagashima, I.D.Hutcheon, A.N.Krot and T.Nakamura
Heavily Metamorphosed Clasts from the CV Chondrite Breccias Mokoia and Yamato-86009
Meteoritics and Planetary Science, **47** (2013) 2251.
- A.Tsuchiyama, T.Nakano, K.Uesugi, M.Uesugi, A.Takeuchi, Y.Suzuki, R.Noguchi, T.Matsumoto, J.Matsuno, T.Nagano, Y.Imai, T.Nakamura, T.Ogami, T.Noguchi, M.Abe, T.Yada and A.Fujimura
Analytical Dual-Energy Microtomography: A New Method for Obtaining Three-Dimensional Mineral Phase Images and its Application to Hayabusa Samples
Geochim. Cosmochim. Acta, **116** (2013) 5.
- A.Ruammitree, H.Nakahara, K.Akimoto, K.Soda and Y.Saito
Determination of Non-Uniform Graphene Thickness on SiC(0001) by X-Ray Diffraction
Appl. Surf. Sci., **282** (2013) 297.

3B

- K.Ozawa, T.Kakubo, K.Shimizu, N.Amino, K.Mase and T.Komatsu
High-Resolution Photoelectron Spectroscopy Analysis of Sulfidation of Brass at the Rubber/Brass Interface
Appl. Surf. Sci., **264** (2013) 297.

- K.Edamoto
The Electronic Properties of Nickel Phosphide Surfaces: Angle-Resolved and Resonant Photoemission Studies
Appl. Surf. Sci., **269** (2013) 7.

- S.Wang, T.Sakurai, X.Hao, W.Fu, S.Masuda and K.Akimoto
Favorable Electronic Structure for Organic Solar Cells Induced by Strong Interaction at Interface
J. Appl. Phys., **114** (2013) 183707.

- S.Wang, T.Sakurai, K.Komatsu and K.Akimoto
Effect of Ag-Doped Bathocuproine on the Recombination Properties of Exciton in Fullerene
J. Cryst. Growth, **378** (2013) 415.

- T.Sakurai, S.Wang, S.Toyoshima and K.Akimoto
Role of Electrode Buffer Layers in Organic Solar Cells
Renewable and Sustainable Energy Conference (IRSEC), 2013 International, (2013) 46.

3C

- T.Yamamoto, K.Hayashi, I.Seki, K.Suzuki and M.Ito
Pd-Based Metallic Glass with a Low Glass Transition Temperature
J. Non-Crystalline Solids, **359** (2013) 46.

M.Ito
Spin and Orbital Form Factor of CeRh₃B₂ Observed by X-Ray Magnetic Diffraction
Extended Abstract of FLIPPER 2013 (Single-Crystal Diffraction with Polarised Neutrons), (2013) 78.

K.Hirano, and Y.Takahashi
Applications of X-Ray Magnifier and Demagnifier to Angle-Resolved X-Ray Computed Tomography
J. Phys.: Conf. Ser., **425** (2013) 192004.

K.Hirano, Y.Ito, Y.Shinohara and Y.Amemiya
Characterization of an X-Ray Diamond Phase Plate by a Polarization Analyzer using Multiple Diffraction
J. Phys.: Conf. Ser., **425** (2013) 052030.

M.Naito, K.Hiragi, A.Sato, H.Maruyama and M.Ito
X-Ray Magnetic Diffraction Experiment of Fe₃Pt Alloy in Order Phase
Key Engineering Materials, **534** (2013) 3.

K.Hirano Y.Takahashi and S.Nagamachi
Application of X-Ray Phase Plate to Grazing Incidence X-Ray Topography for the Control of Penetration Depth
Nucl. Instrum. Meth. Phys. Res. A, **729** (2013) 537.

N.Watanabe, J.Hashizume, M.Goto, M.Yamaguchi, T.Tsujimura and S.Aoki
Differential Phase Microscope and Micro-Tomography with a Foucault Knife-Edge Scanning Filter
J. Phys.: Conf. Series, **463** (2013) 012011.

4A

Y.Takanishi, I.Nishiyama, J.Yamamoto, Y.Ohtsuka and A.Iida
Smectic-C* Liquid Crystals with Six-Layer Periodicity Appearing between the Ferroelectric and Antiferroelectric Chiral Smectic Phases
Phys. Rev. E, **87** (2013) 050503.

A.Iida
Synchrotron Radiation X-Ray Fluorescence Spectrometry
Encyclopedia of Analytical Chemistry, (2013)

Y.Kageyama, N.Tanigake, Y.Kurokome, S.Iwaki, S.Takeda, K.Suzuki and T.Sugawara
Macroscopic Motion of Supramolecular Assemblies Actuated by Photoisomerization of Azobenzene Derivatives
Chem. Comm., **49** (2013) 9386.

R.Nakada, Y.Takahashi and M.Tanimizu
Isotopic and Speciation Study on Cerium during its Solid-Water Distribution with Implication for Ce Stable Isotope as a Paleo-Redox Proxy
Geochim. Cosmochim. Acta, **103** (2013) 49.

Y.Takahashi, T.Furukawa, Y.Kanai, M.Uematsu, G.Zheng and M.A.Marcus
Seasonal Changes in Fe Species and Soluble Fe Concentration in the Atmosphere in the Northwest Pacific Region Based on the Analysis of Aerosols Collected in Tsukuba, Japan
Atmos. Chem. Phys., **13** (2013) 7695.

L.Wang, J.Li, J.Pan, X.Jiang, Y.Ji, Y.Li, Y.Qu, Y.Zhao, X.Wu and C.Chen
Revealing the Binding Structure of the Protein Corona on Gold Nanorods Using Synchrotron Radiation-Based Techniques: Understanding the Reduced Damage in Cell Membranes
J. Am. Chem. Soc., **135** (2013) 17359.

M.Terabayashi, T.Matsui, K.Okamoto, H.Ozawa, Y.Kaneko and S.Maruyama
Micro-X-Ray Absorption Near Edge Structure Determination of Fe³⁺/ΣFe in Omphacite Inclusion within Garnet from Dabie Eclogite, East-Central China Island Arc, **22** (2013) 37.

H.Hanashima, N.Kitajima, T.Abe and A.Hokura
Study on Accumulation Mechanism of Arsenic and Selenium in *Pteris vittata* L. Using Synchrotron Radiation X-Ray Fluorescence Analysis
Adv. X-Ray Chem. Anal. Jpn., **44** (2013) 279. (*in Japanese*).

H.Kagi, S.Odake, H.Ishibashi, K.Shozugawa, M.Matsuo, W.Satake and T.Mikouchi
Oxygen Fugacity and Valence State of Chromium in Ferropiciclast: Can Cr²⁺ Be a Redox Indicator for the Deep Mantle?
J. Mineralogical and Petrological Sciences, **108** (2013) 172.

S.Mitsunobu, C.Muramatsu, K.Watanabe and M.Sakata
Behavior of Antimony(V) during the Transformation of Ferrihydrite and its Environmental Implications
Environ. Sci. Technol., **47** (2013) 9660.

S.Mitsunobu, N.Hamamura, T.Kataoka and F.Shiraishi
Arsenic Attenuation in Geothermal Streamwater Coupled with Biogenic Arsenic(III) Oxidation
Applied Geochemistry, **35** (2013) 154.

4B2

V.Petrykin, K.Macounova, M.Okube, S.Mukerjee and P.Krtil
Local Structure of Co Doped RuO₂ Nanocrystalline Electrocatalytic Materials for Chlorine and Oxygen Evolution
Catal. Today, **202** (2013) 63.

M.Yashima, T.Sekikawa, D.Sato, H.Nakano and K.Omoto
Crystal Structure and Oxide-Ion Diffusion of Nanocrystalline, Compositionally Homogeneous Ceria-Zirconia Ce_{0.5}Zr_{0.5}O₂ up to 1176 K
Crystal Growth and Design, **13** (2013) 829.

- M.Okubo, K.Kagesawa, Y.Mizuno, D.Asakura, E.Hosono, T.Kudo, H.S.Zhou, K.Fujii, H.Uekusa, S.Nishimura, A.Yamada, A.Okazawa and N.Kojima
Reversible Solid State Redox of an Octacyanometallate-Bridged Coordination Polymer by Electrochemical Ion Insertion/Extraction
Inorg. Chem., **52** (2013) 3772.
- K.Fujii, M.Aoki and H.Uekusa
Solid-State Hydration/Dehydration of Erythromycin A Investigated by *ab Initio* Powder X-Ray Diffraction Analysis: Stoichiometric and Nonstoichiometric Dehydrated Hydrate
Cryst. Growth Design, **13** (2013) 2060.
- M.Yashima, U.Fumi, H.Nakano, K.Omoto and J.R.Hester
Crystal Structure, Optical Properties, and Electronic Structure of Calcium Strontium Tungsten Oxynitrides $\text{Ca}_x\text{Sr}_{1-x}\text{WO}_2\text{N}$
J. Phys. Chem. C, **117** (2013) 18529.
- K.Fujii, H.Kato, K.Omoto, M.Yashima, J.Chen and X.Xing
Experimental Visualization of the Bi-O Covalency in Ferroelectric Bismuth Ferrite (BiFeO_3) by Synchrotron X-Ray Powder Diffraction Analysis
Phys. Chem. Chem. Phys., **15** (2013) 6779.
- T.Ye, P.Barpanda, S.Nishimura, N.Furuta, S.-C.Chung and A.Yamada
General Observation of $\text{Fe}^{3+}/\text{Fe}^{2+}$ Redox Couple Close to 4 V in Partially Substituted $\text{Li}_2\text{FeP}_2\text{O}_7$ Pyrophosphate Solid-Solution Cathodes
Chem. Mater., **25** (2013) 3623.
- J.Kim, K.H.Cho, I.Kagomiya and K.Park
Structural Studies of Porous Ni/YSZ Cermets Fabricated by the Solid-State Reaction Method
Ceramics International, **39** (2013) 7467.
- I.Kagomiya, S.Matsumoto, K.Kakimoto, H.Ohsato, H.Sakai and Y.Maeda
Annealing Effect on Temperature Coefficient of Resistivity in $\text{La}_{1-x}\text{Sr}_x\text{MnO}_3$ Ceramics
J. Euro. Ceram. Soc., **33** (2013) 985.
- K.Terada, H.Kurobe, M.Ito, Y.Yoshihashi, E.Yonemochi, K.Fujii and H.Uekusa
Polymorphic and Pseudomorphic Transformation Behavior of Acyclovir Based on Thermodynamics and Crystallography
J. Therm. Anal. Calorim., **113** (2013) 1261.
- I.Kagomiya, K.Jimbo and K.Kakimoto
Distribution Change of Oxygen Vacancies in Layered Perovskite Type $(\text{Sr},\text{La})_{n+1}\text{Fe}_n\text{O}_{3n+1}$ ($n=3$)
J. Sol. Stat. Chem., **207** (2013) 184.
- H.Wadati
Report on JSSRR Scientific Awards Resonant Soft X-Ray Scattering Studies of Transition-Metal-Oxide Thin Films
J. Jpn. Soc. Synchrotron Rad. Res., **26** (2013) 118. (*in Japanese*).
- Y.Yamaki, Y.Yamasaki, H.Nakao, Y.Murakami, Y.Kaneko, and Y.Tokura
X-Ray Photoinduced Persistent and Bidirectional Phase Transition Enabled by Impurity Doping in Layered Manganite
Phys. Rev. B, **87** (2013) 081107.
- M.Kamitani, M.S.Bahramy, R.Arita, S.Seki, T.Arima, Y.Tokura and S.Ishiwata
Superconductivity in Cu_xIrTe_2 Driven by Interlayer Hybridization
Phys. Rev. B, **87** (2013) 180501.
- K.Tomiyasu, Y.Kubota, S.Shimomura, M.Onodera, S.Koyama, T.Nojima, S.Ishihara, H.Nakao and Y.Murakami
Spin-State Responses to Light Impurity Substitution in Low-Spin Perovskite LaCoO_3
Phys. Rev. B, **87** (2013) 224409.
- Y.Ishiguro, K.Kimura, S.Nakatsuji, S.Tsutsui, A.Q.R.Baron T.Kimura and Y.Wakabayashi
Dynamical Spin-Orbital Correlation in the Frustrated Magnet $\text{Ba}_3\text{CuSb}_2\text{O}_9$
Nature Communications, **4** (2013) 3022.
- J.Fujioka, Y.Yamasaki, H.Nakao, R.Kumai, Y.Murakami, M.Nakamura, M.Kawasaki and Y.Tokura
Spin-Orbital Superstructure in Strained Ferrimagnetic Perovskite Cobalt Oxide
Phys. Rev. Lett., **111** (2013) 027206.
- M.Nakamura, R.Imai, N.Otsuka, N.Hoshi and O.Sakata
Ethanol Oxidation on Well-Ordered PtSn Surface Alloy on Pt(111) Electrode
J. Phys. Chem. C, **117** (2013) 18139.
- R.Takahashi, T.Honda, A.Miyake, T.Kagayama, K.Shimizu, T.Ebihara, T.Kimura and Y.Wakabayashi
Valence Ordering in the Intermediate-Valence Magnet YbPd
Phys. Rev. B, **88** (2013) 054109.
- A.Ruammitree, H.Nakahara, K.Akimoto, K.Soda and Y.Saito
Determination of Non-Uniform Graphene Thickness on $\text{SiC}(0001)$ by X-Ray Diffraction
Appl. Surf. Sci., **282** (2013) 297.

- A.Gao, G.-Y. Mei, S.Liu, P.Wang, Q.Tang, Y.-P. Liu, H.Wen, X.-M.An, L.-Q.Zhang, X.-X.Yan and D.-C.Liang
High-Resolution Structures of AidH Complexes Provide Insights into a Novel Catalytic Mechanism for *N*-Acyl Homoserine Lactonase
Acta Cryst. D, **69** (2013) 82.
- T.Yanagisawa, T.Sumida, R.Ishii and S.Yokoyama
A Novel Crystal Form of Pyrrolysyl-tRNA Synthetase Reveals the Pre- and Post-Aminoacyl-tRNA Synthesis Conformational States of the Adenylate and Aminoacyl Moieties and an Asparagine Residue in the Catalytic Site
Acta Cryst. D, **69** (2013) 5.
- N.Saito and Y.Matsuura
A 2.1-Å-Resolution Crystal Structure of Unliganded CRM1 Reveals the Mechanism of Autoinhibition
J. Mol. Biol., **425** (2013) 350.
- K.Makabe, T.Nakamura and K.Kuwajima
Structural Insights into the Stability Perturbations Induced by N-Terminal Variation in Human and Goat α -Lactalbumin.
Protein Eng. Design and Selection, **26** (2013) 165.
- D.F.Li, L.Feng, Y.J.Hou and W.Liu
The Expression, Purification and Crystallization of a Ubiquitin-Conjugating Enzyme E2 from *Agrocybe aegerita* Underscore the Impact of His-Tag Location on Recombinant Protein Properties
Acta Cryst. F, **69** (2013) 153.
- C.Nakamura, S.Yajima, T.Miyamoto and M.Sue
Structural Analysis of an Epsilon-Class Glutathione Transferase from Housefly, *Musca domestica*
Biochem. Biophys. Res. Commun., **430** (2013) 1206.
- J.Otani, K.Arita, T.Kato, M.Kinoshita, H.Kimura, I.Suetake, S.Tajima, M.Ariyoshi and M.Shirakawa
Structural Basis of the Versatile DNA Recognition Ability of the Methyl-CpG Binding Domain of Methyl-CpG Binding Domain Protein 4
J. Biol. Chem., **288** (2013) 6351.
- Y.Itoh, S.Sekine, S.Suetsugu and S.Yokoyama
Tertiary Structure of Bacterial Selenocysteine tRNA
Nucl. Acids Res., **41** (2013) 6729.
- Z.Fujimoto, R.Suzuki, T.Shiotsuki, W.Tsuchiya, A.Tase, M.Momma and T.Yamazaki
Crystal Structure of Silkworm *Bombyx mori* JHBP in Complex with 2-Methyl-2,4-Pentanediol: Plasticity of JH-Binding Pocket and Ligand-Induced Conformational Change of the Second Cavity in JHBP
PLoS One, **8** (2013) e56261.
- Z.Fujimoto, A.Jackson, M.Michikawa, T.Maehara, M.Momma, B.Henrissat, H.J.Gilbert and S.Kaneko
The Structure of a *Streptomyces avermitilis* α -L-Rhamnosidase Reveals a Novel Carbohydrate-Binding Module CBM67 within the Six-Domain Arrangement
J. Biol. Chem., **288** (2013) 12376.
- J.Y.Yoon, J.Kim, D.R.An, S.J.Lee, H.S.Kim, H.N.Im, H.J.Yoon, J.Y.Kim, S.J.Kim, B.W.Han and S.W.Suh
Structural and Functional Characterization of HP0377, a Thioredoxin-Fold Protein from *Helicobacter pylori*
Acta Cryst. D, **69** (2013) 735.
- M.Fujihashi, K.Mito, E.F.Pai and K.Miki
Atomic Resolution Structure of the Orotidine 5'-Monophosphate Decarboxylase Product Complex Combined with Surface Plasmon Resonance Analysis: Implication for the Catalytic Mechanism
J. Biol. Chem., **288** (2013) 9011.
- T.Ouchi, T.Tomita, A.Horie, A.Yoshida, K.Takahashi, H.Nishida, K.Lassak, H.Taka, R.Mineki, T.Fujimura, S.Kosono, C.Nishiyama, R.Masui, S.Kuramitsu, S.-V.Albers, T.Kuzuyama and M.Nishiyama
Lysine and Arginine Biosyntheses Mediated by a Common Carrier Protein in *Sulfolobus*
Nature Chemical Biology, **9** (2013) 277.
- Q.Zhang, S.Qi, M.Xu, L.Yu, Y.Tao, Z.Deng, W.Wu, J.Li, Z.Chen and J.Wong
Structure-Function Analysis Reveals a Novel Mechanism for Regulation of Histone Demethylase LSD2/AOF1/KDM1b
Cell Res., **23** (2013) 225.
- A.Matsumoto, Y.Shimizu, C.Takemoto, T.Ueda, T.Uchiyumi and K.Ito
Crystallization and Preliminary X-Ray Analysis of Peptidyl-tRNA Hydrolase from *Thermus thermophilus* HB8
Acta Cryst. F, **69** (2013) 332.
- T.Miyafusa, J.M.M.Caaveiro, Y.Tanaka, M.E.Tanner and K.Tsumoto
Crystal Structure of the Capsular Polysaccharide Synthesizing Protein CapE of *Staphylococcus aureus*
Biosci. Rep., **33** (2013) 463.
- J.Kobayashi and Y.Matsuura
Structural Basis for Cell-Cycle-Dependent Nuclear Import Mediated by the Karyopherin Kap121p
J. Mol. Biol., **425** (2013) 1852.
- J.Wachino, Y.Yamaguchi, S.Mori, H.Kurosaki, Y.Arakawa and K.Shibayama.
Structural Insights into the Subclass B3 Metallo- β -Lactamase, SMB-1, and the Mode of Inhibition by the Common Metallo- β -Lactamase Inhibitor, Mercaptoacetate
Antimicrobial Agents and Chemotherapy, **57** (2013) 101.
- H.Zheng, T.Miyakawa, Y.Sawano, S.Yamagoe and M.Tanokura
Crystallization and Preliminary X-Ray Analysis of Human Leukocyte Cell-Derived Chemotaxin 2 (LECT2)
Acta Cryst. F, **69** (2013) 316.

- M.Okai, J.Ohtsuka, L.F.Imai, T.Mase, R.Moriuchi, M.Tsuda, K.Nagata, Y.Nagata and M.Tanokura
Crystal Structure and Site-Directed Mutagenesis Analyses of Haloalkane Dehalogenase LinB from *Sphingobium* sp. Strain MI1205
J. Bacteriol., **195** (2013) 2642.
- R.Nasuno, Y.Hirano, T.Itoh, T.Hakoshima, T.Hibi and H.Takagi
Structural and Functional Analysis of the Yeast *N*-Acetyltransferase Mpr1 Involved in Oxidative Stress Tolerance via Proline Metabolism
Proc. Natl. Acad. Sci. USA, **110** (2013) 11821.
- T.Arimori, N.Kawamoto, S.Shinya, N.Okazaki, M.Nakazawa, K.Miyatake, T.Fukamizo, M.Ueda and T.Tamada
Crystal Structures of the Catalytic Domain of a Novel Glycohydrolase Family 23 Chitinase from *Ralstonia* sp. A-471 Reveals a Unique Arrangement of the Catalytic Residues for Inverting Chitin Hydrolysis
J. Biol. Chem., **288** (2013) 18696.
- Y.Nagamatsu, K.Takeda, T.Kuranaga, N.Numoto and K.Miki
Origin of Asymmetry on the Intersubunit Interfaces of V_1 -ATPase from *Thermus thermophilus*
J. Mol. Biol., **425** (2013) 2699.
- Y.Nishitani, R.Aono, A.Nakamura, T.Sato, H.Atomi, T.Imanaka and K.Miki
Structure Analysis of Archaeal AMP Phosphorylase Reveals Two Unique Modes of Dimerization
J. Mol. Biol., **425** (2013) 2709.
- Y.Hattori, K.Furuuta, I.Ohki, T.Ikegami, H.Fukada, M.Shirakawa, T.Fujiwara and C.Kojima
Utilization of Lysine ^{13}C -Methylation NMR for Protein-Protein Interaction Studies
J. Biomol. NMR, **55** (2013) 19.
- K.Taoka, I.Ohki, H.Tsuji, C.Kojima and K.Shimamoto
Structure and Function of Florigen and the Receptor Complex
Trends in Plant Science, **18** (2013) 287.
- M.Chen, J.Yu, Y.Tanaka, M.Tanaka, I.Tanaka and M.Yao
Structure of Dihydrouridine Synthase C (DusC) from *Escherichia coli*
Acta Cryst. F, **69** (2013) 834.
- Y.Yagita, N.Kuse, K.Kuroki, H.Gatanaga, J.M.Carlson, T.Chikata, Z.L.Brumme, H.Murakoshi, T.Akahoshi, N.Pfeifer, S.Mallal, M.John, T.Ose, H.Matsubara, R.Kanda, Y.Fukunaga, K.Honda, Y.Kawashima, Y.Ariumi, S.Oka, K.Maenaka and M.Takiguchi
Distinct HIV-1 Escape Patterns Selected by Cytotoxic T Cells with Identical Epitope Specificity
J. Virol., **87** (2013) 2253.
- T.Hirose, N.Maita, H.Gouda, J.Koseki, T.Yamamoto, A.Sugawara, H.Nakano, S.Hirono, K.Shioimi, T.Watanabe, H.Taniguchi, K.B.Sharpless, S.Omura and T.Sunazuka
Observation of the Controlled Assembly of Preclick Components in the in situ Click Chemistry Generation of a Chitinase Inhibitor
Proc. Natl. Acad. Sci. USA, **110** (2013) 15892.
- A.Nakamura, T.Ishida, S.Fushinobu, K.Kusaka, I.Tanaka, K.Inaka, Y.Higuchi, M.Masaki, K.Ohta, S.Kaneko, N.Niimura, K.Igarashi and M.Samajima
Phase-Diagram-Guided Method for Growth of a Large Crystal of Glycoside Hydrolase Family 45 Inverting Cellulase Suitable for Neutron Structural Analysis
J. Synchrotron Rad., **20** (2013) 859.
- S.Fushinobu, V.D.Alves and P.M.Coutinho
Multiple Rewards from a Treasure Trove of Novel Glycoside Hydrolase and Polysaccharide Lyase Structures: New Folds, Mechanistic Details, and Evolutionary Relationships
Curr. Opin. Struct. Biol., **23** (2013) 652.
- K.Matsumoto, Y.Tanaka, T.Watanabe, R.Motohashi, K.Ikeda, K.Tobitani, M.Yao, I.Tanaka and S.Taguchi
Directed Evolution and Structural Analysis of NADPH-Dependent Acetoacetyl Coenzyme A (Acetoacetyl-CoA) Reductase from *Ralstonia eutropha* Reveals Two Mutations Responsible for Enhanced Kinetics
Appl. Environ. Microbiol., **79** (2013) 6134.
- Z.Gai, A.Nakamura, Y.Tanaka, N.Hirano, I.Tanaka and M.Yao
Crystal Structure Analysis, Overexpression and Refolding Behavior of a DING Protein with Single Mutation
J. Synchrotron Rad., **20** (2013) 854.
- T.Sugawara, D.Yamashita, Y.Tanaka, J.Kaneko, Y.Kamio, I.Tanaka and M.Yao
Preliminary X-Ray Crystallographic Study of Staphylococcal α -Hemolysin Monomer
Acta Cryst. F, **69** (2013) 868.
- Z.Fujimoto
Structure and Function of Carbohydrate-Binding Module Families 13 and 42 of Glycoside Hydrolases, Comprising a β -Trefol Fold
Biosci. Biotechnol. Biochem., **77** (2013) 1363.
- T.Arimori, A.Ito, M.Nakazawa, M.Ueda and T.Tamada
Crystal Structure of Endo-1,4- β -Glucanase from *Eisenia fetida*
J. Synchrotron Rad., **20** (2013) 884.
- T.Miyafusa, J.M.M.Caaveiro, Y.Tanaka and K.Tsumoto
Dynamic Elements Govern the Catalytic Activity of CapE, a Capsular Polysaccharide-Synthesizing Enzyme from *Staphylococcus aureus*
FEBS Lett., **587** (2013) 3824.

- K.Takemoto, T.Matsuda, N.Sakai, D.Fu, M.Noda, S.Uchiyama, I.Kotera, Y.Arai, M.Horiuchi, K.Fukui, T.Ayabe, F.Inagaki, H.Suzuki and T.Nagai
SuperNova, a Monomeric Photosensitizing Fluorescent Protein for Chromophore-Assisted Light Inactivation. *Sci. Rep.*, **3** (2013) 2629.
- Y.Yasutake, T.Nishioka, N.Imoto and T.Tamura
A Single Mutation at the Ferredoxin Binding Site of P450 Vdh Enables Efficient Biocatalytic Production of 25-Hydroxyvitamin D₃
ChemBioChem, **14** (2013) 2284.
- M.Elahi, M.M.Islam, K.Noguchi, M.Yohda and Y.Kuroda
High Resolution Crystal Structure of Dengue-3 Envelope Protein Domain III Suggests Possible Molecular Mechanisms for Serospecific Antibody Recognition Proteins, **81** (2013) 1090.
- J.Matsuzawa, T.Umeda, H.Aikawa, C.Suzuki, Z.Fujimoto, K.Okada, H.Yamane and H.Nojiri
Crystallization and Preliminary X-Ray Diffraction Studies of the Reduced Form of the Terminal Oxygenase Component of the Rieske Nonhaem Iron Oxygenase System Carbazole 1, 9a-Dioxygenase.
Acta Cryst. F, **69** (2013) 1284.
- Y.Kanemaru, F.Hasebe, T.Tomita, T.Kuzuyama and M.Nishiyama
Two ATP-Binding Cassette Transporters Involved in (*S*)-2-Aminoethyl-Cysteine Uptake in *Thermus thermophilus*
J. Bacteriology, **195** (2013) 3845.
- H.Do, J.H.Lee, M.H.Kwon, H.E.Song, J.Y.An, S.H.Eom, S.G.Lee and H.J.Kim
Purification, Characterization and Preliminary X-Ray Diffraction Analysis of a Cold-Active Lipase (CpsLip) from the Psychrophilic Bacterium *Colwellia psychrerythraea* 34H
Acta Cryst. F, **69** (2013) 920.
- R.Kawakami, C.Noguchi, M.Higashi, H.Sakuraba and T.Ohshima
Comparative Analysis of the Catalytic Components in the Archaeal Dye-Linked *L*-Proline Dehydrogenase Complexes
Appl. Microbiol. Biotechnol., **97** (2013) 3419.
- K.Uechi, H.Sakuraba, A.Yoshihara, K.Morimoto and G.Takata
Structural Insight into *L*-Ribulose 3-Epimerase from *Mesorhizobium loti*
Acta Cryst. D, **69** (2013) 2330.
- S.Yoshikawa, M.Kukimoto-Niino, L.Parker, N.Handa, T.Terada, T.Fujimoto, Y.Terazawa, M.Wakiyama, M.Sato, S.Sano, T.Kobayashi, T.Tanaka, L.Chen, Z.-J.Liu, B.-C.Wang, M.Shirouzu, S.Kawa, K.Semba, T.Yamamoto and S.Yokoyama
Structural Basis for the Altered Drug Sensitivities of Non-Small Cell Lung Cancer-Associated Mutants of Human Epidermal Growth Factor Receptor
Oncogene, **32** (2013) 27.
- Y.Itoh, M.J. Bröcker, S.Sekine, G.Hammond, S.Suetsugu, D.Söll and S.Yokoyama
Decameric Sela-tRNA^{S^{ec}} Ring Structure Reveals Mechanism of Bacterial Selenocysteine Formation
Science, **340** (2013) 75.
- X.Zhang, L.Jiang, G.Wang, L.Yu, Q.Zhang, Q.Xin, W.Wu, Z.Gong and Z.Chen
Structural Insights into the Abscisic Acid Stereospecificity by the ABA Receptors PYR/PYL/RCAR
PLOS ONE, **8** (2013) e67477.
- P.Zhou, Z.Chen, Q.Yan, S.Yang, R.Hilgenfeld and Z.Jiang
The Structure of a Glycoside Hydrolase Family 81 Endo- β -1, 3-Glucanase
Acta Cryst. D, **69** (2013) 2027.
- M.Unno, S.Kinjo, K.Kizawa and H.Takahara
Crystallization and Preliminary X-Ray Crystallographic Analysis of Human Peptidylarginine Deiminase Type I
Acta Cryst. F, **69** (2013) 1357.
- M.Unno, A.Ardèvol, C.Rovira and M.Ikeda-Saito
Structures of the Substrate-Free and Product-Bound Forms of HmuO, a Heme Oxygenase from *Corynebacterium diphtheriae*: X-Ray Crystallography and Molecular Dynamics Investigation
J. Biol. Chem., **288** (2013) 34443.
- T.Ogawa, K.Noguchi, M.Saito, Y.Nagahata, H.Kato, A.Ohtaki, H.Nakayama, N.Dohmae, Y.Matsushita, M.Odaka, M.Yohda, H.Nyunoya and Y.Katayama
Carbonyl Sulfide Hydrolase from *Thiobacillus thioparus* Strain THI115 Is One of the β -Carbonic Anhydrase Family Enzymes
J. Am. Chem. Soc., **135** (2013) 3818.
- T.Fujiwara, K.Komoda, N.Sakurai, K.Tajima, I.Tanaka, M.Yao
The C-Di-GMP Recognition Mechanism of the PilZ Domain of Bacterial Cellulose Synthase Subunit A
Biochemical and Biophysical Research Communications, **431** (2013) 802.
- H.Unno, K.Hisamatsu, T.Nagao, Y.Tateya, N.Matsumoto, S.Goda and T.Hatakeyama
Crystallization and Preliminary Crystallographic Study of Oligomers of the Haemolytic Lectin CEL-III from the Sea Cucumber *Cucumaria echinata*
Acta Cryst. F, **69** (2013) 416.

- D.Iino, Y.Takakura, K.Fukano, Y.Sasaki, T.Hoshino, K.Ohsawa, A.Nakamura and S.Yajima
Crystal Structures of the Ternary Complex of APH(4)-Ia/Hph with Hygromycin B and an ATP Analog using a Thermostable Mutant
J. Struct. Biol., **183** (2013) 76.
- N.Kono, U.Ohto, T.Hiramatsu, M.Urabe, Y.Uchida, Y.Satow and H.Arai
Impaired α -TTP-PIPs Interaction Underlies Familial Vitamin E Deficiency
Science, **340** (2013) 1106.
- K.Yamamoto, M.Suzuki, A.Higashiura and A.Nakagawa
Three-Dimensional Structure of a *Bombyx mori* Omega-Class Glutathione Transferase
Biochemical and Biophysical Research Communications, **438** (2013) 588.
- A.Shimizu, A.Kawana-Tachikawa, A.Yamagata, C.Han, D.Zhu, Y.Sato, H.Nakamura, T.Koibuchi, J.Carson, E.Martin, C.J.Brumme, Y.Shi, G.F.Gao, Z.L.Brumme, S.Fukai and A.Iwamoto
Structure of TCR and Antigen Complexes at an Immunodominant CTL Epitope in HIV-1 Infection
Sci. Rep., **3** (2013) 3097.
- S.Sugiyama, N.Shimizu, G.Sasaki, M.Hirose, Y.Takahashi, M.Maruyama, H.Matsumura, H.Adachi, K.Takano, S.Murakami, T.Inoue and Y.Mori
A Novel Approach for Protein Crystallization by a Synthetic Hydrogel with Thermoreversible Gelation Polymer
Cryst. Growth Des., **13** (2013) 1899.
- J.Y.Yoon, D.R.An, H.-J.Yoon, H.S.Kim, S.J.Lee, H.N.Im, J.Y.Jang and S.W.Suh
High-Resolution Crystal Structure of *Streptococcus pyogenes* β -NAD⁺ Glycohydrolase in Complex with its Endogenous Inhibitor IFS Reveals a Highly Water-Rich Interface
J. Synchrotron Rad., **20** (2013) 962.
- J.Hwang, B.S.Kim, S.Y.Jang, J.G.Lim, D.-J.You, H.S.Jung, T.-K.Oh, J.-O.Lee, S.H.Choi and M.H.Kim
Structural Insights into the Regulation of Sialic Acid Catabolism by the *Vibrio vulnificus* Transcriptional Repressor NanR
Proc. Natl. Acad. Sci. USA, **110** (2013) E2829.
- M.Kato, Y.Kezuka, C.Kobayashi, K.Ishibashi, T.Nonaka, M.Ishikawa and E.Katoh
Crystallization and Preliminary X-Ray Crystallographic Analysis of the Inhibitory Domain of the Tomato Mosaic Virus Resistance Protein Tm-1
Acta Cryst. F, **69** (2013) 1411.
- M.Fujihashi, T.Ishida, S.Kuroda, L.P.Kotra, E.F.Pai and K.Miki
Substrate Distortion Contributes to the Catalysis of Orotidine 5'-Monophosphate Decarboxylase
J. Am. Chem. Soc., **135** (2013) 17432.
- T.Tominaga, S.Watanabe, R.Matsumi, H.Atomi, T.Imanaka and K.Miki
Crystal Structures of the Carbamoylated and Cyanated Forms of HypE for [NiFe] Hydrogenase Maturation
Proc. Natl. Acad. Sci. USA, **110** (2013) 20485.
- H.Kim and J.Cho
The X-Ray Crystal Structure of PA1374 from *Pseudomonas aeruginosa*, a Putative Oxidative-Stress Sensing Transcriptional Regulator
Biochem. Biophys. Res. Commun., **431** (2013) 376.
- K.Yamamoto, M.Suzuki, A.Higashiura, K.Aritake, Y.Urade, N.Uodome, M.D.T.Hossain and A.Nakagawa
New Insights into the Catalytic Mechanism of *Bombyx mori* Prostaglandin E Synthase Gained from Structure-Function Analysis
Biochemical and Biophysical Research Communications, **440** (2013) 762.
- R.Satou, A.Miyanaga, H.Ozawa, N.Funa, Y.Katsuyama, K.Miyazono, M.Tanokura, Y.Ohnishi and S.Horinouchi
Structural Basis for Cyclization Specificity of Two *Azotobacter* Type III Polyketide Synthases: A Single Amino Acid Substitution Reverses their Cyclization Specificity
J. Biol. Chem., **288** (2013) 34146.
- K.Suzuki, M.Tsunoda, M.M.Hoque, F.Zhang, J.Jiang, X.Zhang, N.Ohbayashi, H.Tanaka and A.Takenaka
Peculiarity in Crystal Packing of Anti-HIV Lectin Actinohivin in Complex with α (1-2)Mannobiose
Acta Cryst. D, **69** (2013) 1818.
- F.Zhang, M.Tsunoda, K.Suzuki, Y.Kikuchi, O.Wilkinson, C.L.Millington, G.P.Margison, D.M.Williams, E.C.Morishita and A.Takenaka
Structures of DNA Duplexes Containing O⁶-Carboxymethylguanine, a Lesion Associated with Gastrointestinal Cancer, Reveal a Mechanism for Inducing Pyrimidine Transition Mutations
Nucl. Acids Res., **41** (2013) 5524.
- S.Aizawa, M.Senda, A.Harada, N.Maruyama, T.Ishida, T.Aigaki, A.Ishigami and T.Senda
Structural Basis of the γ -Lactone-Ring Formation in Ascorbic Acid Biosynthesis by the Senescence Marker Protein-30/Gluconolactonase
PLoS One, **8** (2013) e53706.
- A.Furukawa, J.Kamishikiryo, D.Mori, K.Toyonaga, Y.Okabe, A.Toji, R.Kanda, Y.Miyake, T.Ose, S.Yamasaki and K.Maenaka
Structural Analysis for Glycolipid Recognition by the C-Type Lectins Mincle and MCL
Proc. Natl. Acad. Sci. USA, **110** (2013) 17438.
- K.R.Kim, S.H.Park, H.S.Kim, K.H.Rhee, B.-G.Kim, D.G.Kim, M.S.Park, H.-J.Kim, S.Kim and B.W.Han
Crystal Structure of Human Cytosolic Aspartyl-tRNA Synthetase, a Component of Multi-tRNA Synthetase Complex
Proteins, **81** (2013) 1840.

6A

- Y.Zhao, K.Hayasaka, G.Matsuba and H.Ito
In Situ Observations of Flow-Induced Precursors during Shear Flow
Macromolecules, **46** (2013) 172.
- H.Okuda, T.Horiuchi, T.Tsukamoto, S.Ochiai, M.Yamasaki and Y.Kawamura
Evolution of Long-Period Stacking Order Structures on Annealing As-Cast Mg₈₅Y₉Zn₆ Alloy Ingot Observed by Synchrotron Radiation Small-Angle Scattering
Scripta Materialia, **68** (2013) 575.
- H.Okuda and S.Ochiai
A Review on Small- and Wide-Angle X-Ray Scattering Applied to the Precipitation Process in Metallic Alloys
Metallurgical and Materials Transactions A, **44** (2013) 94.
- H.Yokoyama
Small Angle X-Ray Scattering Studies of Nanocellular and Nanoporous Structures
Polymer J., **45** (2013) 3.
- D.Sato, K.Obara, M.Iwahashi, Y.Kawabata and T.Kato
Re-entrant Lamellar/Onion Transition with Varying Temperature under Shear Flow
Langmuir, **29** (2013) 121.
- M.Yoshino, T.Kikukawa, H.Takahashi, T.Takagi, Y.Yokoyama, H.Amii, T.Baba, T.Kanamori and M.Sonoyama
Physicochemical Studies of Bacteriorhodopsin Reconstituted in Partially Fluorinated Phosphatidylcholine Bilayers
J. Phys. Chem. B, **117** (2013) 5422.
- Y.Sugimoto, M.Shioya, H.Matsumoto, M.Minagawa and A.Tanioka
Structure Changes during Tensile Deformation and Mechanical Properties of a Twisted Carbon Nanotube Yarn
Carbon, **60** (2013) 193.
- H.Takeno and W.Nakamura
Structural and Mechanical Properties of Composite Hydrogels Composed of Clay and a Polyelectrolyte Prepared by Mixing
Colloid and Polymer Science, **291** (2013) 1393.
- M.Harada, M.Yamada, Y.Kimura and K.Saijo
Influence of the Organization of Water-in-Ionic Liquid Microemulsions on the Size of Silver Particles during Photoreduction
J. Colloid Interface Sci., **406** (2013) 94.
- K.Nagata, N.Hongo, Y.Kameda, A.Yamamura, H.Sasaki, W.C.Lee, K.Ishikawa, E.Suzuki and M.Tanokura
The Structure of Brazzein, a Sweet-Tasting Protein from the Wild African Plant *Pentadiplandra brazzeana*.
Acta Cryst. D, **69** (2013) 642.
- K.Matsui, S.Seno, Y.Nozone, Y.Shinohara, Y.Amemiya, E.B.Berda, G.Rojas and K.B.Wagener
Influence of Branch Incorporation into the Lamella Crystal on the Crystallization Behavior of Polyethylene with Precisely Spaced Branches
Macromolecules, **46** (2013) 4438.
- K.Fukuhara, Y.Fujii, Y.Nagashima, M.Hara, S.Nagano, and T.Seki
Liquid-Crystalline Polymer and Block Copolymer Domain Alignment Controlled by Free-Surface Segregation
Angew. Chem. Int. Ed., **52** (2013) 5988.
- G.Cui, S.Ohya, T.Matsutani, S.Nagano, T.Dohi, S.Nakamura, S.Sakurai, T.Miyazaki and K.Yamamoto
Perpendicular Orientation of Sub-10 nm Channels in Polystyrene-*b*-Poly(4-Hydroxyl Styrene)/PEG Oligomer Blend Thin Films
Nanoscale, **5** (2013) 6713.
- F.Kaneko, N.Seto, K.Sasaki, S.Sakurai and T.Kimura
Simultaneous SAXS and WAXS Study on the Guest Exchange Process of Syndiotactic Polystyrene: Crystalline Complex Formation with Triethylene Glycol Dimethyl Ether
Macromol. Chem. Phys., **214** (2013) 1893.
- Y.Matsumura, M.Shinjo, T.Matsui, K.Ichimura, J.Song and H.Kihara
Structural Study of hNck2 SH3 Domain Protein in Solution by Circular Dichroism and X-Ray Solution Scattering
Biophys. Chem., **175** (2013) 39.
- Y.Matsumura, M.Shinjo, S.J.Kim, N.Okishio, M.Gruebele and H.Kihara
Transient Helical Structure during PI3K and Fyn SH3 Domain Folding
J. Phys. Chem. B, **117** (2013) 4836.
- M.Morimoto, T.Morita, T.Takanohashi and K.Nishikawa
Specific Asphaltene Aggregation in Toluene at Around 50 mg/L
J. Jpn. Petrol. Inst., **56** (2013) 58.
- T.Morita, K.Kurihara, O.Yoshida, H.Imamura, Y.Hatakeyama, K.Nishikawa and N.Uehara
Fusion Growth of Gold Nanoparticles Induced by the Conformational Change of a Thermoresponsive Polymer Studied by Distance Distribution Functions
J. Phys. Chem. C, **117** (2013) 13602.
- A.Nakamura, T.Ishida, S.Fushinobu, K.Kusaka, I.Tanaka, K.Inaka, Y.Higuchi, M.Masaki, K.Ohta, S.Kaneko, N.Niimura, K.Igarashi and M.Samajima
Phase-Diagram-Guided Method for Growth of a Large Crystal of Glycoside Hydrolase Family 45 Inverting Cellulase Suitable for Neutron Structural Analysis
J. Synchrotron Rad., **20** (2013) 859.

- S.Fushinobu, V.D.Alves and P.M.Coutinho
Multiple Rewards from a Treasure Trove of Novel Glycoside Hydrolase and Polysaccharide Lyase Structures: New Folds, Mechanistic Details, and Evolutionary Relationships
Curr. Opin. Struct. Biol., **23** (2013) 652.
- Y.Takenaka, Y.Kawabata, H.Kitahata, M.Yoshida, Y.Matsuzawa and T.Ohzo
Effects of Surfactant Concentration on Formation of High-Aspect-Ratio Gold Nanorods
J. Colloid Interface Sci., **407** (2013) 265.
- Z.Fujimoto
Structure and Function of Carbohydrate-Binding Module Families 13 and 42 of Glycoside Hydrolases, Comprising a β -Trefoil Fold
Biosci. Biotechnol. Biochem., **77** (2013) 1363.
- N.Suzuki, Y-M.Kim, M.Momma, Z.Fujimoto, M.Kobayashi, A.Kimura and K.Funane
Crystallization and Preliminary X-Ray Crystallographic Analysis of Cycloisomaltooligosaccharide Glucanotransferase from *Bacillus circulans* T-3040
Acta Cryst. F, **69** (2013) 946.
- T.Hiromoto, E.Honjo, T.Tamada, N.Noda, K.Kazuma, M.Suzuki and R.Kuroki
Crystal Structure of UDP-Glucose:Anthocyanidin 3-*O*-Glucosyltransferase from *Clitoria ternatea*
J. Synchrotron Rad., **20** (2013) 894.
- A.A.Timchenko, O.V.Novosylina, E.A.Prituzhalov, H.Kihara, A.V.El'skaya, B.S.Negrutskii and I.N.Serdyuk
Different Oligomeric Properties and Stability of Highly Homologous A1 and Proto-Oncogenic A2 Variants of Mammalian Translation Elongation Factor eEF1
Biochemistry, **52** (2013) 5345.
- H.Takeno and T.Mochizuki
A Structural Development of an Organogel Explored by Synchrotron Time-Resolved Small-Angle X-Ray Scattering
Colloid Polym. Sci., **291** (2013) 2783.
- T.Ogawa, K.Noguchi, M.Saito, Y.Nagahata, H.Kato, A.Ohtaki, H.Nakayama, N.Dohmae, Y.Matsushita, M.Odaka, M.Yohda, H.Nyunoya and Y.Katayama
Carbonyl Sulfide Hydrolase from *Thiobacillus thioparus* Strain THI115 Is One of the β -Carbonic Anhydrase Family Enzymes
J. Am. Chem. Soc., **135** (2013) 3818.
- D.Iino, Y.Takakura, K.Fukano, Y.Sasaki, T.Hoshino, K.Ohsawa, A.Nakamura and S.Yajima
Crystal Structures of the Ternary Complex of APH(4)-Ia/Hph with Hygromycin B and an ATP Analog using a Thermostable Mutant
J. Struct. Biol., **183** (2013) 76.
- T.Shinkai, M.Ito, K.Sugiyama, K.Ito and H.Yokoyama
Retrograde Order-Disorder Transition of a Semi-Fluorinated Block Copolymer Induced by Supercritical Carbon Dioxide
Soft Matter, **9** (2013) 10689.
- N.Yoshimoto, T.Itoh, Y.Inaba, H.Ishii and K.Yamamoto
Structural Basis for Inhibition of Carboxypeptidase B by Selenium-Containing Inhibitor: Selenium Coordinates to Zinc in Enzyme
J. Med. Chem., **56** (2013) 7527.
- T.Nakano, D.Kawaguchi and Y.Matsushita
Anisotropic Self-Assembly of Gold Nanoparticle Grafted with Polyisoprene and Polystyrene Having Symmetric Polymer Composition
J. Am. Chem. Soc., **135** (2013) 6798.

6C

S.Hosokawa, N.Happo, T.Ozaki, H.Ikemoto, T.Shishido and K.Hayashi
Extent and Feature of Lattice Distortions around Ga Impurity Atoms in InSb Single Crystal
Phys. Rev. B, **87** (2013) 094104.

M.Okube and S.Sasaki
Accurate Determination of Anomalous Scattering Factor near Fe *K* Absorption Edge
J. Phys.: Conf. Ser., **425** (2013) 202002.

M.Okube, A.Kinoshita, J.Yoshizaki, T.Toyoda and S.Sasaki
Spin Orientation in (Ti-Mn) Ba Ferrite Estimated from Resonant X-Ray Magnetic Scattering
J. Phys.: Conf. Ser., **425** (2013) 102005.

K.Hayashi
Atomic Resolution Holography
Butsuri, **68** (2013) 217. (*in Japanese*).

K.Fukuda, J.Sato, T.Saida, W.Sugimoto, Y.Ebina, T.Shibata, M.Osada and T.Sasaki
Fabrication of Ruthenium Metal Nanosheets via Topotactic Metallization of Exfoliated Ruthenate Nanosheets
Inorg. Chem., **52** (2013) 2280.

K.Hayashi, N.Happo and S.Hosokawa
Evaluation of Local Lattice Distortion by X-Ray Fluorescence Holography
J. Jpn. Soc. Synchrotron Rad. Res., **26** (2013) 195. (*in Japanese*).

T.Ozawa, K.Fukuda, Y.Ebina and T.Sasaki
Soft-Chemical Exfoliation of RbSrNb₂O₆F into Homogeneously Unilamellar Oxyfluoride Nanosheets
Inorganic Chemistry, **52** (2013) 415.

M.Kimura and R.Murao
Continuous Cooling Transformation(CCT) Concept for Iron Ore Sintering using *In Situ* Quick X-Ray Diffraction and Confocal Laser Microscope
ISIJ International, **53** (2013) 2047.

7A

S.M.Suturin, V.V.Fedorov, A.G.Banshchikov, D.A.Baranov, K.V.Koshmak, P.Torelli, J.Fujii, G.Panaccione, K.Amemiya, M.Sakamaki, T.Nakamura, M.Tabuchi, L.Pasquali and N.S.Sokolov
Proximity Effects and Exchange Bias in Co/MnF₂(111) Heterostructures Studied by X-Ray Magnetic Circular Dichroism
J. Phys.: Condens. Matter, **25** (2013) 046002.

M.Sakamaki and K.Amemiya
Effect of Structural Strain on Magnetic Anisotropy Energy of Each Element in Alternately Layered FeNi Thin Films
Phys. Rev. B, **87** (2013) 014428.

H.Niwa, M.Saito, M.Kobayashi, Y.Harada, M.Oshima, S.Moriya, K.Matsubayashi, Y.Nabae, S.Kuroki, T.Ikeda, K.Terakura, J.Ozaki and S.Miyata
Probing Carbon Edge Exposure of Iron Phthalocyanine-Based Oxygen Reduction Catalysts by Soft X-Ray Absorption Spectroscopy
J. Power Sources, **223** (2013) 30.

J.Okabayashi, S.Kono, Y.Yamada and K.Nomura
Mössbauer and X-Ray Absorption Studies in Fe and V Co-Doped SnO₂
Hyperfine Interact., **217** (2013) 99.

O.Endo, M. Nakamura and K.Amemiya
Depth-Dependent C K-NEXAFS Spectra for Self-Assembled Monolayers of 4-Methylbenzenethiol and 4-Ethylbenzenethiol on Au(1 1 1)
J. Elec. Spec. Relat. Phenom., **187** (2013) 72.

K.Amemiya and M.Sakamaki
Temperature Dependence of Remanent Magnetization of Thin Films at the Interface to a Nonmagnetic Material: Cu/Ni/Cu(100)
Phys. Rev. B, **88** (2013) 014401.

O.Endo, M.Nakamura and K.Amemiya
Separation of C K-NEXAFS Spectra for Layer-by-Layer Analysis of Carbon-Based Thin Films: An *n*-Alkane Monolayer Adsorbed on a Monolayer Graphene Substrate Grown on a Pt(111) Surface
J. Elec. Spec. Relat. Phenom., **189** (2013) 27.

J.Okabayashi, H.Sukegawa, Z.Wen, K.Inomata and S.Mitani
Large Anisotropic Fe Orbital Moments in Perpendicularly Magnetized Co₂FeAl Heusler Alloy Thin Films Revealed by Angular-Dependent X-Ray Magnetic Circular Dichroism
Appl. Phys. Lett., **103** (2013) 102402.

H.-M.Lee, S.-B.Kang K.-B.Chung and H.-K.Kim
Transparent and Flexible Amorphous In-Si-O Films for Flexible Organic Solar Cells
Appl. Phys. Lett., **102** (2013) 021914.

K.-C.Ok, Y.Park, K.-B.Chung and J.-S.Park
The Effect of Ta Doping in Polycrystalline TiO_x and the Associated Thin Film Transistor Properties
Appl. Phys. Lett., **103** (2013) 213501.

O.Endo, M.Nakamura and K.Amemiya
Phase Transition of *n*-C₃₆H₇₄ Monolayer on Pt(111) Covered with Monolayer Graphene Studied by C K-NEXAFS
J. Phys. Chem. C, **117** (2013) 21856.

Y.Matsumoto, S.Entani, A.Koide, M.Ohtomo, P.V.Avramov, H.Naramoto, K.Amemiya, T.Fujikawa and S.Sakai
Spin Orientation Transition Across the Single-Layer Graphene/Nickel Thin Film Interface
J. Mater. Chem. C, **1** (2013) 5533.

7C

F.Liu, K.Asakura, P.Xie, J.Wang and H.He
An XAFS Study on the Specific Microstructure of Active Species in Iron Titanate Catalyst for NH₃-SCR of NO_x
Catal. Today, **201** (2013) 131.

Y.Izumi
Recent Advances in Photocatalytic Conversion of Carbon Dioxide into Fuels with Water and/or Hydrogen using Solar Energy and Beyond
Coordination Chem. Rev., **257** (2013) 171.

T.Kamegawa, D.Yamahana, H.Seto and H.Yamashita
Preparation of Single-Site Ti-Containing Mesoporous Silica with a Nanotube Architecture and its Enhanced Catalytic Activities
J. Mater. Chem. A, **1** (2013) 891.

T.Kamegawa, R.Kido, D.Yamahana and H.Yamashita
Design of TiO₂-Zeolite Composites with Enhanced Photocatalytic Performances under Irradiation of UV and Visible Light
Micropor. Mesopor. Mater., **165** (2013) 142.

D.Asakura, C.H.Li, Y.Mizuno, M.Okubo, H.S.Zhou and D.R.Talham
Bimetallic Cyanide-Bridged Coordination Polymers as Lithium Ion Cathode Materials: Core@Shell Nanoparticles with Enhanced Cyclability
J. Am. Chem. Soc., **135** (2013) 2793.

J.Kim, Y.Kim, S.Han, S.Choi and J.Lee
Photocatalytic Synthesis of Oxygenated Hydrocarbons from Diesel Fuel for Mobile DeNO_x Application
J. Catal., **302** (2013) 58.

- F.Rashidi, T.Sasaki, A.M.Rashidi, A.N.Kharat and K.J.Jozani
Ultradeep Hydrodesulfurization of Diesel Fuels using Highly Efficient Nanoalumina-Supported Catalysts: Impact of Support, Phosphorus, and/or Boron on the Structure and Catalytic Activity
J. Catal., **299** (2013) 321.
- O.Haruyama, K.Kisara, A.Yamashita, K.Kogure, Y.Yokoyama and K.Sugiyama
Characterization of Free Volume in Cold-Rolled $Zr_{75}Cu_{30}Ni_{15}Al_{10}$ Bulk Metallic Glasses
Acta Materialia, **61** (2013) 3224.
- S.Nozaawa, T.Iwazumi, H.Osawa and T.Uozumi
Photoinduced Local Symmetry Breaking in $SrTiO_3$
Applied Physics Express, **6** (2013) 061501.
- O.Haruyama, H.Sawada, K.Yoshikawa, T.Kawamata, Y.Yokoyama and K.Sugiyama
Static Measurements for α - and β -Relaxation below T_g in a $Zr_{75}Cu_{30}Ni_{15}Al_{10}$ BMG
TMS2013 Annual Meeting Supplemental Proceedings, (2013) 273.
- S.Mandal, K.K.Bando, C.Santra, S.Maity, O.O.James, D.Mehta and B.Chowdhury
Sm-CeO₂ Supported Gold Nanoparticle Catalyst for Benzyl Alcohol Oxidation using Molecular O₂
Appl. Catal. A: General, **452** (2013) 94.
- H.Einaga, Y.Teraoka and A.Ogata
Catalytic Oxidation of Benzene by Ozone over Manganese Oxides Supported on USY Zeolite
J. Catal., **305** (2013) 227.
- M.Takachi, T.Matsuda and Y.Moritomo
Structural, Electronic, and Electrochemical Properties of $Li_xCo[Fe(CN)_6]_{0.90}2.9H_2O$
Jpn. J. Appl. Phys., **52** (2013) 044301.
- M.Nakai, T.Funabiki, C.Ohtsuki, M.Harada, A.Ichimura, R.Tanaka, T.Nishioka, I.Kinoshita, M.Mikuriya, J.Guo, H.Benten, H.Ohkita, S.Ito, M.Obata, Y.Nakabayashi and S.Yano
Syntheses, Structures, and Photochemical Properties of $(\mu_3-O)tris[bis(\mu-carboxylato)]trimanganese$ Complexes with Naphthylacetate Ligands with Relevance to Artificial Solar Energy-Harvesting Systems
Inorg. Chim. Acta, **406** (2013) 130.
- Y.Moritomo, M.Takachi, Y.Kurihara and T.Matsuda
Synchrotron-Radiation X-Ray Investigation of Li^+/Na^+ Intercalation into Prussian Blue Analogues
Adv. Mater. Sci. Eng., **2013** (2013) 967285.
- M.Takachi, T.Matsuda and Y.Moritomo
Redox Reactions in Prussian Blue Analogue Films with Fast Na^+ Intercalation
Jpn. J. Appl. Phys., **52** (2013) 090202.
- S.Mandal, C.Santra, K.K.Bando, O.O.James, S.Maity, D.Mehta and B.Chowdhury
Aerobic Oxidation of Benzyl Alcohol over Mesoporous Mn-Doped Ceria Supported Au Nanoparticle Catalyst
Journal of Molecular Catalysis A:Chemical, **378** (2013) 47.
- S.Suzuki, S.Mukai, Y.Koike, K.Kinoshita, K.Fujikawa, W.-J.Chun, M.Nomura and K.Asakura
Improvement of XANAM with a qPlus Sensor for Enhancing Chemical Sensitivity on Surface Analysis
Proc. ALC2013, (2013)
- Z.Quan, E.Ni, S.Hayashi and N.Sonoyama
Structure and Electrochemical Properties of Multiple Metal Oxide Nanoparticles as Cathodes of Lithium Batteries
J. Mater. Chem. A, **1** (2013) 8848.
- H.Yoshitake and R.Otsuka
Grafting of Precoordinated $Cu^{2+}-N-(2-Aminoethyl)$ Aminopropylsilane Complexes onto Mesoporous Silicas and the Adsorption of Aqueous Selenate on them
Langmuir, **29** (2013) 10513.
- Y.Kurihara, T.Matsuda and Y.Moritomo
Structural Properties of Manganese Hexacyanoferrates against Li Concentration
Jpn. J. Appl. Phys., **52** (2013) 017301.
- T.Shimono, D.Tanabe, W.Kobayashi, H.Nitani and Y.Moritomo
Electronic State of P2-Type Na_xMO_2 ($M = Mn$ and Co) as Investigated by In Situ X-Ray Absorption Spectroscopy
J. Phys. Soc. Jpn., **82** (2013) 124717.
- F.Liu, H.He, Z.Lian, W.Shan, L.Xie, K.Asakura, W.Yang and H.Deng
Highly Dispersed Iron Vanadate Catalyst Supported on TiO_2 for the Selective Catalytic Reduction of NO_x with NH_3
J. Catal., **307** (2013) 340.
- F.Liu, H.He and L.Xie
XAFS Study on the Specific Deoxidation Behavior of Iron Titanate Catalyst for the Selective Catalytic Reduction of NO_x with NH_3
ChemCatChem, **5** (2013) 3760.
- T.Toyao, M.Saito, Y.Horiuchi, K.Mochizuki, M.Iwata, H.Higashimura and M.Matsuoka
Efficient Hydrogen Production and Photocatalytic Reduction of Nitrobenzene over a Visible-Light-Responsive Metal-Organic Framework Photocatalyst
Catal. Sci. Technol., **3** (2013) 2092.
- Y.Okuhara, H.Matsubara, C.Numako and M.Takata
Effective Doping of Al in ZnO Films by Multi-Target Reactive Sputtering for Near-Infrared Reflection
Journal of the Australian Ceramic Society, **49** (2013) 15.

L.Chen, T.Mashimo, C.Iwamoto, H.Okudera, E.Omurzak, H.S.Ganapathy, H.Ihara, J.Zhang, Z.Abdullaeva, S.Takebe and A.Yoshiasa
Synthesis of Novel $\text{CoC}_x\text{@C}$ Nanoparticles
Nanotechnology, **24** (2013) 045602.

T.Shimono, W.Kobayashi, H.Nitani, R.Kumai and Y.Moritomo
Electrochemical Lithium Intercalation into $\text{Bi}_2\text{Sr}_2\text{CaCu}_2\text{O}_{8+\delta}$
J. Phys.: Conf. Ser., **428** (2013) 012021.

K.Nakagawa, T.Ogata, K.Yamaguchi, J.Jitoku, K.-I.Sotowa, S.Sugiyama, T.Moriga and M.Adachi
Layered Titanate Nanosheets Prepared by a Surfactant-Templating Approach: Effects of Lamellar Mesostucture on Surface Functionality
Science and Advanced Material, **6** (2013) 1535.

J.Kim, K.H.Cho, I.Kagomiya and K.Park
Structural Studies of Porous Ni/YSZ Cermets Fabricated by the Solid-State Reaction Method
Ceramics International, **39** (2013) 7467.

I.Kagomiya, S.Matsumoto, K.Kakimoto, H.Ohsato, H.Sakai and Y.Maeda
Annealing Effect on Temperature Coefficient of Resistivity in $\text{La}_{1-x}\text{Sr}_x\text{MnO}_3$ Ceramics
J. Euro. Ceram. Soc., **33** (2013) 985.

N.Yabuuchi, Y.Kawamoto, R.Hara, T.Ishigaki, A.Hoshikawa, M.Yonemura, T.Kamiyama and S.Komaba
A Comparative Study of LiCoO_2 Polymorphs: Structural and Electrochemical Characterization of O2-, O3-, and O4-Type Phases
Inorg. Chem., **52** (2013) 9131.

T.Hariu, H.Arima and K.Sugiyama
The Structure of Hydrated Copper-Silicate Gels, an Analogue Compound for Natural Chrysocolia
J. Min. Petrol. Sci., **108** (2013) 111.

I.Kagomiya, K.Jimbo and K.Kakimoto
Distribution Change of Oxygen Vacancies in Layered Perovskite Type $(\text{Sr},\text{La})_{n+1}\text{Fe}_n\text{O}_{3n+1}$ ($n=3$)
J. Sol. Stat. Chem., **207** (2013) 184.

8A

T.Matsuda, M.Takachi and Y.Moritomo
A Sodium Manganese Ferrocyanide Thin Film for Na-Ion Batteries
Chem. Comm., **49** (2013) 2750.

M.Takachi, T.Matsuda and Y.Moritomo
Cobalt Hexacyanoferrate as Cathode Material for Na^+ Secondary Battery
Appl. Phys. Express, **6** (2013) 025802.

T.Kobayashi, S.Miyasaka, S.Tajima, T.Nakano, Y.Nozone, N.Chikumoto, H.Nakao, R.Kumai and Y.Murakami
Change of Electronic State and Crystal Structure by Postannealing in Superconducting $\text{SrFe}_2(\text{As}_{0.65}\text{P}_{0.35})_2$
Phys. Rev. B, **87** (2013) 174520.

M.Takachi, T.Matsuda and Y.Moritomo
Structural, Electronic, and Electrochemical Properties of $\text{Li}_x\text{Co}[\text{Fe}(\text{CN})_6]_{0.90}2.9\text{H}_2\text{O}$
Jpn. J. Appl. Phys., **52** (2013) 044301.

K.Saito, T.Miyazawa, A.Fujiwara, M.Hishida, H.Saitoh, M.Massalska-Arodz and Y.Yamamura
Reassessment of Structure of Smectic Phases: Nano-Segregation in Smectic E Phase in 4-*n*-Alkyl-4'-isothiocyanato-1,1'-biphenyls
J. Chem. Phys., **139** (2013) 114902.

Y.Moritomo, M.Takachi, Y.Kurihara and T.Matsuda
Synchrotron-Radiation X-Ray Investigation of Li^+/Na^+ Intercalation into Prussian Blue Analogues
Adv. Mater. Sci. Eng., **2013** (2013) 967285.

M.Takachi, T.Matsuda and Y.Moritomo
Redox Reactions in Prussian Blue Analogue Films with Fast Na^+ Intercalation
Jpn. J. Appl. Phys., **52** (2013) 090202.

T.Adachi, H.Saitoh, Y.Yamamura, M.Hishida, M.Ueda, S.Ito and K.Saito
Universality of Molten State of Alkyl Chain in Liquid-Crystalline Mesophases: Smectic E Phase of 6-Alkyl-2-Phenylazulene
Bull. Chem. Soc. Jpn., **86** (2013) 1022.

Y.Kurihara, T.Matsuda and Y.Moritomo
Structural Properties of Manganese Hexacyanoferrates against Li Concentration
Jpn. J. Appl. Phys., **52** (2013) 017301.

S.Horiuchi, R.Kumai and Y.Tokura
High-Temperature and Pressure-Induced Ferroelectricity in Hydrogen-Bonded Supramolecular Crystals of Anilic Acids and 2,3-Di(2-Pyridinyl) Pyrazine
J. Am. Chem. Soc., **135** (2013) 4492.

S.Asai, R.Okazaki, I.Terasaki, Y.Yasui, W.Kobayashi, A.Nakao, K.Kobayashi, R.Kumai, H.Nakao, Y.Murakami, N.Igawa, A.Hoshikawa, T.Ishigaki, O.Parkkima, M.Karppinen and H.Yamauchi
Spin State of Co^{3+} in $\text{LaCo}_{1-x}\text{Rh}_x\text{O}_3$ Investigated by Structural Phenomena
J. Phys. Soc. Jpn., **82** (2013) 114606.

Y.Suzuki, S.Shibasaki, Y.Kubozono and T.Kambe
Antiferromagnetic Resonance in the Mott Insulator $\text{fcc-}\text{Cs}_3\text{C}_{60}$
J. Phys.: Condens. Matter, **25** (2013) 366001.

T.Mastuda, Y.Kurihara and Y.Moritomo
Lithium Intercalation Properties in Manganese-Iron Prussian Blue Analogues
J. Phys.: Conf. Ser., **428** (2013) 012019.

T.Shimono, W.Kobayashi, H.Nitani, R.Kumai and Y.Moritomo
Electrochemical Lithium Intercalation into $\text{Bi}_2\text{Sr}_2\text{CaCu}_2\text{O}_{8+\delta}$
J. Phys.: Conf. Ser., **428** (2013) 012021.

T.Isono, H.Kamo, A.Ueda, K.Takahashi, A.Nakao, R.Kumai, H.Nakano, K.Kobayashi, Y.Murakami and H.Mori
Hydrogen Bond-Promoted Metallic State in a Purely Organic Single-Component Conductor under Pressure
Nature Commun., **4** (2013) 1344.

8B

M.Mito, Y.Komorida, H.Deguchi, T.Tajiri, T.Iwamoto and Y.Kitamoto
Artificial Material Manipulation of Magnetic Anisotropy in FePt Magnetic Nanoparticles through Application of Hydrostatic Pressure
J. Appl. Phys., **113** (2013) 044302.

K.Matsuda, K.Yanagi, H.Kyakuno, S.Sagitani, H.Kataura and Y.Maniwa
 ^{13}C -NMR Shift of Highly Concentrated Metallic and Semiconducting Single-Walled Carbon Nanotubes
J. Phys. Soc. Jpn., **82** (2013) 015001.

T.Honda, Y.Hiraoka, Y.Wakabayashi and T.Kimura
Refinement of Crystal Structure of a Magnetoelectric U-Type Hexaferrite $\text{Sr}_4\text{Co}_2\text{Fe}_{36}\text{O}_{60}$
J. Phys. Soc. Jpn., **82** (2013) 025003.

T.Hayashi, H.Shibata, S.Orita and T.Akitsu
Variety of Structures of Binuclear Chiral Schiff Base Ce(III)/Pr(III)/Lu(III)-Ni(II)/Cu(II)/Zn(II) Complexes
Eur. Chem. Bull., **2** (2013) 49.

H.Maeda, Y.Ishiguro, T.Honda, J-S.Jung, S.Michimura, T.Inami, T.Kimura and Y.Wakabayashi
Structural Investigation of Magnetocapacitive SmMnO_3
J. Ceram. Soc. Jpn., **121** (2013) 265.

E.Hosono, T.Saito, J.Hoshino, Y.Mizuno, M.Okubo, D.Asakura, K.Kagesawa, D.Nishio-Hamane, T.Kudo and HS.Zhou
Synthesis of $\text{LiNi}_{0.5}\text{Mn}_{1.5}\text{O}_4$ and $0.5\text{Li}_2\text{MnO}_3\text{-}0.5\text{LiNi}_{1/3}\text{Co}_{1/3}\text{Mn}_{1/3}\text{O}_2$ Hollow Nanowires by Electrospinning
CrystEngComm, **15** (2013) 2592.

N.Hayashi and T.Akitsu
Anisotropic Thermally-Accessible Lattice Distortion of a Cu(II)-Cr(VI) Complex Bimetallic Oxide by Adsorbing a Chiral One-Dimensional Cu(II)-Cr(VI) Coordination Polymer
J. Chem. Chem. Eng., **7** (2013) 306.

Y.Lee, D.Seoung, Y.-N.Jang, T.Vogt and Y.Lee
Pressure-Induced Hydration and Insertion of CO_2 into Ag-Natrolite
Chem. Eur. J., **19** (2013) 5806.

N.J.O.Silva, S.Saisho, M.Mito, A.Millan, F.Palacio, A.Cabot, O.Iglesias and A.Labarta
Pressure Effects in Hollow and Solid Iron Oxide Nanoparticles
J. Magn. Magn. Mater., **335** (2013) 1.

T.Tajiri, N.Terashita, K.Hamamoto, H.Deguchi, M.Mito, Y.Morimoto, K.Konishi and A.Kohno
Size Dependences of Crystal Structure and Magnetic Properties of DyMnO_3 Nanoparticles
J. Magn. Magn. Mater., **345** (2013) 288.

K.Saito, T.Miyazawa, A.Fujiwara, M.Hishida, H.Saitoh, M.Massalska-Arodz and Y.Yamamura
Reassessment of Structure of Smectic Phases: Nano-Segregation in Smectic E Phase in 4-*n*-Alkyl-4'-isothiocyanato-1,1'-biphenyls
J. Chem. Phys., **139** (2013) 114902.

T.Adachi, H.Saitoh, Y.Yamamura, M.Hishida, M.Ueda, S.Ito and K.Saito
Universality of Molten State of Alkyl Chain in Liquid-Crystalline Mesophases: Smectic E Phase of 6-Alkyl-2-Phenylazulene
Bull. Chem. Soc. Jpn., **86** (2013) 1022.

S.Kawaguchi, H.Ishibashi, S.Nishihara, M.Miyagawa, K.Inoue, S.Mori and Y.Kubota
Anomalous Magnetization Behaviour in a Single Crystal of Vanadium Spinel FeV_2O_4
J. Phys.: Condens. Matter, **25** (2013) 416005.

Y.Lee, D.Seoung, Y.-N.Jang, T.Vogt and Y.Lee
Pressure-Induced Hydration and Insertion of CO_2 into Ag-Natrolite
Chem. Eur. J., **19** (2013) 5806.

F.Kagawa, T.Sato, K.Miyagawa, K.Kanoda, Y.Tokura, K.Kobayashi, R.Kumai and Y.Murakami
Charge-Cluster Glass in an Organic Conductor
Nature Physics, **9** (2013) 419.

S.Asai, R.Okazaki, I.Terasaki, Y.Yasui, W.Kobayashi, A.Nakao, K.Kobayashi, R.Kumai, H.Nakao, Y.Murakami, N.Igawa, A.Hoshikawa, T.Ishigaki, O.Parkkima, M.Karppinen and H.Yamauchi
Spin State of Co^{3+} in $\text{LaCo}_{1-x}\text{Rh}_x\text{O}_3$ Investigated by Structural Phenomena
J. Phys. Soc. Jpn., **82** (2013) 114606.

Y.Suzuki, S.Shibasaki, Y.Kubozono and T.Kambe
Antiferromagnetic Resonance in the Mott Insulator fcc- Cs_3C_{60}
J. Phys.: Condens. Matter, **25** (2013) 366001.

H.Kyakuno, K.Matsuda, Y.Nakai, T.Fukuoka, Y.Maniwa, H.Nishihara and T.Kyotani
Amorphous Water in Three-Dimensional Confinement of Zeolite-Templated Carbon
Chem. Phys. Lett., **571** (2013) 54.

T.Tajiri, K.Hamamoto, Y.Ando, H.Deguchi, M.Mito and A.Kohno
Synthesis and Magnetic Properties of DyMnO₃ Nanoparticles in Mesoporous Silica
J. Korean Physical Society, **63** (2013) 826.

D.Seoung, Y.Lee, C.-C.Kao, T.Vogt and Y.Lee
Super-Hydrated Zeolites: Pressure-Induced Hydration in Natrolites
Chem. Eur. J., **19** (2013) 10876.

9A

R.Simura, T.Yagi, K.Sugiyama, T.Yanagida and A.Yoshikawa
Growth of Ce-Doped Ba₃Gd(BO₃)₃ and Sr₃Gd(BO₃)₃ Single Crystals by Micro-Pulling-Down Method and Analysis of Luminescence Properties
J. Cryst. Growth, **362** (2013) 145.

R.Simura, S.Kawai, K.Sugiyama, T.Yanagida, T.Sugawara, T.Shishido and A.Yoshikawa
Valence State of Dopant and Scintillation Properties of Ce-Doped Sr₃Y(BO₃)₃ Crystal
J. Cryst. Growth, **362** (2013) 296.

M.Tada
Hard X-Ray Time-Resolved/Space-Resolved X-Ray Absorption Fine Structure Analysis for Heterogeneous Metal Catalysts
J. Phys. Soc. Jpn., **82** (2013) 021013.

Y.Izumi
Recent Advances in Photocatalytic Conversion of Carbon Dioxide into Fuels with Water and/or Hydrogen using Solar Energy and Beyond
Coordination Chem. Rev., **257** (2013) 171.

T.Kashiwabara, Y.Takahashi, M.A.Marcus, T.Uruga, H.Tanida, Y.Terada and A.Usui
Tungsten Species in Natural Ferromanganese Oxides Related to its Different Behavior from Molybdenum in Oxidic Ocean
Geochim. Cosmochim. Acta, **106** (2013) 364.

W.-J.Chun, K.Miyazaki, N.Watanabe, Y.Koike, S.Takakusagi, K.Fujikawa, M.Nomura, Y.Iwasawa and K.Asakura
Au Clusters on TiO₂(110) (1 × 1) and (1 × 2) Surfaces Examined by Polarization-Dependent Total Reflection Fluorescence XAFS
J. Phys. Chem. C, **117** (2013) 252.

T.Fujimori, Y.Tanino and M.Takaoka
Thermochemical Behavior of Lead Adjusting Formation of Chlorinated Aromatics in MSW Fly Ash
Environ. Sci. Technol., **47** (2013) 2169.

S.Yamashita, M.Katayama and Y.Inada
Reduction Kinetics of Nickel Species Supported on Silica
J. Phys., Conf. Ser., **430** (2013) 012051.

K.Tanaka, A.Sakaguchi, Y.Kanai, H.Tsuruta, A.Shinohara and Y.Takahashi
Heterogeneous Distribution of Radiocesium in Aerosols, Soil and Particulate Matters Emitted by the Fukushima Daiichi Nuclear Power Plant Accident: Retention of Micro-Scale Heterogeneity during the Migration of Radiocesium from the Air into Ground and River Systems
J. Radioanal. Nucl. Chem., **295** (2013) 1927.

N.Yabuuchi, K.Yamamoto, K.Yoshii, I.Nakai, T.Nishizawa, A.Omaru, T.Toyooka and S.Komaba
Structural and Electrochemical Characterizations on Li₂MnO₃-LiCoO₂-LiCrO₂ System as Positive Electrode Materials for Rechargeable Lithium Batteries
J. Electrochem. Soc., **160** (2013) A39.

I.Nakai, A.Hattori, T.Ishii and Y.J.Li
XAS Spectra of Mechanically Milled TiO₂
J. Phys.: Conf. Ser., **430** (2013) 012084.

Z.W.Zhang, G.D.Zheng, K.Shozugawa, M.Matsuo and Y.D.Zhao
Iron and Sulfur Speciation in Some Sedimentary-Transformation-Type of Lead-Zinc Deposits in West Kunlun Lead-Zinc Ore Deposit Zone, Northwest China
J. Radioanal. Nucl. Chem., **297** (2013) 83.

T.Tobase, L.Wang, A.Yoshiasa, M.Okube, T.Nakatani, Y.Hayasaka and H.Isobe
XAFS Study on Ca Local Structure in Natural Glasses and Tektite
J. Phys.: Conf. Ser., **430** (2013) 012070.

L.Wang, A.Yoshiasa, M.Okube, T.Nakatani, Y.Hayasaka and H.Isobe
Local Structure of Titanium in Natural Glasses Probed by X-Ray Absorption Fine Structure
J. Phys.: Conf. Ser., **430** (2013) 012121.

H.Uehara, M.H.B.Hanaffi, Y.Koike, K.Fujikawa, S.Suzuki, H.Ariga, S.Takakusagi, W.J.Chun, Y.Iwasawa and K.Asakura,
Anisotropic Growth of a Nickel Trimer Formed on a Highly-Stepped TiO₂(110) Surface
Chem. Phys. Lett., **570** (2013) 64.

I.Nakai, M.Sasano, K.Inui, T.Korekawa, H.Ishijima, H.Katoh, Y.J.Li and M.Kurisu
Oxygen Vacancy and Magnetism of a Room Temperature Ferromagnet Co-Doped TiO₂
J. Korean Phys. Soc., **63** (2013) 532.

S.Takakusagi, H.Nojima, H.Ariga, H.Uehara, K.Miyazaki, W.-J.Chun, Y.Iwasawa and K.Asakura
Fine Tuning and Orientation Control of Surface Cu Complexes on TiO₂(110) Premodified with Mercapto Compounds: the Effect of Different Mercapto Group Positions
Phys. Chem. Chem. Phys., **15** (2013) 14080.

K.Asakura, S.Takakusagi, H.Ariga, W.-J.Chun, S.Suzuki, Y.Koike, H.Uehara, K.Miyazaki and Y.Iwasawa
Preparation and Structure of a Single Au Atom on the TiO₂(110) Surface: Control of the Au-Metal Oxide Surface Interaction
Faraday Discussions, **162** (2013) 165.

S.Takakusagi, W.-J.Chun, H.Uehara, K.Asakura and Y.Iwasawa
Polarization-Dependent Total-Reflection Fluorescence X-Ray Absorption Fine Structure for 3D Structural Determination and Surface Fine Tuning
Topics in Catal., **56** (2013) 1477.

R.Nakada, Y.Takahashi and M.Tanimizu
Isotopic and Speciation Study on Cerium during its Solid-Water Distribution with Implication for Ce Stable Isotope as a Paleo-Redox Proxy
Geochim. Cosmochim. Acta, **103** (2013) 49.

Y.Takahashi, T.Furukawa, Y.Kanai, M.Uematsu, G.Zheng and M.A.Marcus
Seasonal Changes in Fe Species and Soluble Fe Concentration in the Atmosphere in the Northwest Pacific Region Based on the Analysis of Aerosols Collected in Tsukuba, Japan
Atmos. Chem. Phys., **13** (2013) 7695.

N.Murata, T.Suzuki, M.Kobayashi, F.Togoh and K.Asakura
Characterization of Pt-Doped SnO₂ Catalyst for a High-Performance Micro Gas Sensor
Phys. Chem. Chem. Phys., **15** (2013) 17938.

Y.Idemoto, H.Endo and N.Kitamura
Substitution Effect on Cathode Property, Crystal and Electronic Structures of LiMn_{0.5}Ni_{0.5}O₂ as Cathode Active Material for Li-Ion Battery
Electrochemistry, **81** (2013) 971. (*in Japanese*).

K.Nitta, Y.Omori, T.Miyanaga, K.Takegahara, H.Sugawara, D.Kikuchi and H.Sato
Extended X-Ray Absorption Fine Structure Thermal Factor Analysis of Rattling in Filled Skutterudites RT₄Sb₁₂ (R: La, Ce, Pr, Nd, and Sm; T: Fe, Ru, and Os)
J. Phys. Soc. Jpn., **82** (2013) 044801.

Y.Okuhara, H.Matsubara, C.Numako and M.Takata
Effective Doping of Al in ZnO Films by Multi-Target Reactive Sputtering for Near-Infrared Reflection
Journal of the Australian Ceramic Society, **49** (2013) 15.

T.Hiratoko, A.Yoshiasa, T.Nakatani, M.Okube, A.Nakatsuka and K.Sugiyama
Temperature Dependence of Pre-Edge Features in Ti K-Edge XANES Spectra for ATiO₃(A = Ca and Sr), A₂TiO₄(A = Mg and Fe), TiO₂ Rutile and TiO₂ Anatase
J. Synchrotron Rad., **20** (2013) 641.

H.Hanashima, N.Kitajima, T.Abe and A.Hokura
Study on Accumulation Mechanism of Arsenic and Selenium in *Pteris vittata* L. Using Synchrotron Radiation X-Ray Fluorescence Analysis
Adv. X-Ray Chem. Anal. Jpn., **44** (2013) 279. (*in Japanese*).

9C

M.Tada
Hard X-Ray Time-Resolved/Space-Resolved X-Ray Absorption Fine Structure Analysis for Heterogeneous Metal Catalysts
J. Phys. Soc. Jpn., **82** (2013) 021013.

Y.Izumi
Recent Advances in Photocatalytic Conversion of Carbon Dioxide into Fuels with Water and/or Hydrogen using Solar Energy and Beyond
Coordination Chem. Rev., **257** (2013) 171.

M.Nishi, T.Ohkubo, K.Tsurusaki, A.Itadani, B.Ahmmad, K.Urita, I.Moriguchi, S.Kittaka and Y.Kuroda
Highly Compressed Nanosolution Restricted in Cylindrical Carbon Nanospaces
Nanoscale, **5** (2013) 2080.

M.Okubo, K.Kagesawa, Y.Mizuno, D.Asakura, E.Hosono, T.Kudo, H.S.Zhou, K.Fujii, H.Uekusa, S.Nishimura, A.Yamada, A.Okazawa and N.Kojima
Reversible Solid State Redox of an Octacyanometallate-Bridged Coordination Polymer by Electrochemical Ion Insertion/Extraction
Inorg. Chem., **52** (2013) 3772.

N.Yabuuchi, K.Yamamoto, K.Yoshii, I.Nakai, T.Nishizawa, A.Omaru, T.Toyooka and S.Komaba
Structural and Electrochemical Characterizations on Li₂MnO₃-LiCoO₂-LiCrO₂ System as Positive Electrode Materials for Rechargeable Lithium Batteries
J. Electrochem. Soc., **160** (2013) A39.

J.Kugai, T.Moriya, S.Seino, T.Nakagawa, Y.Ohkubo, H.Nitani and T.A.Yamamoto
Effect of CeO₂ Support Properties on Structure of Pt-Cu Nanoparticles Synthesized by Electron Beam Irradiation Method for Preferential CO Oxidation
Chem. Eng. J., **223** (2013) 347.

- F.Rashidi, T.Sasaki, A.M.Rashidi, A.N.Kharat and K.J.Jozani
Ultradeep Hydrodesulfurization of Diesel Fuels using Highly Efficient Nanoalumina-Supported Catalysts: Impact of Support, Phosphorus, and/or Boron on the Structure and Catalytic Activity
J. Catal., **299** (2013) 321.
- Z.W.Zhang, G.D.Zheng, K.Shozugawa, M.Matsuo and Y.D.Zhao
Iron and Sulfur Speciation in Some Sedimentary-Transformation-Type of Lead-Zinc Deposits in West Kunlun Lead-Zinc Ore Deposit Zone, Northwest China
J. Radioanal. Nucl. Chem., **297** (2013) 83.
- A.Koganemaru, A.Yoshiasa, L.Wang, T.Nakatani, A.Nakatsuka, M.Okube, H.Arima and K.Sugiyama
Effective Pair Potential for Ca-O Bonds in CaGeO₃ Polymorphs
J. Phys.: Conf. Ser., **430** (2013) 012068.
- T.Tobase, L.Wang, A.Yoshiasa, M.Okube, T.Nakatani, Y.Hayasaka and H.Isobe
XAFS Study on Ca Local Structure in Natural Glasses and Tektite
J. Phys.: Conf. Ser., **430** (2013) 012070.
- L.Wang, A.Yoshiasa, M.Okube, T.Nakatani, Y.Hayasaka and H.Isobe
Local Structure of Titanium in Natural Glasses Probed by X-Ray Absorption Fine Structure
J. Phys.: Conf. Ser., **430** (2013) 012121.
- B.Ahmmad, M.Nishi, F.Hirose, T.Ohkubo and Y.Kuroda
Structure of Hydrated Cobalt Ions Confined in the Nanospace of Single-Walled Carbon Nanotubes
Phys. Chem. Chem. Phys., **15** (2013) 8264.
- L.B.Garcia, T.Calveta, M.A.Cuevas-Diarteia, S.Ueno and K.Sato
In situ Observation of Transformation Pathways of Polymorphic Forms of 1,3-Dipalmitoyl-2-Oleoyl Glycerol (POP) Examined with Synchrotron Radiation X-Ray Diffraction and DSC
Cryst. Eng. Comm., **15** (2013) 302.
- T.Yokoyama and K.Eguchi
Anisotropic Thermal Expansion and Cooperative Invar/Anti-Invar Effects in Mn Alloys
Phys. Rev. Lett., **110** (2013) 075901.
- F.Hayashi and M.Iwamoto
Yttrium-Modified Ceria as a Highly Durable Catalyst for the Selective Conversion of Ethanol to Propene and Ethene
ACS Catal., **3** (2013) 14.
- S.Mandal, K.K.Bando, C.Santra, S.Maity, O.O.James, D.Mehta and B.Chowdhury
Sm-CeO₂ Supported Gold Nanoparticle Catalyst for Benzyl Alcohol Oxidation using Molecular O₂
Appl. Catal. A: General, **452** (2013) 94.
- T.Yamada, K.Morita, H.Wang, K.Kume, H.Yoshikawa and K.Awaga
In Situ Seamless Magnetic Measurements for Solid-State Electrochemical Processes in Prussian Blue Analogues
Angew. Chem. Int. Ed., **52** (2013) 6238.
- S.Wada, K.Oka, K.Watanabe and Y.Izumi
Catalytic Conversion of Carbon Dioxide into Dimethyl Carbonate using Reduced Copper-Cerium Oxide Catalysts as Low as 353K and 1.3MPa and the Reaction Mechanism
Frontiers in Chemistry, **1** (2013) 8.
- G.Cui, S.Ohya, T.Matsutani, S.Nagano, T.Dohi, S.Nakamura, S.Sakurai, T.Miyazaki and K.Yamamoto
Perpendicular Orientation of Sub-10 nm Channels in Polystyrene-*b*-Poly(4-Hydroxyl Styrene)/PEG Oligomer Blend Thin Films
Nanoscale, **5** (2013) 6713.
- S.Fujieda, K.Shinoda, S.Suzuki and B.Jeyadevan
Disorder-Order Transformation and Local Structure Changes of FePt Nanoparticles Synthesized by Polyol Process
IEEE Transactions on Magnetics, **49** (2013) 3303.
- M.Yoshida, K.Maeda, D.Lu, J.Kubota and K.Domen
Lanthanoid Oxide Layers on Rhodium-Loaded (Ga_{1-x}Zn_x)(N_{1-x}O_x) Photocatalyst as a Modifier for Overall Water Splitting under Visible-Light Irradiation
J. Phys. Chem. C, **117** (2013) 14000.
- Y.Tasaki-Handa, K.Ooi, M.Tanaka and A.Wakisaka
Tunable Selectivity of Lanthanide Ion Exchange within a Coordination Polymer
Anal. Sci., **29** (2013) 685.
- F.Kaneko, N.Seto, K.Sasaki, S.Sakurai and T.Kimura
Simultaneous SAXS and WAXS Study on the Guest Exchange Process of Syndiotactic Polystyrene: Crystalline Complex Formation with Triethylene Glycol Dimethyl Ether
Macromol. Chem. Phys., **214** (2013) 1893.
- I.Nakai, M.Sasano, K.Inui, T.Korekawa, H.Ishijima, H.Katoh, Y.J.Li and M.Kurisu
Oxygen Vacancy and Magnetism of a Room Temperature Ferromagnet Co-Doped TiO₂
J. Korean Phys. Soc., **63** (2013) 532.
- S.Mandal, C.Santra, K.K.Bando, O.O.James, S.Maity, D.Mehta and B.Chowdhury
Aerobic Oxidation of Benzyl Alcohol over Mesoporous Mn-Doped Ceria Supported Au Nanoparticle Catalyst
Journal of Molecular Catalysis A:Chemical, **378** (2013) 47.
- S.Zhang, S.Muratsugu, N.Ishiguro and M.Tada
Ceria-Doped Ni/SBA-16 Catalysts for Dry Reforming of Methane
ACS Catal., **3** (2013) 1855.

- S.Muratsugu, Z.Weng and M.Tada
Surface Functionalization of Supported Mn Clusters to Produce Robust Mn Catalysts for Selective Epoxidation
ACS Catal., **3** (2013) 2020.
- L.Wang, S.Yamamoto, S.Malwadkar, S.Nagamatsu, T.Sasaki, K.Hayashizaki, M.Tada and Y.Iwasawa
Direct Synthesis of Phenol from Benzene and O₂, Regulated by NH₃ on Pt/ β and Pt-Re/ZSM-5 Catalysts
ChemCatChem, **5** (2013) 2203.
- T.Ohkubo
Hydration and Coordination Structure of d-Block Metals Formed by the Confinement Effect of Carbon Micropores
Tanso, **260** (2013) 297. (*in Japanese*).
- K.Nitta, Y.Omori, T.Miyanaga, K.Takegahara, H.Sugawara, D.Kikuchi and H.Sato
Extended X-Ray Absorption Fine Structure Thermal Factor Analysis of Rattling in Filled Skutterudites RT₄Sb₁₂ (R: La, Ce, Pr, Nd, and Sm; T: Fe, Ru, and Os)
J. Phys. Soc. Jpn., **82** (2013) 044801.
- L.Bayés-García, T.Calvet, M.À.Cuevas-Diarte, S.Ueno and K.Sato
In Situ Observation of Transformation Pathways of Polymorphic Forms of 1,3-Dipalmitoyl-2-Oleoyl Glycerol(POP) Examined with Synchrotron Radiation X-Ray Diffraction and DSC
CrystEngComm, **15** (2013) 302.
- L.Bayés-García, T.Calvet, M.À.Cuevas-Diarte, S.Ueno and K.Sato
Crystallization and Transformation of Polymorphic Forms of Trioyleyl Glycerol and 1,2-Dioleoyl-3-*rac*-linoleoyl Glycerol
J. Phys. Chem. B, **117** (2013) 9170.
- L.Chen, T.Mashimo, C.Iwamoto, H.Okudera, E.Omurzak, H.S.Ganapathy, H.Ihara, J.Zhang, Z.Abdullaeva, S.Takebe and A.Yoshiasa
Synthesis of Novel CoC_x@C Nanoparticles
Nanotechnology, **24** (2013) 045602.
- T.Hiratoko, A.Yoshiasa, T.Nakatani, M.Okube, A.Nakatsuka and K.Sugiyama
Temperature Dependence of Pre-Edge Features in Ti K-Edge XANES Spectra for ATiO₃ (A = Ca and Sr), A₂TiO₄ (A = Mg and Fe), TiO₂ Rutile and TiO₂ Anatase
J. Synchrotron Rad., **20** (2013) 641.
- L.Wang, A.Yoshiasa, M.Okube, T.Hiratoko, Y.Hu, H.Arima and K.Sugiyama
Local Structure of Iron in Tektites and Natural Glass: An Insight through X-Ray Absorption Fine Structure Spectroscopy
Journal of Mineralogical and Petrological Sciences, **108** (2013) 288.
- T.Ye, P.Barpanda, S.Nishimura, N.Furuta, S.-C.Chung and A.Yamada
General Observation of Fe³⁺/Fe²⁺ Redox Couple Close to 4 V in Partially Substituted Li₂FeP₂O₇ Pyrophosphate Solid-Solution Cathodes
Chem. Mater., **25** (2013) 3623.
- A.Itadani, Y.Sogawa, A.Oda, H.Torigoe, T.Ohkubo and Y.Kuroda
Further Evidence for the Existence of a Dual-Cu⁺ Site in MFI Working as the Efficient Site for C₂H₆ Adsorption at Room Temperature
Langmuir, **29** (2013) 9727.
- M.Sato and A.Nakahira
Influence of Fe Addition to Hydroxyapatite by Aqueous Solution Process
J. Ceramic Society of Japan, **121** (2013) 422.
- M.Sato and A.Nakahira
Influence of Fe Addition to Hydroxyapatite by Hydrothermal Process
J. Ceramic Society of Japan, **121** (2013) 559.

10A

- A.Koganemaru, A.Yoshiasa, L.Wang, T.Nakatani, A.Nakatsuka, M.Okube, H.Arima and K.Sugiyama
Effective Pair Potential for Ca-O Bonds in CaGeO₃ Polymorphs
J. Phys.: Conf. Ser., **430** (2013) 012068.
- L.Wang, A.Yoshiasa, M.Okube, T.Nakatani, Y.Hayasaka and H.Isobe
Local Structure of Titanium in Natural Glasses Probed by X-Ray Absorption Fine Structure
J. Phys.: Conf. Ser., **430** (2013) 012121.
- M.Okube and S.Sasaki
Accurate Determination of Anomalous Scattering Factor near Fe K Absorption Edge
J. Phys.: Conf. Ser., **425** (2013) 202002.
- M.Okube, A.Kinoshita, J.Yoshizaki, T.Toyoda and S.Sasaki
Spin Orientation in (Ti-Mn) Ba Ferrite Estimated from Resonant X-Ray Magnetic Scattering
J. Phys.: Conf. Ser., **425** (2013) 102005.
- I.Kusachi, S.Kobayashi, Y.Takechi, Y.Nakamuta, T.Nagase, K.Yokoyama, K.Momma, R.Miyawaki, M.Shigeoka and S.Matsubara
Shimazakiite-4M and Shimazakiite-4O, Ca₂B₂O₅, Two Polytypes of a New Mineral from Fuka, Okayama Prefecture, Japan
Mineralogical Magazine, **77** (2013) 93.
- S.Takenaka, T.Tsukamoto, H.Matsune and M.Kishida
Carbon Nanotube-Supported Pd-Co Catalysts Covered with Silica Layers as Active and Stable Cathode Catalysts for Polymer Electrolyte Fuel Cells
Catal. Sci. Technol., **3** (2013) 2723.

L.Chen, T.Mashimo, C.Iwamoto, H.Okudera, E.Omurzak, H.S.Ganapathy, H.Ihara, J.Zhang, Z.Abdullaeva, S.Takebe and A.Yoshiasa
Synthesis of Novel $\text{CoC}_x\text{@C}$ Nanoparticles
Nanotechnology, **24** (2013) 045602.

A.Yoshiasa

Precise Structure Analyses of the Earth and Planetary Materials by Both Diffraction and XAFS Methods
Japanese Magazine of Mineralogical and Petrological Sciences, **42** (2013) 111. (*in Japanese*).

A.Yoshiasa, A.Nakatsuka, M.Okube and T.Katsura
Single-Crystal Metastable High Temperature $C2/c$ Clinoenstatite Quenched Rapidly from High Temperature and High Pressure
Acta Cryst. B, **69** (2013) 541.

T.Nagase, K.Momma, T.Kuribayashi and M.Tanaka
Texture of Lutecite
J. Mineralogical and Petrological Sci., **108** (2013) 87.

A.Nakatsuka, M.Shimokawa, N.Nakayama, O.Ohtaka, H.Arima, M.Okube and A.Yoshiasa
Static Disorders of Atoms and Experimental Determination of Debye Temperature in Pyrope: Low- and High-Temperature Single-Crystal X-Ray Diffraction Study—Reply
American Mineralogist, **98** (2013) 783.

K.Fujiwara, T.Tamaki, C.Kishimori, R.Titorenkova, A.Nakatsuka and N.Nakayama
Crystal Structures of Cobalt-Exchanged Sodium GTS-Type Titanosilicates and the Elution Test by Acid Solution
Trans. Mat. Res. Soc. Japan, **38** (2013) 455.

N.Nakayama, K.Takahashi, K.Fujiwara, A.Nakatsuka, M.Isobe and Y.Ueda
Structural Phase Transitions of $\text{Li}_2\text{MgSiO}_4$ and $\text{Li}_2\text{MgGeO}_4$
Trans. Mat. Res. Soc. Japan, **38** (2013) 419.

10B

T.Miyanaga, Y.Suzuki, N.Matsumoto, S.Narita, T.Ainai and H.Hoshino,
Formation of Ag Clusters in Zeolite X Studied by in situ EXAFS and Infrared Spectroscopy
Microporous and Mesoporous Material, **168** (2013) 213.

B.O.Leung, F.Jalilehvand, V.Mah, M.Parvez and Q.Wu
Silver(I) Complex Formation with Cysteine, Penicillamine, and Glutathione
Inorg. Chem., **52** (2013) 4593.

A.Gallo, R.Psaro, M.Guidotti, V.D.Santo, R.D.Pergola, D.Masih and Y.Izumi
Cluster-Derived Ir-Sn/SiO₂ Catalysts for the Catalytic Dehydrogenation of Propane: a Spectroscopic Study
Dalton Transactions, **42** (2013) 12714.

10C

T.Sato, K.Tanaka, A.Toyokura, R.Mori, R.Takahashi, K.Terao and S.Yusa
Self-Association of a Thermosensitive Amphiphilic Block Copolymer Poly(*N*-isopropylacrylamide)-*b*-poly(*N*-vinyl-2-pyrrolidone) in Aqueous Solution upon Heating
Macromolecules, **46** (2013) 226.

Y.Sakai, R.Gomi, K.Kato, H.Yokoyama and K.Ito
Structure and Dynamics of Polyrotaxane-Based Sliding Graft Copolymers with Alkyl Side Chains
Soft Matter, **9** (2013) 1895.

S.Nakagawa, T.Tanaka, T.Ishizone, S.Nojima, Y.Kakiuchi, K.Yamaguchi and S.Nakahama
Crystallization behavior of Poly(ϵ -Caprolactone) Chains Confined in Nanocylinders: Effects of Block Chains Tethered to Nanocylinder Interface
Macromolecules, **46** (2013) 2199.

T.Sakurai, H.Nagakura, S.Gondo and S.Nojima
Crystallization of Poly(ϵ -Caprolactone) Blocks Confined in Crystallized Lamellar Morphology of Poly(ϵ -Caprolactone)-Block-Polyethylene Copolymers: Effects of Polyethylene Crystallinity and Confinement Size
Polymer J., **45** (2013) 436.

S.Goda, H.Sadakata, H.Unno and T.Hatakeyama
Effects of Detergents on the Oligomeric Structures of Hemolytic Lectin CEL-III as Determined by Small-Angle X-Ray Scattering
Biosci. Biotechnol. Biochem., **77** (2013) 679.

H.Takeno and W.Nakamura
Structural and Mechanical Properties of Composite Hydrogels Composed of Clay and a Polyelectrolyte Prepared by Mixing
Colloid and Polymer Science, **291** (2013) 1393.

K.Okoshi
Conform to Its Shape
Kobunshi, **62** (2013) 9. (*in Japanese*).

K.Oyamada, K.Terao, M.Suwa, S.Kitamura and T.Sato
Lyotropic Liquid Crystallinity of Amylose Tris(alkylcarbamates): Cholesteric and Smectic Phase Formation in Different Solvents
Macromolecules, **46** (2013) 4589.

K.Terao, K.Shigeuchi, K.Oyamada, S.Kitamura and T.Sato
Solution Properties of a Cyclic Chain Having Tunable Chain Stiffness: Cyclic Amylose Tris(*n*-butylcarbamate) in Θ and Good Solvents
Macromolecules, **46** (2013) 5355.

N.Asano, S.Kitamura and K.Terao
Local Conformation and Intermolecular Interaction of Rigid Ring Polymers Are Not Always the Same as the Linear Analogue: Cyclic Amylose Tris(phenylcarbamate) in Θ Solvents
J. Phys. Chem. B, **117** (2013) 9576.

S.Nakano, N.Tomita and G.Matsuba
Precise Analysis for Amorphous Poly(Acrylo Nitrile)
Gels
Sen'i Gakkaishi, **69** (2013) 210. (*in Japanese*).

T.T.T.Thanh, V.T.T.Tran, Y.Yuguchi, L.M.Bui and
T.T.Nguyen
Structure of Fucoidan from Brown Seaweed *Turbinaria
ornata* as Studied by Electrospray Ionization Mass
Spectrometry (ESIMS) and Small Angle X-Ray
Scattering (SAXS) Techniques
Marine Drugs, **11** (2013) 2431.

S.Gondo, S.Osawa, T.Sakurai and S.Nojima
Crystallization of Double Crystalline Block
Copolymer/Crystalline Homopolymer Blends: 1.
Crystalline Morphology
Polymer, **54** (2013) 6768.

K.Sato, M.Koga, S.Kang, K.Sakajiri, J.Watanabe and
M.Tokita
Lamellar Morphology of an ABA Triblock Copolymer
with a Main-Chain Nematic Polyester Central Block
Macromol. Chem. Phys., **214** (2013) 1089.

K.Kizawa, Y.Jinbo, T.Inoue, H.Takahara, M.Unno,
C.W.Heizmann and Y.Izumi
Human S100A3 Tetramerization Propagates $\text{Ca}^{2+}/\text{Zn}^{2+}$
Binding States
Biochimica et Biophysica Acta, **1833** (2013) 1712.

J.Uewaki, H.Kamikubo, J.Kurita, N.Hiroguchi,
H.Moriuchi, M.Yoshida, M.Kataoka, N.Utsunomiya-Tate
and S.Tate
Preferential Domain Orientation of HMGB2 Determined
by the Weak Intramolecular Interactions Mediated by the
Interdomain Linker
Chemical Physics, **419** (2013) 212.

A.Nakamura, T.Nemoto, I.U.Heinemann, K.Yamashita,
T.Sonoda, K.Komoda, I.Tanaka, D.Söll and M.Yao
Structural Basis of Reverse Nucleotide Polymerization
Proc. Natl. Acad. Sci. USA, **110** (2013) 20970.

T.Nakano, D.Kawaguchi and Y.Matsushita
Anisotropic Self-Assembly of Gold Nanoparticle Grafted
with Polyisoprene and Polystyrene Having Symmetric
Polymer Composition
J. Am. Chem. Soc., **135** (2013) 6798.

M.Hamaguchi, H.Kamikubo, K.N.Suzuki, Y.Hagihara,
I.Yanagihara, I.Sakata, M.Kataoka and D.Hamada
Structural Basis of α -Catenin Recognition by EspB from
Enterohaemorrhagic *E.coli* Based on Hybrid Strategy
using Low-Resolution Structural and Protein Dissection
PLoS One, **8** (2013) e71618.

N.Inoue, D.Hamada, H.Kamikubo, K.Hirata,
M.Kataoka, M.Yamamoto, M.Ikawa, M.Okabe and
Y.Hagihara
Molecular Dissection of IZUMO1, a Sperm Protein
Essential for Sperm-Egg Fusion
Development, **140** (2013) 3221.

Y.Watanabe and Y.Inoko
Characterization of a Large Glycoprotein Proteoglycan
by Size-Exclusion Chromatography Combined with Light
and X-Ray Scattering Methods
J. Chromatography A, **1303** (2013) 100.

M.Hirai, R.Kimura, K.Takeuchi, Y.Hagiwara, R.Kawai-
Hirai, N.Ohta, N.Igarashi and N.Shimizu
Structure of Liposome Encapsulating Proteins
Characterized by X-Ray Scattering and Shell-Modeling
J. Synchrotron Rad., **20** (2013) 869.

M.Hirai, R.Kimura, K.Takeuchi, M.Sugiyama,
K.Kasahara, N.Ohta, B.Farago, A.Stadler and G.Zaccai
Change of Dynamics of Raft-Model Membrane Induced
by Amyloid- β Protein Binding
Eur. Phys. J. E, **36** (2013) 74.

R.Zhu, T.Hoshi, Y.Muroga, T.Hagiwara, S.Yano and
T.Sawaguchi
Microstructure and Mechanical Properties of a
Polyethylene/Polydimethylsiloxane Composite Prepared
using Supercritical Carbon Dioxide
J. Appl. Polym. Sci., **127** (2013) 3388.

T.Hashimoto, M.Harada, S.Nojima and T.Okada
Number Density of Liquid Inclusions Formed in Frozen
Aqueous Electrolyte
ChemPhysChem, **14** (2013) 3410.

Y.Koide, H.Ikake, Y.Muroga and S.Shimizu
Effect of the Cast-Solvent on the Morphology of
Cast Films Formed with a Mixture of Stereoisomeric
Poly(Lactic Acids)
Polymer J., **45** (2013) 645.

H.Aizawa and S.Ichikawa
Effect of Increasing Concentration of Each of Three
Polar Solvents(1,4-Dioxane, Dimethyl Sulfoxide, *N,N*-
Dimethylformamide) on Changes in the Shape of
Polysorbate 20 Micelles
J. Solution Chem., **42** (2013) 882.

11A

T.Kinoshita, K.Arai, K.Fukumoto, T.Ohkochi,
M.Kotsugi, F.Guo, T.Muro, T.Nakamura, H.Osawa,
T.Matsushita and T.Okuda
Observation of Micro-Magnetic Structures by
Synchrotron Radiation Photoelectron Emission
Microscopy
J. Phys. Soc. Jpn., **82** (2013) 021005.

Y.Kitajima, Y.Nanba, M.Tanaka, Y.Koga, A.Ueno,
K.Nakagawa, H.Tokoro, S.Ohkoshi, T.Iwazumi, K.Okada
and Y.Isozumi
Observation of π Backbonding Features in Fe 2p X-Ray
Absorption Spectra and Fe 1s-4p-1s Resonant X-Ray
Emission Spectra of $\text{RbMn}[\text{Fe}(\text{CN})_6]$
J. Phys.: Conf. Ser., **430** (2013) 012082.

Md.A.Mannan, Y.Baba, N.Hirao, T.Kida, M.Nagano and H.Noguchi

Hexagonal Nano-Crystalline BCN Films Grown on Si (100) Substrate Studied by X-Ray Absorption Spectroscopy
Mater. Sci. Appl., **4** (2013) 11.

S.Ueda, K.Hayashida, H.Nakajima, N.Anabuki, H.Tsunemi, H.Kan, T.Kohmura, S.Ikeda, K.Kaneko, T.Watanabe, K.Mori, M.Nobukawa, H.Murakami, K.Sakata, S.Todoroki, N.Yagihashi, E.Mizuno, M.Muramatsu, H.Suzuki and S.Takagi

Measurement of the Soft X-Ray Response of P-Channel Back-Illuminated CCD

Nucl. Instrum. Meth. Phys. Res. A, **704** (2013) 140.

Y.Okuhara, H.Matsubara, C.Numako and M.Takata
Effective Doping of Al in ZnO Films by Multi-Target Reactive Sputtering for Near-Infrared Reflection
Journal of the Australian Ceramic Society, **49** (2013) 15.

H.Nakajima, M.Fujikawa, H.Mori, H.Kan, S.Ueda, H.Kosugi, N.Anabuki, K.Hayashida and H.Tsunemi

Single Event Effect Characterization of the Mixed-Signal ASIC Developed for CCD Camera in Space Use

Nucl. Instrum. Meth. Phys. Res. A, **731** (2013) 166.

S.Ueda, K.Hayashida, H.Nakajima and H.Tsunemi
X-Ray Measurement of the Elemental Abundances at the Outskirts of the Perseus Cluster with Suzaku
Astronomische Nachrichten, **334** (2013) 426.

K.Mori, Y.Nishioka, S.Ohura, Y.Koura, M.Yamauchi, H.Nakajima, S.Ueda, H.Kan, N.Anabuki, R.Nagino, K.Hayashida, H.Tsunemi, T.Kohmura, S.Ikeda, H.Murakami, M.Ozaki, T.Dotani, Y.Maeda and K.Sagara

Proton Radiation Damage Experiment on P-Channel CCD for an X-Ray CCD Camera Onboard the ASTRO-H Satellite

Nucl. Instrum. Meth. Phys. Res. A, **731** (2013) 160.

11B

V.Petrykin, K.Macounova, M.Okube, S.Mukerjee and P.Krttil

Local Structure of Co Doped RuO₂ Nanocrystalline Electrocatalytic Materials for Chlorine and Oxygen Evolution

Catal. Today, **202** (2013) 63.

T.Fujimori, Y.Tanino and M.Takaoka
Thermochemical Behavior of Lead Adjusting Formation of Chlorinated Aromatics in MSW Fly Ash

Environ. Sci. Technol., **47** (2013) 2169.

J.Okamoto, K.Horigane, H.Nakao, K.Amemiya, M.Kubota, Y.Murakami and K.Yamada

Resonant Soft X-Ray Scattering Study of the Magnetic Structures in La_{1.5}Ca_{0.5}CoO₄ using a High Vacuum Diffractometer with a 4-Blade-Slit Detector System

J. Phys.: Conf. Ser., **425** (2013) 202003.

T.Imazono, M.Koike, N.Hasegawa, M.Koeda, T.Nagano, H.Sasai, Y.Oue, Z.Yonezawa, S.Kuramoto, M.Terauchi, H.Takahashi, N.Handa and T.Murano

Development of a Flat-Field Spectrograph with a Wide-Band Multilayer Grating and Prefocusing Mirror Covering 2-4 keV

J. Phys.: Conf. Ser., **425** (2013) 152008.

Y.Hashimoto and N.Yamaguchi
Chemical Speciation of Cadmium and Sulfur K-Edge XANES Spectroscopy in Flooded Paddy Soils Amended with Zerovalent Iron

Soil Sci. Soc. Am. J., **77** (2013) 1189.

L.Wang, J.Li, J.Pan, X.Jiang, Y.Ji, Y.Li, Y.Qu, Y.Zhao, X.Wu and C.Chen

Revealing the Binding Structure of the Protein Corona on Gold Nanorods Using Synchrotron Radiation-Based Techniques: Understanding the Reduced Damage in Cell Membranes

J. Am. Chem. Soc., **135** (2013) 17359.

T.Imazono, M.Koike, T.Kawachi, N.Hasegawa, M.Koeda, T.Nagano, H.Sasai, Y.Oue, Z.Yonezawa, S.Kuramoto, M.Terauchi, H.Takahashi, N.Handa and T.Murano

Development of an Objective Flat-Field Spectrograph for Electron Microscopic Soft X-Ray Emission Spectrometry in 50–4000 eV

Proc. of SPIE, **8848** (2013) 884812.

11D

T.Hatano and S.Aihara
Monochromator Operation in the Carbon Window Region at the Reflectometry Beamline BL-11D of the Photon Factory

J. Phys.: Conf. Ser., **425** (2013) 152018.

T.Tsuru, K.Arai and T.Hatano
Homogenized Ion Milling over the Whole Area of EUV Spherical Multilayer Mirrors for Reflection Phase Error Correction

J. Phys.: Conf. Ser., **425** (2013) 152009.

T.Hatano, S.Aihara, K.Uchida and T.Tsuru
Performance of the Post-Focusing Mirror System at the Reflectometry Beamline BL-11D of the Photon Factory

J. Phys: Conf. Ser., **463** (2013) 012010.

12C

R.Simura, T.Yagi, K.Sugiyama, T.Yanagida and A.Yoshikawa

Growth of Ce-Doped Ba₃Gd(BO₃)₃ and Sr₃Gd(BO₃)₃ Single Crystals by Micro-Pulling-Down Method and Analysis of Luminescence Properties

J. Cryst. Growth, **362** (2013) 145.

R.Simura, S.Kawai, K.Sugiyama, T.Yanagida, T.Sugawara, T.Shishido and A.Yoshikawa

Valence State of Dopant and Scintillation Properties of Ce-Doped Sr₃Y(BO₃)₃ Crystal

J. Cryst. Growth, **362** (2013) 296.

- M.Tada
Hard X-Ray Time-Resolved/Space-Resolved X-Ray Absorption Fine Structure Analysis for Heterogeneous Metal Catalysts
J. Phys. Soc. Jpn., **82** (2013) 021013.
- Y.Izumi
Recent Advances in Photocatalytic Conversion of Carbon Dioxide into Fuels with Water and/or Hydrogen using Solar Energy and Beyond
Coordination Chem. Rev., **257** (2013) 171.
- T.Kashiwabara, Y.Takahashi, M.A.Marcus, T.Uruga, H.Tanida, Y.Terada and A.Usui
Tungsten Species in Natural Ferromanganese Oxides Related to its Different Behavior from Molybdenum in Oxidic Ocean
Geochim. Cosmochim. Acta, **106** (2013) 364.
- S.Yamashita, M.Katayama and Y.Inada
Reduction Kinetics of Nickel Species Supported on Silica
J. Phys., Conf. Ser., **430** (2013) 012051.
- K.Tanaka, A.Sakaguchi, Y.Kanai, H.Tsuruta, A.Shinohara and Y.Takahashi
Heterogeneous Distribution of Radiocesium in Aerosols, Soil and Particulate Matters Emitted by the Fukushima Daiichi Nuclear Power Plant Accident: Retention of Micro-Scale Heterogeneity during the Migration of Radiocesium from the Air into Ground and River Systems
J. Radioanal. Nucl. Chem., **295** (2013) 1927.
- N.Yabuuchi, K.Yamamoto, K.Yoshii, I.Nakai, T.Nishizawa, A.Omaru, T.Toyooka and S.Komaba
Structural and Electrochemical Characterizations on $\text{Li}_2\text{MnO}_3\text{-LiCoO}_2\text{-LiCrO}_2$ System as Positive Electrode Materials for Rechargeable Lithium Batteries
J. Electrochem. Soc., **160** (2013) A39.
- Y.Suzuki, M.Kuchida, Y.Sakama, H.Saiki, I.Karube and N.Tsubaki
Promotion Effect of the Addition of Eu to Co/Silica Catalyst for Fischer-Tropsch Synthesis
Catal. Commun., **36** (2013) 75.
- K.Shiota, G.Imai, K.Oshita and M.Takaoka
Characterization of Lead, Chromium, and Cadmium in Dust Emitted from Municipal Solid Waste Incineration Plants
J. Phys.: Conf. Ser., **430** (2013) 012095.
- Z.W.Zhang, G.D.Zheng, K.Shozugawa, M.Matsuo and Y.D.Zhao
Iron and Sulfur Speciation in Some Sedimentary-Transformation-Type of Lead-Zinc Deposits in West Kunlun Lead-Zinc Ore Deposit Zone, Northwest China
J. Radioanal. Nucl. Chem., **297** (2013) 83.
- M.Tanaka, Y.Takahashi and N.Yamaguchi
A Study on Adsorption Mechanism of Organoarsenic Compounds on Ferrihydrite by XAFS
J. Phys.: Conf. Ser., **430** (2013) 012100.
- S.Nakajima, H.Segawa, S.Yanagida, A.Yasumori and N.Hirosaki
Fabrication of $\text{TiO}_2\text{-SiO}_2$ Glasses Containing Ca- α - SiAlON:Eu^{2+} Phosphor using the Sol-Gel Process
J. Ceramic Soc. Jpn., **121** (2013) 361.
- N.Yabuuchi, M.Yano, H.Yoshida, S.Kuze and S.Komaba
Synthesis and Electrode Performance of O3-Type $\text{NaFeO}_2\text{-NaNi}_{1/2}\text{Mn}_{1/2}\text{O}_2$ Solid Solution for Rechargeable Sodium Batteries
J. Electrochem. Soc., **160** (2013) A3131.
- N.Panitlertumpai, W.Nakbanpote, A.Sangdee, K.Thumanu, I.Nakai and A.Hokura
Zinc and/or Cadmium Accumulation in *Gynura pseudochina* (L.) DC. Studied *in vitro* and the Effect on Crude Protein
J. Molecular Structure, **1036** (2013) 279.
- S.Mandal, K.K.Bando, C.Santra, S.Maity, O.O.James, D.Mehta and B.Chowdhury
Sm-CeO₂ Supported Gold Nanoparticle Catalyst for Benzyl Alcohol Oxidation using Molecular O₂
Appl. Catal. A: General, **452** (2013) 94.
- T.Ohtsuka, N.Yamaguchi, T.Makino, K.Sakurai, K.Kimura, K.Kudo, E.Homma, D.Dong and S.Amachi
Arsenic Dissolution from Japanese Paddy Soil by a Dissimilatory Arsenate-Reducing Bacterium *Geobacter* sp. OR-1
Environ. Sci. Technol., **47** (2013) 6263.
- M.Yoshida, K.Maeda, D.Lu, J.Kubota and K.Domen
Lanthanoid Oxide Layers on Rhodium-Loaded ($\text{Ga}_{1-x}\text{Zn}_x$)(N_{1-x}O_x) Photocatalyst as a Modifier for Overall Water Splitting under Visible-Light Irradiation
J. Phys. Chem. C, **117** (2013) 14000.
- Q.Yu, K.Sasaki, K.Tanaka, T.Ohnuki and T.Hirajima
Zinc Sorption during Bio-Oxidation and Precipitation of Manganese Modifies the Layer Stacking of Biogenic Birnessite
Geomicrobiol. J., **30** (2013) 829.
- Y.Huang, H.Ariga, X.Zheng, X.Duan, S.Takakusagi, K.Asakura and Y.Yuan
Silver-Modulated SiO_2 -Supported Copper Catalysts for Selective Hydrogenation of Dimethyl Oxalate to Ethylene Glycol
J. Catal., **307** (2013) 74.
- M.Yoshida, T.Yomogida, T.Mineo, K.Nitta, K.Kato, T.Masuda, H.Nitani, H.Abe, S.Takakusagi, T.Uruga, K.Asakura, K.Uosaki and H.Kondoh
In situ Observation of Carrier Transfer in the Mn-Oxide/Nb:SrTiO₃ Photoelectrode by X-Ray Absorption Spectroscopy
Chem. Comm., **49** (2013) 7848.

- T.Imaoka, H.Kitazawa, W.J.Chun, S.Omura, K.Albrecht and K.Yamamoto
Magic Number Pt₁₃ and Misshapen Pt₁₂ Clusters: Which One is the Better Catalyst?
J. Am. Chem. Soc., **135** (2013) 13089.
- H.Ikemoto, T.Watanabe and T.Miyanaga
EXAFS Study of the Local Structure of Bismuth Film Deposited at Liquid Nitrogen Temperature
e-J. Surf. Sci. Nanotech., **11** (2013) 110.
- S.Grangéon, F.Claret, C.Lerouge, F.Warmont, T.Sato, S.Anraku, C.Numako, Y.Linard and B.Lanson
On the Nature of Structural Disorder in Calcium Silicate Hydrates with a Calcium/Silicon Ratio Similar to Tobermorite
Cement and Concrete Research, **52** (2013) 31.
- S.Mandal, C.Santra, K.K.Bando, O.O.James, S.Maity, D.Mehta and B.Chowdhury
Aerobic Oxidation of Benzyl Alcohol over Mesoporous Mn-Doped Ceria Supported Au Nanoparticle Catalyst
Journal of Molecular Catalysis A:Chemical, **378** (2013) 47.
- S.Muratsugu, Z.Weng and M.Tada
Surface Functionalization of Supported Mn Clusters to Produce Robust Mn Catalysts for Selective Epoxidation
ACS Catal., **3** (2013) 2020.
- R.Nakada, Y.Takahashi and M.Tanimizu
Isotopic and Speciation Study on Cerium during its Solid-Water Distribution with Implication for Ce Stable Isotope as a Paleo-Redox Proxy
Geochim. Cosmochim. Acta, **103** (2013) 49.
- M.Tanaka, Y.Takahashi, N.Yamaguchi, K.-W.Kim, G.Zheng and M.Sakamitsu
The Difference of Diffusion Coefficients in Water for Arsenic Compounds at Various pH and its Dominant Factors Implied by Molecular Simulations
Geochim. Cosmochim. Acta, **105** (2013) 360.
- Y.Takahashi, T.Furukawa, Y.Kanai, M.Uematsu, G.Zheng and M.A.Marcus
Seasonal Changes in Fe Species and Soluble Fe Concentration in the Atmosphere in the Northwest Pacific Region Based on the Analysis of Aerosols Collected in Tsukuba, Japan
Atmos. Chem. Phys., **13** (2013) 7695.
- N.Murata, T.Suzuki, M.Kobayashi, F.Togoh and K.Asakura
Characterization of Pt-Doped SnO₂ Catalyst for a High-Performance Micro Gas Sensor
Phys. Chem. Chem. Phys., **15** (2013) 17938.
- L.Wang, J.Li, J.Pan, X.Jiang, Y.Ji, Y.Li, Y.Qu, Y.Zhao, X.Wu and C.Chen
Revealing the Binding Structure of the Protein Corona on Gold Nanorods Using Synchrotron Radiation-Based Techniques: Understanding the Reduced Damage in Cell Membranes
J. Am. Chem. Soc., **135** (2013) 17359.
- K.Nitta, Y.Omori, T.Miyanaga, K.Takegahara, H.Sugawara, D.Kikuchi and H.Sato
Extended X-Ray Absorption Fine Structure Thermal Factor Analysis of Rattling in Filled Skutterudites RT₄Sb₁₂ (R: La, Ce, Pr, Nd, and Sm; T: Fe, Ru, and Os)
J. Phys. Soc. Jpn., **82** (2013) 044801.
- J.Chang, Y.Tani, H.Naitou, N.Miyata, H.Seyama and K.Tanaka
Cobalt(II) Sequestration on Fungal Biogenic Manganese Oxide Enhanced by Manganese(II) Oxidase Activity
Applied Geochemistry, **37** (2013) 170.
- F.Liu, W.Shan, Z.Lian, L.Xie, W.Yang and H.He
Novel MnWO_x Catalyst with Remarkable Performance for Low Temperature NH₃-SCR of NO_x
Catal. Sci. Technol., **3** (2013) 2699.
- K.Tanaka, Q.Yu, K.Sasaki and T.Ohnuki
Cobalt(II) Oxidation by Biogenic Mn Oxide Produced by *Pseudomonas* sp. Strain NGY-1
Geomicrobiology Journal, **30** (2013) 874.
- S.Takenaka, T.Tsukamoto, H.Matsune and M.Kishida
Carbon Nanotube-Supported Pd-Co Catalysts Covered with Silica Layers as Active and Stable Cathode Catalysts for Polymer Electrolyte Fuel Cells
Catal. Sci. Technol., **3** (2013) 2723.
- L.Wang, A.Yoshiasa, M.Okube, T.Hiratoko, Y.Hu, H.Arima and K.Sugiyama
Local Structure of Iron in Tektites and Natural Glass: An Insight through X-Ray Absorption Fine Structure Spectroscopy
Journal of Mineralogical and Petrological Sciences, **108** (2013) 288.
- J.Kim, K.H.Cho, I.Kagomiya and K.Park
Structural Studies of Porous Ni/YSZ Cermets Fabricated by the Solid-State Reaction Method
Ceramics International, **39** (2013) 7467.
- I.Kagomiya, S.Matsumoto, K.Kakimoto, H.Ohsato, H.Sakai and Y.Maeda
Annealing Effect on Temperature Coefficient of Resistivity in La_{1-x}Sr_xMnO₃ Ceramics
J. Euro. Ceram. Soc., **33** (2013) 985.
- H.Hanashima, N.Kitajima, T.Abe and A.Hokura
Study on Accumulation Mechanism of Arsenic and Selenium in *Pteris vittata* L. Using Synchrotron Radiation X-Ray Fluorescence Analysis
Adv. X-Ray Chem. Anal. Jpn., **44** (2013) 279. (*in Japanese*).

H.Kagi, S.Odake, H.Ishibashi, K.Shozugawa, M.Matsuo, W.Satake and T.Mikouchi
Oxygen Fugacity and Valence State of Chromium in Ferropicriolite: Can Cr²⁺ Be a Redox Indicator for the Deep Mantle?
J. Mineralogical and Petrological Sciences, **108** (2013) 172.

T.Ozaki, X.Wang and T.Ohnuki
Manganese and Arsenic Oxidation Performance of Bacterium-Yunotaki 86(BY86) from Hokkaido, Japan, and the Bacterium's Phylogeny
Geomicrobiol. J., **30** (2013) 559.

M.Jiang, T.Ohnuki, S.Yamasaki, K.Tanaka and S.Utsunomiya
Adsorption of Ytterbium onto *Saccharomyces cerevisiae* Fungal Cells: A pH-Dependent Contribution of Phosphoryl Functional Group
J. Radioanal. Nucl. Chem., **295** (2013) 2283.

S.Mitsunobu, C.Muramatsu, K.Watanabe and M.Sakata
Behavior of Antimony(V) during the Transformation of Ferrihydrite and its Environmental Implications
Environ. Sci. Technol., **47** (2013) 9660.

I.Kagomiya, K.Jimbo and K.Kakimoto
Distribution Change of Oxygen Vacancies in Layered Perovskite Type(Sr,La)_{n+1}Fe_nO_{3n+1}(n=3)
J. Sol. Stat. Chem., **207** (2013) 184.

13A

S.Shimizu, H.Noritake, T.Koitaya, K.Mukai, S.Yoshimoto and J.Yoshinobu
Site-Specific Chemical States of Adsorbed CO on Pt(997): A High Resolution XPS Study
Surf. Sci., **608** (2013) 220.

T.Koitaya, K.Mukai, S.Yoshimoto and J.Yoshinobu
Energy Level Alignment of Cyclohexane on Rh(111) Surfaces: The Importance of Interfacial Dipole and Final-State Screening
J. Chem. Phys., **138** (2013) 044702.

K.Ozawa, T.Kakubo, K.Shimizu, N.Amino, K.Mase and T.Komatsu
High-Resolution Photoelectron Spectroscopy Analysis of Sulfidation of Brass at the Rubber/Brass Interface
Appl. Surf. Sci., **264** (2013) 297.

K.Ozawa, T.Kakubo, K.Shimizu, N.Amino, K.Mase, Y.Izumi, T.Muro and T.Komatsu
High-Resolution Photoelectron Spectroscopy Study of Degradation of Rubber-to-Brass Adhesion by Thermal Aging
Appl. Surf. Sci., **268** (2013) 117.

T.Kajiwara, Y.Nakamori, A.Visikovskiy, T.Iimori, F.Komori, K.Nakatsuji, K.Mase and S.Tanaka
Graphene Nanoribbons on Vicinal SiC Surfaces by Molecular Beam Epitaxy
Phys. Rev. B, **87** (2013) 121407.

A.Toyoshima, T.Kikuchi, H.Tanaka, K.Mase, K.Amemiya, and K.Ozawa
Performance of PF BL-13A, a Vacuum Ultraviolet and Soft X-Ray Undulator Beamline for Studying Organic Thin Films Adsorbed on Surfaces
J. Phys.: Conf. Ser., **425** (2013) 152019.

R.Toyoshima, M.Yoshida, Y.Monya, K.Suzuki, K.Amemiya, K.Mase, B.S.Mun and H.Kondo
Photoelectron Spectroscopic Study of CO and NO Adsorption on Pd(100) Surface under Ambient Pressure Conditions
Surf. Sci., **615** (2013) 33.

H.Koike, T.Kubo, K.Uchida, M.Chikamatsu, R.Azumi, K.Mase and K.Kanai
Direct Observation of Energy Band Development in a One-Dimensional Biradical Molecular Chain by Ultraviolet Photoemission Spectroscopy
Appl. Phys. Lett., **102** (2013) 134103.

Y.Harada, T.Koitaya, K.Mukai, S.Yoshimoto and J.Yoshinobu
Spectroscopic Characterization and Transport Properties of Aromatic Monolayers Covalently Attached to Si(111) Surfaces
J. Phys. Chem. C, **117** (2013) 7497.

R.Toyoshima, M.Yoshida, Y.Monya, K.Suzuki, K.Amemiya, K.Mase, B.S.Mun and H.Kondoh
In Situ Photoemission Observation of Catalytic CO Oxidation Reaction on Pd(110) under Near-Ambient Pressure Conditions: Evidence for the Langmuir-Hinshelwood Mechanism
J. Phys. Chem. C, **117** (2013) 20617.

K.Niwa, C.Miyakawa, T.Yagi and J.Matsuda
Argon Solubility in SiO₂ Melt under High Pressures: A New Experimental Result using Laser-Heated Diamond Anvil Cell
Earth and Planetary Sci. Lett., **363** (2013) 1.

W.Xie, P.L.Prabhumirashi, Y.Nakayama, K.A.McGarry, M.L.Geier, Y.Uragami, K.Mase, C.J.Douglas, H.Ishii, M.C.Hersam and C.D.Frisbie
Utilizing Carbon Nanotube Electrodes to Improve Charge Injection and Transport in Bis(Trifluoromethyl)-Dimethyl-Rubrene Ambipolar Single Crystal Transistors
ACS Nano, **7** (2013) 10245.

13B

S.Wang, T.Sakurai, X.Hao, W.Fu, S.Masuda and K.Akimoto
Favorable Electronic Structure for Organic Solar Cells Induced by Strong Interaction at Interface
J. Appl. Phys., **114** (2013) 183707.

T.Sakurai, S.Wang, S.Toyoshima and K.Akimoto
Role of Electrode Buffer Layers in Organic Solar Cells
Renewable and Sustainable Energy Conference (IRSEC), 2013 International, (2013) 46.

13C

T.Kinoshita, K.Arai, K.Fukumoto, T.Ohkochi, M.Kotsugi, F.Guo, T.Muro, T.Nakamura, H.Osawa, T.Matsushita and T.Okuda
Observation of Micro-Magnetic Structures by Synchrotron Radiation Photoelectron Emission Microscopy
J. Phys. Soc. Jpn., **82** (2013) 021005.

14A

H.Takahashi, M.Yoshino, T.Takagi, H.Amii, T.Baba, T.Kanamori and M.Sonoyama
Non-Ideal Mixing of Dimyristoylphosphatidylcholine with its Partially Fluorinated Analogue in Hydrated Bilayers
Chem. Phys. Lett., **559** (2013) 107.

S.Kishimoto, H.Yonemura, S.Adachi, S.Shimazaki, M.Ikeno, M.Saito, T.Taniguchi and M.Tanaka
A Fast X-Ray Detector using Silicon Avalanche Photodiodes of 64-Pixel Linear Array
J. Phys.: Conf. Ser., **425** (2013) 062007.

S.Ueda, K.Hayashida, H.Nakajima, N.Anabuki, H.Tsunemi, H.Kan, T.Kohmura, S.Ikeda, K.Kaneko, T.Watanabe, K.Mori, M.Nobukawa, H.Murakami, K.Sakata, S.Todoroki, N.Yagihashi, E.Mizuno, M.Muramatsu, H.Suzuki and S.Takagi
Measurement of the Soft X-Ray Response of P-Channel Back-Illuminated CCD
Nucl. Instrum. Meth. Phys. Res. A, **704** (2013) 140.

N.Yahaba, M.Koshimizu, T.Yanagida, Y.Fujimoto, R.Haruki, F.Nishikido, S.Kishimoto and K.Asai
X-Ray Detection Capability and Luminescence Property of Cs₂ZnCl₄ Single Crystal Scintillators
Houshasen Kagaku, **95** (2013) 27. (*in Japanese*).

M.Koshimizu, T.Yanagida, Y.Fujimoto, A.Yamazaki, K.Watanabe, A.Uritani, K.Fukuda, N.Kawaguchi, S.Kishimoto and K.Asai
Origin of Fast Scintillation Components of LiCaAlF₆ Crystals
Appl. Phys. Express, **6** (2013) 062601.

S.Kishimoto, H.Yonemura, S.Adachi, S.Shimazaki, M.Ikeno, M.Saito, T.Taniguchi, M.Tanaka
64-Pixel Linear-Array Si-APD Detector for X-Ray Time-Resolved Experiments
Nucl. Instrum. Meth. Phys. Res. A, **731** (2013) 53.

H.Nakajima, M.Fujikawa, H.Mori, H.Kan, S.Ueda, H.Kosugi, N.Anabuki, K.Hayashida and H.Tsunemi
Single Event Effect Characterization of the Mixed-Signal ASIC Developed for CCD Camera in Space Use
Nucl. Instrum. Meth. Phys. Res. A, **731** (2013) 166.

S.Ueda, K.Hayashida, H.Nakajima and H.Tsunemi
X-Ray Measurement of the Elemental Abundances at the Outskirts of the Perseus Cluster with Suzaku
Astronomische Nachrichten, **334** (2013) 426.

K.Mori, Y.Nishioka, S.Ohura, Y.Koura, M.Yamauchi, H.Nakajima, S.Ueda, H.Kan, N.Anabuki, R.Nagino, K.Hayashida, H.Tsunemi, T.Kohmura, S.Ikeda, H.Murakami, M.Ozaki, T.Dotani, Y.Maeda and K.Sagara
Proton Radiation Damage Experiment on P-Channel CCD for an X-Ray CCD Camera Onboard the ASTRO-H Satellite
Nucl. Instrum. Meth. Phys. Res. A, **731** (2013) 160.

14B

K.Hirano, and Y.Takahashi
Applications of X-Ray Magnifier and Demagnifier to Angle-Resolved X-Ray Computed Tomography
J. Phys.: Conf. Ser., **425** (2013) 192004.

K.Hirano, Y.Ito, Y.Shinohara and Y.Amemiya
Characterization of an X-Ray Diamond Phase Plate by a Polarization Analyzer using Multiple Diffraction
J. Phys.: Conf. Ser., **425** (2013) 052030.

K.Hirano Y.Takahashi and S.Nagamachi
Application of X-Ray Phase Plate to Grazing Incidence X-Ray Topography for the Control of Penetration Depth
Nucl. Instrum. Meth. Phys. Res. A, **729** (2013) 537.

T.Miyoshi, Y.Arai, T.Chiba, Y.Fujita, K.Hara, S.Honda, Y.Igarashi, Y.Ikegami, Y.Ikemoto, T.Kohriki, M.Ohno, Y.Ono, N.Shinoda, A.Takeda, K.Tauchi, T.Tsuboyama, H.Tadokoro, Y.Unno and M.Yanagihara
Monolithic Pixel Detectors with 0.2 μm FD-SOI Pixel Process Technology
Nucl. Instrum. Meth. Phys. Res. A, **732** (2013) 530.

J.Duan, C.Hu, S.Luo, X.Zhao and T.Wang
Microcomputed Tomography with Diffraction-Enhanced Imaging for Morphologic Characterization and Quantitative Evaluation of Microvessel of Hepatic Fibrosis in Rats
PLOS ONE, **8** (2013) e78176.

A.Ruammitree, H.Nakahara, K.Akimoto, K.Soda and Y.Saito
Determination of Non-Uniform Graphene Thickness on SiC(0001) by X-Ray Diffraction
Appl. Surf. Sci., **282** (2013) 297.

T.Emoto
Behavior of Peak Intensity of Rocking Curve for Asymmetric Bragg Reflection Uniquely Determined by Strain Distribution
e-J. Surf. Sci. Nanotech, **11** (2013) 127.

R.Negishi, T.Fukamachi, S.Jongsukswat, K.Hirano, K.Hirano and T.Kawamura
Phase Determination of the Crystal Structure Factor by Measuring Rocking Curves from a Polar Crystal
J. Appl. Cryst., **46** (2013) 1216.

H.Okamoto and K.Mizuno
Observation of the Japan Ware by the X-Ray Diffraction-Enhanced Imaging Method
Journal of the Tsuruma Health Science Society, **37(2)** (2013) 51. (*in Japanese*).

14C

S.Takeya, A.Yoneyama, K.Ueda, K.Hyodo, H.Yamawaki, H.Fujihisa, Y.Gotoh and T.Takeda
Phase-Contrast X-Ray Images of Ice and Water on Carbon Paper for Fuel Cells Measured by Diffraction-Enhanced Imaging Technique
Jpn. J. Appl. Phys., **52** (2013) 048002.

H.Ito, S.Matsushita, K.Hyodo, Y.Sato and Y.Sakakibara
Using Synchrotron Radiation Angiography with a Highly Sensitive Detector to Identify Impaired Peripheral Perfusion in Rat Pulmonary Emphysema
J. Synchrotron Rad., **20** (2013) 376.

Y.Wu, K.Hyodo, N.Sunaguchi, T.Yuasa and M.Ando
Development of High Sensitivity X-Ray Multiple-Times-Diffraction Enhanced Imaging (M-DEI) Optics
J. Phys.: Conf. Ser., **425** (2013) 192008.

Y.Sung, C.J.R.Sheppard, G.Bartathis, M.Ando and R.Gupta
Full-Wave Approach for X-Ray Phase Imaging
Optics Express, **21** (2013) 17547.

N.Sunaguchi, T.Yuasa and M.Ando
Iterative Reconstruction Algorithm for Analyzer Based Phase-Contrast Computed Tomography of Hard and Soft Tissue
Appl. Phys. Lett., **103** (2013) 143702.

A.Ruammitree, H.Nakahara, K.Akimoto, K.Soda and Y.Saito
Determination of Non-Uniform Graphene Thickness on SiC(0001) by X-Ray Diffraction
Appl. Surf. Sci., **282** (2013) 297.

T.Yuasa, N.Sunaguchi, S.Ichihara and M.Ando
A Physico-Mathematical Formulation Based on Ray Equation for Reconstructing Refraction-Based 3-D Image of Soft Tissue
J. Instrum., **8** (2013) C05001.

H.Okamoto and K.Mizuno
Observation of the Japan Ware by the X-Ray Diffraction-Enhanced Imaging Method
Journal of the Tsuruma Health Science Society, **37(2)** (2013) 51. (*in Japanese*).

M.P.Olbinado, P.Vagovič, W.Yashiro and A.Momose
Demonstration of Stroboscopic X-Ray Talbot Interferometry using Polychromatic Synchrotron and Laboratory X-Ray Sources
Appl. Phys. Express, **6** (2013) 096601.

15A

Y.Sakai, R.Gomi, K.Kato, H.Yokoyama and K.Ito
Structure and Dynamics of Polyrotaxane-Based Sliding Graft Copolymers with Alkyl Side Chains
Soft Matter, **9** (2013) 1895.

S.G.Guryanov, V.V.Filimonov, A.A.Timchenko, B.S.Melnik, H.Kihara, V.P.Kutyshenko, L.P.Ovchinnikov and G.V.Semisotnov
The Major mRNP Protein YB-1: Structural and Association Properties in Solution
Biochim. Biophys. Acta, **1834** (2013) 559.

Y.Morimoto, T.Nakagawa and M.Kojima
Small-Angle X-Ray Scattering Constraints and Local Geometry Like Secondary Structures Can Construct a Coarse-Grained Protein Model at Amino Acid Residue Resolution
Biochem. Biophys. Res. Commun., **431** (2013) 65.

H.Okuda and S.Ochiai
A Review on Small- and Wide-Angle X-Ray Scattering Applied to the Precipitation Process in Metallic Alloys
Metallurgical and Materials Transactions A, **44** (2013) 94.

H.Yokoyama
Small Angle X-Ray Scattering Studies of Nanocellular and Nanoporous Structures
Polymer J., **45** (2013) 3.

D.Sato, K.Obara, M.Iwahashi, Y.Kawabata and T.Kato
Re-entrant Lamellar/Onion Transition with Varying Temperature under Shear Flow
Langmuir, **29** (2013) 121.

K.Saijo, G.Shin, T.Hashimoto, Y.Amemiya and K.Ito
Strain-Phase-Resolved Dynamic SAXS Studies of BCC-Spherical Domains in Block Copolymers under LAOS: Creation of Twinned BCC-Sphere and their Dynamic Response
Macromolecules, **46** (2013) 1549.

N.Sota, K.Saijo, H.Hasegawa, T.Hashimoto, Y.Amemiya, and K.Ito
Directed Self-Assembly of Block Copolymers into Twin BCC-Sphere: Phase Transition Process from Aligned Hex-Cylinder to BCC-Sphere Induced by a Temperature Jump between the Two Equilibrium Phases
Macromolecules, **46** (2013) 2298.

Y.Sugimoto, M.Shioya, H.Matsumoto, M.Minagawa and A.Tanioka
Structure Changes during Tensile Deformation and Mechanical Properties of a Twisted Carbon Nanotube Yarn
Carbon, **60** (2013) 193.

M.Harada, M.Yamada, Y.Kimura and K.Saijo
Influence of the Organization of Water-in-Ionic Liquid Microemulsions on the Size of Silver Particles during Photoreduction
J. Colloid Interface Sci., **406** (2013) 94.

K.Matsui, S.Seno, Y.Nozone, Y.Shinohara, Y.Amemiya, E.B.Berda, G.Rojas and K.B.Wagener
Influence of Branch Incorporation into the Lamella Crystal on the Crystallization Behavior of Polyethylene with Precisely Spaced Branches
Macromolecules, **46** (2013) 4438.

G.Cui, S.Ohya, T.Matsutani, S.Nagano, T.Dohi, S.Nakamura, S.Sakurai, T.Miyazaki and K.Yamamoto
Perpendicular Orientation of Sub-10 nm Channels in Polystyrene-*b*-Poly(4-Hydroxyl Styrene)/PEG Oligomer Blend Thin Films
Nanoscale, **5** (2013) 6713.

K.Oshima and K.Wakabayashi
Structural Basis of Muscle Regulation by Synchrotron X-Ray Diffraction: Head-Head Interactions of Myosin Crossbridges in Resting Higher Vertebrate Striated Muscle
J. Cryst. Soc. Jpn., **55** (2013) 203. (*in Japanese*).

Y.Matsumura, M.Shinjo, T.Matsui, K.Ichimura, J.Song and H.Kihara
Structural Study of hNck2 SH3 Domain Protein in Solution by Circular Dichroism and X-Ray Solution Scattering
Biophys. Chem., **175** (2013) 39.

Y.Matsumura, M.Shinjo, S.J.Kim, N.Okishio, M.Gruebele and H.Kihara
Transient Helical Structure during PI3K and Fyn SH3 Domain Folding
J. Phys. Chem. B, **117** (2013) 4836.

A.A.Timchenko, O.V.Novosylina, E.A.Prituzhalov, H.Kihara, A.V.El'skaya, B.S.Negrutskii and I.N.Serdyuk
Different Oligomeric Properties and Stability of Highly Homologous A1 and Proto-Oncogenic A2 Variants of Mammalian Translation Elongation Factor eEF1
Biochemistry, **52** (2013) 5345.

H.Takeno and T.Mochizuki
A Structural Development of an Organogel Explored by Synchrotron Time-Resolved Small-Angle X-Ray Scattering
Colloid Polym. Sci., **291** (2013) 2783.

L.Bayés-García, T.Calvet, M.À.Cuevas-Diarte, S.Ueno and K.Sato
Crystallization and Transformation of Polymorphic Forms of Trioleoyl Glycerol and 1,2-Dioleoyl-3-*rac*-linoleoyl Glycerol
J. Phys. Chem. B, **117** (2013) 9170.

15B1

H.Koizumi, S.Uda, K.Fujiwara, M.Tachibana, K.Kojima and J.Nozawa
Improvement of Crystal Quality for Tetragonal Hen Egg White Lysozyme Crystals under Application of an External Alternating Current Electric Field
J. Appl. Cryst., **46** (2013) 25.

S.Hosokawa, N.Happo, T.Ozaki, H.Ikemoto, T.Shishido and K.Hayashi
Extent and Feature of Lattice Distortions around Ga Impurity Atoms in InSb Single Crystal
Phys. Rev. B, **87** (2013) 094104.

Y.Kitajima, Y.Nanba, M.Tanaka, Y.Koga, A.Ueno, K.Nakagawa, H.Tokoro, S.Ohkoshi, T.Iwazumi, K.Okada and Y.Isozumi
Observation of π Backbonding Features in Fe 2p X-Ray Absorption Spectra and Fe 1s-4p-1s Resonant X-Ray Emission Spectra of RbMn[Fe(CN)₆]
J. Phys.: Conf. Ser., **430** (2013) 012082.

S.Kawakami, N.Nakajima, T.Takigawa, M.Nakatake, H.Maruyama, Y.Tezuka and T.Iwazumi
UV-Induced Change in the Electronic Structure of SrTiO₃ at Low Temperature Probed by Resonant X-Ray Emission Spectroscopy
J. Phys. Soc. Jpn., **82** (2013) 053701.

K.Mizuno, T.Kobayashi, H.Taniguchi and H.Okamoto
Growth and X-Ray Topographic Characterization of κ -(BEDT-TTF)₂Cu[N(CN)₂]Br Single Crystals
Trans. Mat. Res. Soc. Japan, **38** (2013) 565.

15B2

T.Shirasawa, J.Tsunoda, T.Hirahara and T.Takahashi
Structure of Bi/Bi₂Te₃ Heteroepitaxial Film Studied by X-Ray Crystal Truncation Rod Scattering
Phys. Rev. B, **87** (2013) 075449.

15C

Y.Kato, H.Umezawa, S.Shikata and M.Touge
Effect of an Ultraflat Substrate on the Epitaxial Growth of Chemical-Vapor-Deposited Diamond
Appl. Phys. Express, **6** (2013) 025506.

S.Harada, Y.Yamamoto, K.Seki and T.Ujihara
Reduction of Threading Screw Dislocation Utilizing Defect Conversion during Solution Growth of 4H-SiC
Material Science Forum, **740-742** (2013) 189.

Y.Yamamoto, S.Harada, K.Seki, A.Horio, T.Mitsubishi and T.Ujihara
Effect of Surface Polarity on the Conversion of Threading Dislocations in Solution Growth
Materials Science Forum, **740-742** (2013) 15.

K.Hirano Y.Takahashi and S.Nagamachi
Application of X-Ray Phase Plate to Grazing Incidence X-Ray Topography for the Control of Penetration Depth
Nucl. Instrum. Meth. Phys. Res. A, **729** (2013) 537.

S.Harada, Y.Yamamoto, K.Seki, A.Horio, T.Mitsubishi, M.Tagawa and T.Ujihara
Evolution of Threading Screw Dislocation Conversion during Solution Growth of 4H-SiC
APL Materials, **1** (2013) 022109.

S.Harada, Y.Yamamoto, K.Seki and T.Ujihara
Current Advances in SiC Solution Growth
J. Jpn. Assoc. Cryst., **40** (2013) 25. (*in Japanese*).

T.Emoto
Behavior of Peak Intensity of Rocking Curve for Asymmetric Bragg Reflection Uniquely Determined by Strain Distribution
e-J. Surf. Sci. Nanotech, **11** (2013) 127.

R.Negishi, T.Fukamachi, S.Jongsukswat, K.Hirano, K.Hirano and T.Kawamura
Phase Determination of the Crystal Structure Factor by Measuring Rocking Curves from a Polar Crystal
J. Appl. Cryst., **46** (2013) 1216.

16A

S.M.Suturin, V.V.Fedorov, A.G.Banshchikov, D.A.Baranov, K.V.Koshmak, P.Torelli, J.Fujii, G.Panaccione, K.Amemiya, M.Sakamaki, T.Nakamura, M.Tabuchi, L.Pasquali and N.S.Sokolov
Proximity Effects and Exchange Bias in Co/MnF₂(111) Heterostructures Studied by X-Ray Magnetic Circular Dichroism
J. Phys.: Condens. Matter, **25** (2013) 046002.

H.Wadati
Report on JSSRR Scientific Awards Resonant Soft X-Ray Scattering Studies of Transition-Metal-Oxide Thin Films
J. Jpn. Soc. Synchrotron Rad. Res., **26** (2013) 118. (*in Japanese*).

M.Sakamaki and K.Amemiya
Effect of Structural Strain on Magnetic Anisotropy Energy of Each Element in Alternately Layered FeNi Thin Films
Phys. Rev. B, **87** (2013) 014428.

K.Amemiya, M.Sakamaki, P.Mazalski, I.Sveklo, Z.Kurant, A.Maziewski, M.O.Liedke, J.Fassbender, A.Wawro and L.T.Baczewski
Ga⁺ Ion Irradiation-Induced Changes in Magnetic Anisotropy of a Pt/Co/Pt Thin Film Studied by X-Ray Magnetic Circular Dichroism
EPJ Web of Conferences, **40** (2013) 08002.

S.-M.Huttula, P.Lablanquie, L.Andric, J.Palaudoux, M.Huttula, S.Sheinerman, E.Shigemasa, Y.Hikosaka, K.Ito and F.Penent
Decay of a 2p Inner-Shell Hole in an Ar⁺ Ion
Phys. Rev. Lett., **110** (2013) 113002.

Y.Yamasaki, T.Sudayama, J.Okamoto, H.Nakao, M.Kubota and Y.Murakami
Diffractometer for Small Angle Resonant Soft X-Ray Scattering under Magnetic Field
J. Phys.: Conf. Ser., **425** (2013) 132012.

K.Amemiya, M.Sakamaki, T.Koide, K.Ito, K.Tsuchiya, K.Harada, T.Aoto, T.Shioya, T.Obina, S.Yamamoto and Y.Kobayashi
Fast Polarization Switching in the Soft X-Ray Region at PF BL-16A
J. Phys. Conf. Ser., **425** (2013) 152015.

K.Tsuchiya, T.Shioya, T.Aoto, K.Harada, T.Obina, M.Sakamaki and K.Amemiya
Operation of a Fast Polarization-Switching Source at the Photon Factory
J. Phys. Conf. Ser., **425** (2013) 132017.

J.Okamoto, K.Horigane, H.Nakao, K.Amemiya, M.Kubota, Y.Murakami and K.Yamada
Resonant Soft X-Ray Scattering Study of the Magnetic Structures in La_{1.5}Ca_{0.5}CoO₄ using a High Vacuum Diffractometer with a 4-Blade-Slit Detector System
J. Phys.: Conf. Ser., **425** (2013) 202003.

M.Nakano, F.Penent, M.Tashiro, T.P.Grozdanov, M.Zitnik, S.Carniato, P.Selles, L.Andric, P.Lablanquie, J.Palaudoux, E.Shigemasa, H.Iwayama, Y.Hikosaka, K.Soejima, I.H.Suzuki, N.Kouchi and K.Ito
Single Photon K⁻² and K⁻¹K⁻¹ Double Core Ionization in C₂H_{2n} (n=1-3), CO and N₂ as a Potential New Tool for Chemical Analysis
Phys. Rev. Lett., **110** (2013) 163001.

Y.Hikosaka, M.Sawa, M.Nakano, K.Soejima, P.Lablanquie, F.Penent and K.Ito
Electron Reemission Processes Following Photoelectron Recapture due to Post-Collision Interaction Inner-Shell Photoionization of Water Molecules
J. Chem. Phys., **138** (2013) 214308.

T.Harano, G.Shibata, K.Ishigami, Y.Takahashi, V.K.Verma, V.R.Singh, T.Kadono, A.Fujimori, Y.Takeda, T.Okane, Y.Saitoh, H.Yamagami, T.Koide, H.Yamada, A.Sawa, M.Kawasaki, Y.Tokura, and A.Tanaka
Role of Doped Ru in Coercivity-Enhanced La_{0.6}Sr_{0.4}MnO₃ Thin Film Studied by X-Ray Magnetic Circular Dichroism
Appl. Phys. Lett., **102** (2013) 222404.

K.Amemiya and M.Sakamaki
Temperature Dependence of Remanent Magnetization of Thin Films at the Interface to a Nonmagnetic Material: Cu/Ni/Cu(100)
Phys. Rev. B, **88** (2013) 014401.

M.Nakano, P.Selles, P.Lablanquie, Y.Hikosaka, F.Penent, E.Shigemasa, K.Ito and S.Carniato
Near-Edge X-Ray Absorption Fine Structures Revealed in Core Ionization Photoelectron Spectroscopy
Phys. Rev. Lett., **111** (2013) 123001.

M.Sakamaki, K.Amemiya, A.Nambu, K.Ueda, J.Shimizu and K.Watanabe
Ar⁺ Ion Milling-Induced Suppression of Surface Oxidation in Fe₇₀Co₃₀ Thin Films
Mater. Chem. Phys., **143** (2013) 281.

K.Yoshimatsu, H.Wadati, E.Sakai, T.Harada, Y.Takahashi, T.Harano, G.Shibata, K.Ishigami, T.Kadono, T.Koide, T.Sugiyama, E.Ikenaga, H.Kumigashira, M.Lippmaa, M.Oshima and A.Fujimori
Spectroscopic Studies on the Electronic and Magnetic States of Co-Doped Perovskite Manganite $\text{Pr}_{0.8}\text{Ca}_{0.2}\text{Mn}_{1-y}\text{Co}_y\text{O}_3$ Thin Films
Phys. Rev. B, **88** (2013) 174423.

S.Chakraverty, T.Matsuda, H.Wadati, J.Okamoto, Y.Yamasaki, H.Nakao, Y.Murakami, S.Ishiwata, M.Kawasaki, Y.Taguchi, Y.Tokura and H.Y.Hwang
Multiple Helimagnetic Phases and Topological Hall Effect in Epitaxial Thin Films of Pristine and Co-Doped SrFeO_3
Phys. Rev. B, **88** (2013) 220405.

T.Harano, G.Shibata, K.Yoshimatsu, K.Ishigami, V.K.Verma, Y.Takahashi, T.Kadono, T.Yoshida, A.Fujimori, T.Koide, F.-H.Chang, H.-J.Lin, D.-J.Huang, C.-T.Chen, P.-H.Xiang, H.Yamada and A.Sawa
Phase Diagram of $\text{Ca}_{1-x}\text{Ce}_x\text{MnO}_3$ Thin Films Studied by X-Ray Magnetic Circular Dichroism
Solid State Commun., **174** (2013) 30.

17A

A.Gao, G.-Y. Mei, S.Liu, P.Wang, Q.Tang, Y.-P. Liu, H.Wen, X.-M.An, L.-Q.Zhang, X.-X.Yan and D.-C.Liang
High-Resolution Structures of AidH Complexes Provide Insights into a Novel Catalytic Mechanism for *N*-Acyl Homoserine Lactonase
Acta Cryst. D, **69** (2013) 82.

N.Saito and Y.Matsuura
A 2.1-Å-Resolution Crystal Structure of Unliganded CRM1 Reveals the Mechanism of Autoinhibition
J. Mol. Biol., **425** (2013) 350.

Z.Wang, Y.Wu, L.Li and X.-D.Su
Intermolecular Recognition Revealed by the Complex Structure of Human CLOCK-BMAL1 Basic Helix-Loop-Helix Domains with E-Box DNA
Cell Res., **23** (2013) 213.

S.Liang, J.Dai, S.Hou, L.Su, D.Zhang, H.Guo, S.Hu, H.Wang, Z.Rao, Y.Guo and Z.Lou
Structural Basis for Treating Tumor Necrosis Factor α (TNF α)-Associated Diseases with the Therapeutic Antibody Infliximab
J. Biol. Chem., **288** (2013) 13799.

T.Shiba, Y.Kido, K.Sakamoto, D.K.Inaoka, C.Tsuge, R.Tatsumi, G.Takahashi, E.O.Balogun, T.Nara, T.Aoki, T.Honma, A.Tanaka, M.Inoue, S.Matsuoka, H.Saimoto, A.L.Moore, S.Harada and K.Kita
Structure of the Trypanosome Cyanide-Insensitive Alternative Oxidase
Proc. Natl. Acad. Sci. USA, **110** (2013) 4580.

T.Ito, T.Katayama, M.Hattie, H.Sakurama, J.Wada, R.Suzuki, H.Ashida, T.Wakagi, K.Yamamoto, K.A.Stubbs and S.Fushinobu
Crystal Structures of a Glycoside Hydrolase Family 20 Lacto-*N*-Biosidase from *Bifidobacterium bifidum*
J. Biol. Chem., **288** (2013) 11795.

W.J.Li, D.F.Li, Y.L.Hu, X.E.Zhang, L.J.Bi and D.C.Wang.
Crystal Structure of L,D-Transpeptidase Ldt_{Mt2} in Complex with Meropenem Reveals the Mechanism of Carbapenem Against *Mycobacterium tuberculosis*
Cell Res., **5** (2013) 728.

J.Otani, K.Arita, T.Kato, M.Kinoshita, H.Kimura, I.Suetake, S.Tajima, M.Ariyoshi and M.Shirakawa
Structural Basis of the Versatile DNA Recognition Ability of the Methyl-CpG Binding Domain of Methyl-CpG Binding Domain Protein 4
J. Biol. Chem., **288** (2013) 6351.

Z.Fujimoto, R.Suzuki, T.Shiotsuki, W.Tsuchiya, A.Tase, M.Momma and T.Yamazaki
Crystal Structure of Silkworm *Bombyx mori* JHBP in Complex with 2-Methyl-2,4-Pentanediol: Plasticity of JH-Binding Pocket and Ligand-Induced Conformational Change of the Second Cavity in JHBP
PLoS One, **8** (2013) e56261.

K.J.Cho, J.-H.Lee, K.W.Hong, S.-H.Kim, Y.Park, J.Y.Lee, S.Kang, S.Kim, J.H.Yang, E.-K.Kim, J.H.Seok, S.Unzai, S.Y.Park, X.Saelens, C.-J.Kim, J.-Y.Lee, C.Kang, H.-B.Oh, M.S.Chung and K.H.Kim
Insight into Structural Diversity of Influenza Virus Hemagglutinin
J. Gen. Virol., **94** (2013) 1712.

B.Li, Q.Wang, X.Pan, I.F.Castro, Y.Sun, Y.Guo, X.Tao, C.Risco, S.-F.Sui and Z.Lou
Bunyamwera Virus Possesses a Distinct Nucleocapsid Protein to Facilitate Genome Encapsidation
Proc. Natl. Acad. Sci. USA, **110** (2013) 9048.

T.-Y.Jung, Y.-S.Kim, B.-H.Oh and E.Woo
Identification of a Novel Ligand Binding Site in Phosphoserine Phosphatase from the Hyperthermophilic Archaeon *Thermococcus onnurineus*
Proteins, **81** (2013) 819.

D.Sasaki, S.Watanabe, R.Matsumi, T.Shoji, A.Yasukochi, K.Tagashira, W.Fukuda, T.Kanai, H.Atomi, T.Imanaka and K.Miki
Identification and Structure of a Novel Archaeal HypB for [NiFe] Hydrogenase Maturation
J. Mol. Biol., **425** (2013) 1627.

H.Sasanuma, M.S.Tawaramoto, J.P.Lao, H.Hosaka, E.Sanda, M.Suzuki, E.Yamashita, N.Hunter, M.Shinohara, A.Nakagawa, A.Shinohara
A New Protein Complex Promoting the Assembly of Rad51 Filaments
Nature Commun., **4** (2013) 1676.

- A.Matsumoto, Y.Shimizu, C.Takemoto, T.Ueda, T.Uchiyumi and K.Ito
Crystallization and Preliminary X-Ray Analysis of Peptidyl-tRNA Hydrolase from *Thermus thermophilus* HB8
Acta Cryst. F, **69** (2013) 332.
- J.Kobayashi and Y.Matsuura
Structural Basis for Cell-Cycle-Dependent Nuclear Import Mediated by the Karyopherin Kap121p
J. Mol. Biol., **425** (2013) 1852.
- H.Makyio, T.Takeuchi, M.Tamura, K.Nishiyama, H.Takahashi, H.Natsugari, Y.Arata, K.Kasai, Y.Yamada, S.Wakatsuki and R.Kato
Structural Basis of Preferential Binding of Fucose-Containing Saccharide by the *Caenorhabditis elegans* Galectin LEC-6
Glycobiology, **23** (2013) 797.
- R.Nasuno, Y.Hirano, T.Itoh, T.Hakoshima, T.Hibi and H.Takagi
Structural and Functional Analysis of the Yeast *N*-Acetyltransferase Mpr1 Involved in Oxidative Stress Tolerance via Proline Metabolism
Proc. Natl. Acad. Sci. USA, **110** (2013) 11821.
- T.Arimori, N.Kawamoto, S.Shinya, N.Okazaki, M.Nakazawa, K.Miyatake, T.Fukamizo, M.Ueda and T.Tamada
Crystal Structures of the Catalytic Domain of a Novel Glycohydrolase Family 23 Chitinase from *Ralstonia* sp. A-471 Reveals a Unique Arrangement of the Catalytic Residues for Inverting Chitin Hydrolysis
J. Biol. Chem., **288** (2013) 18696.
- Y.Nagamatsu, K.Takeda, T.Kuranaga, N.Numoto and K.Miki
Origin of Asymmetry on the Intersubunit Interfaces of V_1 -ATPase from *Thermus thermophilus*
J. Mol. Biol., **425** (2013) 2699.
- K.J.Cho, J.-H.Lee, K.W.Hong, S.-H.Kim, Y.Park, J.Y.Lee, S.Kang, S.Kim, J.H.Yang, E.-K.Kim, J.H.Seok, S.Unzai, S.Y.Park, X.Saelens, C.-J.Kim, J.-Y.Lee, C.Kang, H.-B.Oh, M.S.Chung and K.H.Kim
Insight into Structural Diversity of Influenza Virus Haemagglutinin
J. General Virology, **94** (2013) 1712.
- W.Zhang, Y.Shi, X.Lu, Y.Shu, J.Qi and G.F.Gao
An Airborne Transmissible Avian Influenza H5 Hemagglutinin Seen at the Atomic Level
Science, **340** (2013) 1463.
- S.Okazaki, S.Nakano, D.Matsui, S.Akaji, K.Inagaki and Y.Asano
X-Ray Crystallographic Evidence for the Presence of the Cysteine Tryptophylquinone Cofactor in L-Lysine ϵ -Oxidase from *Marinomonas mediterranea*
J. Biochem., **154** (2013) 233.
- T.Hirose, N.Maita, H.Gouda, J.Koseki, T.Yamamoto, A.Sugawara, H.Nakano, S.Hirono, K.Shiomi, T.Watanabe, H.Taniguchi, K.B.Sharpless, S.Omura and T.Sunazuka
Observation of the Controlled Assembly of Preclick Components in the in situ Click Chemistry Generation of a Chitinase Inhibitor
Proc. Natl. Acad. Sci. USA, **110** (2013) 15892.
- T.Kinoshita, T.Nakaniwa, Y.Sekiguchi, Y.Sogabe, A.Sakurai, S.Nakamura and I.Nakanishi
Crystal Structure of Human CK2 α at 1.06 Å Resolution
J. Synchrotron Rad., **20** (2013) 974.
- A.Nakamura, T.Ishida, S.Fushinobu, K.Kusaka, I.Tanaka, K.Inaka, Y.Higuchi, M.Masaki, K.Ohta, S.Kaneko, N.Niimura, K.Igarashi and M.Samajima
Phase-Diagram-Guided Method for Growth of a Large Crystal of Glycoside Hydrolase Family 45 Inverting Cellulase Suitable for Neutron Structural Analysis
J. Synchrotron Rad., **20** (2013) 859.
- S.Fushinobu, V.D.Alves and P.M.Coutinho
Multiple Rewards from a Treasure Trove of Novel Glycoside Hydrolase and Polysaccharide Lyase Structures: New Folds, Mechanistic Details, and Evolutionary Relationships
Curr. Opin. Struct. Biol., **23** (2013) 652.
- T.Osawa, H.Inanaga and T.Numata
Crystallization and Preliminary X-Ray Diffraction Analysis of the Cmr2-Cmr3 Subcomplex in the CRISPR-Cas RNA-Silencing Effector Complex
Acta Cryst. F, **69** (2013) 585.
- T.Osawa, H.Inanaga and T.Numata
Crystal Structure of the Cmr2-Cmr3 Subcomplex in the CRISPR-Cas RNA Silencing Effector Complex
J. Mol. Biol., **425** (2013) 3811.
- Z.Gai, A.Nakamura, Y.Tanaka, N.Hirano, I.Tanaka and M.Yao
Crystal Structure Analysis, Overexpression and Refolding Behavior of a DING Protein with Single Mutation
J. Synchrotron Rad., **20** (2013) 854.
- Z.Fujimoto
Structure and Function of Carbohydrate-Binding Module Families 13 and 42 of Glycoside Hydrolases, Comprising a β -Trefol Fold
Biosci. Biotechnol. Biochem., **77** (2013) 1363.
- T.Arimori, A.Ito, M.Nakazawa, M.Ueda and T.Tamada
Crystal Structure of Endo-1,4- β -Glucanase from *Eisenia fetida*
J. Synchrotron Rad., **20** (2013) 884.

- K.Takemoto, T.Matsuda, N.Sakai, D.Fu, M.Noda, S.Uchiyama, I.Kotera, Y.Arai, M.Horiuchi, K.Fukui, T.Ayabe, F.Inagaki, H.Suzuki and T.Nagai
SuperNova, a Monomeric Photosensitizing Fluorescent Protein for Chromophore-Assisted Light Inactivation.
Sci. Rep., **3** (2013) 2629.
- Y.Kuwano, K.Yoneda, Y.Kawaguchi and T.Araki
The Tertiary Structure of an I-Type Lysozyme Isolated from the Common Orient Clam (*Meretrix lusoria*)
Acta Cryst. F, **69** (2013) 1202.
- T.Mori, Y.Shimokawa, T.Matsui, K.Kinjo, R.Kato, H.Noguchi, S.Sugio, H.Morita and I.Abe
Cloning and Structure-Function Analyses of Quinolone- and Acridone-Producing Novel Type III Polyketide Synthases from *Citrus microcarpa*
J. Biol. Chem., **288** (2013) 28845.
- M.Elahi, M.M.Islam, K.Noguchi, M.Yohda and Y.Kuroda
High Resolution Crystal Structure of Dengue-3 Envelope Protein Domain III Suggests Possible Molecular Mechanisms for Serospecific Antibody Recognition
Proteins, **81** (2013) 1090.
- J.-H.Ha, Y.Eo, A.Grishaev, M.Guo, J.A.I.Smith, H.O.Sintim, E.-H.Kim, H.-K.Cheong, W.E.Bentley and K.-S.Ryu
Crystal Structures of the LsrR Proteins Complexed with Phospho-AI-2 and Two Signal-Interrupting Analogues Reveal Distinct Mechanisms for Ligand Recognition
J. Am. Chem. Soc., **135** (2013) 15526.
- Y.K.Kim, M.-J.Kwak, B.Ku, H.-Y.Suh, K.Joo, J.Lee, J.U.Jung and B.-H.Oh
Structural Basis of Intersubunit Recognition in Elongin BC-Cullin 5-SOCS Box Ubiquitin-Protein Ligase Complexes
Acta Cryst. D, **69** (2013) 1587.
- T.Nishiyama, H.Noguchi, H.Yoshida, S.-Y.Park and J.R.H.Tame
The Structure of the Deacetylase Domain of *Escherichia coli* PgaB, an Enzyme Required for Biofilm Formation: a Circularly Permuted Member of the Carbohydrate Esterase 4 Family
Acta Cryst. D, **69** (2013) 44.
- Y.Itoh, M.J. Bröcker, S.Sekine, G.Hammond, S.Suetsugu, D.Söll and S.Yokoyama
Decameric SelA-tRNA^{Sec} Ring Structure Reveals Mechanism of Bacterial Selenocysteine Formation
Science, **340** (2013) 75.
- J.Son, E.H.Lee, M.Park, J.H.Kim, J.Kim, S.Kim, Y.H.Jeond and K.Y.Hwang
Conformational Changes in Human Prolyl-tRNA Synthetase upon Binding of the Substrates Proline and ATP and the Inhibitor Halofuginone
Acta Cryst. D, **69** (2013) 2136.
- E.Kim, H.-C.Lu, H.Y.Zoghbi and J.-J.Song
Structural Basis of Protein Complex Formation and Reconfiguration by Polyglutamine Disease Protein Ataxin-1 and Capicua
Genes and Development, **27** (2013) 590.
- H.Zhou, Y.Sun, Y.Wang, M.Liu, C.Liu, W.Wang, X.Liu, L.Li, F.Deng, H.Wang, Y.Guo and Z.Lou
The Nucleoprotein of Severe Fever with Thrombocytopenia Syndrome Virus Processes a Stable Hexameric Ring to Facilitate RNA Encapsidation
Protein and Cell, **4** (2013) 445.
- T.Wang, J.Ding, Y.Zhang, D.-C.Wang and W.Liu
Complex Structure of Type VI Peptidoglycan Muramidase Effector and a Cognate Immunity Protein
Acta Cryst. D, **69** (2013) 1889.
- S.Sugiyama, N.Shimizu, G.Sazaki, M.Hirose, Y.Takahashi, M.Maruyama, H.Matsumura, H.Adachi, K.Takano, S.Murakami, T.Inoue and Y.Mori
A Novel Approach for Protein Crystallization by a Synthetic Hydrogel with Thermoreversible Gelation Polymer
Cryst. Growth Des., **13** (2013) 1899.
- J.Hwang, B.S.Kim, S.Y.Jang, J.G.Lim, D.-J.You, H.S.Jung, T.-K.Oh, J.-O.Lee, S.H.Choi and M.H.Kim
Structural Insights into the Regulation of Sialic Acid Catabolism by the *Vibrio vulnificus* Transcriptional Repressor NanR
Proc. Natl. Acad. Sci. USA, **110** (2013) E2829.
- Y.Hou, D.-F.Li and D.-C.Wang
Crystallization and Preliminary X-Ray Analysis of the Flagellar Motor 'Brake' Molecule YcgR with c-di-GMP from *Escherichia coli*
Acta Cryst. F, **69** (2013) 663.
- K.J.Yeo, Y.-H.Han, Y.Eo and H.-K.Cheong
Expression, Purification, Crystallization and Preliminary X-Ray Analysis of the Extracellular Sensory Domain of DraK Histidine Kinase from *Streptomyces Coelicolor*
Acta Cryst. F, **69** (2013) 909.
- L.-J.Yu, M.Unno, Y.Kimura, K.Yanagimoto, H.Oh-oka, Z.-Y.Wang-Otomo
Structure Analysis and Characterization of the cytochrome c-554 from Thermophilic Green Sulfur Photosynthetic Bacterium *Chlorobaculum tepidum*
Photosynthesis Research, **118** (2013) 249.
- T.Miyakawa, Y.Sawano, K.Miyazono, Y.Miyauchi, K.Hatano and M.Tanokura
A Thermoacidophile-Specific Protein Family, DUF3211, Functions as a Fatty Acid Carrier with Novel Binding Mode
J. Bacteriol., **195** (2013) 4005.

- F.Zhang, M.Tsunoda, K.Suzuki, Y.Kikuchi, O.Wilkinson, C.L.Millington, G.P.Margison, D.M.Williams, E.C.Morishita and A.Takenaka
Structures of DNA Duplexes Containing O⁶-Carboxymethylguanine, a Lesion Associated with Gastrointestinal Cancer, Reveal a Mechanism for Inducing Pyrimidine Transition Mutations
Nucl. Acids Res., **41** (2013) 5524.
- S.Aizawa, M.Senda, A.Harada, N.Maruyama, T.Ishida, T.Aigaki, A.Ishigami and T.Senda
Structural Basis of the γ -Lactone-Ring Formation in Ascorbic Acid Biosynthesis by the Senescence Marker Protein-30/Gluconolactonase
PLoS One, **8** (2013) e53706.
- Y.Yamada, L.M.G.Chavas, N.Igarashi, M.Hiraki, S.Wakatsuki and N.Matsugaki
Improvements toward Highly Accurate Diffraction Experiments at the Macromolecular Micro-Crystallography Beamline BL-17A
J. Synchrotron Rad., **20** (2013) 938.
- X.Xu, X.Wang, Y.Zhang, D.C.Wang and J.Ding
Structural Basis for the Unique Heterodimeric Assembly between Cerebral Cavernous Malformation 3 and Germinal Center Kinase III
Structure, **21** (2013) 1059.
- A.Furukawa, J.Kamishikiryo, D.Mori, K.Toyonaga, Y.Okabe, A.Toji, R.Kanda, Y.Miyake, T.Ose, S.Yamasaki and K.Maenaka
Structural Analysis for Glycolipid Recognition by the C-Type Lectins Mincle and MCL
Proc. Natl. Acad. Sci. USA, **110** (2013) 17438.
- Y.Zhang, L.Li, X.Liu, S.Dong, W.Wang, T.Huo, Y.Guo, Z.Rao and C.Yang
Crystal Structure of Junin Virus Nucleoprotein
J Gen Virol., **94** (2013) 2175.
- M.-K.Kim, Y.J.An, C.-S.Jeong, J.M.Song, M.H.Kang, Y.-H.Lee and S.-S.Cha
Expression at 279 K, Purification, Crystallization and Preliminary X-Ray Crystallographic Analysis of a Novel Cold-Active β -1,4-D-Mannanase from the Antarctic Springtail *Cryptopygus antarcticus*
Acta Cryst. F, **69** (2013) 1007.
- S.-S.Cha, Y.J.An, C.-S.Jeong, M.-K.Kim, J.H.Jeon, C.-M.Lee, H.S.Lee, S.G.Kang and J.-H.Lee
Structural Basis for the β -Lactamase Activity of EstU1, a Family VIII Carboxylesterase
Proteins, **81** (2013) 2045.
- M.-K.Kim, Y.J.An and S.-S.Cha
The Crystal Structure of a Novel Phosphopantothenate Synthetase from the Hyperthermophilic Archaea, *Thermococcus onnurineus* NA1
Biochemical and Biophysical Research Communications, **439** (2013) 533.
- T.Ohnuma, N.Umemoto, T.Taira, T.Fukamizo and T.Numata
Crystallization and Preliminary X-Ray Diffraction Analysis of an Active-Site Mutant of 'Loopless' Family GH19 Chitinase from *Bryum coronatum* in a Complex with Chitotetraose
Acta Cryst. F, **69** (2013) 1360.
- T.Ohnuma, N.Umemoto, K.Kondo, T.Numata and T.Fukamizo
Complete Subsite Mapping of a Loopful GH19 Chitinase from Rye Seeds based on its Crystal Structure
FEBS Letters, **587** (2013) 2691.
- M.Ogata, N.Umemoto, T.Ohnuma, T.Numata, A.Suzuki, T.Usui and T.Fukamizo
A Novel Transition-State Analogue for Lysozyme, 4-O- β -Tri-N-Acetylchitotriosyl Moranoline, Provided Evidence Supporting the Covalent Glycosyl-Enzyme Intermediate
J. Biol. Chem., **288** (2013) 6072.
- S.Hu, S.Liang, H.Guo, D.Zhang, H.Li, X.Wang, W.Yang, W.Qian, S.Hou, H.Wang, Y.Guo and Z.Lou
Comparison of the Inhibition Mechanisms of Adalimumab and Infliximab in Treating Tumor Necrosis Factor α -Associated Diseases from a Molecular View
J. Biol. Chem., **288** (2013) 27059.
- S.Liang, J.Dai, S.Hou, L.Su, D.Zhang, H.Guo, S.Hu, H.Wang, Z.Rao, Y.Guo and Z.Lou
Structural Basis for Treating Tumor Necrosis Factor α (TNF α)-Associated Diseases with the Therapeutic Antibody Infliximab
J. Biol. Chem., **288** (2013) 13799.

18A

- A.Tosaka, I.Mochizuki, R.Negishi and Y.Shigeta
Strain Induced Intermixing of Ge Atoms in Si Epitaxial Layer on Ge(111)
J. Appl. Phys., **113** (2013) 073511.

- R.Friedlein, A.Fleurence, J.T.Sadowski and Y.Yamada-Takamura
Tuning of Silicene-Substrate Interactions with Potassium Adsorption
Appl. Phys. Lett., **102** (2013) 221603.

18B

- S.Chandran, J.K.Basu and M.K.Mukhopadhyay
Variation in Glass Transition Temperature of Polymer Nanocomposite Films Driven by Morphological Transitions
J. Chem. Phys., **138** (2013) 014902.

- U.Subbarao, A.Sebastian, S.Rayaprol, C.S.Yadav, A.Svane, G.Vaitheeswaran and S.C.Peter
Metal Flux Crystal Growth Technique in the Determination of Ordered Superstructure in EuInGe
Crystal Growth and Design, **13** (2013) 352.

H.-S.Youn, M.-K.Kim, G.B.Kang, T.G.Ki, J.-G.Lee, J.Y.An, K.R.Park, Y.Lee, J.Y.Kang, H.-E.Song, I.Park, C.Cho, S.Fukuoka, S.H.Eom
Crystal Structure of *Sus scrofa* Quinolate Phosphoribosyltransferase in Complex with Nicotinate Mononucleotide
PLoS ONE, **8** (2013) e62027.

S.Fushinobu, V.D.Alves and P.M.Coutinho
Multiple Rewards from a Treasure Trove of Novel Glycoside Hydrolase and Polysaccharide Lyase Structures: New Folds, Mechanistic Details, and Evolutionary Relationships
Curr. Opin. Struct. Biol., **23** (2013) 652.

Z.Fujimoto
Structure and Function of Carbohydrate-Binding Module Families 13 and 42 of Glycoside Hydrolases, Comprising a β -Trefoil Fold
Biosci. Biotechnol. Biochem., **77** (2013) 1363.

S.Gayen, M.K.Sanyal, B.Satpati, A.Rahman
Diameter-Dependent Coercivity of Cobalt Nanowires
Appl. Phys. A, **112** (2013) 775.

K.Malik, D.Das, S.Bandyopadhyay, P.Mandal, A.K.Deb, V.Srihari and A.Banerjee
Temperature-Dependent Structural Property and Power Factor of n Type Thermoelectric Bi_{0.90}Sb_{0.10} and Bi_{0.86}Sb_{0.14} Alloys
Appl. Phys. Lett., **103** (2013) 242108.

D.Maiti, U.Manju, S.Velaga and P.S.Devi
Phase Evolution and Growth of Iron Oxide Nanoparticles: Effect of Hydrazine Addition during Sonication
Appl. Catal. B, **13** (2013) 3637.

S.M.Amir, M.Gupta, S.Potdar, A.Gupta and J.Stahn
Study of Surfactant Mediated Growth of Ni/V Superlattices
J. Appl. Phys., **114** (2013) 024307.

18C

Y.Yoshimura, H.Abe, Y.Imai, T.Takekiyo and N.Hamaya
Decompression-Induced Crystal Polymorphism in a Room-Temperature Ionic Liquid, *N,N*-Diethyl-*N*-Methyl-*N*-(2-methoxyethyl) Ammonium Tetrafluoroborate
J. Phys. Chem. B, **117** (2013) 3264.

T.Sato, H.Takada, T.Yagi, H.Gotou, T.Okada, D.Wakabayashi and N.Funamori
Anomalous Behavior of Cristobalite in Helium under High Pressure
Phys. Chem. Minerals, **40** (2013) 3.

T.Matsushita, Y.Ishii and S.Kawasaki
Sodium Ion Battery Anode Properties of Empty and C₆₀-Inserted Single-Walled Carbon Nanotubes
Materials Express, **3** (2013) 30.

H.Song, Y.Ishii, A.Al-Zubaidi, T.Sakai and S.Kawasaki
Temperature-Dependent Water Solubility of Iodine-Doped Single-Walled Carbon Nanotubes Prepared using an Electrochemical Method
Phys. Chem. Chem. Phys., **15** (2013) 5767.

Y.Yoshimura, H.Abe, T.Takekiyo, M.Shigemi, N.Hamaya, R.Wada and M.Kato
Superpressing of a Room Temperature Ionic Liquid, 1-Ethyl-3-Methylimidazolium Tetrafluoroborate
J. Phys. Chem. B, **117** (2013) 12296.

T.Sato, N.Funamori and T.Yagi
Differential Strain and Residual Anisotropy in Silica Glass
J. Appl. Phys., **114** (2013) 103509.

A.Shinozaki, H.Hirai, H.Ohfuji, T.Okada, S.Machida and T.Yagi
Influence of H₂ Fluid on the Stability and Dissolution of Mg₂SiO₄ Forsterite under High Pressure and High Temperature
American Mineralogist, **98** (2013) 1604.

T.Tanaka, H.Hirai, T.Matsuoka, Y.Ohishi, T.Yagi, M.Ohtake, Y.Yamamoto, S.Nakano and T.Irifune
Phase Changes of Filled Ice Ih Methane Hydrate under Low Temperature and High Pressure
J. Chem. Phys., **139** (2013) 104701.

19A

T.Kinoshita, K.Arai, K.Fukumoto, T.Ohkochi, M.Kotsugi, F.Guo, T.Muro, T.Nakamura, H.Osawa, T.Matsushita and T.Okuda
Observation of Micro-Magnetic Structures by Synchrotron Radiation Photoelectron Emission Microscopy
J. Phys. Soc. Jpn., **82** (2013) 021005.

K.Yaji, I.Mochizuki, S.Kim, Y.Takeichi, A.Harasawa, Y.Ohtsubo, P.Le F'evre, F.Bertran, A.Taleb-Ibrahimi, A.Kakizaki and F.Komori
Fermi Gas Behavior of a One-Dimensional Metallic Band of Pt-Induced Nanowires on Ge(001)
Phys. Rev. B, **87** (2013) 241413.

19B

T.Hayashi, H.Shibata, S.Orita and T.Akitsu
Variety of Structures of Binuclear Chiral Schiff Base Ce(III)/Pr(III)/Lu(III)-Ni(II)/Cu(II)/Zn(II) Complexes
Eur. Chem. Bull., **2** (2013) 49.

N.Hayashi and T.Akitsu
Anisotropic Thermally-Accessible Lattice Distortion of a Cu(II)-Cr(VI) Complex Bimetallic Oxide by Adsorbing a Chiral One-Dimensional Cu(II)-Cr(VI) Coordination Polymer
J. Chem. Chem. Eng., **7** (2013) 306.

T.Tsuchiya, S.Miyoshi, Y.Yamashita, H.Yoshikawa, K.Terabe, K.Kobayashi and S.Yamaguchi
Room Temperature Redox Reaction by Oxide Ion Migration at Carbon/Gd-Doped CeO₂ Heterointerface Probed by an *in situ* Hard X-Ray Photoemission and Soft X-Ray Absorption Spectroscopies
Sci. Technol. Adv. Mater., **14** (2013) 045001.

20A

Y.Kumagai, T.Odagiri, M.Nakano, T.Tanabe, I.H.Suzuki, K.Hosaka, M.Kitajima and N.Kouchi
Cross Sections for the Formation of H(*n* = 2) Atom via Superexcited States in Photoexcitation of Methane and Ammonia
J. Chem. Phys., **139** (2013) 164307.

20B

L.E.Wedlock, J.B.Aitken, S.J.Berners-Price and P.J.Barnard
Bromide Ion Binding by a Dinuclear Gold(I) *N*-Heterocyclic Carbene Complex: a Spectrofluorescence and X-Ray Absorption Spectroscopic Study
Dalton Trans., **42** (2013) 1259.

B.Tooth, B.Etschmann, G.S.Pokrovski, D.Testemale, J.L.Hazemann, P.V.Grundler and J.Brugger
Bismuth Speciation in Hydrothermal Fluids: An X-Ray Absorption Spectroscopy and Solubility Study
Geochim. Cosmochim. Acta, **101** (2013) 156.

EM.Likosova, RN.Collins, J.Keller and S.Freguia
Anodic Reactivity of Ferrous Sulfide Precipitates Changing over Time due to Particulate Speciation
Environ. Sci. Technol., **47** (2013) 12366.

R.He, R.K.Hocking and T.Tsuzuki
Local Structure and Photocatalytic Property of Mechanochemical Synthesized ZnO Doped with Transition Metal Oxides
Journal of the Australian Ceramic Society, **49** (2013) 76.

D.P.Anderson, R.H.Adnan, J.F.Alvino, O.Shipper, B.Donoeva, J.-Y.Ruzicka, H.A.Qahtani, H.H.Harris, B.Cowie, J.B.Aitken, V.B.Golovko, G.F.Metha and G.G.Andersson
Chemically Synthesised Atomically Precise Gold Clusters Deposited and Activated on Titania. Part II
Phys. Chem. Chem. Phys., **15** (2013) 14806.

R.Tian, R.Donelson, C.D.Ling, P.E.R.Blanchard, T.Zhang, D.Chu, T.T.Tan and S.Li
Ga Substitution and Oxygen Diffusion Kinetics in Ca₃Co₄O_{9+δ}-Based Thermoelectric Oxides
J. Phys. Chem. C, **117** (2013) 13382.

LE.Wedlock, JB.Aitken, SJ.Berners-Price and PJ.Barnard
Bromide Ion Binding by a Dinuclear Gold(I) *N*-Heterocyclic Carbene Complex: a Spectrofluorescence and X-Ray Absorption Spectroscopic Study
Dalton Transactions, **42** (2013) 1259.

T.D.Keene, D.Rankine, J.D.Evans, P.D.Southon, C.J.Kepert, J.B.Aitken, C.J.Sumby and C.J.Doonan
Solvent-Modified Dynamic Porosity in Chiral 3D Kagome Frameworks
Dalton Transactions, **42** (2013) 7871.

M.Fekete, R.K.Hocking, S.L.Y.Chang, C.Italiano, A.F.Patti, F.Arena and L.Spaccia
Highly Active Screen-Printed Electrocatalysts for Water Oxidation Based on β-Manganese Oxide
Energy Environ. Sci., **6** (2013) 2222.

C.K.J.Chen, J.Z.Zhang, J.B.Aitken and T.W.Hambley
Influence of Equatorial and Axial Carboxylato Ligands on the Kinetic Inertness of Platinum(IV) Complexes in the Presence of Ascorbate and Cysteine and within DLD-1 Cancer Cells
J. Med. Chem., **56** (2013) 8757.

Y.Yang, W.Liu and M.Chen
A Copper and Iron *K*-Edge XANES Study on Chalcopyrite Leached by Mesophiles and Moderate Thermophiles
Minerals Engineering, **48** (2013) 31.

27A

Y.Baba, T.Sekiguchi, I.Shimoyama and N.Hirao
Electronic Structures of Silicon Monoxide Film Probed by X-Ray Absorption Spectroscopy
Surf. Sci., **612** (2013) 77.

R.Shinoda, M.Itou, Y.Sakurai, H.Yamamoto, N.Hirao, Y.Baba, A.Iwase and T.Matsui
Magnetic Compton Scattering Studies of Magneto-Dielectric Ba(Co_{0.85}Mn_{0.15})O_{3-δ}
J. Appl. Phys., **113** (2013) 17E307.

Md.A.Mannan, Y.Baba, N.Hirao, T.Kida, M.Nagano and H.Noguchi
Hexagonal Nano-Crystalline BCN Films Grown on Si (100) Substrate Studied by X-Ray Absorption Spectroscopy
Mater. Sci. Appl., **4** (2013) 11.

M.Honda, M.Yanagida and L.Han
Effect of Co-Adsorption Dye on the Electrode Interface (Ru Complex/TiO₂) of Dye-Sensitized Solar Cells
AIP Advances, **3** (2013) 072113.

M.Honda, M.Yanagida, L.Han and K.Miyano
X-Ray Characterization of Dye Adsorption in Coadsorbed Dye-Sensitized Solar Cells
J. Phys. Chem. C, **117** (2013) 17033.

S.Ishiyama, Y.Baba, R.Fujii, M.Nakamura and Y.Imahori
Direct Synthesis of Li₃N Thin Layer on Lithium Target Surface for BNCT in N₂ Gaseous Conditions
Materials Transactions, **54** (2013) 1765.

S.Ishiyama, Y.Baba, R.Fujii, M.Nakamura and Y.Imahori
Thermal Stability of BNCT Neutron Production Target Synthesized *In-Situ* Lithium Deposition and Ion Implantation
Materials Transactions, **54** (2013) 1760.

27B

N.Autsavapromporn, M.Suzuki, T.Funayama, N.Usami, I.Plante, Y.Yokota, Y.Mutou, H.Ikeda, K.Kobayashi, Y.Kobayashi, Y.Uchihori, T.K.Hei, E.I.Azzam and T.Murakami
Gap Junction Communication and the Propagation of Bystander Effects Induced by Microbeams Irradiation in Human Fibroblast Cultures: The Impact of Radiation Quality
Radiation Research, **180** (2013) 367.

M.Maeda, K.Kobayashi, H.Matsumoto, N.Usami and M.Tomita
X-Ray-Induced Bystander Responses Reduce Spontaneous Mutations in V79 Cells
J. Radiat. Res., **54** (2013) 1043.

T.Ozaki, X.Wang and T.Ohnuki
Manganese and Arsenic Oxidation Performance of Bacterium-Yunotaki 86(BY86) from Hokkaido, Japan, and the Bacterium's Phylogeny
Geomicrobiol. J., **30** (2013) 559.

28A

T.Kinoshita, K.Arai, K.Fukumoto, T.Ohkochi, M.Kotsugi, F.Guo, T.Muro, T.Nakamura, H.Osawa, T.Matsushita and T.Okuda
Observation of Micro-Magnetic Structures by Synchrotron Radiation Photoelectron Emission Microscopy
J. Phys. Soc. Jpn., **82** (2013) 021005.

S.Ideta, T.Yoshida, I.Nishi, A.Fujimori, Y.Kotani, K.Ono, Y.Nakashima, S.Yamaichi, T.Sasagawa, M.Nakajima, K.Kihou, Y.Tomioka, C.H.Lee, A.Iyo, H.Eisaki, T.Ito, S.Uchida and R.Arita
Dependence of Carrier Doping on the Impurity Potential in Transition-Metal-Substituted FeAs-Based Superconductors
Phys. Rev. Lett., **110** (2013) 107007.

Y.Tanaka, T.Sato, K.Nakayama, S.Souma, T.Takahashi, Z.Ren, M.Novak, K.Segawa and Y.Ando
Tunability of the *k*-Space Location of the Dirac Cones in the Topological Crystalline Insulator $Pb_{1-x}Sn_xTe$
Phys. Rev. B, **87** (2013) 155105.

T.Okuda, R.Kajimoto, M.Okawa and T.Saitoh
Effects of Hole-Doping and Disorder on the Magnetic States of Delafossite $CuCrO_2$ Having a Spin-3/2 Antiferromagnetic Triangular Sublattice
Int. J. Mod. Phys. B, **27** (2013) 1330002.

S.Ideta, T.Yoshida, M.Nakajima, W.Malaeb, T.Shimajima, K.Ishizaka, A.Fujimori, H.Kumigashira, K.Ono, K.Kihou, Y.Tomioka, C.H.Lee, A.Iyo, H.Eisaki, T.Ito and S.Uchida
Effects of Zn Substitution on the Electronic Structure of $BaFe_2As_2$ Revealed by Angle-Resolved Photoemission Spectroscopy
Phys. Rev. B, **87** (2013) 201110.

T.Yokobori, M.Okawa, K.Konishi, R.Takei, K.Katayama, S.Oozono, T.Shinmura, T.Okuda, H.Wadati, E.Sakai, K.Ono, H.Kumigashira, M.Oshima, T.Sugiyama, E.Ikenaga, N.Hamada and T.Saitoh
Electronic Structure of Hole-Doped Delafossite Oxides $CuCr_{1-x}Mg_xO_2$
Phys. Rev. B, **87** (2013) 195124.

K.Tsubota, T.Wakita, H.Nagao, C.Hiramatsu, T.Ishiga, M.Sunagawa, K.Ono, H.Kumigashira, M.Danura, K.Kudo, M.Nohara, Y.Muraoka and T.Yokoya
Collapsed Tetragonal Phase Transition of $Ca(Fe_{1-x}Rh_x)_2As_2$ Studied by Photoemission Spectroscopy
J. Phys. Soc. Jpn., **82** (2013) 073705.

K.Yoshimatsu, E.Sakai, M.Kobayashi, K.Horiba, T.Yoshida, A.Fujimori, M.Oshima and H.Kumigashira
Determination of the Surface and Interface Phase Shifts in Metallic Quantum Well Structures of Perovskite Oxides
Phys. Rev. B, **88** (2013) 115308.

H.Suzuki, T.Yoshida, S.Ideta, G.Shibata, K.Ishigami, T.Kadono, A.Fujimori, M.Hashimoto, D.H.Lu, Z.-X.Shen, K.Ono, E.Sakai, H.Kumigashira, M.Matsuo and T.Sasagawa
Absence of Superconductivity in the Hole-Doped Fe Pnictide $Ba(Fe_{1-x}Mn_x)_2As_2$: Photoemission and X-Ray Absorption Spectroscopy Studies
Phys. Rev. B, **88** (2013) 100501.

T.Sato, Y.Tanaka, K.Nakayama, S.Souma, T.Takahashi, S.Sasaki, Z.Ren, A.A.Taskin, K.Segawa and Y.Ando
Fermiology of the Strongly Spin-Orbit Coupled Superconductor $Sn_{1-x}In_xTe$: Implications for Topological Superconductivity
Phys. Rev. Lett., **110** (2013) 206804.

Y.Tanaka, T.Shoman, K.Nakayama, S.Souma, T.Sato, T.Takahashi, M.Novak, K.Segawa and Y.Ando
Two Types of Dirac-Cone Surface States on the (111) Surface of the Topological Crystalline Insulator $SnTe$
Phys. Rev. B, **88** (2013) 235126.

M.Sakano, M.S.Bahramy, A.Katayama, T.Shimajima, H.Murakawa, Y.Kaneko, W.Malaeb, S.Shin, K.Ono, H.Kumigashira, R.Arita, N.Nagaosa, H.Y.Hwang, Y.Tokura and K.Ishizaka
Strongly Spin-Orbit Coupled Two-Dimensional Electron Gas Emerging near the Surface of Polar Semiconductors
Phys. Rev. Lett., **110** (2013) 107204.

NE1A

S.Ono

Equation of State and Elasticity of B2-Type FeSi: Implications for Silicon in the Inner Core
Phys. Earth Planet. Inter., **224** (2013) 32.

R.Iizuka, T.Yagi, K.Komatsu, H.Gotou, T.Tsuchiya, K.Kusaba and H.Kagi
Crystal Structure of the High-Pressure Phase of Calcium Hydroxide, Portlandite: In Situ Powder and Single-Crystal X-Ray Diffraction Study
American Mineralogist, **98** (2013) 1421.

D.Nishio-Hamane, N.Tomita, T.Minakawa and S.Inaba
Iseite, $Mn_2Mo_3O_8$, a New Mineral from Ise, Mie Prefecture, Japan
Journal of Mineralogical and Petrological Sciences, **108** (2013) 37.

M.Ohnishi, N.Shimobayashi, D.Nishio-Hamane, K.Shinoda, K.Momma and T.Ikeda
Minohlite, a New Copper-Zinc Sulfate Mineral from Minoh, Osaka, Japan
Mineralogical Magazine, **77** (2013) 335.

D.Nishio-Hamane, T.Minakawa and Y.Ohgoshi
Takanawaite-(Y), a New Mineral of the M-Type Polymorph with $Y(Ta,Nb)O_4$ from Takanawa Mountain, Ehime Prefecture, Japan
Journal of Mineralogical and Petrological Sciences, **108** (2013) 335.

K.Niwa, T.Tanaka, M.Hasegawa, T.Okada, T.Yagi and K.Kikegawa
Pressure-Induced Noble Gas Insertion into Linde-Type A Zeolite and its Incompressible Behaviors at High Pressure
Micropor. Mesopor. Mater., **182** (2013) 191.

NE3A

K.Yoneda, H.Sakuraba, T.Araki, T.Shibata, T.Nikki, and T.Ohshima
Crystallization and Preliminary X-Ray Analysis of L-Serine 3-Dehydrogenase Complexed with $NADP^+$ from the Hyperthermophilic Archaeon *Pyrobaculum calidifontis*
Acta Cryst. F, **69** (2013) 134.

S.Arai, S.Saijo, K.Suzuki, K.Mizutani, Y.Kakinuma, Y.Ishizuka-Katsura, N.Ohsawa, T.Terada, M.Shirouzu, S.Yokoyama, S.Iwata, I.Yamato and T.Murata
Rotation Mechanism of *Enterococcus hirae* V_1 -ATPase Based on Asymmetric Crystal Structures
Nature, **493** (2013) 703.

H.Tanji, U.Ohto, T.Shibata, K.Miyake and T.Shimizu
Structural Reorganization of the Toll-Like Receptor 8 Dimer Induced by Agonistic Ligands
Science, **339** (2013) 1426.

Y.Murayama, S.Sekine and S.Yokoyama
Crystallization and Preliminary X-Ray Crystallographic Analyses of *Thermus thermophilus* Backtracked RNA Polymerase
Acta Cryst. F, **69** (2013) 174.

J.Otani, K.Arita, T.Kato, M.Kinoshita, H.Kimura, I.Suetake, S.Tajima, M.Ariyoshi and M.Shirakawa
Structural Basis of the Versatile DNA Recognition Ability of the Methyl-CpG Binding Domain of Methyl-CpG Binding Domain Protein 4
J. Biol. Chem., **288** (2013) 6351.

H.S.Kim, J.Kim, H.N.Im, J.Y.Yoon, D.R.An, H.J.Yoon, J.Y.Kim, H.K.Min, S.J.Kim, J.Y.Lee, B.W.Han, and S.W.Suh
Structural Basis for the Inhibition of *Mycobacterium tuberculosis* L,D-Transpeptidase by Meropenem, a Drug Effective against Extensively Drug-Resistant Strains
Acta Cryst. D, **69** (2013) 420.

Z.Fujimoto, R.Suzuki, T.Shiotsuki, W.Tsuchiya, A.Tase, M.Momma and T.Yamazaki
Crystal Structure of Silkworm *Bombyx mori* JHBP in Complex with 2-Methyl-2,4-Pentanediol: Plasticity of JH-Binding Pocket and Ligand-Induced Conformational Change of the Second Cavity in JHBP
PLoS One, **8** (2013) e56261.

T.Ouchi, T.Tomita, A.Horie, A.Yoshida, K.Takahashi, H.Nishida, K.Lassak, H.Taka, R.Mineki, T.Fujimura, S.Kosono, C.Nishiyama, R.Masui, S.Kuramitsu, S.-V.Albers, T.Kuzuyama and M.Nishiyama
Lysine and Arginine Biosyntheses Mediated by a Common Carrier Protein in *Sulfolobus*
Nature Chemical Biology, **9** (2013) 277.

Q.Zhang, S.Qi, M.Xu, L.Yu, Y.Tao, Z.Deng, W.Wu, J.Li, Z.Chen and J.Wong
Structure-Function Analysis Reveals a Novel Mechanism for Regulation of Histone Demethylase LSD2/AOF1/KDM1b
Cell Res., **23** (2013) 225.

T.Miyafusa, J.M.M.Caaveiro, Y.Tanaka, M.E.Tanner and K.Tsumoto
Crystal Structure of the Capsular Polysaccharide Synthesizing Protein CapE of *Staphylococcus aureus*
Biosci. Rep., **33** (2013) 463.

N.T.Vu, Y.Moriwaki, J.M.M.Caaveiro, T.Terada, H.Tsutsumi, I.Hamachi, K.Shimizu and K.Tsumoto
Selective Binding of Antimicrobial Porphyrins to the Heme-Receptor IsdH-NEAT3 of *Staphylococcus aureus*
Protein Science, **22** (2013) 942.

Y.Chiba, S.Horita, J.Ohtsuka, H.Arai, K.Nagata, Y.Igarashi, M.Tanokura and M.Ishii
Structural Units Important for Activity of a Novel-Type Phosphoserine Phosphatase from *Hydrogenobacter thermophilus* TK-6 Revealed by Crystal Structure Analysis
J. Biol. Chem., **288** (2013) 11448.

- T.Miyazaki, A.Nishikawa and T.Tonozuka
Novel Findings of the Structure and Substrate Specificity of Glucosidases Belonging to Glycoside Hydrolase Family 63
Oyo Toshitsu Kagaku, **3** (2013) 151. (*in Japanese*).
- T.Arimori, N.Kawamoto, S.Shinya, N.Okazaki, M.Nakazawa, K.Miyatake, T.Fukamizo, M.Ueda and T.Tamada
Crystal Structures of the Catalytic Domain of a Novel Glycohydrolase Family 23 Chitinase from *Ralstonia* sp. A-471 Reveals a Unique Arrangement of the Catalytic Residues for Inverting Chitin Hydrolysis
J. Biol. Chem., **288** (2013) 18696.
- Y.Nagamatsu, K.Takeda, T.Kuranaga, N.Numoto and K.Miki
Origin of Asymmetry on the Intersubunit Interfaces of V₁-ATPase from *Thermus thermophilus*
J. Mol. Biol., **425** (2013) 2699.
- Y.Nishitani, R.Aono, A.Nakamura, T.Sato, H.Atomi, T.Imanaka and K.Miki
Structure Analysis of Archaeal AMP Phosphorylase Reveals Two Unique Modes of Dimerization
J. Mol. Biol., **425** (2013) 2709.
- J.-H.Liao, K.Ihara, C.-I.Kuo, K.-F.Huang, S.Wakatsuki, S.-H.Wu and C.-I.Chang
Structures of an ATP-Independent Lon-Like Protease and its Complexes with Covalent Inhibitors
Acta Cryst. D, **69** (2013) 1395.
- G.Lu, Y.Hu, Q.Wang, J.Qi, F.Gao, Y.Li, Y.Zhang, W.Zhang, Y.Yuan, J.Bao, B.Zhang, Y.Shi, J.Yan and G.F.Gao
Molecular Basis of Binding between Novel Human Coronavirus MERS-CoV and its Receptor CD26
Nature, **500** (2013) 227.
- T.Hirose, N.Maita, H.Gouda, J.Koseki, T.Yamamoto, A.Sugawara, H.Nakano, S.Hirono, K.Shioimi, T.Watanabe, H.Taniguchi, K.B.Sharpless, S.Omura and T.Sunazuka
Observation of the Controlled Assembly of Preclick Components in the in situ Click Chemistry Generation of a Chitinase Inhibitor
Proc. Natl. Acad. Sci. USA, **110** (2013) 15892.
- T.Kinoshita, T.Nakaniwa, Y.Sekiguchi, Y.Sogabe, A.Sakurai, S.Nakamura and I.Nakanishi
Crystal Structure of Human CK2 α at 1.06 Å Resolution
J. Synchrotron Rad., **20** (2013) 974.
- A.Nakamura, T.Ishida, S.Fushinobu, K.Kusaka, I.Tanaka, K.Inaka, Y.Higuchi, M.Masaki, K.Ohta, S.Kaneko, N.Niimura, K.Igarashi and M.Samajima
Phase-Diagram-Guided Method for Growth of a Large Crystal of Glycoside Hydrolase Family 45 Inverting Cellulase Suitable for Neutron Structural Analysis
J. Synchrotron Rad., **20** (2013) 859.
- S.Fushinobu, V.D.Alves and P.M.Coutinho
Multiple Rewards from a Treasure Trove of Novel Glycoside Hydrolase and Polysaccharide Lyase Structures: New Folds, Mechanistic Details, and Evolutionary Relationships
Curr. Opin. Struct. Biol., **23** (2013) 652.
- K.Suzuki, J.Sumitani, Y-W.Nam, T.Nishimaki, S.Tani, T.Wakagi, T.Kawaguchi and S.Fushinobu
Crystal Structures of Glycoside Hydrolase Family 3 β -Glucosidase 1 from *Aspergillus aculeatus*
Biochem. J., **452** (2013) 211.
- H.Nakamura, Y.L.Xue, T.Miyakawa, F.Hou, H.M.Qin, K.Fukui, X.Shi, E.Ito, S.H.Park, Y.Miyauchi, A.Asano, N.Totsuka, T.Ueda, M.Tanokura and T.Asami
Molecular Mechanism of Strigolactone Perception by DWARF14
Nature Commun., **4** (2013) 3613.
- Y.Yasutake, T.Nishioka, N.Imoto and T.Tamura
A Single Mutation at the Ferredoxin Binding Site of P450 Vdh Enables Efficient Biocatalytic Production of 25-Hydroxyvitamin D₃
ChemBioChem, **14** (2013) 2284.
- Y.Kanemaru, F.Hasebe, T.Tomita, T.Kuzuyama and M.Nishiyama
Two ATP-Binding Cassette Transporters Involved in (*S*)-2-Aminoethyl-Cysteine Uptake in *Thermus thermophilus*
J. Bacteriology, **195** (2013) 3845.
- X.Zhang, L.Jiang, G.Wang, L.Yu, Q.Zhang, Q.Xin, W.Wu, Z.Gong and Z.Chen
Structural Insights into the Abscisic Acid Stereospecificity by the ABA Receptors PYR/PYL/RCAR
PLOS ONE, **8** (2013) e67477.
- P.Zhou, Z.Chen, Q.Yan, S.Yang, R.Hilgenfeld and Z.Jiang
The Structure of a Glycoside Hydrolase Family 81 Endo- β -1, 3-Glucanase
Acta Cryst. D, **69** (2013) 2027.
- X.Chu, X.Qin, H.Xu, L.Li, Z.Wang, F.Li, X.Xie, H.Zhou, Y.Shen and J.Long
Structural Insights into Paf1 Complex Assembly and Histone Binding
Nucleic Acids Research, **41** (2013) 10619.
- B.Cui, X.Yang, S.Li, Z.Lin, Z.Wang, C.Dong and Y.Shen
The Inhibitory Helix Controls the Intramolecular Conformational Switching of the C-Terminus of STIM1
PLOS ONE, **8** (2013) e74735.
- S.Aizawa, M.Senda, A.Harada, N.Maruyama, T.Ishida, T.Aigaki, A.Ishigami and T.Senda
Structural Basis of the γ -Lactone-Ring Formation in Ascorbic Acid Biosynthesis by the Senescence Marker Protein-30/Gluconolactonase
PLOS One, **8** (2013) e53706.

S.-Y.Jun, J.-S.Kim, K.-H.Choi, J.Cha and N.-C.Ha
Structure of a Novel α -Amylase AmyB from *Thermotoga neapolitana* that Produces Maltose from the Nonreducing End of Polysaccharides
Acta Cryst. D, **69** (2013) 442.

K.Harris, Q.-F.Sun, S.Sato and M.Fujita
M₁₂L₂₄ Spheres with Endo and Exo Coordination Sites: Scaffolds for Non-Covalent Functionalization
J. Am. Chem. Soc., **135** (2013) 12497.

H.Tanji, U.Ohto and T.Shimizu
Crystal Structures of Innate Immune RNA Receptor TLR8
J. Cryst. Soc. Jpn., **55** (2013) 285. (*in Japanese*).

NE5C

Y.Mori, Y.Kaihara, S.Nakamura, T.Yoshino and K.Takarabe
High-Pressure X-Ray Diffraction Study and Thermoelectric Measurements of Mg₂Si
Phys. Status Solidi C, **10** (2013) 1847.

NE7A

T.Matsushita, E.Arakawa, W.Voegeli and Y.F.Yano
A Simultaneous Multiple Angle-Wavelength Dispersive X-Ray Reflectometer Using a Bent-Twisted Polychromator Crystal
J. Synchrotron Rad., **20** (2013) 80.

E.Arakawa, W.Voegeli, T.Matsushita, Y.F.Yano and T.Hatano
Quick X-Ray Reflectometry in the Simultaneous Multiple Angle-Wavelength Dispersive Mode
J. Phys.: Conf. Ser., **425** (2013) 092002.

W.Voegeli, T.Matsushita, E.Arakawa, T.Shirasawa, T.Takahashi and Y.F.Yano
A Method for Measuring the Specular X-Ray Reflectivity with Millisecond Time Resolution
J. Phys.: Conf. Ser., **425** (2013) 092003.

H.Ito, S.Matsushita, K.Hyodo, Y.Sato and Y.Sakakibara
Using Synchrotron Radiation Angiography with a Highly Sensitive Detector to Identify Impaired Peripheral Perfusion in Rat Pulmonary Emphysema
J. Synchrotron Rad., **20** (2013) 376.

N.Yahaba, M.Koshimizu, T.Yanagida, Y.Fujimoto, R.Haruki, F.Nishikido, S.Kishimoto and K.Asai
X-Ray Detection Capability and Luminescence Property of Cs₂ZnCl₄ Single Crystal Scintillators
Houshasen Kagaku, **95** (2013) 27. (*in Japanese*).

M.Koshimizu, T.Yanagida, Y.Fujimoto, A.Yamazaki, K.Watanabe, A.Uritani, K.Fukuda, N.Kawaguchi, S.Kishimoto and K.Asai
Origin of Fast Scintillation Components of LiCaAlF₆ Crystals
Appl. Phys. Express, **6** (2013) 062601.

N.Sunaguchi, T.Yuasa, K.Hyodo and T.Zeniya
Fluorescent X-Ray Computed Tomography using the Pinhole Effect for Biomedical Applications
Optics Commun., **297** (2013) 210.

A.E.Gleason, C.E.Quiroga, A.Suzuki, R.Pentcheva and W.L.Mao
Symmetrization Driven Spin Transition in ϵ -FeOOH at High Pressure
Earth and Planetary Sci. Lett., **379** (2013) 49.

Y.F.Yano, E.Arakawa, W.Voegeli and T.Matsushita
Real-Time Investigation of Protein Unfolding at an Air-Water Interface at the 1 s Time Scale
J. Synchrotron Rad., **20** (2013) 980.

K.Sasaki, S.Matsushita, F.Sato, C.Tokunaga, K.Hyodo and Y.Sakakibara
Cardiac Sympathetic Activity Assessed by Heart Rate Variability Indicates Myocardial Ischemia on Cold Exposure in Diabetes
Ann. Vasc. Dis., **6** (2013) 583.

S.Ono, T.Kikegawa and Y.Higo
In Situ Observation of a Phase Transition in Fe₂SiO₄ at High Pressure and High Temperature
Phys. Chem. Minerals, **40** (2013) 811.

A.Suzuki
Compression Behavior of Manganite
Journal of Mineralogical and Petrological Sciences, **108** (2013) 295.

NW2A

M.Tada
Hard X-Ray Time-Resolved/Space-Resolved X-Ray Absorption Fine Structure Analysis for Heterogeneous Metal Catalysts
J. Phys. Soc. Jpn., **82** (2013) 021013.

S.Yamashita, M.Katayama and Y.Inada
Reduction Kinetics of Nickel Species Supported on Silica
J. Phys., Conf. Ser., **430** (2013) 012051.

M.Katayama, Y.Niwa, K.Do, S.Yamashita and Y.Inada
Kinetic Study of Reduction Reaction for Supported PdO Species by Means of Dispersive XAFS Method
J. Phys., Conf. Ser., **430** (2013) 012053.

W.Voegeli, T.Matsushita, E.Arakawa, T.Shirasawa, T.Takahashi and Y.F.Yano
A Method for Measuring the Specular X-Ray Reflectivity with Millisecond Time Resolution
J. Phys.: Conf. Ser., **425** (2013) 092003.

T.Asai, S.Otsuki, T.Taniguchi, K.Monde, K.Yamashita, H.Sakurai, T.Ozeki and Y.Oshima
Structures and Absolute Configurations of Short-Branched Fatty Acid Dimers from an Endophytic Fungus of *Aloe arborescens*
Tetrahedron Lett., **54** (2013) 3402.

D.Takahashi, K.Nakabayashi, S.Tanaka and S.Ohkoshi
Two-Dimensional Octacyano-Bridged Mn(II)-Nb(IV)
Bimetal Assembly with Four Different Configurations of
3-Hydroxypyridines
Inorg. Chem. Commun., **27** (2013) 47.

T.Morimoto, C.Nishiura, M.Tanaka, J.Rohacova,
Y.Nakagawa, Y.Funada, K.Koike, Y.Yamamoto,
S.Shishido, T.Kojima, T.Saeki, T.Ozeki and O.Ishitani
Ring-Shaped Re(I) Multinuclear Complexes with Unique
Photofunctional Properties
J. Am. Chem. Soc., **135** (2013) 13266.

H.Kitagawa, H.Ohtsu and M.Kawano
Kinetic Assembly of a Thermally Stable Porous
Coordination Network Based on Labile CuI Units and
the Visualization of I₂ Sorption
Angew. Chem. Int. Ed., **52** (2013) 12395.

J.-D.Compain, K.Nakabayashi and S.Ohkoshi
Multilayered Networks Built from Polyoxometalates and
Cyanometalates
Polyhedron, **66** (2013) 116.

M.Kimura, Y.Niwa, K.Uemura, T.Nagai, Y.Inada and
M.Nomura
In Situ and Simultaneous Observation of Palladium
Redox and Oxygen Storage/Release in Pd/Sr-Fe-O
Perovskite Catalysts using Dispersive XAFS
Materials Transactions, **54** (2013) 246.

T.Sawaki, T.Ishizuka, M.Kawano, Y.Shiota,
K.Yoshizawa and T.Kojima
Complete Photochromic Structural Changes in
Ruthenium(II)-Diimine Complexes, Based on Control of
the Excited States by Metalation
Chem. Eur. J., **19** (2013) 8978.

NW10A

T.Miyanaga, Y.Suzuki, N.Matsumoto, S.Narita, T.Ainai
and H.Hoshino,
Formation of Ag Clusters in Zeolite X Studied by in situ
EXAFS and Infrared Spectroscopy
Microporous and Mesoporous Material, **168** (2013) 213.

M.Tada
Hard X-Ray Time-Resolved/Space-Resolved X-Ray
Absorption Fine Structure Analysis for Heterogeneous
Metal Catalysts
J. Phys. Soc. Jpn., **82** (2013) 021013.

Y.Izumi
Recent Advances in Photocatalytic Conversion of Carbon
Dioxide into Fuels with Water and/or Hydrogen using
Solar Energy and Beyond
Coordination Chem. Rev., **257** (2013) 171.

S.Sugiyama, H.Tanaka, T.Bando, K.Nakagawa,
K.Sotowa, Y.Katou, T.Mori, T.Yasukawa and
W.Ninomiya
Liquid-Phase Oxidation of Propylene Glycol using
Heavy-Metal-Free Pd/C under Pressurized Oxygen
Catal. Today, **203** (2013) 116.

M.Nishi, T.Ohkubo, K.Tsurusaki, A.Itadani,
B.Ahmmad, K.Urita, I.Moriguchi, S.Kittaka and
Y.Kuroda
Highly Compressed Nanosolution Restricted in
Cylindrical Carbon Nanospaces
Nanoscale, **5** (2013) 2080.

M.Katayama, Y.Niwa, K.Do, S.Yamashita and Y.Inada
Kinetic Study of Reduction Reaction for Supported PdO
Species by Means of Dispersive XAFS Method
J. Phys., Conf. Ser., **430** (2013) 012053.

N.Ichikuni, Y.Nakao, K.Ishizuki, T.Hara and S.Shimazu
Effect of Local Structure of Mo Oxide on Selective Photo-
Oxidation of Propane to Acetone
Catal. Lett., **143** (2013) 154.

Y.Ohkubo, M.Shibata, S.Kageyama, S.Seino,
T.Nakagawa, J.Kugai and T.A.Yamamoto
Carbon-Supported AuPd Bimetallic Nanoparticles
Synthesized by High-Energy Electron Beam Irradiation
for Direct Formic Acid Fuel Cell
J. Mater. Sci., **48** (2013) 2142.

J.Kugai, T.Moriya, S.Seino, T.Nakagawa, Y.Ohkubo,
H.Nitani, K.Ueno and T.A.Yamamoto
Structure and Catalytic Performance of Pt-Cu Bimetallic
Catalysts Synthesized by Radiation-Induced Reduction
Method in Aqueous Phase: Influence of Support Material
and Sulfate Ion in the Precursor
J. Phys. Chem. C, **117** (2013) 5742.

J.Kugai, T.Moriya, S.Seino, T.Nakagawa, Y.Ohkubo,
H.Nitani and T.A.Yamamoto
Comparison of Structure and Catalytic Performance
of Pt-Co and Pt-Cu Bimetallic Catalysts Supported
in Al₂O₃ and CeO₂ Synthesized by Electron Beam
Irradiation Method for Preferential CO Oxidation
Int. J. Hydrogen Energy, **38** (2013) 4456.

J.Kugai, T.Moriya, S.Seino, T.Nakagawa, Y.Ohkubo,
H.Nitani and T.A.Yamamoto
Effect of CeO₂ Support Properties on Structure of Pt-Cu
Nanoparticles Synthesized by Electron Beam Irradiation
Method for Preferential CO Oxidation
Chem. Eng. J., **223** (2013) 347.

Y.J.Li, I.Nakai, Y.Amakai and S.Murayama
Relation between the Atomic Distance and the Valence
of Amorphous Ce_xRu_{100-x}
J. Phys.: Conf. Ser., **430** (2013) 012110.

- F.Rashidi, T.Sasaki, A.M.Rashidi, A.N.Kharat and K.J.Jozani
Ultradeep Hydrodesulfurization of Diesel Fuels using Highly Efficient Nanoalumina-Supported Catalysts: Impact of Support, Phosphorus, and/or Boron on the Structure and Catalytic Activity
J. Catal., **299** (2013) 321.
- K.Shiota, G.Imai, K.Oshita and M.Takaoka
Characterization of Lead, Chromium, and Cadmium in Dust Emitted from Municipal Solid Waste Incineration Plants
J. Phys.: Conf. Ser., **430** (2013) 012095.
- S.Muratsugu and M.Tada
Molecularly Imprinted Ru Complex Catalysts Integrated on Oxide Surfaces
Accounts of Chemical Research, **46** (2013) 300.
- B.Ahmmad, M.Nishi, F.Hirose, T.Ohkubo and Y.Kuroda
Structure of Hydrated Cobalt Ions Confined in the Nanospace of Single-Walled Carbon Nanotubes
Phys. Chem. Chem. Phys., **15** (2013) 8264.
- Y.Ohkubo, Y.Hamaguchi, S.Seino, T.Nakagawa, S.Kageyama, J.Kugai, H.Nitani, K.Ueno and T.A.Yamamoto
Preparation of Carbon-Supported PtCo Nanoparticle Catalysts for the Oxygen Reduction Reaction in Polymer Electrolyte Fuel Cells by an Electron-Beam Irradiation Reduction Method
J. Mater. Sci., **48** (2013) 5047.
- H.Narita, M.Tanaka, H.Shiwaku, Y.Okamoto, A.Ikeda-Ohno and T.Yaita
Inner-Sphere Structure of Rhodium Complexes with Tin(II) Chloride in Concentrated Hydrochloric Acid Solution
Bull. Chem. Soc. Jpn., **86** (2013) 203.
- T.Komanoya, H.Kobayashi, K.Hara, W.-J.Chun and A.Fukuoka
Simultaneous Formation of Sorbitol and Gluconic Acid from Cellobiose using Carbon-Supported Ruthenium Catalysts
J. Energy Chem., **22** (2013) 290.
- M.Harada, M.Yamada, Y.Kimura and K.Saijo
Influence of the Organization of Water-in-Ionic Liquid Microemulsions on the Size of Silver Particles during Photoreduction
J. Colloid Interface Sci., **406** (2013) 94.
- H.Einaga, Y.Teraoka and A.Ogata
Catalytic Oxidation of Benzene by Ozone over Manganese Oxides Supported on USY Zeolite
J. Catal., **305** (2013) 227.
- Y.Okamoto, M.Nakada, M.Akabori, S.Komamine, T.Fukui, E.Ochi, H.Nitani and M.Nomura
High-Temperature X-Ray Imaging Study of Simulated High-Level Waste Glass Melt
Electrochemistry, **81** (2013) 543.
- S.Sugiyama, T.Bando, Y.Seno, E.Watanabe, K.Nakagawa, M.Katoh, K-I.Sotowa, Y.Katou, S.Akihara and W.Ninomiya
The Oxidative Esterification of Propionaldehyde to Methyl Propionate in the Liquid-Phase Using a Heterogeneous Palladium Catalyst
J. Chem. Eng. Jpn., **46** (2013) 455.
- Y.Huang, H.Ariga, X.Zheng, X.Duan, S.Takakusagi, K.Asakura and Y.Yuan
Silver-Modulated SiO₂-Supported Copper Catalysts for Selective Hydrogenation of Dimethyl Oxalate to Ethylene Glycol
J. Catal., **307** (2013) 74.
- Y.Ohkubo, S.Kageyama, S.Seino, T.Nakagawa, J.Kugai, H.Nitani and T.A.Yamamoto
Radiolytic Synthesis of Carbon-Supported PtRu Nanoparticles Using High-Energy Electron Beam: Effect of pH Control on the PtRu Mixing State and the Methanol Oxidation Activity
J. Nanopart. Res., **15** (2013) 1597.
- A.Gallo, R.Psaro, M.Guidotti, V.D.Santo, R.D.Pergola, D.Masih and Y.Izumi
Cluster-Derived Ir-Sn/SiO₂ Catalysts for the Catalytic Dehydrogenation of Propane: a Spectroscopic Study
Dalton Transactions, **42** (2013) 12714.
- S.Muratsugu, M.H.Lim, T.Itoh, W.Thumrongpatanaraks, M.Kondo, S.Masaoka, T.S.A.Hor and M.Tada
Dispersed Ru Nanoclusters Transformed from a Grafted Trinuclear Ru Complex on SiO₂ for Selective Alcohol Oxidation
Dalton Trans., **42** (2013) 12611.
- Y.Sasada, T.Tajima, T.Wada, T.Uchida, M.Nishi, T.Ohkubo and Y.Takaguchi
Photosensitized Hydrogen Evolution from Water Using Single-Walled Carbon Nanotube/Fullerodendron/Pt(II) Coaxial Nanohybrids
New J. Chem., **37** (2013) 4214.
- N.Murata, T.Suzuki, M.Kobayashi, F.Togoh and K.Asakura
Characterization of Pt-Doped SnO₂ Catalyst for a High-Performance Micro Gas Sensor
Phys. Chem. Chem. Phys., **15** (2013) 17938.
- T.Ohkubo
Hydration and Coordination Structure of d-Block Metals Formed by the Confinement Effect of Carbon Micropores
Tanso, **260** (2013) 297. (*in Japanese*).

- K.Nitta, Y.Omori, T.Miyanaga, K.Takegahara, H.Sugawara, D.Kikuchi and H.Sato
Extended X-Ray Absorption Fine Structure Thermal Factor Analysis of Rattling in Filled Skutterudites RT₄Sb₁₂ (R: La, Ce, Pr, Nd, and Sm; T: Fe, Ru, and Os)
J. Phys. Soc. Jpn., **82** (2013) 044801.
- J.Ohyama, T.Sato, Y.Yamamoto, S.Arai and A.Satsuma
Size Specifically High Activity of Ru Nanoparticles for Hydrogen Oxidation Reaction in Alkaline Electrolyte
J. Am. Chem. Soc., **135** (2013) 8016.
- H.Yoshida, Y.Fujimura, H.Yuzawa, J.Kumagai and T.Yoshida
A Heterogeneous Palladium Catalyst Hybridised with a Titanium Dioxide Photocatalyst for Direct C-C Bond Formation between an Aromatic Ring and Acetonitrile
Chem. Comm., **49** (2013) 3793.
- M.Hirano, K.Enokida, K.Okazaki, S.Kuwabata, H.Yoshida and T.Torimoto
Composition-Dependent Electrocatalytic Activity of AuPd Alloy Nanoparticles Prepared *via* Simultaneous Sputter Deposition into an Ionic Liquid
Phys. Chem. Chem. Phys., **15** (2013) 7286.
- K.Tanimoto, H.Kato, M.Hidaka, S.Hinokuma, K.Ikeue and M.Machida
Nanometric Colloidal Sols of CeO₂-ZrO₂ Solid Solution as Catalyst Modifiers. I. Preparation and Structure
Bull. Chem. Soc. Jpn., **86** (2013) 1210.
- A.Itadani, Y.Sogawa, A.Oda, H.Torigoe, T.Ohkubo and Y.Kuroda
Further Evidence for the Existence of a Dual-Cu⁺ Site in MFI Working as the Efficient Site for C₂H₆ Adsorption at Room Temperature
Langmuir, **29** (2013) 9727.
- T.Hariu, H.Arima and K.Sugiyama
The Structure of Hydrated Copper-Silicate Gels, an Analogue Compound for Natural Chrysocolla
J. Min. Petrol. Sci., **108** (2013) 111.
- M.Kimura, Y.Niwa, K.Uemura, T.Nagai, Y.Inada and M.Nomura
In Situ and Simultaneous Observation of Palladium Redox and Oxygen Storage/Release in Pd/Sr-Fe-O Perovskite Catalysts using Dispersive XAFS
Materials Transactions, **54** (2013) 246.
- NW12A**
- A.Gao, G.-Y. Mei, S.Liu, P.Wang, Q.Tang, Y.-P. Liu, H.Wen, X.-M.An, L.-Q.Zhang, X.-X.Yan and D.-C.Liang
High-Resolution Structures of AidH Complexes Provide Insights into a Novel Catalytic Mechanism for *N*-Acyl Homoserine Lactonase
Acta Cryst. D, **69** (2013) 82.
- T.Yanagisawa, T.Sumida, R.Ishii and S.Yokoyama
A Novel Crystal Form of Pyrrolysyl-tRNA Synthetase Reveals the Pre- and Post-Aminoacyl-tRNA Synthesis Conformational States of the Adenylate and Aminoacyl Moieties and an Asparagine Residue in the Catalytic Site
Acta Cryst. D, **69** (2013) 5.
- S.Ha, J.Tong, H.Yang, H.-S.Youn, S.H.Eom and Y.J.Im
Crystallization and Preliminary X-Ray Crystallographic Analysis of Sterol Transcription Factor Upc2 from *Saccharomyces cerevisiae*
Acta Cryst. F, **69** (2013) 147.
- J.Nyirenda, S.Matsumoto, T.Saitoh, N.Maita, N.N.Noda, F.Inagaki and D.Kohda
Crystallographic and NMR Evidence for Flexibility in Oligosaccharyltransferases and its Catalytic Significance Structure, **21** (2013) 32.
- S.Arai, S.Saijo, K.Suzuki, K.Mizutani, Y.Kakinuma, Y.Ishizuka-Katsura, N.Ohsawa, T.Terada, M.Shirouzu, S.Yokoyama, S.Iwata, I.Yamato and T.Murata
Rotation Mechanism of *Enterococcus hirae* V₁-ATPase Based on Asymmetric Crystal Structures
Nature, **493** (2013) 703.
- H.Tanji, U.Ohto, T.Shibata, K.Miyake and T.Shimizu
Structural Reorganization of the Toll-Like Receptor 8 Dimer Induced by Agonistic Ligands
Science, **339** (2013) 1426.
- K.Makabe, T.Nakamura and K.Kuwajima
Structural Insights into the Stability Perturbations Induced by N-Terminal Variation in Human and Goat α -Lactalbumin.
Protein Eng. Design and Selection, **26** (2013) 165.
- D.F.Li, J.Y.Zhang, Y.J.Hou, L.Liu, Y.Hu, S.J.Liu, D.C.Wang and W.Liu
Structures of Aminophenol Dioxygenase in Complex with Intermediate, Product and Inhibitor
Acta Cryst. D, **69** (2013) 32.
- B.-C.Jeong, S.H.Park, K.S.Yoo, J.S.Shin and H.K.Song
Crystal Structure of the Single Cystathionine β -Synthase Domain-Containing Protein CBSX1 from *Arabidopsis thaliana*
Biochem. Biophys. Res. Commun., **430** (2013) 265.
- Y.Koga, M.Inazato, T.Nakamura, C.Hashikawa, M.Chirifu, A.Michi, T.Yamashita, S.Toma, A.Kuniyasu, S.Ikemizu, Y.Nakabeppu and Y.Yamagata
Crystallization and Preliminary X-Ray Analysis of Human MTH1 with a Homogeneous N-Terminus
Acta Cryst. F, **69** (2013) 45.
- J.Kondo, M.Koganei, J.P.Maianti, V.L.Ly and S.Hanessian
Crystal Structures of a Bioactive 6'-Hydroxy Variant of Sisomicin Bound to the Bacterial and Protozoal Ribosomal Decoding Sites
ChemMedChem, **8** (2013) 733.

- J.Otani, K.Arita, T.Kato, M.Kinoshita, H.Kimura, I.Suetake, S.Tajima, M.Ariyoshi and M.Shirakawa
Structural Basis of the Versatile DNA Recognition Ability of the Methyl-CpG Binding Domain of Methyl-CpG Binding Domain Protein 4
J. Biol. Chem., **288** (2013) 6351.
- A.Kobe, J.M.M.Caaveiro, S.Tashiro, D.Kajihara, M.Kikkawa, T.Mitani and K.Tsumoto
Incorporation of Rapid Thermodynamic Data in Fragment-Based Drug Discovery
J. Med. Chem., **56** (2013) 2155.
- N.N.Noda, Y.Fujioka, T.Hanada, Y.Ohsumi and F.Inagaki
Structure of the Atg12-Atg5 Conjugate Reveals a Platform for Stimulating Atg8-PE Conjugation
EMBO Reports, **14** (2013) 206.
- Y.Itoh, M.J.Bröcker, S.Sekine, G.Hammond, S.Suetsugu, D.Söll and S.Yokoyama
Decameric SelA•tRNA^{Sec} Ring Structure Reveals Mechanism of Bacterial Selenocysteine Formation
Science, **340** (2013) 75.
- Z.Fujimoto, R.Suzuki, T.Shitsuki, W.Tsuchiya, A.Tase, M.Momma and T.Yamazaki
Crystal Structure of Silkworm *Bombyx mori* JHBP in Complex with 2-Methyl-2,4-Pentanediol: Plasticity of JH-Binding Pocket and Ligand-Induced Conformational Change of the Second Cavity in JHBP
PLoS One, **8** (2013) e56261.
- Z.Fujimoto, A.Jackson, M.Michikawa, T.Maehara, M.Momma, B.Henrissat, H.J.Gilbert and S.Kaneko
The Structure of a *Streptomyces avermitilis* α -L-Rhamnosidase Reveals a Novel Carbohydrate-Binding Module CBM67 within the Six-Domain Arrangement
J. Biol. Chem., **288** (2013) 12376.
- T.Uejima, K.Ihara, M.Sunada, M.Kawasaki, T.Ueda, R.Kato, A.Nakano and S.Wakatsuki
Direct Metal Recognition by Guanine Nucleotide-Exchange Factor in the Initial Step of the Exchange Reaction
Acta Cryst. D, **69** (2013) 345.
- T.-Y.Jung, Y.-S.Kim, B.-H.Oh and E.Woo
Identification of a Novel Ligand Binding Site in Phosphoserine Phosphatase from the Hyperthermophilic Archaeon *Thermococcus onnurineus*
Proteins, **81** (2013) 819.
- M.Fujihashi, K.Mito, E.F.Pai and K.Miki
Atomic Resolution Structure of the Orotidine 5'-Monophosphate Decarboxylase Product Complex Combined with Surface Plasmon Resonance Analysis: Implication for the Catalytic Mechanism
J. Biol. Chem., **288** (2013) 9011.
- T.Ouchi, T.Tomita, A.Horie, A.Yoshida, K.Takahashi, H.Nishida, K.Lassak, H.Taka, R.Mineki, T.Fujimura, S.Kosono, C.Nishiyama, R.Masui, S.Kuramitsu, S.-V.Albers, T.Kuzuyama and M.Nishiyama
Lysine and Arginine Biosyntheses Mediated by a Common Carrier Protein in *Sulfolobus*
Nature Chemical Biology, **9** (2013) 277.
- Q.Chang, R.Nitta, S.Inoue and N.Hirokawa
Structural Basis for the ATP-Induced Isomerization of Kinesin
J. Mol. Biol., **425** (2013) 1869.
- C.Pathak, S.-B.Jang, H.Im, H.-J.Yoon and B.-J.Lee
Overexpression, Crystallization and Preliminary X-Ray Crystallographic Analysis of Hypothetical Protein SAV0479 from *Staphylococcus aureus* Mu50
Acta Cryst. F, **69** (2013) 405.
- A.Matsumoto, Y.Shimizu, C.Takemoto, T.Ueda, T.Uchiumi and K.Ito
Crystallization and Preliminary X-Ray Analysis of Peptidyl-tRNA Hydrolase from *Thermus thermophilus* HB8
Acta Cryst. F, **69** (2013) 332.
- M.Okai, J.Ohtsuka, L.F.Imai, T.Mase, R.Moriuchi, M.Tsuda, K.Nagata, Y.Nagata and M.Tanokura
Crystal Structure and Site-Directed Mutagenesis Analyses of Haloalkane Dehalogenase LinB from *Sphingobium* sp. Strain MI1205
J. Bacteriol., **195** (2013) 2642.
- T.Miyazaki, A.Nishikawa and T.Tonozuka
Novel Findings of the Structure and Substrate Specificity of Glucosidases Belonging to Glycoside Hydrolase Family 63
Oyo Toshitsu Kagaku, **3** (2013) 151. (*in Japanese*).
- H.Niwa, N.Handa, Y.Tomabechei, K.Honda, M.Toyama, N.Ohsawa, M.Shirouzu, H.Kagechika, T.Hirano, T.Umehara and S.Yokoyama
Structures of Histone Methyltransferase SET7/9 in Complexes with Adenosylmethionine Derivatives
Acta Cryst. D, **69** (2013) 595.
- T.Miyazaki, M.Yoshida, M.Tamura, Y.Tanaka, K.Umezawa, A.Nishikawa and T.Tonozuka
Crystal Structure of the N-Terminal Domain of a Glycoside Hydrolase Family 131 Protein from *Coprinopsis cinerea*
FEBS Lett., **587** (2013) 2193.
- T.Arimori, N.Kawamoto, S.Shinya, N.Okazaki, M.Nakazawa, K.Miyatake, T.Fukamizo, M.Ueda and T.Tamada
Crystal Structures of the Catalytic Domain of a Novel Glycohydrolase Family 23 Chitinase from *Ralstonia* sp. A-471 Reveals a Unique Arrangement of the Catalytic Residues for Inverting Chitin Hydrolysis
J. Biol. Chem., **288** (2013) 18696.

- Y.Nishitani, R.Aono, A.Nakamura, T.Sato, H.Atomi, T.Imanaka and K.Miki
Structure Analysis of Archaeal AMP Phosphorylase Reveals Two Unique Modes of Dimerization
J. Mol. Biol., **425** (2013) 2709.
- Y.Yagita, N.Kuse, K.Kuroki, H.Gatanaga, J.M.Carlson, T.Chikata, Z.L.Brumme, H.Murakoshi, T.Akahoshi, N.Pfeifer, S.Mallal, M.John, T.Ose, H.Matsubara, R.Kanda, Y.Fukunaga, K.Honda, Y.Kawashima, Y.Ariumi, S.Oka, K.Maenaka and M.Takiguchi
Distinct HIV-1 Escape Patterns Selected by Cytotoxic T Cells with Identical Epitope Specificity
J. Virol., **87** (2013) 2253.
- N.Maita, T.Tsukimura, T.Taniguchi, S.Saito, K.Ohno, H.Taniguchi and H.Sakuraba
Human α -L-Iduronidase Uses its Own N-Glycan as a Substrate-Binding and Catalytic Module
Proc. Natl. Acad. Sci. USA, **110** (2013) 14628.
- A.Miyanaga, S.Fujisawa, N.Furukawa, K.Arai, M.Nakajima and H.Taguchi
The Crystal Structure of D-Mandelate Dehydrogenase Reveals its Distinct Substrate and Coenzyme Recognition Mechanisms from those of 2-Ketopantoate Reductase
Biochem. Biophys. Res. Commun., **439** (2013) 109.
- T.Miyazaki, M.Ichikawa, G.Yokoi, M.Kitaoka, H.Mori, Y.Kitano, A.Nishikawa and T.Tonozuka
Structure of a Bacterial Glycoside Hydrolase Family 63 Enzyme in Complex with its Glycosynthase Product, and Insights into the Substrate Specificity
FEBS J., **280** (2013) 4560.
- T.Hirose, N.Maita, H.Gouda, J.Koseki, T.Yamamoto, A.Sugawara, H.Nakano, S.Hirono, K.Shioimi, T.Watanabe, H.Taniguchi, K.B.Sharpless, S.Omura and T.Sunazuka
Observation of the Controlled Assembly of Preclick Components in the in situ Click Chemistry Generation of a Chitinase Inhibitor
Proc. Natl. Acad. Sci. USA, **110** (2013) 15892.
- Y.Matsumoto, Y.Yasutake, Y.Takeda, T.Tamura, A.Yokota and M.Wada
Crystallization and Preliminary X-Ray Diffraction Studies of D-threo-3-Hydroxyaspartate Dehydratase Isolated from *Delftia* sp. HT23
Acta Cryst. F, **69** (2013) 1131.
- A.Nakamura, T.Ishida, S.Fushinobu, K.Kusaka, I.Tanaka, K.Inaka, Y.Higuchi, M.Masaki, K.Ohta, S.Kaneko, N.Niimura, K.Igarashi and M.Samajima
Phase-Diagram-Guided Method for Growth of a Large Crystal of Glycoside Hydrolase Family 45 Inverting Cellulase Suitable for Neutron Structural Analysis
J. Synchrotron Rad., **20** (2013) 859.
- S.Fushinobu, V.D.Alves and P.M.Coutinho
Multiple Rewards from a Treasure Trove of Novel Glycoside Hydrolase and Polysaccharide Lyase Structures: New Folds, Mechanistic Details, and Evolutionary Relationships
Curr. Opin. Struct. Biol., **23** (2013) 652.
- K.Suzuki, J.Sumitani, Y-W.Nam, T.Nishimaki, S.Tani, T.Wakagi, T.Kawaguchi and S.Fushinobu
Crystal Structures of Glycoside Hydrolase Family 3 β -Glucosidase 1 from *Aspergillus aculeatus*
Biochem. J., **452** (2013) 211.
- C.Pathak, H.Im, Y.-J.Yang, H.-J.Yoon, H.-M.Kim, A.-R.Kwon and B.-J.Lee
Crystal Structure of Apo and Copper Bound HP0894 Toxin from *Helicobacter pylori* 26695 and Insight into mRNase Activity
Biochimica et Biophysica Acta, **1834** (2013) 2579.
- Z.Fujimoto
Structure and Function of Carbohydrate-Binding Module Families 13 and 42 of Glycoside Hydrolases, Comprising a β -Trefold Fold
Biosci. Biotechnol. Biochem., **77** (2013) 1363.
- N.Suzuki, Y.-M.Kim, M.Momma, Z.Fujimoto, M.Kobayashi, A.Kimura and K.Funane
Crystallization and Preliminary X-Ray Crystallographic Analysis of Cycloisomaltotooligosaccharide Glucanotransferase from *Bacillus circulans* T-3040
Acta Cryst. F, **69** (2013) 946.
- M.Yamada, T.Tamada, K.Takeda, F.Matsumoto, H.Ohno, M.Kosugi, K.Takaba, Y.Shoyama, S.Kimura, R.Kuroki and K.Miki
Elucidations of the Catalytic Cycle of NADH-Cytochrome b_5 Reductase by X-Ray Crystallography: New Insights into Regulation of Efficient Electron Transfer
J. Mol. Biol., **425** (2013) 4295.
- J.Nomura, H.Hashimoto, T.Ohta, Y.Hashimoto, K.Wada, Y.Naruta, K-I.Oinuma and M.Kobayashi
Crystal Structure of Aldoxime Dehydratase and its Catalytic Mechanism Involved in Carbon-Nitrogen Triple-Bond Synthesis
Proc. Natl. Acad. Sci. USA, **110** (2013) 2810.
- K.Takemoto, T.Matsuda, N.Sakai, D.Fu, M.Noda, S.Uchiyama, I.Kotera, Y.Arai, M.Horiuchi, K.Fukui, T.Ayabe, F.Inagaki, H.Suzuki and T.Nagai
SuperNova, a Monomeric Photosensitizing Fluorescent Protein for Chromophore-Assisted Light Inactivation.
Sci. Rep., **3** (2013) 2629.
- T.Mori, Y.Shimokawa, T.Matsui, K.Kinjo, R.Kato, H.Noguchi, S.Sugio, H.Morita and I.Abe
Cloning and Structure-Function Analyses of Quinolone- and Acridone-Producing Novel Type III Polyketide Synthases from *Citrus microcarpa*
J. Biol. Chem., **288** (2013) 28845.

- Y.Yasutake, T.Nishioka, N.Imoto and T.Tamura
A Single Mutation at the Ferredoxin Binding Site of P450 Vdh Enables Efficient Biocatalytic Production of 25-Hydroxyvitamin D₃
ChemBioChem, **14** (2013) 2284.
- J.Matsuzawa, T.Umeda, H.Aikawa, C.Suzuki, Z.Fujimoto, K.Okada, H.Yamane and H.Nojiri
Crystallization and Preliminary X-Ray Diffraction Studies of the Reduced Form of the Terminal Oxygenase Component of the Rieske Nonhaem Iron Oxygenase System Carbazole 1, 9a-Dioxygenase.
Acta Cryst. F, **69** (2013) 1284.
- Y.Kanemaru, F.Hasebe, T.Tomita, T.Kuzuyama and M.Nishiyama
Two ATP-Binding Cassette Transporters Involved in (*S*)-2-Aminoethyl-Cysteine Uptake in *Thermus thermophilus*
J. Bacteriology, **195** (2013) 3845.
- Y.Itoh, M.J. Bröcker, S.Sekine, G.Hammond, S.Suetsugu, D.Söll and S.Yokoyama
Decameric SelA-tRNA^{Sec} Ring Structure Reveals Mechanism of Bacterial Selenocysteine Formation
Science, **340** (2013) 75.
- A.Nishikimi, M.Kukimoto-Niino, S.Yokoyama and Y.Fukui
Immune Regulatory Functions of DOCK Family Proteins in Health and Disease
Experimental Cell Research, **319** (2013) 2343.
- B.-C.Jeong, S.H.Park, K.S.Yoo, J.S.Shin and H.K.Song
Change in Single Cystathionine β -Synthase Domain-Containing Protein from a Bent to Flat Conformation upon Adenosine Monophosphate Binding
J. Struct. Biol., **183** (2013) 40.
- K.H.Sung, S.Y.Lee and H.K.Song
Structural and Biochemical Analyses of the Eukaryotic Heat Shock Locus V(HslV) from *Trypanosoma brucei*
J. Biol. Chem., **288** (2013) 23234.
- M.Unno, A.Ardèvol, C.Rovira and M.Ikeda-Saito
Structures of the Substrate-Free and Product-Bound Forms of HmuO, a Heme Oxygenase from *Corynebacterium diphtheriae*: X-Ray Crystallography and Molecular Dynamics Investigation
J. Biol. Chem., **288** (2013) 34443.
- T.Ogawa, K.Noguchi, M.Saito, Y.Nagahata, H.Kato, A.Ohtaki, H.Nakayama, N.Dohmae, Y.Matsushita, M.Odaka, M.Yohda, H.Nyunoya and Y.Katayama
Carbonyl Sulfide Hydrolase from *Thiobacillus thioparvus* Strain TH115 Is One of the β -Carbonic Anhydrase Family Enzymes
J. Am. Chem. Soc., **135** (2013) 3818.
- A.Shimizu, A.Kawana-Tachikawa, A.Yamagata, C.Han, D.Zhu, Y.Sato, H.Nakamura, T.Koibuchi, J.Carlson, E.Martin, C.J.Brumme, Y.Shi, G.F.Gao, Z.L.Brumme, S.Fukai and A.Iwamoto
Structure of TCR and Antigen Complexes at an Immunodominant CTL Epitope in HIV-1 Infection
Sci. Rep., **3** (2013) 3097.
- M.Kato, Y.Kezuka, C.Kobayashi, K.Ishibashi, T.Nonaka, M.Ishikawa and E.Katoh
Crystallization and Preliminary X-Ray Crystallographic Analysis of the Inhibitory Domain of the Tomato Mosaic Virus Resistance Protein Tm-1
Acta Cryst. F, **69** (2013) 1411.
- T.Tominaga, S.Watanabe, R.Matsumi, H.Atomi, T.Imanaka and K.Miki
Crystal Structures of the Carbamoylated and Cyanated Forms of HypE for [NiFe] Hydrogenase Maturation
Proc. Natl. Acad. Sci. USA, **110** (2013) 20485.
- R.Satou, A.Miyanaga, H.Ozawa, N.Funa, Y.Katsuyama, K.Miyazono, M.Tanokura, Y.Ohnishi and S.Horinouchi
Structural Basis for Cyclization Specificity of Two *Azotobacter* Type III Polyketide Synthases: A Single Amino Acid Substitution Reverses their Cyclization Specificity
J. Biol. Chem., **288** (2013) 34146.
- H.M.Qin, A.Yamamura, T.Miyakawa, M.Kataoka, S.Maruoka, J.Ohtsuka, K.Nagata, S.Shimizu and M.Tanokura
Crystal Structure of Conjugated Polyketone Reductase(CPR-C1) from *Candida parapsilosis* IFO 0708 Complexed with NADPH
Proteins, **81** (2013) 2059.
- T.Miyakawa, Y.Sawano, K.Miyazono, Y.Miyauchi, K.Hatano and M.Tanokura
A Thermoacidophile-Specific Protein Family, DUF3211, Functions as a Fatty Acid Carrier with Novel Binding Mode
J. Bacteriol., **195** (2013) 4005.
- T.Tsurumura, Y.Tsumori, H.Qiu, M.Oda, J.Sakurai, M.Nagahama and H.Tsuge
Arginine ADP-Ribosylation Mechanism Based on Structural Snapshots of Iota-Toxin and Actin Complex
Proc. Natl. Acad. Sci. USA, **110** (2013) 7524.
- T.Tsurumura, H.Qiu, T.Yoshida, Y.Tsumori, D.Hatakeyama, T.Kuzuhara and H.Tsuge
Conformational Polymorphism of m⁷GTP in Crystal Structure of the PB2 Middle Domain from Human Influenza A Virus
PLoS ONE, **8** (2013) e82020.
- X.Xu, X.Wang, Y.Zhang, D.C.Wang and J.Ding
Structural Basis for the Unique Heterodimeric Assembly between Cerebral Cavemous Malformation 3 and Germinal Center Kinase III
Structure, **21** (2013) 1059.

H.M.Ta, S.Bae, S.Han, J.Song, T.K.Ahn, S.Hohng, S.Lee and K.K.Kim

Structure-Based Elucidation of the Regulatory Mechanism for Aminopeptidase Activity
Acta Cryst. D, **69** (2013) 1738.

H.Tanji, U.Ohto and T.Shimizu

Crystal Structures of Innate Immune RNA Receptor TLR8

J. Cryst. Soc. Jpn., **55** (2013) 285. (*in Japanese*).

T.Shimizu

Structural Basis for β -Galactosidase Associated with Lysosomal Disease

Yakugaku Zasshi, **133** (2013) 509. (*in Japanese*).

L.M.G.Chavas, T.Nagae, H.Yamada, N.Watanabe, Y.Yamada, M.Hiraki and N.Matsugaki

New Methodologies at PF AR-NW12A: the Implementation of High-Pressure Macromolecular Crystallography

J. Synchrotron Rad., **20** (2013) 838.

L.M.G.Chavas, Y.Yamada, M.Hiraki, N.Igarashi, N.Matsugaki and S.Wakatsuki

10 Years of Protein Crystallography at AR-NW12A Beamline

J. Phys.: Conf. Ser., **425** (2013) 012008.

NW14A

Y.Moritomo, H.Kamioka, T.Shibata, S.Noizawa, T.Sato and S.Adachi

Photoinduced Phase Transition into a Hidden Phase in Cobalt Hexacyanoferrate as Investigated by Time-Resolved X-Ray Absorption Fine Structure

J. Phys. Soc. Jpn., **82** (2013) 033601.

M.Hoshino

Visualization of an Organic Photocatalyst 'in Action' by a Pump-Probe Single Crystal X-Ray Structure Analysis

J. Cryst. Soc. Jpn., **55** (2013) 2. (*in Japanese*).

T.Sato

The Structure of $^3\text{MLCT}$ State of $[\text{Ru}^{\text{II}}(\text{bpy})_3]^{2+}$ in Aqueous Solution Observed by Time-Resolved XAFS

J. Cryst. Soc. Jpn., **55** (2013) 14. (*in Japanese*).

H.Sekiguchi, A.Nakagawa, K.Moriya, K.Makabe, K.Ichiyanagi, S.Noizawa, T.Sato, S.Adachi, K.Kuwajima, M.Yohda and Y.C.Sasaki

ATP Dependent Rotational Motion of Group II Chaperonin Observed by X-Ray Single Molecule Tracking

PLoS ONE, **8** (2013) e64176.

K.H.Kim, J.H.Lee, J.Kim, S.Noizawa, T.Sato, A.Tomita, K.Ichiyanagi, H.Ki, J.Kim, S.Adachi and H.Ihee

Solvent-Dependent Molecular Structure of Ionic Species Directly Measured by Ultrafast X-Ray Solution Scattering

Phys. Rev. Lett., **110** (2013) 165505.

M.Hoshino, S.Noizawa, T.Sato, A.Tomita, S.Adachi and S.Koshihara

Time-Resolved X-Ray Crystal Structure Analysis for Elucidating the Hidden 'Over-Neutralized' Phase of TTF-CA

RSC Adv., **3** (2013) 16313.

M.Hoshino

Observation of a Three-Dimensional Molecular Structure at a Photo-Excited State by Pump-Probe Single Crystal X-Ray Structure Analysis

Hyomen Kagaku, **34** (2013) 598. (*in Japanese*).

K.H.Kim, H.Ki, K.Y.Oang, S.Noizawa, T.Sato, J.Kim, T.K.Kim, J.Kim, S.Adachi and H.Ihee

Global Reaction Pathways in the Photodissociation of I_3^- Ions in Solution at 267 and 400 nm Studied by Picosecond X-Ray Liquidography

ChemPhysChem, **14** (2013) 3687.

J.Hu, K.Ichiyanagi, T.Doki, A.Goto, T.Eda, K.Norimatsu, S.Harada, D.Horiuchi, Y.Kabasawa, S.Hayashi, S.Uozumi, N.Kawai, S.Noizawa, T.Sato, S.Adachi and K.G.Nakamura

Complex Structural Dynamics of Bismuth under Laser-Driven Compression

Appl. Phys. Lett., **103** (2013) 161904.

SPF

H.Terabe, S.Iida, K.Wada, T.Hyodo, A.Yagishita and Y.Nagashima

Efficient Emission of Positronium Atoms from a Na-Coated Polycrystalline Tungsten Surface

J. Phys. Conf. Ser., **443** (2013) 012075.

Y.Fukaya, I.Mochizuki, M.Maekawa, K.Wada, T.Hyodo, I.Matsuda and A.Kawasuso

Structure of Silicene on a Ag(111) Surface Studied by Reflection High-Energy Positron Diffraction

Phys. Rev. B, **88** (2013) 205413.